University of Belgrade

National and Kapodistrian University of Athens

Nenad Vranješ

A SEARCH FOR NEW HEAVY CHARGED GAUGE BOSONS AT ATLAS

Doktorska disertacija
A dissertation submitted in fulfilment of the requirements for the degree of Doctor of Philosophy in Physics

Belgrade, Athens

July 2011

Apstrakt

U tezi su prikazani rezultati traganja za novim teškim naelektrisanim gradijentnim bozonima na Velikom hadronskom kolajderu. Rezultati su dobijeni analiziranjem 36 pb^{-1} podataka iz proton-proton sudara na energiji 7 TeV prikupljenih na detektoru ATLAS tokom 2010. godine. Postojanje novih gradijentnih bozona je predviđeno u mnogim proširenjima Standardnog modela. Rezultati u ovoj doktorskoj disertaciji su dobijeni koristeći model u kome novi teški naelektrisani gradijentni bozon (W') predstavlja kopiju W bozona iz Standardnog modela: sprezanja W' sa fermionima su ista kao kod W bozona, a interakcije sa drugim gradijentnim bozonima su zabranjene. Pored ovog modela, razmatran je i model u kome se novi bozon (označen sa W^*) pojavljuje kao naelektrisani partner hiralnih bozona. Izučavani su leptonski kanali raspada W' i W^* čiju eksperimentalnu signaturu čine prisustvo tačno jednog leptona (miona ili elektrona) vrlo velikog transverzalnog impulsa i velika nedostajuća transverzalna energija koja potiče od neutrina.

Za selekciju događaja iz raspada $W'(W^*)$ korišćena je raspodela transverzalne mase, pošto se longitudinalna komponenta energije neutrina ne može rekonstruisati, U tezi su analizirane karaketeristike objekata potrebnih za rekonstrukciju transverzalne mase $W'(W^*)$. Najpre su analizirane karakteristike rekonstrukcije miona u podacima prikupljenim krajem 2009. godine i tokom 2010. godine, i uspostavljeni su selekcioni uslovi koji omogućavaju efikasnu rekonstrukciju miona velikog impulsa uz dobru rezoluciju. Pored toga, analizirani su kriterijumi za identifikaciju elektrona i uspostavljeni selekcioni uslovi za suzbijanje fona koji potiče od lažnih leptona visokog impulsa.

Nivo glavnih fonskih procesa, W/Z i $t\bar{t}$, je procenjen korišćenjem teorijskog preseka u NNLO aproksimaciji i Monte Karlo simulacija. Nivo fona koji potiče od kosmičkog zračenja kao i fona od produkcije džetova, procenjen je direktno iz podataka i pokazano je da taj doprinos mali u odnosu na glavne fonske procese. Efikasnost za rekonstrukciju signala i nivo glavnih fonskih procesa korigovani su kako bi se uračunale razlike između Monte Karlo simulacija i podataka iz protonskih sudara.

Dobijeni rezultati su konzistentni sa predviđanjima Standardnog modela. Pošto novi gradi-

jentni bozoni nisu pronađeni, izračunati su gornji limiti na presek za produkciju $W'(W^*)$ pomnožen faktorom grananja za leptone (σB). Limiti na σB na nivou poverenja 95% C.L. izračunati su za mionski i elektronski kanal, kao i za kombinaciju dva kanala. Iz kombinacije dobijenih limita i zavisnosti σB od mase novog gradijentnog bozona, dobijeni su donji maseni limiti za W' bozon ($m_{W'} > 1.49$ TeV) i W^* ($m_{W^*} > 1.35$ TeV). Dobijeni maseni limit na W' je znatno uvećan u odnosu na limit dobijen na Tevatronu, dok limit na W^* predstavlja prvi direktni limit za ovaj tip bozona. Takođe, prikazani su i preliminarni rezultati traganja za W' bozonom dobijene kombinacijom podatka iz proton-proton sudara u 2010. i 2011. godini. Podaci nisu pokazali statistički značajno odstupanje od predviđanja SM, a maseni limit je uvećan na $m_{W'} > 1.70$ TeV. Na kraju su analizirane mogućnosti za detekciju W' bozona u zavisnosti od energije sudara i količine prikupljenih podataka na LHC-u u narednom periodu.

Contents

List of Figures

List of Tables

Chapter 1

Introduction

Standard Model of elementary particles (SM) has had enormous phenomenological success during the past half of century. All fermions predicted by the SM were discovered, and existence of all gauge bosons, the mediators of the three forces (weak, strong and electromagnetic) was established. Despite increasingly accurate and precise experiments, no significant deviation between the Standard Model predictions and experimental data could be established. However, it is generaly believed that Standard Model is a low energy limit of a more general theory. One intriguing feature of SM lays in fact that charged current of the weak interaction is restricted to left-handed particles only. The extension by a right-handed sector has not only aesthetic reasons, but it provides a mechanism for parity violation which has to be implemented by hand in the Standard Model. Further, increasing amount of data from neutrino experiments seems to confirm existence of a new phenomenon: mixing between neutrino families, known also as neutrino oscillations. Neutrino oscillations are not possible if neutrinos are massless particles, as they are in the Standard Model. On top of this, unnatural fine tuning of the SM parameters is required in order to keep the mass of hypothetical Higgs boson stable when extrapolating to the very high energies where the unification of the three forces should occur. It is however, generally known that SM itself does not provide unification of three forces at very high energy scale. Numerous theories are studied in order to address at least some of the opened issues. One attractive way to go beyond SM is by enlarging its gauge group $SU(3)_c \otimes SU(2)_L \otimes U(1)_Y$, either by creating new symmetries or by unifying the symmetries already recognized. A consequence of the enlarging SM gauge group, common to many models, is the existance of additional heavy gauge bosons, the charged ones commonly denoted W'. Many of these theories and models indicate that new phenomena are likely to appear at the TeraElectronVolt (TeV) scale. Direct probe of TeV scale is possible with the Large Hadron Collider (LHC) at CERN, the world most powerful accelerator in terms of energy and collision rate.

This thesis was carried out within the collaboration of the ATLAS experiment, one of two general purpose experiments at the LHC. In the thesis a search for a new heavy charged gauge boson with its subsequent decay into a lepton (a muon or an electron) and a neutrino is studied. The analysis is performed with data taken between March and October 2010 corresponding to an integrated luminosity of about 36 pb^{-1} . This was the first year of LHC operation at the center of mass collision energy of 7 TeV. The search for new gauge boson has been optimized using, as benchmark, the model in which W' has the same couplings to fermions as Standard Model W boson, with ineteractions with other gauge bosons excluded. Thus, the total (and partial) widths increase linearly with W' mass. Prior to data taking at 7 TeV, evaluation of the discovery potential, as well as exclusion power, have been performed using state of the art simulation of the ATLAS detector. The results indicated that even with a modest amount of data, it is possible to discover or exclude W' above its stringent mass limit set by the Tevatron collider to be of about 1.1 TeV. In addition to W', another model, in which new gauge boson (W^*) represents the charged partner to the chiral bosons, has been considered. Magnetic moment type coupling of W^* leads to kinematic distributions quite different from those of W', and the results presented here correspond to the first direct search for this type of boson.

The signal in this search is characterized by events with a high lepton-neutrino mass. This mass is not observable because the longitudinal momentum of the neutrino cannot be measured by the detector. However, the transverse components of the neutrino momentum can be estimated from the missing transverse energy($\not{E}_T$) in the event and combined with the transverse momentum of the lepton (p_T) to define the transverse mass:

$$m_{\mathrm{T}} = \sqrt{2 p_T \not{E}_T (1 - \cos\varphi)} \tag{1.1}$$

where φ is the angle between the transverse momentum of the lepton and the $\not{E}_T$. The transverse mass has a Jacobian peak which falls sharply at the W' mass. Hence, m_{T} serves as the primary discriminant for identifying W' candidates. The same discriminant is used for the search for W^* boson.

The thesis is structured as follows. In the next chapter an overview of the Standard Model and the motivation for the existence of the phenomena beyond SM is given. The so-called reference model containing benchmark W' is briefly described, as well as W^* model. In the third chapter the simulation of the W' (and W^*) at the LHC is explained. In this chapter, author's results on the evaluation of the higher order corrections to the W' production cross section with detail study on the related systematic uncertainties are described. ATLAS detector, including all relevant detector systems, trigger, data quality and simulation and computing infrastructure

are described in Chapter 4. Relevant results concerning readiness of ATLAS for the data taking obtained from studies with cosmic rays are also discussed. Chapter 5 is the central part of the thesis, containing most of the results which the candidate has obtained during the study of 2009 and 2010 data. Muon reconstruction at ATLAS addressing chalenges for measurement of very high-p_T muon is presented, as well as author's work on the performance of muon reconstruction with first collision data at 900 GeV and on tuning muon selection in W' search. Studies of differences from data to simulation as well as other applied selection cuts are addressed here as well. Uncorrected results for the $W' \to \mu\nu (W^* \to \mu\nu)$ search are presented in this chapter, and possible additional selection requirements are discussed. In Chapter 6, data driven estimation of the cosmic and background arising from QCD multijet production are presented. Detector related systematic uncertainties for signal and background, and higher order corrections and theoretical uncertainties for the background are evaluated. Final results and uncertainties for the muon channel are given at the end of this chapter. Electron identification, and electron selection requirements applied to select high mass electron-neutrino candidates are discussed in Chapter 7. Corrected results and final systematic uncertainties for $W' \to e\nu$ (and $W^* \to e\nu$) search can be found here. Since no excess above SM prediction is observed, limits on $W' \to \ell\nu$ and $W^* \to \ell\nu$ production are given in Chapter 8 titled Limits and Prospects. The obtained cross section limits are converted into mass limits on the new bosons presenting mass reach obtained with ATLAS using 2010 dataset. Prospects for discovery reach as well as exclusion potential within some possible LHC running scenarios in the coming period are presented at the end of this Chapter. Concluding remarks are given at the end.

Chapter 2

Theoretical Foundations

2.1 Standard Model

A brief overview of the Standard Model of electroweak and strong interactions is given in this section. More formal aspects and details of the model can be found in the vast literature on this subject, from various textbooks and school proceedings [1] to reviews [2].

2.1.1 Standard Model in brief

Standard Model [3] includes the Glashow-Salam-Weinberg (GSW) theory as the unified theory of the electromagnetic and weak interactions, and quantum chromodynamics (QCD) as the theory of the strong interactions. Both GSW and QCD are non-Abelian gauge theories, based on the principle of local gauge invariance. The gauge symmetry group of the GSW theory is $SU(2)_L \otimes U(1)_Y$ with the quantum numbers weak isospin and hypercharge, while $SU(3)_c$ is gauge symmetry group of QCD with color as the corresponding quantum number. The subscripts indicate the quantum numbers: L stands for left-handed weak isospin, Y for weak hypercharge and c for the color charge.

According to the gauge symmetry groups there are eight massless gluons mediating the strong interactions, one massless photon for the electromagnetic interaction and three vector bosons $W^{\pm}$ and Z^0 for the charged and neutral weak interactions. These bosons are usually collectively denoted as gauge bosons because their existence is a direct consequence of local gauge invariance. The weak vector bosons acquire their masses by the spontaneous breaking of the electroweak symmetry group. The matter particles have spin-$\frac{1}{2}$ and are grouped into famous three families of quarks and leptons with identical characteristics but increasing mass. The fermions appear as left-handed and right-handed states, except for the neutrinos(antineutrinos)

which in the SM are only left-handed (right-handed) and massless. The left-handed fermions are grouped in isodoublets, the right-handed fermions are isosinglets. The quark generations are mixed by the charged weak currents. This quark mixing is described by the Cabibbo-Kobayashi-Maskawa (CKM) matrix[4] which is parametrized by three mixing angles and a $CP-$violating phase. In the present formulation of the SM there is no mixing between lepton families. While this is true to a high accuracy for the charged leptons, compelling experimental data show this is not true for the neutrino sector because neutrino oscillations occur (for the review see [5]). The particle content of the Standard Model is presented in Tables 2.1 and 2.2.

Table 2.1: A summary table of fundamental fermions in the Standard Model. The quantum numbers shown represent spin (s), weak isospin (T), third component of weak isospin (T_3), electric charge (Q) and weak hypercharge (Y). Antiparticles (except for neutrinos) are not presented. Each quark has 3 colour states.

Family	I	II	III	s	T	T_3	Q	Y
Leptons	$\begin{pmatrix} \nu_e \\ e^- \end{pmatrix}_L$	$\begin{pmatrix} \nu_\mu \\ \mu^- \end{pmatrix}_L$	$\begin{pmatrix} \nu_\tau \\ \tau^- \end{pmatrix}_L$	1/2 1/2	1/2 1/2	1/2 -1/2	0 -1	-1 -1
	$\bar{\nu}_R^e$	$\bar{\nu}_R^\mu$	$\bar{\nu}_R^\tau$	1/2	0	0	0	0
	e_R^-	μ_R^-	τ_R^-	1/2	0	0	-1	-2
Quarks	$\begin{pmatrix} u \\ d \end{pmatrix}_L$	$\begin{pmatrix} c \\ s \end{pmatrix}_L$	$\begin{pmatrix} t \\ b \end{pmatrix}_L$	1/2 1/2	1/2 1/2	1/2 -1/2	2/3 -1/3	1/3 1/3
	u_R	c_R	t_R	1/2	0	0	2/3	4/3
	d_R	s_R	b_R	1/2	0	0	-1/3	-2/3

The gauge symmetry group of the GSW theory is spontaneously broken via the Higgs mechanism from $SU(2)_L \otimes U(1)_Y$ to the electromagnetic $U(1)_{em}$. The spontaneous breaking of the electroweak symmetry is achieved by introducing one doublet of complex scalar Higgs fields [7]. This is the minimum number of Higgs fields necessary to spontaneously break the $SU(2) \otimes U(1)$ symmetry and to introduce the mass terms for all particles apart from the neutrinos. After spontaneous symmetry breaking there remains one neutral scalar Higgs particle as physical state. The other three scalar fields become the longitudinal components of the massive $W^\pm$ and Z^0 bosons.

Table 2.2: Boson sector of the Standard Model. Masses are obtained from[6].

Boson	Mass [GeV]	Electric charge	Spin	Interaction
gluon, g	0	0	1	Strong
photon, γ	0	0	1	Electromagnetic
Z	91.188 ± 0.002	0	1	Weak
W	80.399 ± 0.023	± 1	1	Weak
Higgs, H	?	0	0	-

The formulation of the Standard Model constitutes a remarkable intellectual achievement of the twentieth century. The formulation of the theory as a renormalizable quantum theory[8] preserves its predictive power beyond tree-level computations and allows for the probing of quantum effects. An array of experimental results confirm every feature of the theory to a high degree of precision, at the level of testing higher order perturbation theory[9].

2.1.2 Gauge invariance

Recognizing symmetry in nature and deducing its implications for the elementary particles and their interactions is of fundamental importance. Equation of motion derived from the variation principle makes general and systematic procedure available for establishing conservation laws and constants of motion as a consequence of invariant properties. Conversely observed laws and selection rules may be imposed as symmetries of the Lagrangian restricting or prescribing its form. The general framework for this program is provided by Noethere's theorem[10] which correlates any continuous symmetry transformation (under which Lagrangian is invariant in form) with a conservation law.

The first important class of symmetries are so called global symmetries where a global gauge transformation applied to the equation of motion keeps it unchanged. In other words doesn't affect any observable quantity. The global symmetries make physics invariant under translations, rotations and constant motion with respect to any inertial frame implying energy, momentum and angular momentum are conserved. The second class of symmetries are local symmetries where gauge transformation applied to the to the equation of motion keeping it unchanged is a function of space-time (position).

The simplest case of local gauge invariance is demonstrated on the fermionic field ψ of mass m described by the Lagrange density equation:

$$\mathscr{L}_{\mathrm{f}} = \overline{\psi}(x)(i\gamma^{\mu}\partial_{\mu} - m)\psi(x) \tag{2.1}$$

with $\psi = \psi^+\gamma^0$ ($\hbar = 1 = c$). Applying the Euler-Lagrange-formalism to $\mathscr{L}_\mathrm{f}$ one gets the well known Dirac equation for the free motion of fermion ψ without interaction:

$$(i\gamma^\mu\partial_\mu - m)\psi(x) = 0. \tag{2.2}$$

The Dirac equation is invariant under a global $U(1)$ transformation

$$U_1 = e^{i\alpha}, \tag{2.3}$$

because exponential factors cancel out when making the transformation $\psi \to \psi' = U_1\psi$. This equation however is not invariance under a local $U(1)$ transformation:

$$U_1(x) = e^{i\alpha(x)}, \tag{2.4}$$

where phase factor α is a function of $x = (t, \vec{x})$. Global invariance should necessary hold locally, and in order to so one has to replace the usual derivative ∂_μ by the so called covariant derivative D_μ: $\partial_\mu \to D_\mu = \partial_\mu + igA_\mu(x)$ The following transformation rule under the $U(1)$ transformation described here is defined for the field A_μ which is contained in the covariant derivative. This filed transforms under local gauge transformation as:

$$A_\mu(x) \to A'_\mu(x) = A_\mu(x) - \frac{1}{g}\partial_\mu\alpha(x). \tag{2.5}$$

Therefore, the redefined Lagrange density is invariant under local $U(1)$ transformations. The field A_μ, that emerged from the demand of gauge invariance, generates an extra term

$$-g\overline{\psi}(x)\gamma^\mu A_\mu(x)\psi(x). \tag{2.6}$$

The equation 2.6 represents the well known quantum electrodynamics (QED) interaction between a fermion ψ with charge g and an external electromagnetic potential $A_\mu(x)$. Instead of being an external potential, $A_\mu(x)$ can be turned into a free photon field by adding the appropriate free Lagrangian (kinetic energy which describes motion of free photons)

$$\mathscr{L}_A = -\frac{1}{4}F_{\mu\nu}F^{\mu\nu} \tag{2.7}$$

with $F_{\mu\nu} = \partial_\mu A_\nu - \partial_\nu A_\mu$, to the overall Lagrange density. $A_\mu(x)$ itself is then treated as free field in the Lagrange formalism. If photon could have been particle with non-zero mass additional term $\frac{1}{2}M^2A^\mu A_\mu$should be present in the equation 2.7. Since expression $A^\mu A_\mu$ is

not gauge invariant under $U(1)$ local gauge transformation, mass of photon should be, as it is, $M = 0$.

The demand of local gauge invariance gives a well defined scheme to generate interaction terms between forces and particle fields. The covariant derivative is not just a simple tool convereting globally invariant Lagrangian into a locally invariant one: it introduces field which requires its own free Lagrangian, and the field must be massless in order not to spoil local gauge invariance of QED. This conclusion is of a general importance: choosing the symmetries of a physical system predicts its dynamics, or, put differently, nature is not invariant under local gauge transformation unless interactions are present.

Gauge symmetries are continuous and are classified in Lie groups with infinitesimal generators which set the basis for any transformation within the group. In contemporary particle physics many symmetry groups have been explored, but as stated in the first section the groups describing symmetries of electromagnetic, weak and strong interactions are well established: the transformations that provide the SM with interactions can be fitted into a combination of $SU(3)_c \otimes SU(2)_L \otimes U(1)_Y$.

The general form of transformations under these groups are the following:

$$\begin{aligned} U(1)_Y: &\quad \psi(x) \to e^{i\alpha(x)}\psi(x), \\ SU(2)_L: &\quad \psi(x) \to e^{i\beta(x)_i\sigma_i/2}\psi(x), \quad i = 1,2,3 \\ SU(3)_c: &\quad \psi(x) \to e^{i\gamma(x)_j\lambda_j/2}\psi(x), \quad j = 1,...,8 \end{aligned} \tag{2.8}$$

where $\alpha(x)$, $\beta(x)$ and $\gamma(x)$ are free space-time dependent parameters, σ_i are the three Pauli matrices and are a representation of the infinitesimal generators of the group $SU(2)$, while λ_j are the eight Gell-Mann matrices and are a representation of the infinitesimal generators of the group $SU(3)$. The $SU(2)$ and $SU(3)$ symmetry groups are non-Abelian, and as an important consequence, the $W^{\pm}$ and gluon gauge bosons carry weak and colour charge respectively. They can therefore self-couple, contributing to their self-energy and thus to the running of the coupling constants.

This combination of symmetry group sets the bosonic field content of the SM as one vector field will be required for each generator in order to keep the Lagrangian density symmetric. Furthermore, it is the spontaneous breakdown of the $SU(2)_L \otimes U(1)_Y$ group into $U(1)_{em}$, the electromagnetic gauge symmetry, that provides masses for the particles of the SM.

2.1.3 Electroweak interactions

The Standard Model of electroweak interactions is based on the gauge group $SU(2)_L \otimes U(1)_Y$, where the generators of $SU(2)_L$ correspond to the three components of weak isospin T_i and the $U(1)_Y$ generator to the weak hypercharge Y. These are related to the electric charge by $Q = T_3 + Y/2$. The Lagrangian describing the electroweak interactions can be written in the form:

$$\mathscr{L}_{EW} = \sum_{j=1}^{3} i\bar{\psi}_j(x)\gamma^\mu D_\mu \psi_j - \frac{1}{4}W^i_{\mu\nu}W_i^{\mu\nu} - \frac{1}{4}B_{\mu\nu}B^{\mu\nu} \tag{2.9}$$

with the field strength tensors $W^i_{\mu\nu}$ i $B_{\mu\nu}$ for $SU(2)_L$ i $U(1)_Y$,

$$\begin{aligned} W^i_{\mu\nu} &= \partial_\mu W^i_\nu - \partial_\nu W^i_\mu + g\varepsilon^{ijk}W_{\mu j}W_{\mu k} \\ B_{\mu\nu} &= \partial_\mu B_\nu - \partial_\nu B_\mu, \end{aligned} \tag{2.10}$$

and D_μ covariant derivative,

$$D_\mu = \partial_\mu - igT_iW^i_\mu - ig^{'}\frac{Y}{2}B_\mu. \tag{2.11}$$

g i $g^{'}$ are coupling strengths of $SU(2)_L$ and $U(1)_Y$ fields, representing free parameters of the model.

Four vector bosons W^i_μ i B_μ are associated with two charged vector bosons in the following way:

$$W^\pm = (W^1_\mu \mp W^2_\mu)/\sqrt{2}, \tag{2.12}$$

while the third component of W^3_μ mix with field $U(1)$ giving physics states, Z boson and photon γ:

$$\begin{aligned} Z_\mu &= W^3_\mu cos\theta_W - B_\mu sin\theta_W \\ A_\mu &= W^3_\mu sin\theta_W + B_\mu cos\theta_W, \end{aligned} \tag{2.13}$$

with Weinberg angle θ_W. Weinberg angle is connected with coupling strengths g i $g^{'}$: $tan\theta_W = g^{'}/g$.

The Lagrangian 2.9 describes charged and neutral interactions associated with weak decays, such as the decays of charged pions, muons and neutrons, transitions between down and up-type quarks, or between charged leptons (like electrons or muons and the corresponding neutrinos). It incorporates QED and self-interactions between the gauge bosons. Nevertheless it is in strong disagreement with experimental facts: the W and Z bosons and the fermions are massive objects, and mass terms for any of these particles violate explicitly the local gauge symmetry.

2.1.4 QCD

The large number of known mesonic and baryonic states clearly signals the existence of a deeper level of elementary constituents of matter: quarks. Assuming that mesons are quark-antiquark bound states, while baryons have three quark constituents, one can nicely classify the entire hadronic spectrum. However, in order to satisfy the Fermi-Dirac statistics one needs to assume the existence of a new quantum number, colour, such that each species of quark may have N_c = 3 different colours: $q_\alpha, \alpha = 1,2,3$ (red, green, blue). Baryons (B) and mesons (M) are then described by the colour-singlet combinations:

$$B = \frac{1}{\sqrt{6}}\varepsilon^{\alpha\beta\gamma}|q_\alpha q_\beta q_\gamma\rangle, \quad M = \frac{1}{\sqrt{3}}\delta^{\alpha\beta}|q_\alpha \bar{q}_\beta\rangle. \tag{2.14}$$

The Lagrangian of QCD interactions has the form:

$$\mathscr{L}_{QCD} = \sum_f \bar{q}_f(i\gamma^\mu\partial_\mu - m_f)q_f - g_s G_a^\mu \Sigma_f \bar{q}_f^\alpha \gamma_\mu (\frac{\lambda^a}{2})_{\alpha\beta} q_f^\beta - \frac{1}{4}G_a^{\mu\nu}G_{\mu\nu}^a, \tag{2.15}$$

where the strength of the interaction is g_s, which is universal for all the quark flavors. The second term includes Gell-Man matrices and represents the interaction between the quarks and the gluon field G_a^μ. The kinetic term for the gluons is the thirdone, with $G_a^{\mu\nu} = \partial^\mu G_a^\nu - \partial^\nu G_a^\mu - g_s f^{abc} G_b^\mu G_c^\nu$, where f^{abc} are the $SU(3)$ structure constants. There are eight gluons which also carry color charge due to the non-Abelian nature of the group.

QCD has two special properties[11]:

- Confinement, which describes the rapid increase of the strong force when trying to separate two coloured particles (in contrast to all other forces which decrease with distance between the interacting objects).

- Asymptotic freedom, which means that at very small distances (or equivalently very high-energy reactions) coloured particles interact very weakly.

As a consequence of QCD confinement and asymptotic freedom perturbation theory can be used to describe high-energy processes, but not in the low energy regime. Further coloured particles (gluons and quarks) undergo so-called hadronisation, before they could be possibly observed. In the process of hadronisation, the coloured objects are grouped into colour singlet objects - baryons and mesons. A collimated jet of such baryons and mesons is detected in the detector, if the initial quark or gluon is generated with high momentum, that is it originates from a hard-scattering process.

2.1.5 Higgs

In the previous sections, mass terms for fermions and bosons were shown to break the invariance of the Lagrange density under gauge transformation. In order to keep local gauge invariance, but also to generate the masses of W and Z bosons (photon and gluons are massles) and fermions, the mechanism of spontaneous symmetry breaking is introduced into the Standard Model. The mechanism, known as the Higgs mechanism, introduces a field with a nonzero vacuum expectation value, breaking the symmetry property of the vacuum state. The Higgs field is a complex spinor of the group $SU(2)$:

$$\phi = \begin{pmatrix} \phi^+ \\ \phi^0 \end{pmatrix} \tag{2.16}$$

with the following free Lagrange density:

$$\mathscr{L}_\phi = |D_\mu \phi(x)|^2 - V(\phi), \tag{2.17}$$

where D_μ is the covariant derivative 2.11, and $V(\phi) = \mu^2|\phi(x)|^2 + \lambda|\phi(x)|^4$ is the postulated external potential of the Higgs field. The Lagrangian that includes this potential is invariant under $SU(2)_L \otimes U(1)_Y$ transformations. The existence of minima for the Higs potential is guaranteed by taking $\lambda > 0$. Appart from the trivial minimum for $\mu^2 > 0$, for the choice of $\mu^2 < 0$ the minimum obeys the following (with v being vacuum expectation value)

$$\langle 0|\phi|0\rangle = \begin{pmatrix} 0 \\ v \end{pmatrix}, \quad v = \sqrt{-\frac{\mu^2}{2\lambda}} > 0. \tag{2.18}$$

In the presence of such a potential with a non zero minimum, the field ϕ does not vanish in the absence of any excitation. This also implies that interactions of the Higgs field with other fields do not vanish. These non-zero ground state interactions will finally lead to the desired mass terms.

As an isospin doublet of two complex fields the Higgs field has four degrees of freedom. Three of these four degrees of freedom mix with the $W^\pm$ and Z, giving them masses. So there is one degree of freedom left in the Higgs doublet, giving rise to the prediction of a new massive scalar particle, the Higgs boson. The Higgs mass is however a free parameter of the model given by $m_H = \sqrt{2\lambda}v$. The vacuum expectation value is obtained from the partial width of the muon decay $\mu \to e\bar{\nu}_e\nu_\mu$ and it is related to the Fermi constant:

$$v = (\sqrt{2}G_F)^{-\frac{1}{2}} = 246 \text{ GeV}. \tag{2.19}$$

This sets the scale of the electroweak symmetry braking. Mass terms for fermions are not an intrinsic part of the Higgs mechanism. To generate fermion masses, Yukawa interaction terms between the Higgs doublet and the fermions are postulated. The couplings between fermions and the Higgs boson are arbitrary. They are related to the fermion masses which are free parameters of the model.

The Higgs mechanism is a requirement for the validity of the Standard Model, and it is well motivated. The predicted Higgs boson has not been discovered yet.

2.2 Beyond Standard Model

Standard Model has enormous success as a theory of elementary particles. One can point out some of them focusing on different aspects of the model, and they can be listed as follows:

- SM unifies the electromagnetic and weak forces.
- It is a renormalizabile theory which preserves its predictive power beyond tree-level computations and allows for the probing of quantum effects.
- Predictions of the theory are in impressive agreement with all accelerator-based experimental data.
- In particular, the gauge sector of the SM has been extremely well tested. If radiative corrections are included, the theoretical predictions are in excellent agreement with the data of LEP, SLC, Tevatron, HERA and the B factories. Some observables have been measured with an error of less than one per mill, while the theoretical predictions have a similar accuracy.

Despite its phenomenological success, it is generally believed that the SM is an incomplete theory. One can, as in the case of the successes, list its limitations according to his/her taste. The main limitation of the Standard Model we highlight are the following.

- Why does the weak force distinguish left and right? Do right-handed charged-current weak interactions exist in nature?
- In its present form the model cannot describe the recent experimental results on neutrino oscillations, which are only possible if the neutrinos have mass. Even more, the nature of the neutrinos (Dirac or Majorana particles) is unknown.

- The model clearly distinguishes strong and electroweak interactions and no real unification between them exist, as the evolution of the three SM coupling constants does not lead to a common crossing point at a high energy scale $M_{GUT} \sim 10^{16}$ GeV.

- Standard Model contains considerable number of free parameters: three coupling constants, all fermion masses, four fermion mixing parameters, a Higgs mass, and one independent gauge boson mass. The values of these constants in the model are still unconstrained and lack a fundamental explanation: they are put in the theory "by hand".

- In the Standard model the Higgs mass is extremely sensitive to radiative corrections so that a fine-tuning of the Higgs mass is required. This is also known as a hierarchy problem: why is the electroweak scale so different from the scale of grand unification?

- The model does not consider gravitation interaction at all.

Beside of all these, SM does not address the questions why there are three fermion generations, nor explains the hierarchy of masses of more then five orders of magnitude from top quark to electron. Going beyond particle experiments, the SM has no candidate for dark matter which should be four times more abundant than the ordinary one[12], and does not explain the baryon asymmetry in the universe, nor why the spacetime is 4-dimensional.

As pointed above there is the hierarchy problem that involves the Higgs boson. Unlike the other logarithmic divergences found in the SM when including higher order corrections, the Higgs mass (since Higgs is a scalar particle) has a quadratic one. Introducing a cut-off Λ, above which the Standard Model is not valid theory, the physical mass m_H gets the contribution proportional to Λ^2 . Setting Λ to the scale of grand unification ($\sim 10^{16}$ GeV) one must arrange for a cancellation of more than 10 digits to obtain $m_H < 1$ TeV. This very *unnatural* fine-tuning is viewed as a strong motivation for the appearance of new physics effects, likely at the TeV scale.

Finally, the Higgs sector itself has not been tested up to now. In particular, the Higgs boson has not been found yet, thus Higgs mechanism as a mechanism of symmetry braking cannot be taken for granted. When, and if Higgs boson is found, and its mass is measured, SM will come to the test one more time when measurements of the Higgs couplings to other bosons and fermions, as well as its self-couplings are confronted to the theoretical predictions.

This list of unanswered questions provides the motivation for consideration of physics beyond the SM. Numerous theories are studied in order to address at least some of the opened issues. These theories and related phenomena are usually collectively called Beyond Standard

Mode (BSM) physics, referring to any possible extension of the Standard Model, whether or not the extension solves any particular set of problems left unresolved in the Standard Model.

However, no single theory has been invented that successfully addresses all of these questions simultaneously. Unfortunately, since data agree with the SM so well, there is no enough experimental input to provide guidance for extending the Standard Model, or even to directly prove BSM physics really exists[1].

2.3 New Heavy Charged Gauge Bosons

2.3.1 Motivation

As stated there are many ways to go beyond the Standard Model. For some reviews of the Beyond Standard Model physics see [13, 14, 15]. A large variety of theories Beyond the Standard Model, predict existence of additional gauge bosons. A charged, spin 1 gauge boson which is not included in the Standard Model is usually denoted as W'. It is not possible to go into details about specific models that predict existence of a such new boson. Rather we list some of these theories just briefly describing basic ideas in order to motivate search for the W' at the LHC.

One attractive way to go beyond SM is by enlarging the gauge group $SU(3)_c \otimes SU(2)_L \otimes U(1)_Y$, either by creating new symmetries or by unifying the symmetries already recognized. An example of this are so called Left-Right symmetric models, such as those based on the gauge symmetry $SU(3)_c \otimes SU(2)_L \otimes SU_R \otimes U(1)_{B-L}$, where $SU(2)_R$ symmetry is broken at a higher scale than the $SU(2)_L$. In the Standard Model parity violation is introduced by hand, therefore the extension by a right-handed sector has not only aesthetic reasons, it provides a mechanism for parity violation. For a detailed discussion of the Left-Right Symmetric Model consult [16]-[24]. After spontaneous symmetry breaking, the model predicts a right-handed W_R gauge boson mixes with the left-handed W_L boson of the Standard Model. This mixing is in principle small for $m_{W_R} >> m_W$, thus W_R becomes very attractive W' candidate. The Left-Right Symmetric Model provides small standard neutrino masses because it incorporates the seesaw mechanism

[1] J. D. Lykken[13]: "What is missing? Perhaps our implementation of supersymmetry or the basic idea of partners is too naive. Perhaps we need to deconstruct our thinking about degrees of freedom in general, not just for extra dimensions. Perhaps everything comes ultimately from strong dynamics and we just don't have the tools to figure out the rules. Perhaps gauge theories and/or quantum field theory is just an emergent approximation for a deeper underlying framework. Perhaps the Standard Model (tweaked to accommodate neutrino masses) is all there is, the parameters of the SM are determined by initial conditions of the Big Bang, dark matter is all black holes, and the accelerating expansion of the observable universe has a purely macroscopic origin. What is missing? **Enough data** from enough experiments to point us in a clear direction, and start to resolve at least some of our long-standing puzzles. We hope that the advent of the LHC, along with exciting results from astrophysics, direct dark matter detection, neutrinos, and searches for rare processes, will do the job".

[25]. The symmetry breaking assigns masses to Majorana neutrinos, resulting in three heavy (N) and three light neutrinos (ν). The order of magnitude of the heavy neutrino is determined by the scale W_R, but it is possible to generate small neutrino masses even if the right-handed neutrino is light [26].

Grand Unified Theories, on the other hand, seek to find a simple symmetry group with $G \supset SU(3)_c \otimes SU(2)_L \otimes U(1)_Y$ that contains the known interactions [16], [27]-[29]. The GUT gauge group is unbroken at energies higher than the GUT scale M_{GUT}, and is spontaneously broken to the SM gauge group at lower energies. The smallest semi-simple GUT group is $SU(5)$, but has been rooled out due to lower bound on the proton lifetime [30]. The other possible choices for the GUT group are $SO(10)$, $E(6)$ etc. Any enlarging of the gauge group triggers existence of new gauge bosons, leading to at least one observable W' at the LHC.

In a recently constructed class of theories, called little Higgs models [31], the SM symmetries are enlarged in such a way that the Higgs boson becomes a pseudo-Goldstone boson, and its mass corrections vanish at one loop. On the other hand, the two-loop m_H corrections allow to push SM up to about 10 TeV without giving rise to fine-tuning problems [32]-[34]. The models require new heavy fermionic partners for quarks and leptons, and also TeV-scale partners for gauge bosons, and new heavy charged gauge boson occur.

The existence of new heavy gauge bosons arise in some more exotic theories and models like Kaluza-Klein theories [35]-[38]. The problem of understanding the gravitational interactions (due to the fact there is no renornalizable theory of quantum gravity) seem to imply the existence of extended objects living in more than four dimensions. As one consequence of invoking extra dimensions could be existence of gauge-boson KK-excitations in form of towers of new gauge bosons, among which the charged $W_{KK}^{(n)}$ gauge-boson.

Finally, some models address the possibility that Higgs sector is strongly interacts i.e. the possibility of breaking electroweak symmetry without an elementary Higgs is possible [39]. As a consequence, new heavy gauge resonances may be detected.

2.3.2 Reference model

Due to the large variety of models that predict existence of W' listed in the previous section, it is not realistic to perform the equivalent number of independent searches, and optimize selection accordingly. Therefore, it is common in the BSM physics to stick with one or few *benchmark* models (or points in the new physics parameter space) used to optimize the searches (in sense of signal significance maximization), and to set the limit if no signal is observed.

For the results presented in this thesis a more general approach is considered, namely the

Reference Model which has been discussed first by Altarelli et al. [40]. In this model the new charged gauge boson W' appears as a heavier version of the lefthanded Standard Model W boson. The couplings of the W' boson to quarks, leptons and gauge bosons of the electroweak interaction are assumed to be identical to the Standard Model couplings. As a consequence of this approach, the new decay channel $W' \to WZ$ is dominant for high masses $m_{W'} > 2m_Z$. This leads to widths of the W' boson which are larger than the mass for $m_{W'} > 500$ GeV. Considering extended gauge models, like the Left-Right Symmetric Model, this channel is suppressed by the mixing angle between W_L and W_R. As it has been mentioned in the previous section, the mixing is vanishing for $m_{W_R} >> m_W$. Since no W_R has been observed (as discussed in the next section), the decay channel $W' \to WZ$ is suppressed.

The benchmark model W' used here assumes that there is no mixing between W' and SM W boson, and the branching ratio $B(W' \to WZ)$ =0. The production and subsequent decay of such a W' (W'^+, W'^-, left- or right-handed) into an lepton (where by lepton, muon or electron are considered) and a light, non-detectable neutrino is searched for.

The partial width into fermion pairs of such a gauge boson scales with mass of W'

$$\Gamma(W' \to f_i \bar{f_j}) = \Gamma(W \to f_i \bar{f_j}) \frac{m_{W'}}{m_W}. \tag{2.20}$$

This behavior translates also into the total width. One has to take into account that the decay channel into the third quark family, $W' \to tb$, opens for masses beyond the kinematic threshold ($m_t + m_b \approx 180$ GeV). For $m_{W'} >> m_W$:

$$\Gamma_{W'} = \frac{4}{3} \Gamma_W \frac{m_{W'}}{m_W}. \tag{2.21}$$

In case of the existence of additional generations of fermions, it is assumed that they are too heavy to be produced by a W' decay.

2.3.3 The heavy charged partner to the chiral boson (W^*)

Beside W' with Standard Model like couplings to fermions, another model, particularly denoted as W^*, is considered in this thesis. W^* represents the charged partner to the chiral bosons described in [41]. The motivation for such a model is described in [42], and is given from a hierarchy problem point of view. It is shown that such states are predicted by three different classes of theories that represent different approaches for explaining the relative lightness of the Higgs doublets. The crucial common feature of all three approaches is, that they are based on the

existence of $U(3)_W = SU(3)_W \otimes U(1)_W$ gauge extension of the $SU(2)_W \otimes U(1)Y$ electroweak group , which is spontaneously broken down to the latter at some high-mass scale. This group is decomposed in such a way that massive vector fields appear during the spontaneous symmetry breaking. The magnetic moment type coupling of the W^* leads to kinematic distributions quite different from those of the SM-like W', in particular the Jacobian peak in transverse mass is absent. To fix the coupling strength, we adopt the reference model of [43] which has total and partial decay widths equal the W' ones (with the same mass of W' and W^*).

2.3.4 Searches for W' with other experiments and ATLAS sensitivity prospects

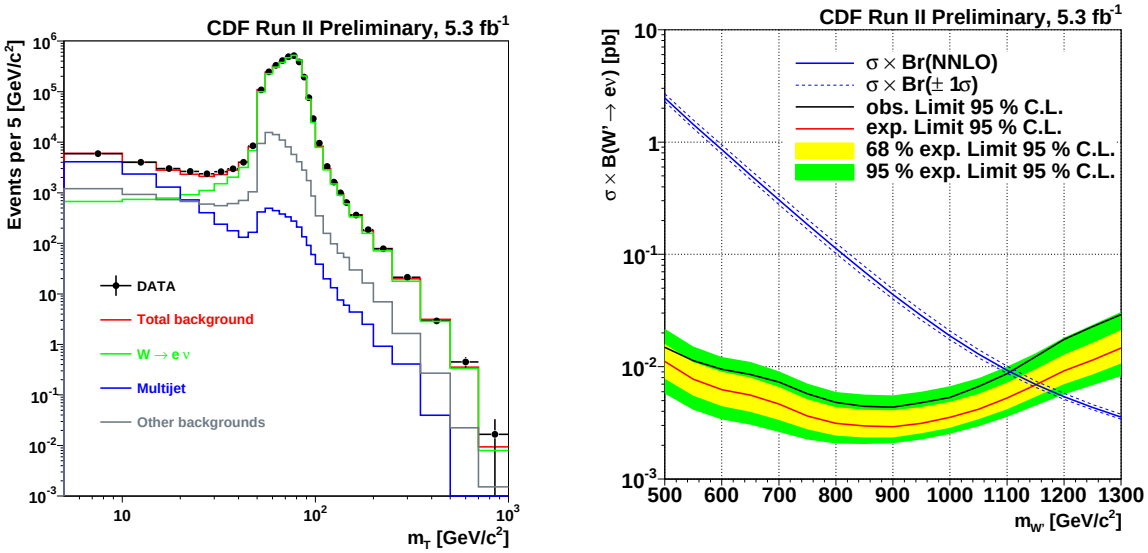

Figure 2.1: Left: The transverse mass distributions of $e\nu$ W' candidate events compared to the Standard Model backgrounds. The results correspond to 5.3 fb^{-1}of data at 1.96 TeV collision energy collected with detector CDF at Tevatron collider. Right: The 95% CL expected and observed limits on cross section times branching ratio as a function of W' mass. The intercept of the cross section limit curve and the lower bound of the theoretical cross section yields $m_{W'} > 1.12$TeV at the 95% CL. Both figures are taken from [44].

The W' boson has been searched for by other experiments. The most sensitive searches have been performed at the Tevatron experiments CDF and DØ, since Tevatron collider hold the highest colliding energy before LHC has started operation. The most stringent limit on the Standard-Model like W' on σB (cross section times branching ratio) as a function of W' mass has been obtained by the CDF [44]. Converted into a mass limit CDF has excluded W' with mass $m_{W'} < 1.12$ TeV at the 95% C.L. analyzing 5.3 fb^{-1}of data collected at energy of $\sqrt{s}$ =1.96 TeV. The results from CDF are shown in Fig2.1. The highest mass limit before that

has been reported by DØ [45] where $m_{W'} < 1$ TeV has been obtained with 1 fb^{-1}of data at the same energy. It should be noted that the mass reach has been slightly increased even though the amount of collected data increased five times. Another important point that should be noted is that both CDF and DØ collaborations performed their searches using electron plus missing energy final state, due to significant deterioration of the muon resolution at very high momenta.

The physics potential of the ATLAS experiment to establish a discovery of such a high mass state, has been evaluated earlier [46, 47]. Prior data taking at 7 TeV, evaluation of the discovery potential, as well as exclusion reach with the ATLAS detector at 7 TeV LHC energy has been performed using state of the art simulation of ATLAS detector [48]. The discovery potential, as well as exclusion reach are presented in Fig2.2(a). The results indicate that even with a modest amount of LHC data at 7 TeV energies, it is possible to discover or exclude new heavy charged gauge bosons above their stringent mass limit set by the Tevatron.

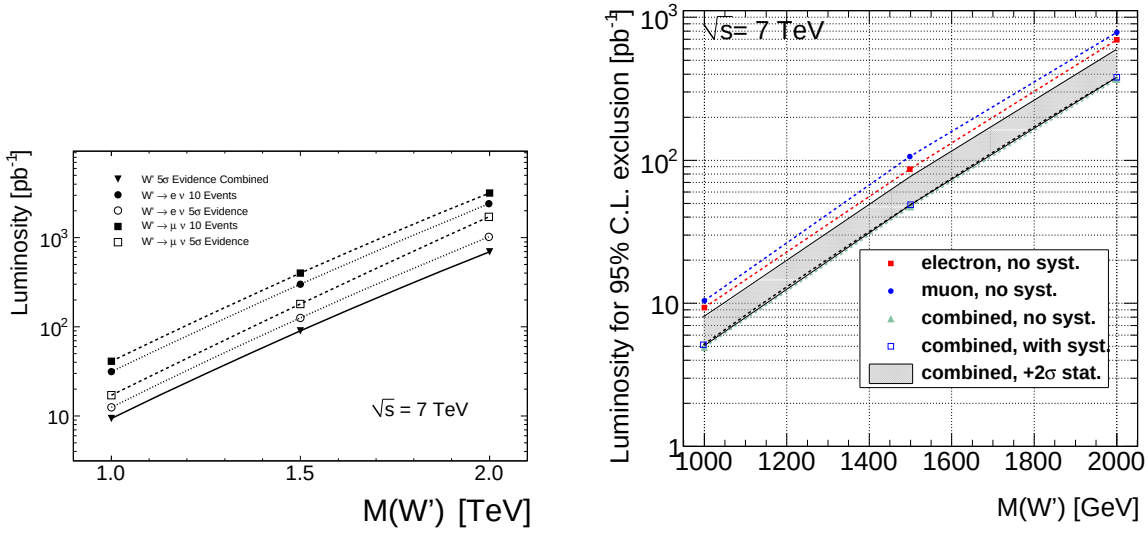

(a) (b)

Figure 2.2: (a) Integrated luminosity needed to yield ten signal events or a 5σ significance for a W' signal (b) Integrated luminosity needed to set 95% C.L. exclusion limits on the W' production cross section as a function of its mass. Both Figures are part of [48].

Parallel with the search for W' boson performed in 2010 by the ATLAS Collaboration[49], presented in this thesis, the same study has been performed by the CMS Collaboration [50]. The result obtained by CMS is similar to the one obtained by ATLAS, and will be discussed in the concluding chapter. Also, the first direct search for W^* is performed with ATLAS data collected during 2010, and these results are part of the thesis.

Bibliography

[1] C.Quigg, Gauge theories of the strong, weak and electromagnetic interactions, The Benjamin/Cummings Publishing Company (1983); C.Quigg, Spontaneous Symmetry Breaking as a Basis of Particle Mass, hep-ph/0704.2232v2, (2007); G. Kane, Modern Elementary Particle Physics, Addison-Wesley, (1987); D. Griffits, Introduction to Elementary Particles, Harper and Row Publishers (1987); Dragan S. Popović, Teorija elektroslabih interakcija, SFIN VIII(2) 1-78, Beograd (1995); S.F.Novaes, Standard Model:An Introduction, arXiv:0001283 [hep-ph]; A. Pich, The Standard Model of Electroweak interactions, arXiv:0502010 [hep-ph].

[2] E. S. Abers and B. W. Lee, Phys. Rep. 9, 1 (1973); M. Levine J. E. Kim, P. Langacker and H. H. Williams, Rev. Mod. Phys. 53, 211 (1981); M. A. B. Beg and A. Sirlin, Phys. Rep. 88, 1 (1982); M. S. Chanowitz, Ann. Rev. Nucl. Part. Sci. 38, 323 (1988).

[3] S.L. Glashow, Nucl. Phys. 22 (1961) 579, S. Weinberg, Phys. Rev. Lett. 19 (1967) 1264, A. Salam, Gauge Unification of Fundamental Forces. Rev. Mod. Phys., 52:525-538, (1980).

[4] M. Kobayashi and T. Maskawa. CP Violation in the Renormalizable Theory of Weak Interaction. Prog. Theor. Phys., 49:652-657, (1973). N. Cabibbo. Unitary Symmetry and Leptonic Decays. Phys. Rev. Lett., 10:531-533, (1963).

[5] U. Dore and D. Orestano, Experimental results on neutrino oscillations, Rep. Prog. Phys. 71, arXiv:0811.1194.

[6] K.Nakamura et al.(Particle Data Group), Review of Particle Physics, J. Phys. G 37 075021 (2010). `http://pdg.lbl.gov`

[7] P.W. Higgs, Broken Symmetries, Massless Particles and Gauge Fields, Phys. Lett. 12 132 (1964). P. W. Higgs, Broken Symmetries and the Masses of Gauge Bosons, Phys. Rev. Lett. 13 508 (1964). P. W. Higgs, Spontaneous Symmetry Breakdown without Massless Bosons, Phys. Rev. 145 1156 (1966).

[8] G.t Hooft and M. J. G. Veltman, Regularization And Renormalization Of Gauge Fields, Nucl. Phys. B 44 (1972) 189. G.t Hooft and M. J. G. Veltman, Combinatorics of gauge fields, Nucl. Phys. B 50 (1972) 318.

[9] ALEPH Collaboration, CDF Collaboration, D0 Collaboration, DELPHI Collaboration, L3 Collaboration, OPAL Collaboration, SLD Collaboration, LEP Electroweak Working Group, Tevatron Electroweak Working Group, SLD electroweak heavy flavour groups Precision Electroweak Measurements and Constraints on the Standard Model, CERN-PH-EP/2009-023, arXiv:0911.2604v2 [hep-ex] and reference therein. See also: `http://www.cern.ch/LEPEWWG` and `http://tevewwg.fnal.gov`

[10] E. Noether. Invariante Variationsprobleme. Nachr. d. Konig. Gesellsch. d. Wiss. zu Gottingen, pages 235-257, (1918).

[11] Y.A. Simonov. The Confnement. Phys. Usp., 39:313-336, 1996. arXiv:hep-ph/9709344. D. J. Gross and Frank Wilczek. Asymptotically Free Gauge Theories. 1. Phys. Rev.,D8:3633-3652, (1973). H. David Politzer. Reliable perturbative results for strong interactions? Phys. Rev. Lett.,30:1346-1349, (1973).

[12] N. A. Bahcall, J. P. Ostriker, S. Perlmutter and P. J. Steinhardt, The Cosmic Triangle: Revealing the State of the Universe, Science 284 (1999) 1481, arXiv:9906463 [astro-ph], and reference there in.

[13] J. D. Lykken: Beyond the Standard Model, arXiv:1005.1676v2 [hep-ph].

[14] John Ellis, Searching for Particle Physics Beyond the Standard Model at the LHC and Elsewhere, arXiv:1102.5009v1 [hep-ph], CERN-PH-TH/2011-003.

[15] Chris Quigg, Beyind Standard Model in many directions, arXiv:0404228v1 [hep-ph], FERMILAB-Conf-04/049-T; B. Mele, Beyond the Standard Model: Expectations at the LHC, arXiv:0407204v2 [hep-ph].

[16] P. Langacker, R. W. Robinett, and J. L. Rosner, New heavy gauge bosons in pp and $p\bar{p}$ collisions, Phys. Rev. D30 (1984) 1470.

[17] J. C. Pati, A. Salam, Lepton Number as the fourth color, Phys. Rev. D10, 275 (1974).

[18] G. Senjanovic, R. N. Mohapatra, Exact left-right symmetry and spontaneous violation of parity, Phys. Rev. D12, 1502 (1975).

[19] R. N. Mohapatra, J. C. Pati, Left-right gauge symmetry and an isoconjugate model of CP violation, Phys. Rev. D11, 566 (1975).

[20] R. N. Mohapatra, J. C. Pati, Natural left-right symmetry, Phys. Rev. D11, 2558 (1975).

[21] G. Azuelos, K. Benslama, and J. Ferland, Prospects for the Search for a Doubly-Charged Higgs in the Left-Right Symmetric Model with ATLAS, J. Phys. G32 (2006) 7392, arXiv:0503096 [hep-ph].

[22] G. Beall, M. Bander, and A. Soni, Constraint on the Mass Scale of a Left-Right-Symmetric Electroweak Theory from the $K_L - K_S$ Mass Difference, Phys. Rev. Lett. 48 (1982) 848.

[23] P. L. Cho and M. Misiak, $b \to s$ Decay in $SU(2)_L \times SU(2)_R \times U(1)$ Extensions of the Standard Model, Phys. Rev. D49 (1994) 58945903, arXiv:hep-ph/9310332.

[24] M. Cvetic and S. Godfrey, Discovery and Identification of Extra Gauge Bosons, arXiv:hep-ph/9504216.

[25] R. N. Mohapatra, G. Senjanovic, Neutrino Mass and Spontaneous Parity Nonconservation, Phys. Rev. Lett. 44 (14): 912915 (1979).

[26] D. Chang, R. N. Mohapatra, Small and Calculable Dirac Neutrino Mass, Phys. Rev. Lett. 58, 16001603 (1987)

[27] R. N. Mohapatra, Unification and Supersymmetry, Springer-Verlag (1986).

[28] F. Buccella, G. Mangano, O. Pisanti, and L. Rosa, Phys. Atom. Nucl. 61 (1998) 983990, arXiv:9709416 [hep-ph].

[29] R. W. Robinett, Neutral currents in E6, Phys. Rev. D26 (1982) 2388.

[30] B. Bajc, P. Fileviez Perez and G. Senjanovic, Proton Decay in Minimal Supersymmetric SU(5), Phys. Rev. D 66 (2002) 075005, arXiv:0204311 [hep-ph].

[31] M. Schmaltz and D. Tucker-Smith, Annu. Rev. Nucl. Part. Sci. 55 (2005) 229 arXiv:0502182 [hep-ph]; M. Perelstein, Prog. Part. Nucl. Phys. 58 (2007) 247 arXiv:0512128 [hep-ph].

[32] N. Arkani-Hamed, A. G. Cohen and H. Georgi, Electroweak symmetry breaking from dimensional deconstruction, Phys. Lett. B 513, 232 (2001) arXiv:0105239 [hep-ph].

[33] T. Han, H. E. Logan, B. McElrath, and L.-T. Wang, Phenomenology of the Little Higgs Model, Phys. Rev. D67, 095004 (2003), arXiv:0301040 [hep-ph].

[34] G. Azuelos et al. (2004), Exploring Little Higgs Models with ATLAS at the LHC, Eur.Phys.J. C39S2 (2005) 13-24, arXiv:0402037 [hep-ph].

[35] I. Antoniadis, K. Benakli, and M. Quiros, Production of Kaluza-Klein States at Future Colliders, Phys. Lett. B331 (1994) 313320, arXiv:9403290 [hep-ph].

[36] G. Azuelos and G. Polesello, Prospects for the detection of Kaluza-Klein excitations of gauge bosons in the ATLAS detector at the LHC, Eur. Phys. J. C39S2 (2005) 111.

[37] G. Polesello and M. Prata, Prospects for observing the Kaluza-Klein excitations of the W boson in the ATLAS detector at the LHC, Eur. Phys. J. C32S2 (2003) 5567.

[38] T. G. Rizzo and J. D. Wells, Electroweak precision measurements and collider probes of the Standard Model with large extra dimensions, Phys. Rev. D61 (2000) 016007, arXiv:9906234 [hep-ph].

[39] P. Chiappetta, Introduction to Strong Higgs Sector, arXiv:9405251 [hep-ph].

[40] G. Altarelli, B. Mele, and M. Ruiz-Altaba, Searching for new heavy vector bosons in $p\bar{p}$ colliders, Z. Phys. C45, 109 (1989).

[41] M. V. Chizhov, V. A. Bednyakov, and J. A. Budagov, Proposal for Chiral-Boson Search at LHC via Their Unique New Signature, Physics of Atomic Nuclei 71 (2008) 20962100.

[42] M. Chizhov and G. Dvali, Origin and Phenomenology of Weak-Doublet Spin-1 Bosons, arXiv:0908.0924 [hep-ph].

[43] M. V. Chizhov, V. A. Bednyakov, and J. A. Budagov, Anomalously interacting extra neutral bosons, Nuovo Cimento C33 (2010) 343.

[44] T. Aaltonen et al. (CDF Collaboration), Search for a New Heavy Gauge Boson Wprime with Electron + missing ET Event Signature in $p\bar{p}$ collisions at $\sqrt{s}$=1.96 TeV, Phys. Rev. D83, 031102 (2011), arXiv:1012.5145 [hep-ex].

[45] V. Abazov et al. (D0 Collaboration), Search for W' bosons decaying to an electron and a neutrino with the D0 detector, Phys. Rev. Lett. 100, 031804 (2008), arXix:0710.2966 [hep-ex].

[46] ATLAS Collaboration, CERN/LHCC 99-15 (1999).

[47] D.L. Adams,...,N.Vranjes, Lepton plus Missing Transverse Energy Signals at High Mass, ATL-PHYS-PUB-2009-071 (part of CERN-OPEN-2008-020).

[48] ATLAS Collaboration, ATLAS sensitivity prospects to W' and Z' in the decay channels $W' \to \ell\nu$ and $Z' \to \ell\ell$ at $\sqrt{s}$=7 TeV, ATL-PHYS-PUB-2010-007, ATL-COM-PHYS-2010-381.

[49] G.Aad et al (ATLAS Collaboration), Search for high-mass states with one lepton plus missing transverse momentum in proton-proton collisions at $\sqrt{s}$ = 7 TeV with the ATLAS detector, Phys.Lett. B701 (2011) 50-69, arXiv:1103.1391v2 [hep-ex].

[50] V. Khackatryan et al (CMS Collaboration), Search for a heavy gauge boson W' in the final state with an electron and large missing transverse energy in pp collisions at $\sqrt{s}$ = 7 TeV, Phys. Lett. B 698 21 (2011), arXiv:1012.5945v2 [hep-ex]. (CMS Collaboration), Search for a W' boson decaying to a muon and a neutrino in pp collisions at sqrt(s) = 7 TeV, Phys. Lett. B 701, 160179 (2011), arXiv:1103.0030v1 [hep-ex].

Chapter 3

Simulation of W' Production at the LHC

3.1 Phenomenology of pp collisions

The production of heavy particles (like W'), at hadron colliders (such as Tevatron and LHC) usually occurs in interactions with high momentum transfer (Q^2). The heavy particle is produced via "parton-parton" scattering where by "partons" one thinks of the constituents within the incoming hadrons (here valence quark, sea quark, or gluon). The rest of the hadrons (spectator partons) then undergo the process of fragmentation and hadronisation which causes hadronic deposits in the detector. This process is usually denoted as the underlying event. The production of a V boson (V=$W'/W/Z$) is illustrated in Fig3.1(a).

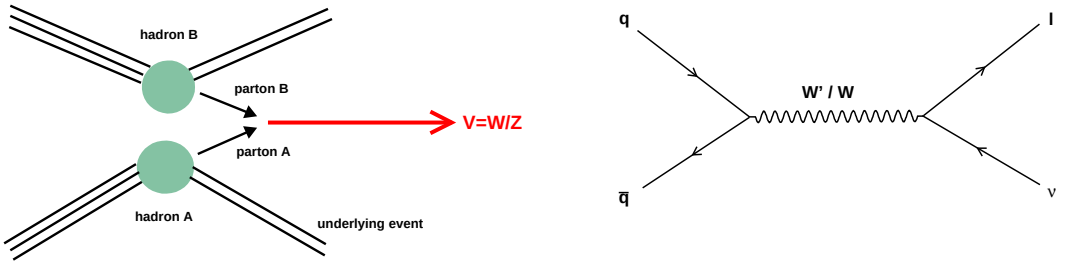

(a) (b)

Figure 3.1: (a) Schematic representation of a production of V boson ($V = W/Z$) in a hadron collider. (b) Leading order Feynman diagram for the production and decay of W or W' at the LHC.

The measurable production cross section for the process $pp \to W' + X$ can be calculated as follows:

$$\sigma = \sum_{i,j} \int_0^1 dx_1 \int_0^1 dx_2 (\hat{\sigma}(x_1 P_1, x_2 P_2, Q, \alpha_s^m(Q))\, f_i(x_1, Q^2)\, f_j(x_2, Q^2), \tag{3.1}$$

where the sum runs over all possible initial and final spin and colour states. In the given equation, $x_{1,2}$ represents the fraction of the incoming hadron momentum $P_{1,2}$ carried by the interacting parton, $\alpha_s^m(Q)$ is the strong coupling constant calculated in $m-$th order, and Q is the momentum transfer (scale of the process). The probability to find a parton in the proton with momentum fraction x is given by the corresponding Parton Distribution Function (PDF), $f_{parton}(x, Q^2)$. The partonic cross section, $\hat{\sigma}$, represent the cross section for a process $q_i\overline{q}'_j \to W'$, which in the Leading Order (LO) is represented in Fig3.1(b) [1] and is proportional to a matrix element squared[2]. The parton-parton interaction like $q_i\overline{q}'_j \to W'$ is usually denoted as a hard scattering process. The splitting into hard scattering process, with a partonic cross section $\hat{\sigma}$, and a soft part (low Q^2), hidden in the PDFs, is called factorisation. The scale which is assumed to separate the hard process and the soft contributions, is called the factorisation scale μ_F. The cross sections are always calculated at a fixed order in perturbation theory, thus result depends on the choice of factorisation scale (which is equal to the momentum transfer). This dependency becomes weaker with increasing orders of calculation, thus it is desirable to calculate the cross section for a given process at highest possible order. The variation of unphysical scales involved in the calculations, the factorisation scale μ_F and renormalisation scale μ_R (the scale at which α_s is evaluated), represent sources of theoretical uncertainty of the production cross section. Another source of theoretical uncertainty on the production cross section comes from the choice of the PDF. PDFs represent analytical fits obtained using a combination of theory and experimental data (mainly from deep -inelastic scattering experiments of the H1 and ZEUS experiments at the HERA collider) which describe the momentum distributions of partons inside a hadron. One possible parameterization of the PDFs, namely MSTW2008[1] is shown in Fig3.2. The figure shows Next-to-Leading-Order (NLO) PDFs for different partons inside protons obtained at scales of $Q^2 = 10$ GeV^2 and $Q^2 = 10^4$ GeV^2, including the associated one-sigma (68%) confidence level (C.L.) uncertainty bands.

3.2 W' LO cross section

Monte Carlo (MC) programs are used to used to calculate cross sections and to determine acceptances and model the properties of the studied processes. W' MC samples in this thesis are simulated using `PYTHIA`[2] MC program with MRST LO*[6] parton distribution functions used. Further details on signal (and background) MC samples used please see 5.2.2. Signal samples

[1] Please note that the diagram for the production of W' boson is identical to the diagram for the production of the Standard Model W boson.

[2] The matrix element is an amplitude for the process to occur, and may be computed by summing over initial state interaction amplitudes. The square of the matrix element is related to the interaction probability.

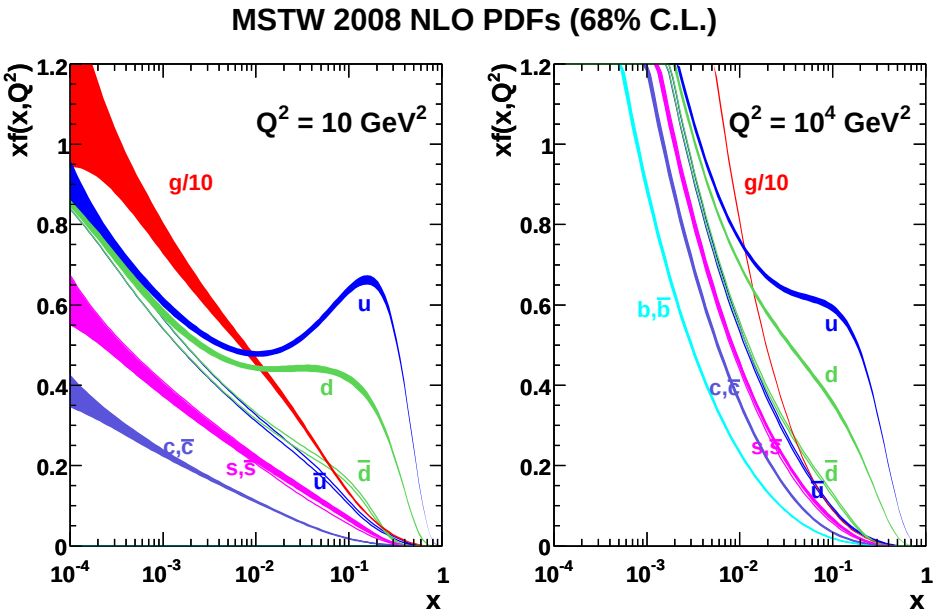

Figure 3.2: MSTW 2008 NLO PDFs at $Q^2 = 10GeV^2$ and $Q^2 = 10^4 GeV^2$, [1].

$W' \to \ell\nu$ ($\ell = e, \mu, \tau$) are generated with PYTHIA for a series of masses. The PYTHIA default settings are used, meaning that W' has the same $V-A$ couplings as the standard model W boson but interference between the W' and W is not included. Cross sections for eight $W' \to \mu\nu$ masses are listed in the table 3.1 with the corresponding widths and branching ratios. It is assumed that cross sections for $W' \to e\nu$ and $W' \to \tau\nu$ are the same as for $W' \to \mu\nu$ process.

Table 3.1: Monte Carlo W' samples. The cross sections are obtained with Pythia, meaning they are Leading Order.

Mass [GeV]	Γ [GeV]	B($W' \to \mu\nu$)	σB [pb]
500	16.684	0.08520	15.55
750	25.77	0.08313	2.931
1000	34.75	0.08246	0.7792
1250	43.70	0.08216	0.2555
1500	52.65	0.08202	0.09257
1750	61.60	0.08193	0.03622
2000	70.55	0.08189	0.04496
2500	88.46	0.08184	0.009425

Some basic kinematic distributions for leptons are given: muon momentum (Fig3.3(a))

and pseudorapidity (Fig3.3(b)), as well as transverse mass distribution for all $W' \to \mu\nu$ events (3.4(a)), and events with $p_T(\mu) > 25$ GeV, $|\eta|$ <2.5 and $p_T(\nu) > 25$ GeV (3.4(b)). The distribution of neutrino transverse momentum is similar to the lepton transverse momentum. Distributions are presented for the muon decay channel, and the similar distributions are those of the electron decay channel. All presented distributions are obtained at the generator level, i.e, without any detector simulation, but after fragmentation and hadronization, as well as initial state radiation, simulated with PYTHIA. All distributions are normalized to the PYTHIA (LO) cross section.

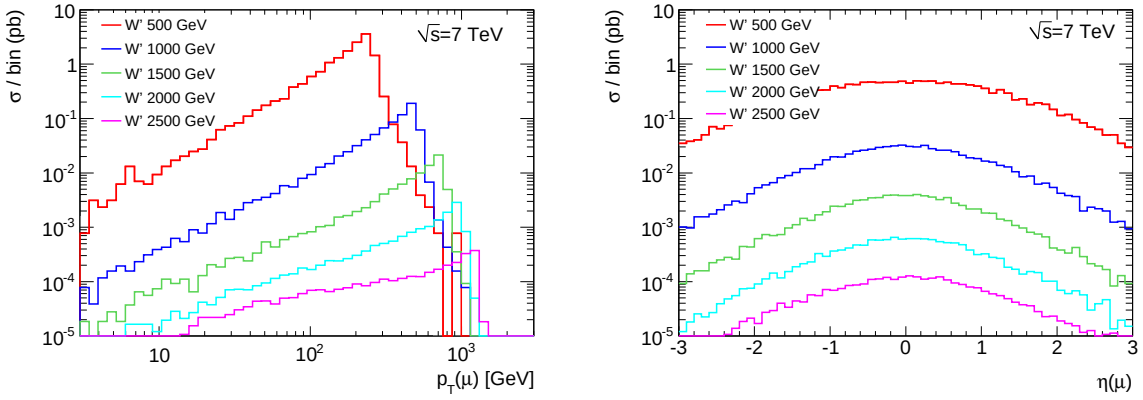

(a) (b)

Figure 3.3: (a) Generated muon momentum distribution in $W' \to \mu\nu$ events for a serie of W' masses. (b) Pseudorapidity distribution of muons for a serie of W' masses.

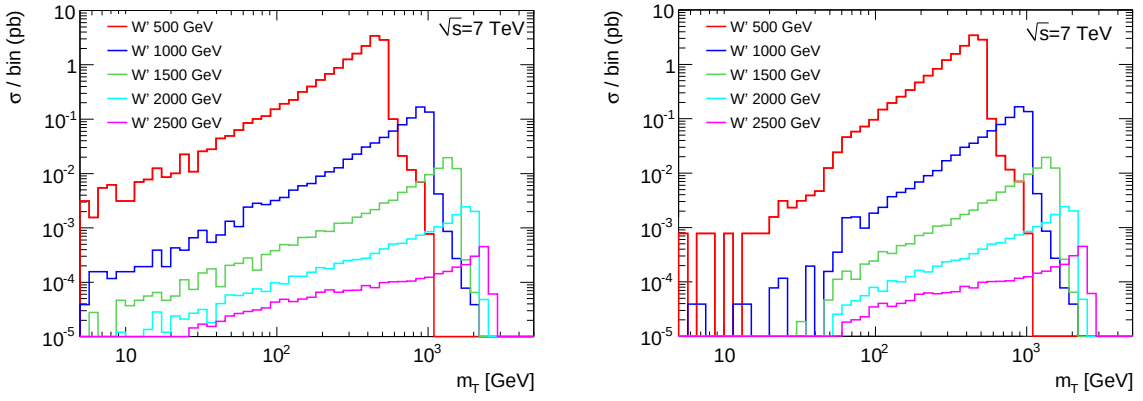

(a) (b)

Figure 3.4: (a) Generated transverse mass distribution in all $W' \to \mu\nu$ events. (b) Generated transverse mass distribution in $W' \to \mu\nu$ events with $p_T(\mu) > 25$ GeV, $|\eta|$ <2.5 and $p_T(\nu) > 25$ GeV.

From the plots and the Table3.1 it can be observed that the cross section falls steeply with increasing mass of W'. It can be also concluded that events are becoming more central (lower $|\eta|$ values) and the characteristic triangular shape of the lepton momentum distribution is changing as the mass increase. The change in shape is more pronounced for the transverse mass distribution. When imposing weak kinematic cuts (as on Fig3.4(b)), the relative efficiency of the events that pass the cuts is smaller for higher W' masses. The reason for this is due to the fact that interacting quarks are required to carry a significant amount of the proton momentum. This is illustrated in Fig3.5(a) and 3.5(b) for $m_{W'}$ =1000 GeV and $m_{W'}$ =2000 GeV respectively. The higher the mass, partons has to carry higher fraction of the proton momentum, which should be less probable. This effect is clearly visible comparing Fig3.6(a) to Fig3.6(b), i.e. true W' mass distribution in events without and with $m_T > \frac{1}{2}m_{W'}$ requirement. It is clear that for higher masses, larger fraction of events is produced with the off-shell boson. The PDFs suppress the on-shell production of extremely (with respect the collision energy) heavy gauge bosons.

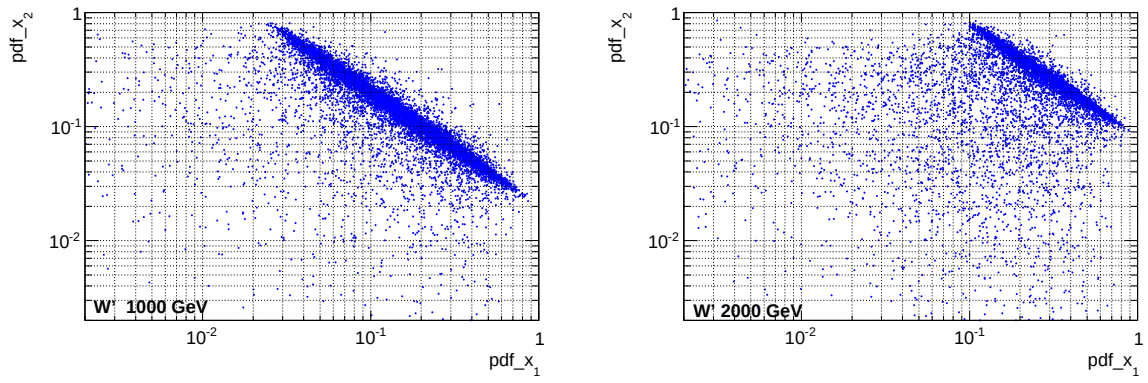

(a) (b)

Figure 3.5: Momentum fractions x of the two quarks that annihilate and produce the W' boson force $m_{W'} = 1000$ GeV (a) and $m_{W'} = 2000$ GeV at $\sqrt{s}$ =7 TeV.

3.3 W' NNLO cross section

3.3.1 Calculation of higher order corrections

In order to get more accurate prediction for the W' production cross section, a study is performed to calculate Next-to-Next-to-Leading-Order (NNLO) cross sections in QCD using the `FEWZ` program [2, 3]. Since it is assumed that W' has the same $V-A$ couplings as the standard model W boson and interference between the W' and W is small, this study is performed using `FEWZ`

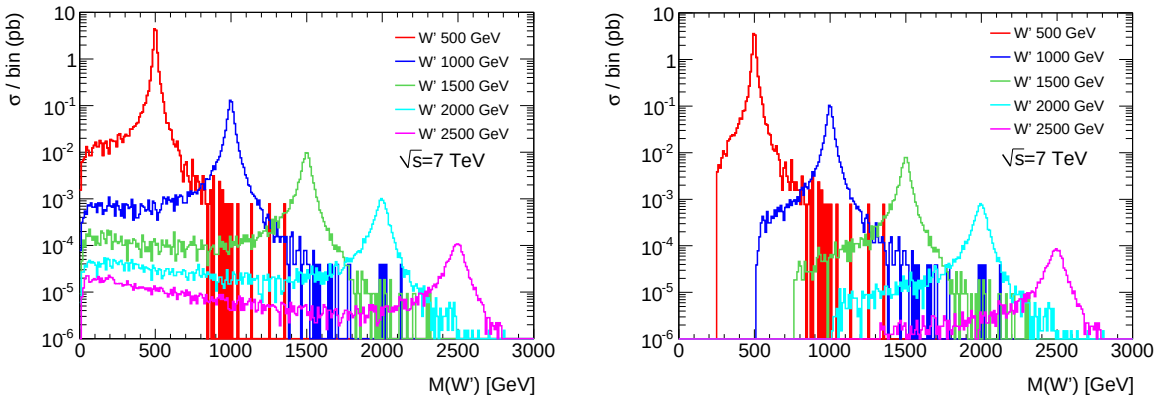

(a) (b)

Figure 3.6: Generated true mass of W' boson in all $W' \to \mu\nu$ events (a), and events with $m_T > \frac{1}{2}m_{W'}$ (b).

Standard Model W production. As program input for this calculation, the mass of the W boson is set to the mass of the W' and the total and partial widths are set to the W' values calculated with PYTHIA. The values used are those listed in Table 3.1.

Renormalization and factorization scales are set to the W' boson mass. Values for other relevant input parameters are $\sin^2(\theta)$ =0.232, $1/\alpha_{QED}$ =0.0078125, and $G_\mu = 1.16637 \times 10^{-5}$ GeV^{-2}. The central cross-section values for different W' masses are obtained using the MSTW2008NNLO PDF set[1]. In addition to the central PDF set, the MSTW2008 PDF's include 40 eigenvector error sets for each fit, corresponding to either a 68% or 90% CL limit as well as two PDF sets (at 68% and 90% CL) where the PDF fit is kept fixed while α_s is allowed to vary accordingly within the experimental errors. The fit incorporates a large amount of data from fixed-target experiments, HERA and the Tevatron (which cover a range from 0.0001 to 0.5 in x), starting from input parton distributions parametrized at Q^2 = 1 GeV. Cross sections for $W' \to e\nu$ process are calculated without any kinematic cuts imposed, and also with the following kinematic cuts: $p_T > 25$ GeV, $|\eta| < 2.5$, $p_T^\nu > 25$ GeV, and $m_T > \frac{1}{2}m_{W'}$. The resulting cross sections are listed in the Table 3.2 and compared to the ones obtained with PYTHIA. Corresponding K factors are also given. It is assumed that the cross sections are the same for all three flavors of leptons.

The W' production cross section as a function of its mass is shown in Figure 3.7. This figure and Table 3.2 show that the NNLO cross section with electroweak corrections is very close to the PYTHIA value for masses below 1 TeV, but significantly smaller at higher masses: 20% lower at 1.5 TeV and 35% at 2 TeV.

Beside total, FEWZ generator allows also calculation of QCD differential distributions with the same accuracy. Hence, in the Table 3.2 the $W' \to \ell\nu$ cross sections calculated in a fiducial

Table 3.2: Values for σB for several W' mass points obtained with PYTHIA (LO) and FEWZ (NNLO) using the central value of MSTW2008 NNLO PDF. Values are calculated without any kinematic cuts, and with kinematic cuts listed in the table. The ratio $K_{\text{fid}} = \frac{\sigma B_{NNLO}}{\sigma B_{LO}}$ provides the factor that corrects the event selection efficiency to account for differences in kinematical distributions at LO and NNLO.

W' mass [GeV]	500	750	1000	1250	1500	1750	2000	2500
$W' \to e\nu$ with no kinematic cuts								
σB_{LO} [pb]	15.55	2.931	0.779	0.256	0.0926	0.0362	0.0150	0.00314
σB_{NNLO} [pb]	17.25	3.200	0.837	0.261	0.0887	0.0325	0.0126	0.00234
$K_{\text{NNLO}} = \frac{\sigma B_{NNLO}}{\sigma B_{LO}}$	1.11	1.09	1.07	1.02	0.96	0.90	0.84	0.76
$W' \to e\nu$ with $p_T^e > 25$ GeV, $\lvert\eta^e\rvert < 2.5$, $p_T^\nu > 25$ GeV, $m_{\text{T}} > \frac{1}{2} m_{W'}$								
σB_{LO} [pb]	11.72	2.202	0.581	0.186	0.0646	0.0237	0.0091	0.00133
σB_{NNLO} [pb]	13.34	2.466	0.635	0.194	0.0646	0.0219	0.0076	0.00092
$K_{\text{fid}} = \frac{\sigma B_{NNLO}}{\sigma B_{LO}}$	1.14	1.12	1.09	1.04	1.00	0.93	0.84	0.69
W' event selection efficiency correction factor.								
$K_{\text{fid}}/K_{\text{NNLO}}$	1.025	1.026	1.019	1.024	1.042	1.031	0.994	0.923

volume which mimics most of the criteria used to select events is also presented. The final row in the table gives the NNLO/LO ratio of events in this acceptance, and so provides an estimate of the factor by which the event selection efficiencies differ from those that would be obtained if the full simulation was done to NNLO.

At this point, it should be noted that in the current version of FEWZ SM W production calculation is not optimized for events with invariant masses far away from W mass [4]. It appears that Vegas routine is not adapting the grid correctly for the values of high mass, and it is expected this problem is fixed in a new version of the program. Thus, it is probable that for higher masses of W' cross section is underestimated a bit due to off-shell production of the new heavy gauge boson. At this search of W' mass presented in this thesis, the effect is not accepted to be high, but should be investigated for future analysis when larger amount of data available. This will have to be verified with new version of FEWZ.

Beside the higher order corrections calculated in the QCD, in priciple additional corrections are present due to electroweak corrections. Assuming a new gauge boson (W', and also Z') is not charged under $SU(3)$, the QCD corrections to its production and decay will be identical to those of a Standard Model gauge boson to all orders. However, the W and Z are charged under $SU(2) \otimes U(1)$, so the electroweak corrections include VVV ($V = W/Z$) coupling terms. These will in general be different for a W' such as considered in the search described in the thesis. One must specify how the W' mix with the SM W and Z and how to renormalize their couplings

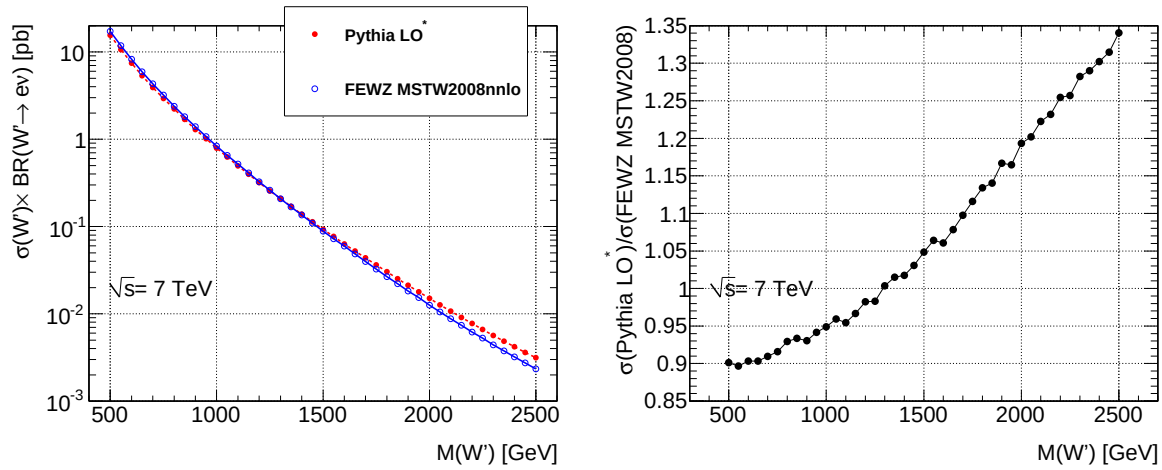

Figure 3.7: Left: W' cross section times branching ratio to electron and neutrino as function of W' mass calculated to LO with PYTHIA, to NNLO with FEWZ. Right: The ratio of the two higher order calculations to PYTHIA obtained using MRST LO* PDFs.

consistently. Since it is assumed that $W' \to q\bar{q}$ and $W' \to \ell\nu$ are the same as in the Standard Model and that $W' \to WZ$ is zero or at least small, the theory of such a boson is the effective one, but does not define a consistent field theory, and the Standard Model electroweak correction is not applicable. Thus, electroweak corrections are not considered. These corrections are however considered for the high mass tails of SM W/Z, and are found to be significant (by reducing the cross section up to 20%). The electroweak corrections for W/Z are described in Chapter 6.

3.3.2 Uncertainties on W' cross section

Two sources of uncertainty are considered for the W' cross section calculations: scale variations and PDF uncertainties. The statistical uncertainty in the calculation is at the 1% level and is negligible compared to these. The kinematic (e.g. m_{T}) dependence of the cross section is different at LO and NNLO and this is accounted for by using K-factors evaluated with the kinematic cuts (last row in Table 3.2). For W' mass below 2 TeV, the K-factor changes by only a few percent when all kinematic cuts are dropped and so any uncertainty arising from the m_{T} or any other kinematic dependence of the K-factors is neglected. Uncertainties arising from the uncertainty in α_s are also neglected.

Uncertainty arising from the choice of factorization and renormalization scale (μ_F and μ_R) is evaluated by varying one scale by a factor of two while keeping the other fixed at its central value. The result of these variations is presented in the Table 3.3. The largest deviation to the

nominal cross section is taken as the corresponding scale uncertainty.

Table 3.3: Change in NNLO $W' \to e\nu$ cross section as computed with FEWZ for various changes in scale factors. The last line is the maximum change.

$M(W')$ [GeV]	500	750	1000	1250	1500	1750	2000	2500
$\mu_F = 2\mu_R$	+1.2%	+1.5%	+1.3%	+1.5%	+2.1%	+3.5%	+3.4%	+4.4%
$\mu_F = 0.5\mu_R$	-1.4%	-0.7%	-0.9%	-0.5%	-0.5%	-1.9%	-2.3%	-1.1%
$\mu_R = 2\mu_F$	+1.8%	+2.2%	+2.1%	+2.0%	+3.1%	+1.4%	+2.0%	+1.8%
$\mu_R = 0.5\mu_F$	-1.6%	-2.0%	-2.0%	-1.7%	-1.3%	-0.1%	-0.1%	-0.4%
Scale uncertainty	1.8%	2.2%	2.1%	2.0%	3.1%	3.5%	3.4%	4.4%

The uncertainties arising from the PDFs are estimated using the 40 MSTW NNLO PDF error eigenvector sets at the 90% C.L. limit. For each eigenvector *i*, cross sections σ^+ and σ^- for ± 1 standard deviation error PDF set are computed. The uncertainties on cross sections are then calculated using both a symmetric prescription and an asymmetric prescription. In the symmetric prescription, the cross section uncertainty is calculated according to the formula:

$$\Delta\sigma^+ = \Delta\sigma^- = \frac{1}{2}\sqrt{\sum_i (\sigma_i^+ - \sigma_i^-)^2} \tag{3.2}$$

and for the asymmetric prescription, separate uncertainties are calculated for positive and negative shifts of the cross section:

$$\Delta\sigma^+ = \sqrt{\sum_i [max(\sigma_i^+ - \sigma_0, \sigma_i^- - \sigma_0, 0)]^2} \tag{3.3}$$

$$\Delta\sigma^- = \sqrt{\sum_i [max(\sigma_0 - \sigma_i^+, \sigma_0 - \sigma_i^-, 0)]^2} \tag{3.4}$$

The results of these variations are presented in Table 3.4. The numbers are relative changes from the values obtained using the central value of MSTW2008 NNLO PDF.

The MSTW cross sections used in our calculations are compared with the CTEQ6.6 [19] in Table 3.5. The magnitude of the difference between these is taken as the uncertainty arising from the choice of PDF set.

The overall uncertainty on the cross section is obtained by adding the scale, PDF error and PDF choice uncertainties. Results are in Table 3.6.

The cross section calculated at NNLO in QCD as function of W' mass along as all included uncertainties, is shown in Fig3.8. The inrerpolation between the calculated points is linear.

Table 3.4: NNLO $W' \to e\nu$ cross section uncertainties evaluated with MSTW2008NNLO PDF error sets as described in the text. The last line gives the cross section uncertainty used in the limit calculations taken to be the largest fluctuation for each mass.

$M(W')$ [GeV]	500	750	1000	1250	1500	1750	2000	2500
symmetric	4.1%	4.4%	5.3%	6.4%	8.0%	9.2%	10.3%	10.6%
asymm. $\Delta\sigma^+$	+6.9%	+4.5%	+6.1%	+8.0%	+10.8%	+12.8%	+14.7%	+14.9%
asymm. $\Delta\sigma^-$	−1.9%	−4.7%	−4.8%	−5.2%	−5.8%	−6.7%	−7.5%	−6.8%
PDF error unc.	6.9%	4.7%	6.1%	8.0%	10.8%	12.8%	14.7%	14.9%

Table 3.5: Cross sections obtained with `FEWZ` using the central values of MSTW2008 NNLO and CTEQ6.6 PDFs. Cross sections are calculated without any kinematic cuts.

W' mass [GeV]	500	750	1000	1250	1500	1750	2000	2500
σ_{MSTW} [pb]	17.253	3.1997	0.8366	0.2606	0.08870	0.03246	0.01260	0.002342
σ_{CTEQ} [pb]	16.908	3.1096	0.8117	0.2550	0.08889	0.03258	0.01298	0.002576
$CTEQ/MSTW-1$	-2.0%	-2.8%	-3.0%	-2.1%	+0.2%	+0.4%	+3.0%	+10.0%

Table 3.6: Overall $W' \to \ell\nu$ cross section uncertainties.

W' mass [GeV]	500	750	1000	1250	1500	1750	2000	2500
Overall uncertainty	7.4%	5.9%	7.1%	8.5%	11.2%	13.3%	15.4%	18.5%

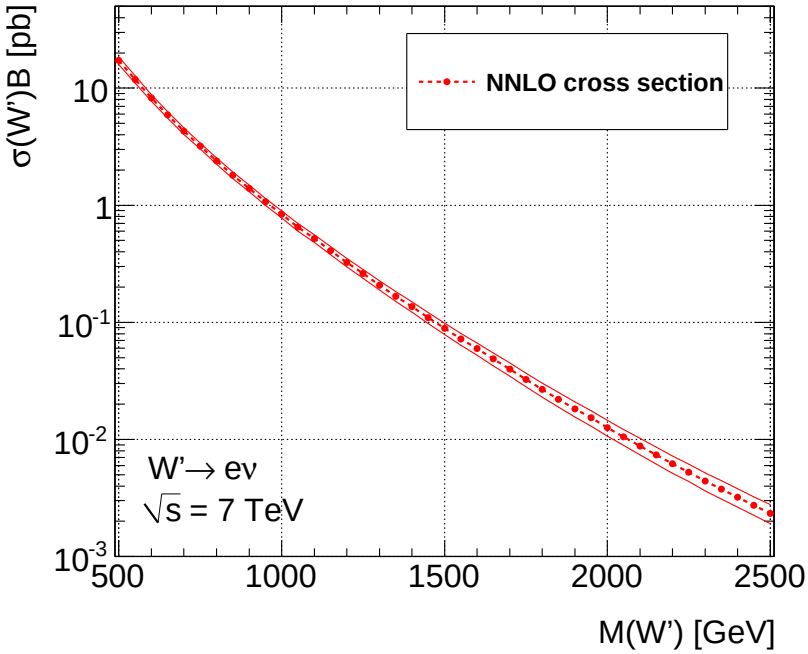

Figure 3.8: W' cross section as a function of the mass. The cross section is given for one lepton flavor (electron, muon, or tau). It is assumed that branching ratios for these three flavors are the same.

3.4 Comparison of W^* and W' cross sections

Monte Carlo samples $W^* \to \ell\nu$ ($\ell = e, \mu$) are obtained with COMPHEP[7] used for generating the matrix elements followed by PYTHIA for parton showering and underlying event description. CTEQ6l1[8] parton distribution functions are used in this case. Samples are listed in the table 3.7, with the cross sections close to the ones of W'. However, as stated before, there are substantial differences in the shape of basic kinematical variables between W' and W^* decay products. These differences are due to different nature of W^* couplings. For a comparison, distributions of two varaibles are shown in Figures3.9(a), and 3.9(b). The "gap" in the central region of the detector ($\eta \sim 0$) and the distortion of the peak at m_{T} distribution will lead to a lower signal efficiency for W^* and therefore lower mass limit on this new heavy charged boson.

The systematic uncertainties on the W^* production cross section are outside the scope of this thesis. They have been estimated elsewhere, please see [11].

Table 3.7: Monte Carlo W^* samples. The cross sections are leading order.

M[GeV]	Γ [GeV]	B($W^* \to l\nu$)	σB [pb]
500	16.929	0.08305	12.590
750	25.389	0.08327	2.339
1000	33.836	0.08331	0.6098
1250	42.290	0.08333	0.1884
1500	50.745	0.08333	0.0636
1750	59.202	0.08333	0.0226

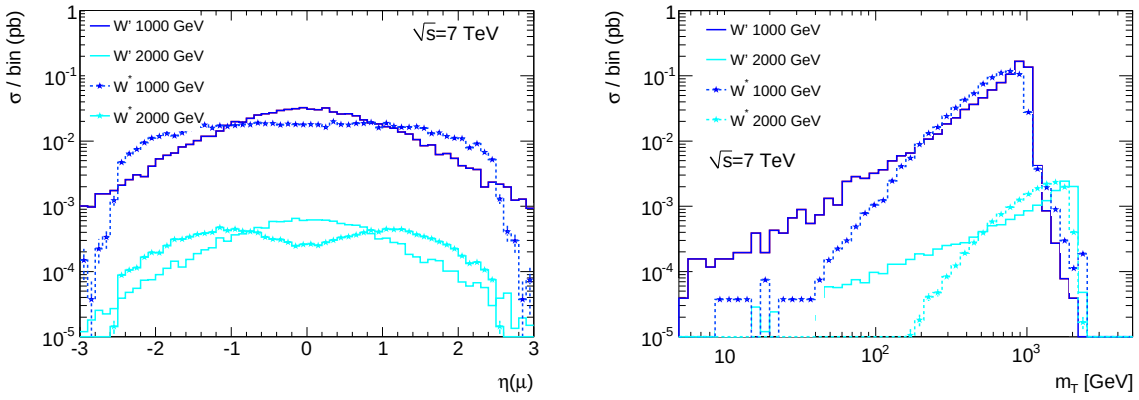

(a) (b)

Figure 3.9: (a) Pseudorapidity muon distribution for W' and W^* of masses 1000 GeV and 2000 GeV respectively. (b) m_{T} distributions for the same masses. No other kinematic cut is imposed.

Bibliography

[1] A.D. Martina, W.J. Stirlingb, R.S. Thornec and G. Wattc, Parton distributions for the LHC, Eur.Phys.J.C63:189-285,2009, arXiv:0901.0002v3 [hep-ph].

[2] T. Sjostrand et al., JHEP 05, 026. 352 (2006).

[3] K. Melnikov, F. Petriello, Electroweak gauge boson production at hadron colliders through O(alpha(s)**2), Phys. Rev. **D74**, 114017, [hep-ph/0609070] (2006).

[4] R. Gavin, Y. Li, F. Petriello *et al.*, FEWZ 2.0: A code for hadronic Z production at next-to-next-to-leading order, [arXiv:1011.3540 [hep-ph]] (2010).

[5] F. Petriello, private communication.

[6] A. Sherstnev and R. S. Thorne, Parton Distributions for LO Generators, Eur. Phys. J. C55 (2008) 1296 553575, arXiv:hep-ph/0711.2473 [hep-ph].

[7] E. Boos et al. (CompHEP Collaboration), Nucl. Instr. Meth. A534, 250 (2004), hep-ph/0403113.

[8] J. Pumplin et al., JHEP 07, 012 (2002).

[9] D.L. Adams,...,D. Fassouliotis,...,C. Kourkoumelis,...,D. Popovic,..., N. Vranjes et al. Search for high-mass states with lepton plus missing transverse energy using the ATLAS Detector with 36 pb^{-1} of pp collisions at $\sqrt{s}$ = 7 TeV, ATL-COM-PHYS-2010-1073.

Chapter 4

ATLAS Experiment

4.1 The Large Hadron Collider at CERN

The Large Hadron Collider (LHC) [1, 2] located at CERN, is a two-ring-superconducting-hadron accelerator and collider installed in 26.7 km tunnel that was constructed between 1984 and 1989 for the Large Electron Positron (LEP) collider. LHC is re-using not only the LEP tunnel, but also its injection chain (LINAC-to-Proton Synchrotron-to-Proton Synchrotron Booster-to-Super Proton Synchrotron). Figure 4.1 shows schematic view of the LHC accelerator complex.

In total there are eight straight sections and eight arcs at the LHC, which allow for a maximum of eight collision points. Experiments which study the particles produced in the LHC collisions are located at four of these eight points. Two large general purpose detectors are **A** **T**oroidal **L**HC **A**pparatu**S** (ATLAS) [3] and the **C**ompact **M**uon **S**olenoid Experiment (CMS) [4] located at Point 1 and Point 5, respectively. Two smaller specialised experiments, **A** **L**arge **I**on **C**ollider **E**xperiment (ALICE) [5], which study the products of lead-lead collisions, and the **L**arge **H**adron **C**ollider **B**eauty Experiment (LHCb) [6], an experiment designed to study physics using bottom quarks, are located at Point 2 and Point 8, respectively. The remaining points contain equipment used for beam cleaning, radio-frequency cavities and location for the beam dump [1].

LHC is the worlds most powerful experimental tool for research in particle physics: it is designed to collide protons at a center-of-mass energy $\sqrt{s}$ =14 TeV once it is fully commissioned, and with rate higher than at any previuous collider. The number of events per second generated

[1] Beside ATLAS, CMS, ALICE and LHCb, there are two more smaller experiments TOTEM [7] and LHCf [8], located near CMS and ATLAS detectors reprectively. TOTEM and LHCf detectors are constructed with the aim to observe very forward particles, which the general purpose detectors cannot detect.

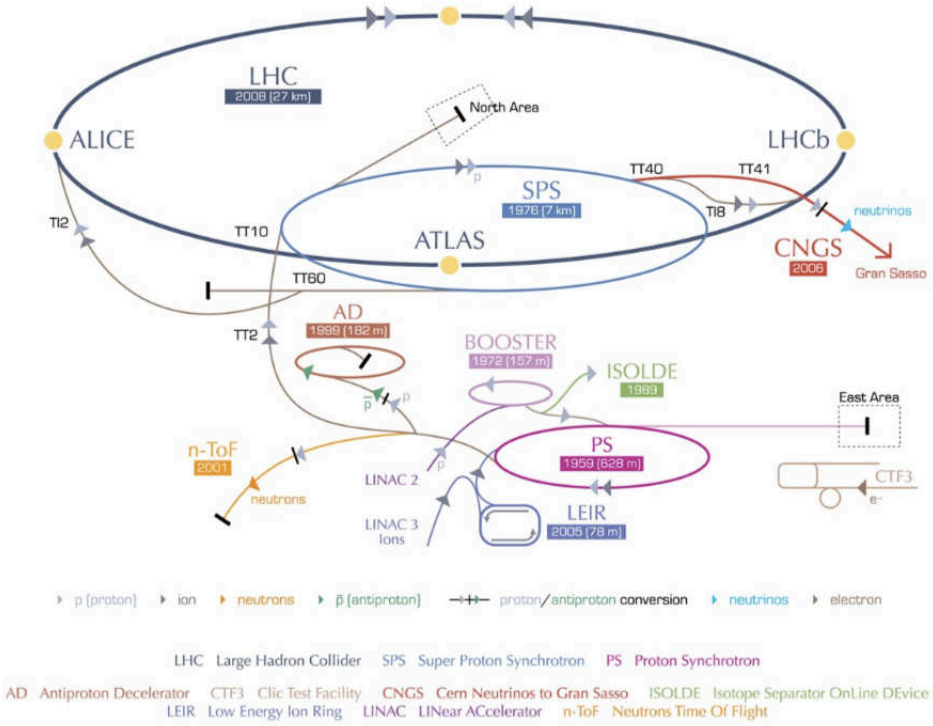

Figure 4.1: The CERN accelerator complex.

in the LHC collisions is given by:

$$N_{event} = L\sigma_{event} \tag{4.1}$$

where σ_{event} is the cross section of the process under study, and L is the machine luminosity. The machine luminosity depends only on the beam parameters and can be written for a Gaussian beam as:

$$L = \frac{N_b^2 n_b f_{rev} \gamma_r}{4\pi\varepsilon_n \beta^*} F \tag{4.2}$$

where N_b is the number of particles per bunch, n_b the number of bunches per beam, f_{rev} the revolution frequency, γ_r relativistic gamma factor, ε_n the normalized transverese beam emitance, β^* is the beta function at the collision point, and F is the geometric luminosity reduction factor due to the crossing angle at the interaction point (IP).

The design of LHC allows for proton beams to be stored in the ring with 2808 bunches, each containing about 110×10^9 protons, with a 'distance' of 25 ns, or roughly 7 m between each other. Thus collisions or bunch-crossings occur at a frequency of 40 MHz. Two high luminosity LHC experiments ATLAS and CMS aim at peak luminosity of $L = 10^{34}$ cm^{-2}s^{-1} for proton operation. LHCb and TOTEM are considered as low luminosity experiments aiming at

peak luminosity of $L = 10^{32}$ cm^{-2}s^{-1} and $L = 10^{29}$ cm^{-2}s^{-1} respectively. ALICE experiment aims at peak luminosity of $L = 10^{29}$ cm^{-2}s^{-1} for nominal lead-lead ion operation. Collider cannot achive maximum designed luminosity quickly, and the increase of the luminosity could be obtained by increasing the bunch crossing frequency $n_b f_{rev}$, or increasing density of protons ($N_p^2/4\pi\varepsilon_n\beta^*$). Increasing of the bunch crossing frequency is limited by the experiment's electronics and trigger speed. Increasing the proton density leads to increasing of multiple interactions per bunch crossing. This effect is usually refered to as pile up. At nominal LHC luminosity with 40 MHz bunch crossing frequency there will be in average 23 pileup events.

The luminosity in the LHC is not constant over a physics run, but decays due to the degradation of intensities and emittances of the circulating beams. The main cause of the luminosity decay during nominal LHC operation is the beam loss from collisions. The overall collider efficiency depends on the ratio of the length of the run to the average turnaround time. Assuming the machine can be operated for 200 days per year and assuming the luminosity lifetime of 15 hours, the optimum run time is 12 hours or 5.5 hours, for the average turnaround times of 7 hours and 1.15 hours, respectively. This leads to average integrated luminoisty of $\mathscr{L}_{\text{int}}\bar{1}00$ fb^{-1}per year at the peak luminosity of $L = 10^{34}$ cm^{-2}s^{-1}.

4.1.1 LHC Running Conditions in 2009 and 2010

The first proton beam was injected in the LHC on the 10 September 2008. Unfortunately, just over a week later on 19 September, during powering tests of the main dipole circuit of Sector 3-4 of the LHC, a fault occurred in the electrical bus connection between a dipole and a quadrupole magnet [9]. A number of magnets underwent mechanical damage and a significant amount of helium was released into the tunnel. This incident led to a delay in the LHC operation of more than a year while the magnets were repaired and a protection system was developed to detect abnormal electrical resistance in bus bars and the interconnections between magnets. The first proton-proton (pp) collisions were produced by the LHC on 23 November 2009 at $\sqrt{s}$ =900 GeV. The first collisions with the stable beam flag[2] were recorded on 30 November 2009 and about 12 μb^{-1} of data at $\sqrt{s}$ =900 GeV were recorded by the end of 2009. The highest energy at a collider was reached on 8 December 2009, when protons were collided at $\sqrt{s}$ =2.36 TeV. The first collisions at $\sqrt{s}$ =7.0 TeV were recorded on 30 March 2010 with all detectors fully operational. LHC continued to run on this energy untill the beggining of November 2010. The ATLAS and CMS detectors have recorded about 45 pb^{-1} of pp data during this period. The

[2]The stable beam flag is one of the operating states of the LHC. It is declared once the beam is fully under control and no further adjustments are required. After the stable beams have been declared, the more sensitive detectors can be switched on.

end of 2010 was marked with collisions of lead ions at energy of 2.76 TeV per nucleon, with $\sim$10 μb^{-1} of data collected by the experiments. Figure 4.2 shows the luminosity delivered by

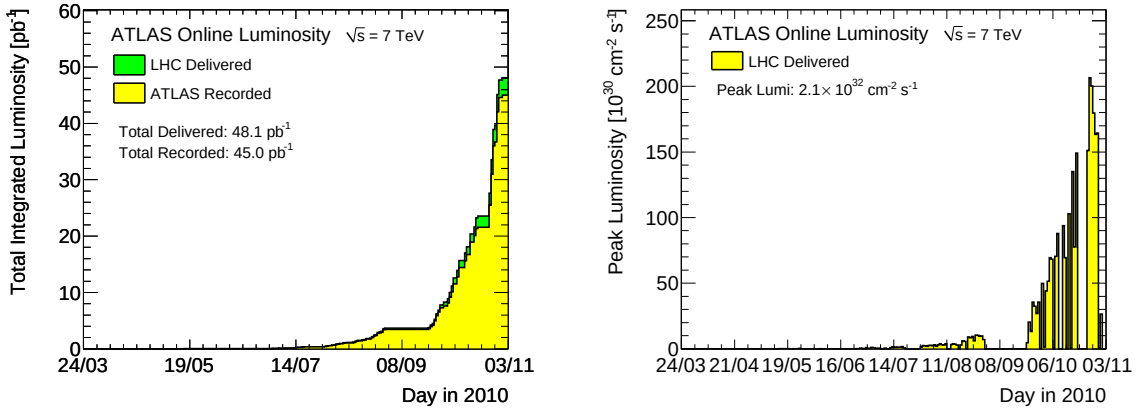

Figure 4.2: Left: Cumulative luminosity versus day delivered to (green), and recorded by ATLAS (yellow) during stable beams and for pp collisions at 7 TeV. The delivered luminosity accounts for the luminosity delivered from the start of stable beams until the LHC requests ATLAS to turn the sensitive detector off to allow a beam dump or beam studies. The systematic uncertainty of the luminosity measurement is estimated to be 11%. An additional 0.8 pb^{-1} was delivered by the LHC between the request for ATLAS to turn off the sensitive detectors and the end of stable beam conditions. Right: The maximum instantaneous luminosity versus day delivered to ATLAS. Only the peak luminosity during stable beam periods is shown. The figures are taken from [10].

the LHC and recorded by ATLAS detector of LHC operation at 7 TeV during 2010, as well as peak of instantaneous luminosity versus day. It is obviuous that the increase in luminosity of LHC has been dramatic, and the most of the data were collected in the last 45 days of the operation. The peak luminosity in pp collisions was 2.07×10^{32} cm^{-2}s^{-1}. The other beam conditions during pp run in 2010 are summarized in the Table 4.1.

4.2 ATLAS: A Toroidal LHC ApparatuS

LHC provides a rich physics potential, ranging from more precise measurements of Standard Model parameters to the search for new physics phenomena. Furthermore, nucleus-nucleus collisions at the LHC provide an unprecedented opportunity to study the properties of strongly interacting matter at extreme energy density. Requirements for the ATLAS detector system have been defined using a set of processes covering a large number of the new phenomena which one can hope to observe at the TeV scale [3, 12, 13].

To ilustrate this usually the production of the Standard Model Higgs boson is taken as a

Table 4.1: Beam conditions in pp collisions during 2010 run. $<\mu>$ is the average number of inelastic interactions per bunch crossing. The first number in the bunch structure column represents maximum number of bunches in the shown period while the second is the maximum number of bunch trains. Information is assembled from [10]. The periods correspond to the ATLAS run periods A, B, C, D, E, F, G, H and I. A run is defined as a longer period of data taking with the same trigger selection on the same fill in the accelerator.

Starting/ end time	Maximum intensity	Maximum lifetime	Peak luminosity	Peak $<\mu>$	Bunch structure
30 Mar/18 Apr	0×10^{11}	56 h	0.0043×10^{30}	0.0384	1 ; 0
23 Apr/17 May	1.07×10^{11}	92 h	0.0068×10^{30}	0.144	3 ; 1
18 May/05 Jun	2.05×10^{11}	15 h	0.24×10^{30}	0.185	8 ; 1
24 Jun/19 Jul	6.67×10^{11}	15 h	1.6×10^{30}	2.13	8 ; 1
19 Aug/30 Aug	101×10^{11}	45 h	10.0×10^{30}	2.05	36 ; 1
22 Sep/07 Oct	628×10^{11}	46 h	71.0×10^{30}	2.82	186 ; 24
08 Oct/18 Oct	342×10^{11}	23 h	150×10^{30}	3.21	295 ; 38
24 Oct/29 Oct	437×10^{11}	20 h	207×10^{30}	3.82	348 ; 46

benchmark. The decay modes of the Higgs boson are a function of the Higgs mass resulting in very different final state topologies, which then set stringent requirements on the detector performance. In the low mass region ($m_H \sim$120 GeV) the $H \to \gamma\gamma$ channel calls for excellent electromangetic calorimetry, while the vector boson fusion $q\bar{q}H \to \tau\tau$ channel requires high efficiency in τ leptons and jet tagging. For masses above 130 GeV the $H \to ZZ^* \to 4\ell$ channel requires efficient lepton identification and precise determination of their momentum, direction and production point. The $H \to WW^{(*)} \to \ell\nu\ell\nu$ which is the most important channel for a Higgs mass around 160 GeV, results in final states with significant energy imbalance in the transverse plane due to neutrinos escaping detection. If the Higgs Boson is heavy (with mass of few hundreds of GeV), measurement of jet energy will be of high importance for processes susch as $H \to WW \to \ell\nu jj$. Further, physics beyond Standard Model (BSM) consits of various searches for the additional Higgs bosons predicted by the Minimal supersymetic extensions of the Standard Model (MSSM), supersymmetric particles in different symmetry breaking scenarios, searches for new heavy gauge bosons, and many other phenomena. These processes lead to detector signatures characterized by the presence of high energetic jets, τ-leptons and b-jets, high momentum leptons and photons, or large missing energy. In particular new heavy gauge bosons (W'/Z') are accessible at the LHC for masses up to 6 TeV via their leptonic decays resulting in very high-p_T leptons. Thus, high-resolution lepton measurements and charge identification are important ingredients of such searches.

Physics processes explained above, impose strict requirements in the design of the detector and its subsystems:

- Efficient and precise reconstruction of charged particles and good peformance in tagging of b-jets and τ-leptons through secondary vertex reconstruction.
- Efficient muon identification and good momentum resolution over three orders of magnitude in momentum $\mathcal{O}(1)$ GeV-$\mathcal{O}(1)$ TeV. Low charge misidentification probability for high-p_T muons is of fundamental importance.
- Excellent electromagnetic calorimetry for electron and photon identification and measurements. Hadronic calorimetry providing accurate jet measurements. An important requirement for ATLAS calorimetry is hermeticity, which is required for good missing transverse energy measurement.
- Large acceptance in pseudorapidity with almost full azimuthal angle coverage.
- Highly efficient triggering on low transverse-momentum objects with sufficient background rejection. This is a prerequisite to achieve an acceptable trigger rate for most physics processes of interest.
- Radiation hardness to tolerate the large particle fluxes provided by the LHC without loss of performance or important ageing effects[3]. In addition, high detector granularity is needed to handle the particle fluxes and to reduce the influence of overlapping events.

Although not strictly part of the detector, computing infrastructure including Worldwide LHC Computing Grid is a vital part of the experiment. ATLAS trigger system provides events at the strongly reduced rate of 200 Hz. With an expected event size of about 1.6 MB per event, this will result in approximately 320 MB/s written to storage. This rate has been exceeded in 2010 already, with maximum rate raching twice stated value. The ATLAS experiment produced several PB of real data, with Monte Carlo (MC) simulation of all processes under study summed up to 2-3 times the volume of data. Both data and MC require a considerable amount of processing power and need to be distributed to a global physicist community. Physicists performing physics analysis will require computing power far beyond what can be provided by

[3]The experimental conditions at the LHC will be challenging: the unprecedented radiation levels are expected to result in activated detector components and severe beam-induced backgrounds. To mitigate their impact, the ATLAS shielding layout and the LHC beam-pipe design were carefully optimised. Institute of Physics Belgrade joined ATLAS Collaboration in 2003 with in-kind contribution in the shielding system. Shielding disk, produced by Lola Corporation, Železnik, Serbia, has threfold purpose: it supports the muon chambers in the first end-cap muon station, it shields these chambers from background radiation emerging from the calorimeters, and it provides a well-defined path for the magnetic field flux return from the solenoid magnet.

a desktop machine or local systems. Facing these requirements the ATLAS Computing Model [14] embraces the Grid paradigm and a high degree of decentralisation and sharing of computing resources. Hence, off-site facilities will be vital to the operation of ATLAS in a way that was not the case for previous experiment based at CERN.

4.2.1 Detector Overview

ATLAS has classical cylindric shape, with a diameter of 25 m, a length of 46 m and weight of about 7000 tons. The nominal interaction point is defined as the origin of the right-handed Cartesian coordinate system, while the beam direction defines the *z*-axis and the $x-y$ plane is transverse to the beam direction. The positive *x*-axis is defined as pointing from the interaction point to the centre of the LHC ring and the positive *y*-axis is defined as pointing upwards. The side-A of the detector is defined as that with positive *z*, and side-C is that with negative *z*. The azimuthal angle ϕ (going from -π to +π) is measured as usual around the beam axis, and the polar angle θ (from 0 to +π) is the angle from the beam axis. The pseudorapidity is defined as η = - ln tan(θ/2). The transverse momentum p_T is defined in the $x-y$ plane as p_T = p sin(θ), and similar for the transverse energy E_T. Since difference in pseduorapidity is Lorentz invariant, and boosts along the beam axis also do not affect ϕ, it is useful to measure distance ΔR in the η -ϕ space: $\Delta R_{ij} = \sqrt{(\phi_i - \phi_j)^2 + (\eta_i - \eta_j)^2}$.

The ATLAS detector has been installed underground in a huge cavern, situated at point 1 on the LHC ring, directly opposite the main entrance to the CERN site. Two huge access shafts were used for the detector instalation. ATLAS cavern is ilustrated in Fig 4.3.

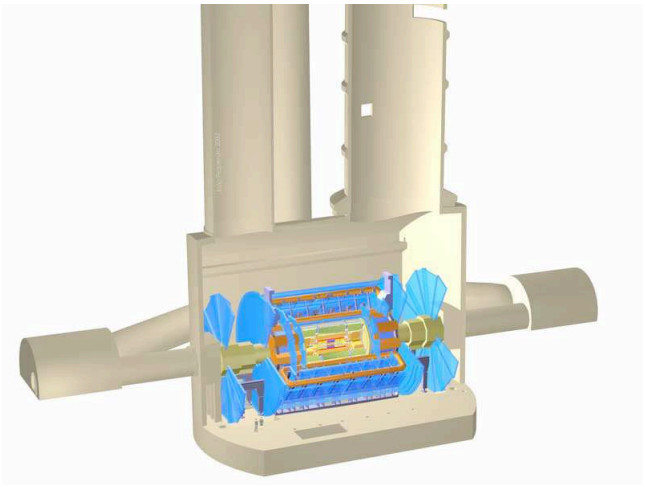

Figure 4.3: The ATLAS detector cavern.

The overall detector layout of ATLAS is shown in Fig. 4.2.1. The detector is nominally

forward-backward symmetric with respect to the interaction point and consists of a series of concentric detector systems around the interaction point. The main components of the detector are: the Inner Detector (ID) used for tracking of charged particles, the electromagnetic and hadronic calorimeters used for measuring the energy of electrons, photons and jets, the Muon Spectrometer (MS) for identifying and measuring muons, and the magnet system. A characteristic feature of the ATLAS detector is its enormous magnet system. The magnet configuration is based on an inner thin superconducting 2 T solenoid surrounding the inner detector cavity, and three large superconducting air-core toroids with mean field value of 1 T consisting of independent coil. The subdetector requirements described in the previous section and characteristics are summarized in the Table 4.2. Their main properties, including the trigger and software framework, will be briefly discussed in next sections. More information can be found in [3, 12, 14].

Table 4.2: General performance goals of the ATLAS detector [3]. For high-p_T muons, the Muon Spectrometer performance is independent of the Inner Detector system. The units for E and p_T are in GeV.

Detector Component	**Required resolution**	**η coverage**	
		measurement	trigger
Tracking	$\sigma_{p_T}/p_T = 0.05\% p_T \oplus 1\%$	$\pm$2.5	$\pm$2.5
EM calorimetry	$\sigma_{E/E} = 10\%/\sqrt{E} \oplus 0.7\%$	$\pm$3.2	$\pm$2.5
Hadronic calorimetry (jets)			
barrel and end-cup	$\sigma_{E/E} = 50\%/\sqrt{E} \oplus 3\%$	$\pm$3.2	$\pm$3.2
forward	$\sigma_{E/E} = 100\%/\sqrt{E} \oplus 10\%$	3.1$<|\eta|<$4.9	3.1$<|\eta|<$4.9
Muon spectrometer	$\sigma_{p_T}/p_T = 10\%$ at $p_T = 1$ TeV	$\pm$ 2.7	$\pm$ 2.4

4.3 Inner Detector

The Inner Detector (ID) [3, 16] shown in Fig. 4.5 is located at the innermost part of ATLAS. The detector is designed to provide hermetic and robust pattern recognition, excellent momentum resolution and both primary and secondary vertex measurements for charged tracks above a given p_T threshold (nominally 0.5 GeV, but could be as low as 0.1 GeV). Geometrical coverage is up to $|\eta|<$2.5, and full in ϕ. ID also provides electron identification over $|\eta|<$2.0 and for a wide range of energies (0.5 GeV-150 GeV). It comprises of three complementary sub-detectors: the Pixel Detector, the Semi-Conductor Tracker (SCT) and the Transition Radiation Tracker (TRT). ATLAS Inner Detector is described briefly below, full details can be found elsewhere.

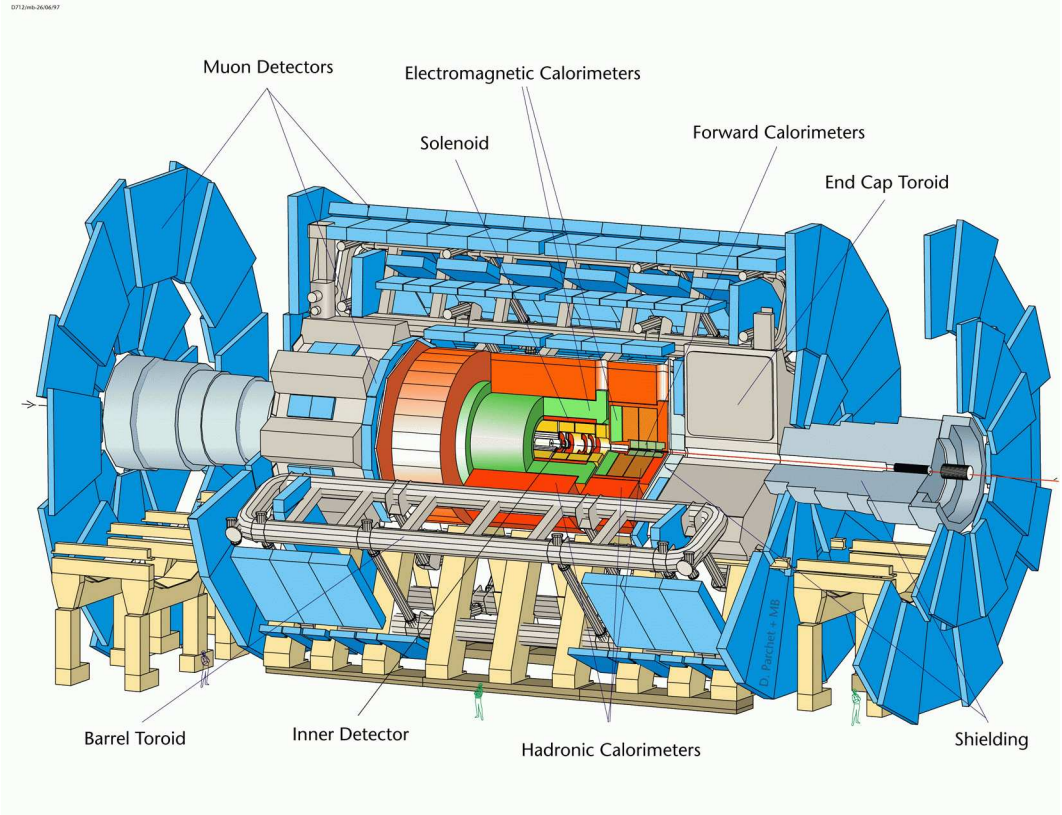

Figure 4.4: The layout of the ATLAS detector.

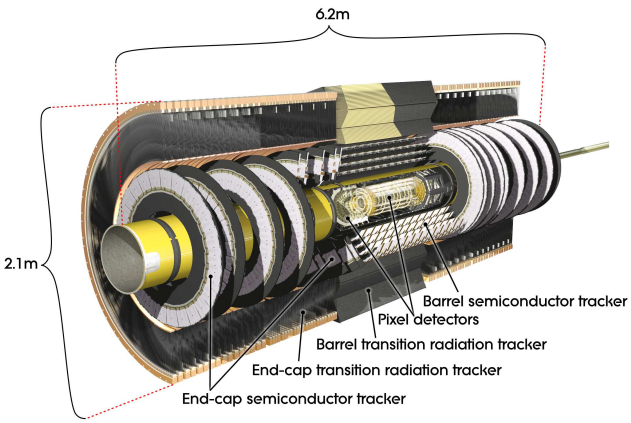

Figure 4.5: The layout of the ATLAS Inner Detector. It is cylindrical in shape with a length of 7024 mm and a radius of 1150 mm which permits pseudorapidity coverage in the region $|\eta| < 2.5$

The Pixel Detector sensitive elements cover radial distances between 50 mm and 150 mm and up to $|\eta| < 2.5$. The detector consists of 1744 silicon pixel modules arranged in three concentric barrel layers and two endcaps of three disks each. The innermost Pixel layer (known

as the B-layer) is located just outside the beam pipe at a radius of 50 mm. Pixel detector provides typically three measurement points for particles originating in the beam-interaction region. Each module covers an active area of 16.4 mm$\times$60.8 mm and contains 47 232 pixels, most of size 50 mm$\times$400 mm. The direction of the shorter pitch defines the local x-coordinate on the module and corresponds to the high precision position measurement in the $R-\phi$ plane. The longer pitch, corresponding to the local y-coordinate, is oriented approximately along the z direction in the barrel and along R in the endcaps. The pixel modules have a resolution of 10 μm in the $R-\phi$ coordinate, and 115 μm in the z-coordinate. A module is read out by 16 radiation-hard frontend chips bump-bonded to the sensor; the total number of readout channels is $\sim$80.4 million. Hits in a pixel are read out if the signal exceeds a tunable threshold.

The SemiConductor Tracker sensitive elements span radial distances from 299 mm to 560 mm and cover the region $|\eta|$ <2.5. The detector consists of 4088 modules of silicon-strip detectors arranged in four concentric barrels ($|\eta|$ <1.4) and two endcaps of nine disks each. It provides typically eight strip measurements (four space-points) for particles originating in the beam-interaction region. The strips in the barrel are approximately parallel to the solenoid field and beam axis, and have a constant pitch of 80 mm, while in the endcaps the strip direction is radial and of variable pitch. Most modules consist of four silicon-strip sensors. Two sensors on each side are daisy-chained together to give 768 strips of approximately 12 cm in length. A second pair of identical sensors is glued back-to-back with the first pair at a stereo angle of 40 mrad to provide space points. The position resolution of the detector is 10 μm in the precision coordinate and 580 μm along z for the barrel and R for the end-cap. The strips are read out by radiation-hard front-end readout chips, each chip reading out 128 channels. The total number of readout channels is $\sim$6.3 million.

The Transition Radiation Tracker (TRT) sensitive volume covers radial distances from 563 mm to 1066 mm. The detector consists of 298 304 proportional drift tubes (straws), 4 mm in diameter, read out by 350 848 channels of electronics. The straws in the barrel region are arranged in three cylindrical layers and 32 ϕ sectors. They have split anodes and are read out from each side. The straws in the endcap regions are radially oriented and arranged in 80 wheel-like modular structures. The TRT straw layout is designed so that charged particles with transverse momentum p_T > 0.5 GeV and with pseudorapidity $|\eta| < 2.0$ cross typically more than 30 straws. The TRT provides electron identification via transition radiation from polypropylene fibres (barrel) or foils (endcaps) interleaved between the straws. The much higher energy of the transition radiation photons ($\sim$6 keV compared with the few hundred eV deposited by an ionising particle in the Xe, CO_2, O_2 gas) is detected by a second, high-threshold, discriminator.

The ID system provides tracking measurements in a range matched by the precision mea-

surements of the electromagnetic calorimeter. The electron identification capabilities are enhanced by the detection of transition-radiation photons in the xenon-based gas mixture of the straw tubes. The semiconductor trackers also allow impact parameter measurements and vertexing for heavy flavour and τ-lepton tagging. The secondary vertex measurement performance is enhanced by the innermost layer of pixels, at a radius of about 5 cm.

4.4 Calorimeters

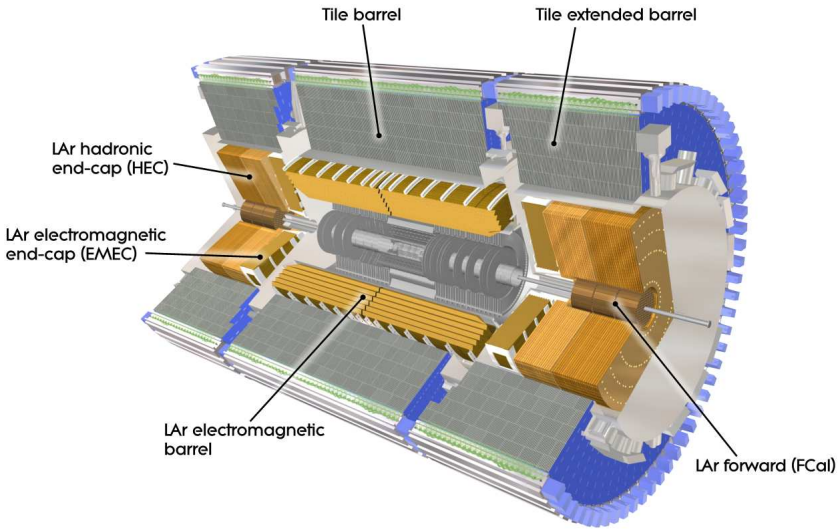

Figure 4.6: ATLAS Calorimeters.

The ATLAS calorimeters described in detail in [3, 17, 18], are located between the Inner Detector and the Muon Spectrometer, and provide coverage over $|\eta| < 4.9$. In the η region covered by the Inner Detector an electromagnetic calorimeter with fine granularity has been deployed to provide precision measurements and identification of electrons and photons. The coarser granularity of the rest of the calorimeter is sufficient to satisfy the physics requirements for jet reconstruction and transverse missing energy measurement. The layout of the system is presented in Fig4.6.

Calorimeters must provide good containment for electromagnetic and hadronic showers, and must also limit punch-through into the muon system. Hence, calorimeter depth is an important design consideration. The total thickness of the Electromagnetic calorimeter (EM) is > 22 and > 24 radiation lengths[4] (X_0) in the barrel and in the end-caps respectively. The approximate 9.7

[4]For electrons radiation length is defined as the mean distance over which high-energy electron loses all but $1/e$

interaction lengths[5] (λ) of active calorimeter in the barrel (10 λ in the end-caps) are adequate to provide good resolution for high-energy jets. The total thickness, including 1.3 λ from the outer support, is 11 λ at η = 0 and has been shown both by measurements and simulations to be sufficient to reduce punch-through well below the irreducible level of prompt or decay muons. Together with the large η - coverage, this thickness will also ensure a good measurement of the missing energy.

LAr electromagnetic calorimeter is composed of sampling detectors with full azimuthal symmetry housed in one barrel and two endcap cryostats. More specifically, a highly granular EM calorimeter with accordion-shaped electrodes and lead absorbers in liquid argon covers the pseudorapidity range $|\eta| <$3.2, and contains a barrel part ($|\eta| <$1.475) and an endcap part (1.375$< |\eta| <$3.2). For $|\eta| <$1.8, a presampler (PS), consisting of an active LAr layer and installed directly in front of the EM calorimeters, provides a measurement of the energy lost upstream. For $|\eta| <$2.5 the calorimeter is longitudinally segmented in three layers. The inner layer, which has an approximately constant thickness of 5 X_0, is equipped with thin strips of 5 mm length along η . The segmentation is $\Delta\eta \times \Delta\phi$ = 0.003$\times$0.1 providing good position resolution. The same compartment acts as a preshower, used for γ/π^0 separation. The middle layer is segmented in towers with $\Delta\eta \times \Delta\phi$= 0.02$\times$50.025. The total calorimeter thickness up to the end of the middle compartment exceeds 20X_0. The segmentation of the last compartment is $\Delta\eta \times \Delta\phi$ = 0.05$\times$0.025 and its thickness varies between 2 and 12X_0.

Hadronic calorimeters consist of hadronic Tile calorimeter spanning the pseudorapidity region $|\eta| <$1.7 in the barrel and LAr hadronic end-cap (1.5$< |\eta| <$3.2) and forward calorimeters (3.1$< |\eta| <$4.9).

The Tile calorimeter (TileCal) is placed directly outside the EM calorimeter envelope. Its barrel and two extended barrels cover the region $|\eta| <$1.0, and 0.8$< |\eta| <$1.7 respectively. It is a sampling calorimeter using steel as the absorber and scintillating tiles as the active material. The barrel and extended barrels are divided azimuthally into 64 modules. It is segmented in depth in three layers, approximately 1.5, 4.1 and 1.8λ thick for the barrel and 1.5, 2.6, and 3.3λ for the extended barrel. Two sides of the scintillating tiles are read out by wavelength shifting fibres into two separate photomultiplier tubes. In η, the readout cells built by grouping fibres into the photomultipliers are pseudo-projective towards the interaction region. The granularity of the Tile is $\Delta\eta \times \Delta\phi$ is 0.1$\times$0.1 in the first two samplings and 0.1$\times$0.2 in the outermost sampling.

of its energy by bremsstrahlung.

[5]Interaction length is the mean path length required to reduce the energy of relativistic charged particles by the factor 1/*e* as they pass through matter.

The Hadronic End-cap Calorimeter (HEC) consists of two independent wheels per end-cap, located directly behind the end-cap electromagnetic calorimeter and sharing the same LAr cryostats. To reduce the drop in material density at the transition between the end-cap and the forward calorimeter (around $|\eta|$ = 3.1), the HEC extends out to $|\eta|$ = 3.2 thereby overlapping with the forward calorimeter. Similarly, the HEC range also slightly overlaps that of the tile calorimeter ($|\eta| <$1.7) by extending to $|\eta| =$1.5. Each wheel is built from 32 identical wedge-shaped modules, assembled with fixtures at the periphery and at the central bore. Each wheel is divided into two segments in depth, for a total of four layers per end-cap. The wheels closest to the interaction point are built from 25 mm parallel copper plates, while those further away use 50 mm copper plates (for all wheels the first plate is half-thickness).

The Forward Calorimeter (FCal) is integrated into the end-cap cryostats, as this provides clear benefits in terms of uniformity of the calorimetric coverage as well as reduced radiation background levels in the muon spectrometer. In order to reduce the amount of neutron albedo in the inner detector cavity, the front face of the calorimeter is recessed by about 1.2 m with respect to the EM calorimeter front face. This severely limits the depth of the calorimeter and therefore calls for a high-density design. It is approximately 10λ deep, and consists of three modules in each end-cap: the first, made of copper, is optimised for electromagnetic measurements, while the other two, made of tungsten, measure predominantly the energy of hadronic interactions.

4.5 Muon Spectrometer

The Muon Spectrometer of the ATLAS detector (MS) [3, 19] is designed to provide triggering and bunch crossing identification of events with high-p_T muons, and muon identification and momentum measurement independent of the Inner Detector. Muon momentum measurements are based on the magnetic deflection of muon tracks in the large superconducting air-core toroid magnets, instrumented with separate trigger and high-precision tracking chambers. The driving performance goal is a stand-alone transverse momentum resolution of approximately 10% for 1 TeV tracks, with minimum charge misidentification. The associated sagitta of 500 μm for such tracks requires a resolution of 50 μm, obtained with precise knowledge of the magnetic field and chamber positioning. In Fig. 4.7 a quadrant of the MS is shown with the three detector technologies indicated. A brief description of the toroid magnets and these technologies is given in the following subsections.

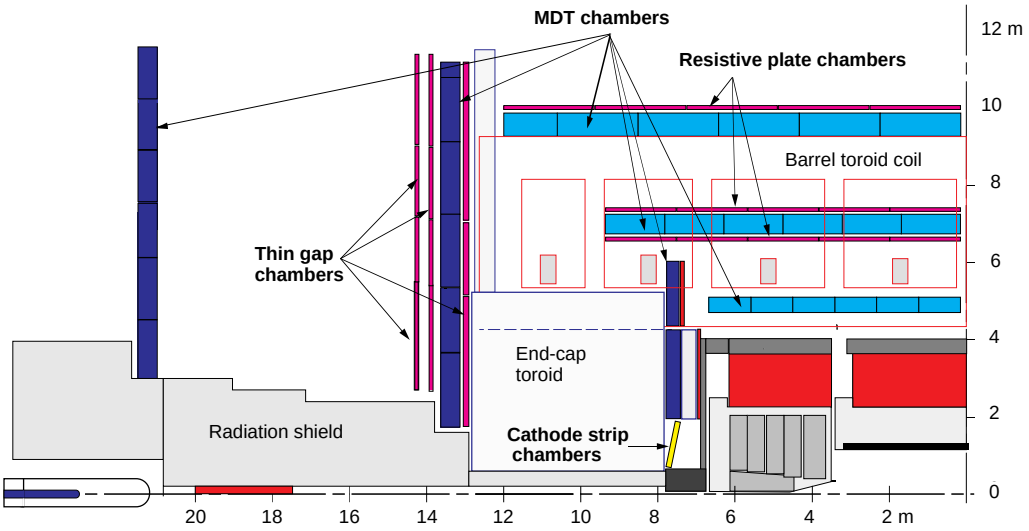

Figure 4.7: Cross-section of a quadrant of the Muon Spectrometer parallel to the beam axis. Different detector technologies are indicated.

4.5.1 The toroid magnets

The toroidal configuration provides a field which is mostly orthogonal to the muon trajectories over a large volume and little material in the measurement regions, minimizing the degradation of resolution due to multiple scattering. Over the range of $|\eta|$ <1.4, magnetic bending is provided by the large barrel toroid. Eight coils are arranged symmetrically around the beam axis, extending radially from 9.4 m to 22 m, with a length of 25.3 m. For 1.6< $|\eta|$ <2.7, muon tracks are detected by two smaller end-cap magnets inserted into both ends of the barrel system. The end-cap toroids are rotated in azimuth by an angle of 22.5^0 with respect to the barrel coils to provide for radial overlap, and to optimize the bending power in the transition region (1.4< $|\eta|$ <1.6). Nevertheless, due to the finite number of coils, the field confguration is not perfectly toroidal. Regions with degraded momentum resolution exist due to the low feld integral, represented in Fig.4.8. The bending power is particulary lower in the transition regions where the two magnets overlap.

4.5.2 Muon chambers

The chamber geometry follows the eight-fold symmetry of the toroid magnets, as illustrated in Fig.4.9. Each octant in the azimuthal direction is divided in a large and a small sector. The large chambers occupy the region between the barrel coils, while the small sectors are aligned with them. Overlaps in the boundaries of the sectors minimize gaps in detector coverage and

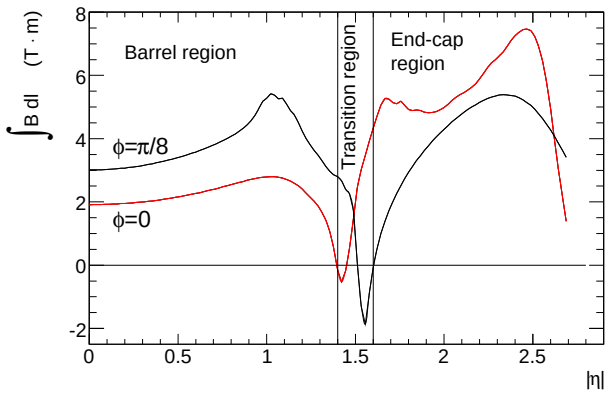

Figure 4.8: The bending power, $\int \vec{B}d\vec{l}$, of the azimuthal component of the magnetic field, integrated between the first and the last muon station, as a function of η [3].

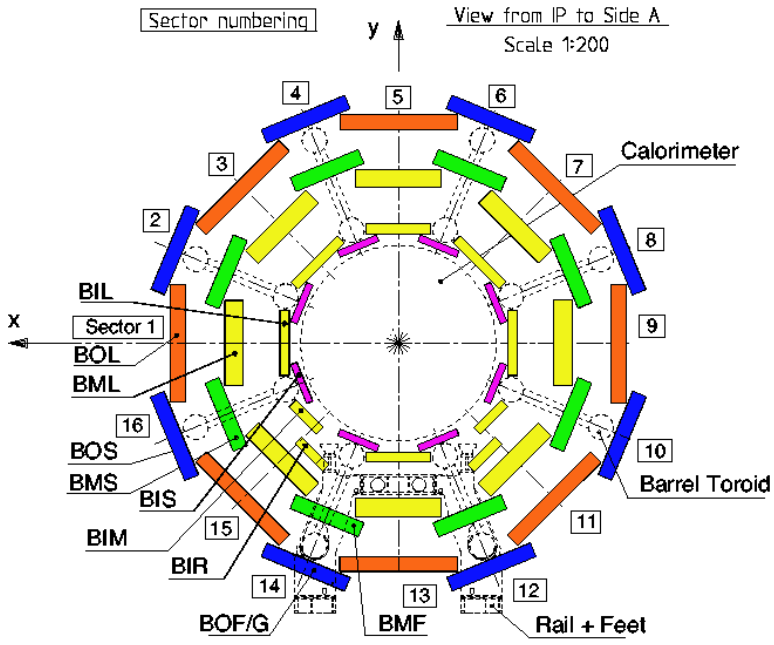

Figure 4.9: Schematic view of the muon spectrometer in the *xy* projection (perpendicular to the beam axis). Three concentric cylindrical layers of eight large and eight small chambers are shown.

also allow for the relative alignment of adjacent sectors using tracks recorded by both a large and a small chamber. In the barrel region, tracks are measured in chambers arranged in three cylindrical layers around the beam axis, at radii of approximately 5 m, 7.5 m, and 10 m. In the transition and end-cap regions, the chambers are installed in planes perpendicular to the beam, also in three layers, located at distances of $|z| \approx$7.4 m, 10.8 m, 14 m (transition region), and 21.5 m (end-cap) from the interaction point. Extra stations in the barrel-end cap transition region are positioned in a wheel at $|z|$ = 10.4 m, called the extended stations. The installation of parts of these stations is staged. In the center of the detector ($\eta \sim 0$), a gap in chamber coverage has been left open to allow for services to the solenoid magnet, the calorimeters and the Inner Detector. The size of the gap varies from sector to sector depending on the service necessities, the biggest gaps of 1-2 m being located in the large sectors. This region extend up to $|\eta|$ = 0.08 for large chambers and $|\eta|$ = 0.04 for small sectors. Additional gaps in the acceptance occur in sectors 12 and 14 due to the detector support structure (so called "feet" region).

The Muon Spectrometer deploys Monitored Drift Tube (MDT) chambers to make precision measurements in the region of $|\eta| <$2.4. MDTs were chosen because of their high measurement accuracy, predictability of mechanical deformations and simplicity of construction. In the forward region (2.0$< |\eta| <$2.7), the innermost layer is equipped with a radiation hard technology of Cathode Strip Chambers (CSC), better suited for handling the expected particle fluxes. CSCs provide measurements of both coordinates and additionally good timing resolution. Fast triggering and second coordinate (ϕ) determination is provided by Resistive Plate Chambers (RPC) in the barrel and Thin Gap Chambers (TGC) in the end-caps. Both systems are able to separate beam crossings with intrinsic timing accuracies of a few nanoseconds and provide rough estimates of the track momentum.

A naming scheme is adopted for the MDT stations, according to the position of the stations in the spectrometer. The muon stations are named Inner, Middle, and Outer, according to the distance from the Interaction Point. The three stations for the barrel are denoted BI, BM, and BO, and for the End-Cap EI, EM, and EO, respectively. Some special stations that do not follow this naming scheme are placed in regions with low coverage, for instance in the regions between the feet of the barrel toroid. Along the $z-$axis, the MS is divided into two sides, called side A (positive z) and C (negative z).

Monitored drift tube chambers provide most of the precision measurements in the Muon Spectrometer. Fig 4.10(a) shows a typical middle or outer MDT barrel station with two multilayers consisting of three layers of MDTs. The inner stations are equipped with four layers per multilayer to improve the local pattern recognition. An MDT consists of an aluminium tube with a radius of 30 mm filled with a drift gas mixture of Ar : CO_2 = 93 : 7 at a pressure of 3 bar.

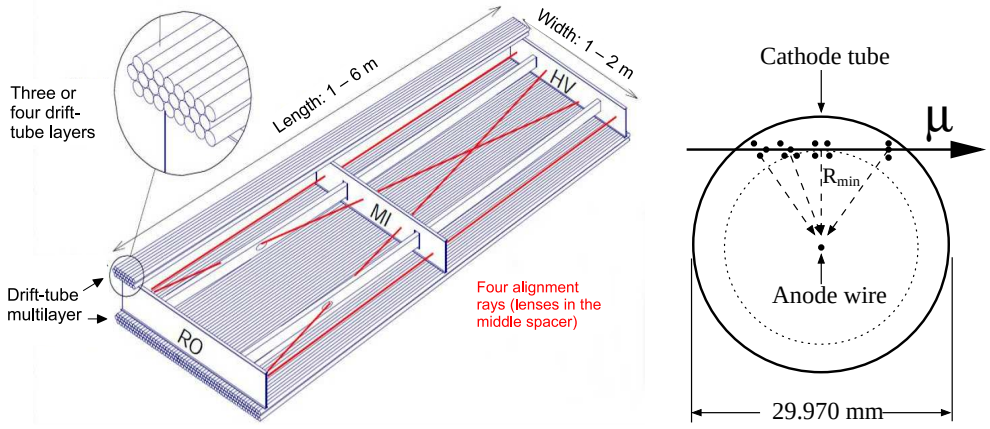

(a) (b)

Figure 4.10: Schematic overview of a barrel MDT station (a). Part of the top multi-layer is removed to show the interior of the station. Cross-section of a MDT tube (b).

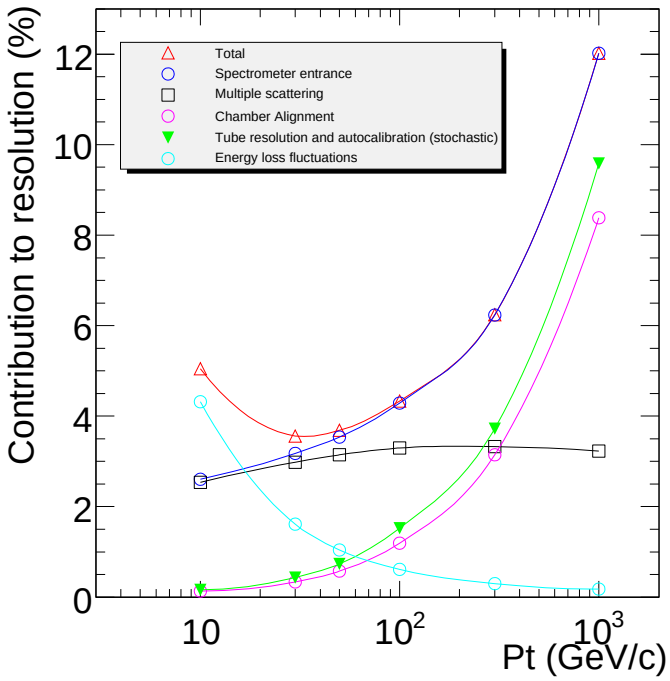

Figure 4.11: Contributions to the designed momentum resolution for muons reconstructed in the Muon Spectrometer as a function of transverse momentum for $|\eta| < 1.5$. The alignment curve is for an uncertainty of 30 μm in the chamber positions [13].

The gold plated tungsten anode wire with a diameter of 50 μm is kept at 3080 V, generating a radial electric field. When a charged particle traverses the tube, ionization clusters are produced in the drift gas, which drift to the wire, creating a signal as ilustrated in Fig 4.10(b). The distance between the particle and the wire is determined by measuring the arrival time of the first cluster that reaches the wire causing the signal to pass a threshold. The measured drift time is converted to a drift radius of the measurement via a radius-time relation. This relation is not linear and is sensitive to various external conditions such as temperature, gas-mixture and magnetic field. These local conditions are monitored with magnetic field sensors and temperature sensors installed on the MDT stations. Measurements from the RPCs or extrapolation from the Inner Detector system provides the second coordinate of the measurement. The MDT stations are positioned such that the precision plane is in the bending plane of the toroid magnetic field.

Figure 4.11 shows the transverse momentum resolution of the MDT chambers for the barrel ($|\eta| <$1.5). For muons with a transverse momentum of less than 20 GeV, energy loss fluctuations in the calorimeters form the dominant contribution to the momentum resolution. For muons with transverse momenta between 20 GeV and 200 GeV, multiple scattering dominates the resolution. For very high transverse momentum muons, over 200 GeV, the resolution is dominated by the intrinsic MDT tube resolution and chamber alignment.

Cathode strip chambers are installed in the region of 2$< |\eta| <$2.7 in the inner wheel of the end caps. The expected particle rate of over 150 kHz/cm^2 gives a too high occupancy for MDT chambers. The CSCs can handle this high rate and achieve a typical resolution of 40 μm in the precision plane and 5 mm in the second coordinate. Eight small and eight large stations are installed in sectors like the MDT chambers. CSCs are multi-wire proportional chambers with anode wires oriented radially and cathode strips oriented perpendicular to them, segmented in either η or ϕ. Interpolation of the charge picked up by the strips provides a position measurement. Each crossing muon will give four measurements in both η and ϕ planes, making it possible to resolve multiple particles per station. The small gas volume and gas mixture (Ar : CO_2 = 80 : 20) provide small drift times resulting in a time resolution of 7 ns.

Resistive plate chambers have two stations mounted on the middle barrel MDT chambers, while the outer barrel MDT chambers are equipped with one RPC station, like in Fig 4.7. Each RPC station provides two measurements in η and ϕ, giving a total of six measurements per muon traversing the barrel spectrometer. The ϕ measurements provide the second coordinate for the MDT precision measurements. The typical resolution of the RPC measurements is 10 mm in both the bending and the non-bending plane. The RPC is a gaseous parallel electrode-plate detector. Two resistive plates made of phenolic-melamine plastic are kept parallel at a distance of 2 mm. As drift gas, a mixture of $C_2H_2F_4$: Iso-C_4H_{10} : SF_6 = 94.7 : 5 : 0.3 is used.

This gas-mixture allows operation at a voltage of 9.8 kV and gives a signal width of 5 ns. Per gas gap, the signal is read out via metallic strips in η and ϕ. Each RPC station consists of two gas gaps.

Thin gap chambers are multi-wire proportional detectors operating with a gas mixture of CO_2 : C_5H_{12} = 55 : 45, operated at 2.9 kV. The radial coordinate is measured with gold-coated tungsten anode wires, the azimuthal position is measured by pick-up strips. A TGC unit consists of two gas gaps (doublet) or three gas gaps (triplet). The units are installed in four wheels per end cap, Fig 4.7. A doublet unit is positioned before the inner MDT wheel, a triplet before the middle MDT wheel. Two doublet units after the middle MDT wheel give a total of 9 measurements per particle traversing the end cap spectrometer. The typical resolution of the TGC chambers is 2-6 mm in the bending plane and 3-7 mm in the non-bending plane.

4.5.3 Alignment system

Although construction quality ensures a good precision for the chamber elements and the chambers as a whole, chamber positioning accuracy is limited to 5 mm, and additional deformations up to a few hundred microns due to thermal gradients and gravity are expected. This is two orders of magnitude above the 50 μm resolution on sagitta measurements that are required for momentum determination of 10% at 1 TeV.

To reach this goal, a sophisticated optical alignment system was built to relate the position of each chamber to that of its neighbours within the same layer or tower continuously. In practice, the positions are measured and a new set of alignment constants are derived every 20 minutes. Given the present stability of the system, the measurements are only performed once per hour. Three different technologies, described in [3] are applied for the more than 12 000 lines, based on optoelectronic image sensors that monitor an illuminated target. In the barrel, a row of MDT chambers are referenced to each other by praxial and axial systems, while the projective system links inner, middle and outer stations. Additional reference lines connect chambers with the barrel toroid, or small to large sectors. In the end-cap, polar lines and azimuthal lines linked to a grid of alignment bars are also used, extending the coverage to CSC chambers. The global position determination of the barrel and end-cap muon-chamber systems with respect to each other and to the Inner Detector are complemented by track-based alignment algorithms. The latter ones exploit the nearly straight trajectories of high-p_T muons, or eventually might use dedicated runs without toroidal field. Individually, both optical and track-based alignment can only reach a precision a few hundred microns. The desired accuracy in the sagitta measurement of 50 μm or below can only be achieved with their combination.

As the result of commissioning studies from 2009 and 2010, on a large sample of cosmic ray events and samples of straight tracks obtained in periods of collision data taken with no magnetic field in the muon system, initial alignment accuracy was established. These values are obtained from the cosmic ray data and collision runs with no toroidal magnetic field (straight track runs).For the barrel, accuracy of alignment wass found to be 100 ± 20 μm, while for the endcap (and transition) region 100 ± 20 μm. About 10% of the chambers in the transition region were not monitored with alignment sensors, and their position had been known at the level of about 1 mm. The position of the CSC chambers has been measured with straight muon tracks and found to agree within 700 μm with the positions used in track reconstruction.

4.6 Forward detectors

For completeness three ATLAS forward detectors LUCID, ALFA, and ZDC are briefly mentioned [3]. The main function of the first two detectors is to determine the luminosity delivered to ATLAS, and ZDC is designed to determine the centrality of heavy-ion collisions. LUCID (LUminosity measurement using Čerenkov Integrating Detector) is placed at $\sim$17 m from the IP. It detects inelastic pp scattering in the forward direction, and is the main online relative-luminosity monitor for ATLAS. The ALFA (Absolute Luminosity For ATLAS) detector is located at $\sim$240 m. It consists of scintillating fibre trackers located inside Roman pots which are designed to approach as close as 1 mm to the beam. The Zero-Degree Calorimeter (ZDC) is located at $\sim$140 m from the interaction point, just beyond the point where the common straight-section vacuum-pipe divides back into two independent beam-pipes. The ZDC modules will measure neutral particles at pseudorapidities $|\eta| > 8.2$.

4.7 Trigger and Data Acquisition, Detector Control System and Data Quality

Proton-proton interaction rate at LHC peak luminosity of $L = 10^{34}$ cm^{-2}s^{-1} is at the order of GHz. Event data recording, due to technology and resource limitations, is expected to be limited to about 200 Hz. Thus, an overall rejection factor of 5×10^{6} against minimum-bias processes while maintaining maximum efficiency for the physics processes of interest is required. Therefore, a dedicated trigger system [3, 20, 21, 22] is developed for the ATLAS experiment.

In addition to controlling movement of data down the trigger selection chain, the data acquisition system also provides for the configuration, control and monitoring of the ATLAS detector

during data-taking. Supervision of the detector hardware (gas systems, power-supply voltages, etc.) is provided by the Detector Control System (DCS) [23]. Information from the DCS must be taken into account when making a decision about whether to use a given dataset for physics analysis.

ATLAS trigger and and Data Acquisition system, and Detector Control System and Data Quality framework are briefly described in the next two subsection.

4.7.1 Trigger

The trigger system has three distinct levels: level one (L1), level two (L2), and the event filter (EF); L2 and EF together form High-Level-Trigger (HLT). Each trigger level refines the decisions made at the previous level and, where necessary, applies additional selection criteria.

The L1 trigger searches for signatures from high-p_T muons, electrons/photons, jets, and τ-leptons decaying into hadrons, as well as large missing and total transverse energy. The L1 trigger uses reduced-granularity information from a subset of detectors: the Resistive Plate Chambers and Thin-Gap Chambers for high-p_T muons, and all the calorimeter sub-systems for electromagnetic clusters, jets, τ-leptons, missing and total transverse energy[6]. The maximum L1 accept rate which the detector readout systems can handle is 75 kHz (upgradeable to 100 kHz), and the L1 decision must reach the front-end electronics within 2.5 μs after the bunch-crossing with which it is associated. Results from the L1 muon and calorimeter triggers are processed by the central trigger processor, which implements a trigger menu made up of combinations of trigger selections. Prescaling of trigger menu items is also available, allowing optimal use of the bandwidth as luminosity and background conditions change.

The HLT algorithms use the full granularity and precision of calorimeter and muon chamber data, as well as the data from the inner detector, to refine the trigger selections. Better information on energy deposition improves the threshold cuts, while track reconstruction in the inner detector significantly enhances the particle identification (for example distinguishing between electrons and photons). The L2 trigger reduces the event rate to below 3.5 kHz, with an average event processing time of approximately 40 ms, while EF reduces the event rate to approximately 200 Hz, with an average event processing time of order four seconds. The event selection at both L1 and L2 primarily uses inclusive criteria, for example high-E_T objects above defined thresholds. Events selected by the EF are moved to permanent storage at the CERN computer

[6] At the beggining of collisions at $\sqrt{s}$ =900 GeV events were collected using the Minimum Bias Trigger Scintillators (MBTS). The MBTS are segmented scintillator paddles located close to the beam-pipe, which trigger on the energy deposited by charged particles traversing the scintillator, thus the event triggered by the MBTS doesn't need to have high-p_T object.

centre. The trigger used for triggering W' candidates in 2010 data will be described in Sections 5.3 and 7.1

4.7.2 Detector Control System and Data Quality

The Detector Control System permits the coherent and safe operation of the ATLAS detector hardware, and serves as a homogeneous interface to all sub-detectors and to the technical infrastructure of the experiment. It controls, continuously monitors and archives the operational parameters, signals any abnormal behaviour to the operator, and allows automatic or manual corrective actions to be taken through a human interface for the full control of ATLAS and its sub-detectors. The DCS also enables bi-directional communication with the data acquisition system in order to synchronise the state of the detector with data taking. It also handles the communication between the subdetectors and other systems which are controlled independently, such as the LHC accelerator, the CERN technical services, the ATLAS magnets, and the detector safety system. The DCS comprises a set of common software tools and packages, used by sub-detector controls and the Common Infrastructure Control. All status information and measured data can be transferred to the ATLAS wide conditions database, COOL. All DCS information from the detector is written to the ATLAS online database, and every 15 minutes a process is run to copy a sub-set of this data to the offline database. Conditions data, such as calibration, alignment or DCS, are nonevent experiment data describing the state of the detector at the time of data taking, and are characterised by the fact that they vary in time and may have different versions.

In order to be able to diagnose problems as soon as they occur during data processing, as to avoid processing delays and to verify the data integrity, tools for prompt monitoring and archiving of the quality of the processed data have been developed and have become an essential part of the data processing chain. This collection of software is part of the ATLAS Data Quality Monitoring Framework (DQMF)[24], which comprises of both online (before processing) and offline (after processing) data quality operations. The DQMF also provides a tool for monitoring the history, i.e. the evolution over several runs, of the DQ results. Furthermore, the most relevant results of the automated histogram checks, the status flags green, yellow, red, gray and black, are archived in the ATLAS condition database. Once the final flags are filled, physics performance groups provide thier own quality flags which verify the status of the reconstruction algorithms for particular object of interest (muons for example). In addition to the different requirements made by each performance group there are flags which are of global interest (like Central Trigger Processor hardware for example), which are combined into a single flag AT-

LAS Global DQ. All archived DQ status flags are then used to filter on good data runs and luminosity blocks (corresponding to approximately two minutes of data taking with a constant instantaneous luminosity), by appliying DQ flag selection criteria. The resulting lists are also known as good run lists (GRLs).

The status flags output by the DCS Status Calculator can be easily viewed using standard ATLAS tools, including a web-based database browser. An example of the database browser is shown in figure 4.12. This tool is widely used within the Data Quality group to browse database entries from all data quality inputs (online and offline automatic checks and shifter inputs), as well as the DCS results.

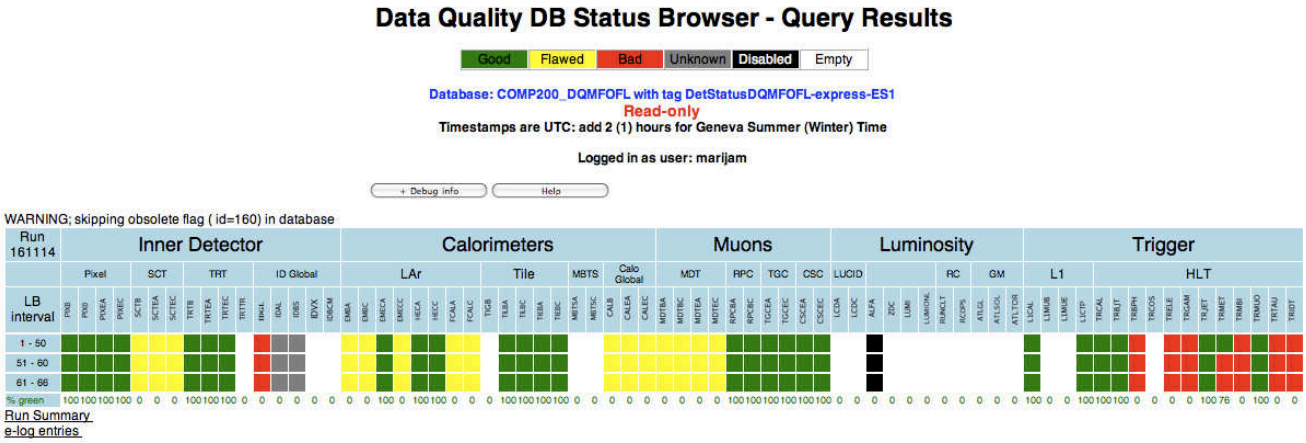

Figure 4.12: Data Quality data base status Browser.

4.8 ATLAS Computing

In present HEP experiments like ATLAS, computing physics tools are as important as any other part of the detector. This is due to the expected huge amount of data, performed calculations and large number of collaborators involved in the experiment. In this section a brief description of ATLAS computing and simulation infrastructure, as well as some basic concepts of grid computing are given. Information and references concerning the online and offline software used by the ATLAS collaboration can be found in [14] and also in [25]. Detail description the Worldwide LHC Coputing Grid can be found in [26].

ATLAS simulation infrastructure. In order to study the detector response for a wide range of physics processes and scenarios, a detailed simulation that carries events from the event generation through to output in a format which is identical to that of the true detector has

been implemented. The simulation program is integrated into the ATLAS software framework, Athena[27], and uses the GEANT4 simulation toolkit[28, 29].

The simulation software chain is generally divided into three steps, though they may be combined into a single job: generation of the event and immediate decays, simulation of the detector and physics interactions, and digitization of the energy deposited in the sensitive regions of the detector into voltages and currents for comparison to the readout of the ATLAS detector.

A generator produces events from prompt decays and also from initial and final state radiation, fragmentation and hadronization, underlying event and multiple interactions. Thus, a generator stores any stable particle (produced in an generated process) expected to propagate through a part of the detector. Because it only considers immediate decays, there is no need to consider detector geometry during the generation step, except in controlling what particles are considered stable. These generated events are then read into the simulation. For the simulation, each particle from the generator is propagated through the full ATLAS detector by GEANT4. The configuration of the detector, including misalignments and distortions, can be set at run time by the user. The energies deposited in the sensitive portions of the detector are recorded as hits, containing the total energy deposition, position, and time, and are written to a simulation output file, called a hit file. The digitization takes hit output from simulated events: hard scattering signal, minimum bias, beam halo, beam gas, and cavern background events[7]. Each type of event can be overlaid at a user-specified rate before the detector signal is generated. The overlay (pileup) is done during digitization to save the CPU time required by the simulation. At this stage, detector noise is added to the event. The first level trigger, implemented with hardware on the real detector, is also simulated in a pass mode. Here no events are discarded but each trigger hypothesis is evaluated. The digitization first constructs digits, inputs to the Read Out Drivers (RODs) in the detector electronics. The ROD functionality is then emulated, and the output is a Raw Data Object (RDO) file. The output from the ATLAS detector itself is in byte stream format, which can be fairly easily converted to and from RDO file format. The two are similar, and in some subdetectors they are almost interchangeable. The ATLAS HLT and reconstruction [30] run on these RDO files. The reconstruction is identical for the simulation and the data, with the exception that truth information can be treated and is available only in simulated data. Thus, both the simulated and real data from the detector can then be run through the same

[7] Beam halo is the background resulting from interactions between the beam and upstream accelerator elements. Beam gas includes the residual hydrogen, oxygen, and carbon gasses in the ATLAS beam pipe. The cavern background consists mainly of thermalized slow neutrons, that may propagate through the ATLAS cavern for a few seconds before they are thermalized, thus producing a neutronphoton gas. This gas produces a constant background of low-energy electrons and protons from spallation. The cavern background consists mainly of thermalized slow neutrons, longlived neutral kaons and low-energy photons escaping the calorimeter and the forward shielding elements. Muon detectors are most affected by high cavern-background rates.

ATLAS trigger and reconstruction packages. During data taking, the HLT is run on bytestream files, however all hypotheses and additional test hypotheses may be evaluated by translating the RDOs into bytestream format.

Types of data files that contain objects from the reconstruction suitable for physics analysis are Event Summary Data (ESD), Analysis Object Data(AOD), TAG, and Derived Physics Data(DPD) files. ESD is the resulting event data containing physics objects from the reconstruction which are stored in POOL ROOT format. Its content is detailed and technical enough to make possible a rerun of the reconstruction, so-called reprocessing, hence access to RDO data is unnecessary. AODs are derived from ESDs and provide an event representation suitable for analysis. The AOD physics objects provide sufficiently detailed information for most analyses while at the same time make the event size small enough to allow the files to be widely replicated in an affordable way. TAG is the event level metadata[8] which provides thumbnail information about the event, for example number of physics objects. The DPDs span from very general ones, often provided by physics working groups, which are typically called primary or secondary DPDs (D1PD, D2PD) to very specialized ones. These are produced from ESDs or AODs by keeping only relevant information (containers or part of containers), or events that pass some preselection requirements. The size of D3PDs can be significantly reduced, so the analysis is performed on local cluster or even laptop, and the files are capable of a ROOT[31] analysis independent of the large Athena software framework (which is needed for the analysis of ESDs/AODs).

Because of the complicated detector geometry and detailed physics description used by the ATLAS `GEANT4` simulation, it is impossible to achieve high simulated statistics fast, so several varieties of fast simulation programs have been developed to complement the `GEANT4` simulation. A fast simulation program, `ATLFAST`[32], (sometimes refered to as `ATLFAST-I`) has a factor of 1000 speed (in CPU) increase over full simulation described above. This type of simulation is used for physics parameter space scans and studies that require very large statistics but do not require the level of detail contained in the full simulation (for example study of systematic uncertainties in early data analyses). On the other hand, `ATLFAST` does not provide realistic detector description, so studies of detector-based quantities, such as calorimeter sampling energies and track hit positions, are not possible. Simulation of reconstruction efficiency or misidentification rates, which means the presence of genuine physics objects are overestimated while fake objects are not modeled (except for fake b-jets and taus). Improved version of fast simulation (`ATLFAST-II`) is developed at ATLAS[33]. The aim is to try to simulate events as fast as possible while still being able to run the standard ATLAS reconstruction.

[8]Metadata, or “data about data”, is the information about data that is necesary for the analysis.

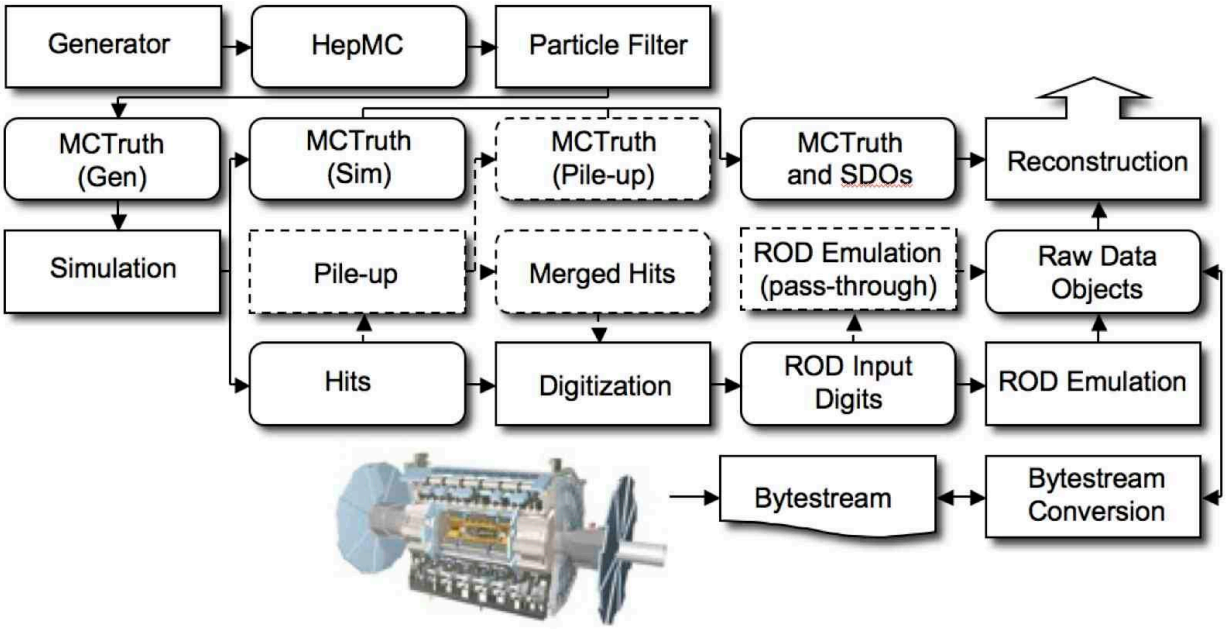

Figure 4.13: The flow of the ATLAS simulation software, from event generators (top left) through reconstruction (top right). Algorithms are placed in square-cornered boxes and persistent data objects are placed in rounded boxes. The optional pile-up portion of the chain, used only when events are overlaid, is dashed. During the digitization stage, Read Out Driver (ROD) electronics are simulated.

An overview of the ATLAS simulation data flow can be seen in Fig. 4.13. Algorithms and applications to be run are placed in square-cornered boxes, and persistent data objects are placed in round-cornered boxes. The optional steps required for pile-up or event overlay are shown with a dashed outline.

Grid Computing. Both data and MC require a considerable amount of processing power, disk storage, and need to be distributed to a global physicist community. CERN has embraced the Grid computing[9] as the model for the LHC computing infrastructure.

The mission of the Worldwide LHC Computing Grid project (WLCG)[26] is to build and maintain a data storage and analysis infrastructure for the entire high energy physics community that will use the LHC. WLCG consists of a set of services and applications (for Distributed Data Management, Distributed Analysis and Monitoring) running on the Grid infrastructures

[9]Grid computing is a form of distributed parallel computing characterized by combining resources from multiple administrative domains with a common security mechanism. This distinguishes it from conventional parallel computing models: a computing center with a homogeneous set of resources, employing a batch system and a storage system. The Grid allows the combination of computing resources like CPUs and storage elements irrespective of type and distance, including the possibility to unite computing centers into one large system. Ideally, the user should experience it as one homogeneous supercomputer in spite of its relative internal heterogeneity and loose coupling between its various sites. The eponymous Grid paradigm is to ultimately make access to computing resources as easy as to the electric power grid.

provided by the WLCG partners. These infrastructures at present are provided by the Enabling Grid for e-Science (EGEE) project in Europe, the Open Science Grid (OSG) project mostly in US, and the Nordic Data Grid Facility (NorduGrid), mostly in the Nordic European countries.

The WLCG environment is hierarchically structured in 3 Tiers.

- Tier-0: The original raw data emerging from the data acquisition systems of the experiments is recorded by the Tier-0 centre at CERN. The first-pass reconstruction takes place at the Tier-0, where a copy of the reconstructed data is stored. The Tier-0 distributes a second copy of the raw data to the Tier-1 centres associated with the experiment. Additional copies of the reconstructed data are also distributed to the Tier-1 centres.

- Tier-1: The role of the Tier-1 centres[10] varies depending on the experiment, but in general they have the responsibility for managing the permanent data storage (raw, simulated and processed data) and providing computational capacity for re-processing and for analysis processes that require access to large amounts of data.

- Tier-2: The role of Tier-2 centres is to provide computational capacity and appropriate storage services for Monte Carlo event simulation and for end-user analysis. The Tier-2 centres obtain data as required from Tier-1 centres, and the data generated at Tier-2 centres is sent to Tier-1 centres for permanent storage. About 160 Tier-2 centres are used by ATLAS.

Besides these 3 Tiers, there are other computing facilities in universities and laboratories that will take part in the processing and analysis of LHC data. These are called Tier-3 centres. Any group of scientists associated to a Tier-2 centre (with minimum requirements for computation power and data storage) can be a Tier-3. For the time being, these centres are outside the scope of the WLCG Project, although they must have access to the data and analysis facilities, as decided by the experiments.

Users access the resources and data through a valid Grid proxy which defines their identity and membership in the ATLAS Virtual Organization (VO)[11]. The membership information is registered in a Virtual Organization Management Service (VOMS) database. When creating a proxy, users contact a VOMS server using a client tool (`voms-proxy-init`) and are granted access according to their registered role (administrator, production manager or normal user).

[10] Currently there are 11 Tier-1 centers: ASGC (Taiwan), BNL and Fermilab (USA), RAL (UK), IN2P3 (France), INFN (Italy), KIT (Germany), NDGF (Nordic countries), NIKHEF/SARA (Netherlands), PIC (Spain), and TRIUMF (Canada).

[11] A Virtual Organization (VO) is a set of individuals who collaborate to achieve a common goal. The rules of sharing computing power, storage space, software and data are defined in terms of these VOs.

For distributed analysis users submit their analysis preparation DPD production or the actual analysis jobs to the Grid. A typical task on the Grid is separated into many jobs depending on the content and complexity of the task. A job can be completed by a single CPU within the maximum allowed time for a job on the Grid ($\mathcal{O}$(day)). The output, including log files, of every Grid job is registered with the ATLAS Distributed Data Management system (DDM)[34]. The DDM uses Don Quijote 2 (DQ2)[35] for dataset bookkeeping, and allows users to search for datasets on the Grid, analyze them in place, and, if necessary, retrieve them. Separate Grid software controls the distribution of jobs to the various Grid sites.

In order to provide simple access to the Grid, ATLAS users may choose between two tools. `pAthena` is a PanDA[36] pilot based command-line submission tool capable of sending jobs to all three ATLAS Grid infrastructures, while `Ganga`[37] is a more general computational task management tool. The global computing environment of the LHC experiments requires reliable, informative and user friendly monitoring systems. The CERN-based developers team maintain the Dashboard project for LHC experiments where ATLAS has its own service covering a variety of Grid activities. It monitors the processing and data management, both at the Tier-0 and on the world wide production system, user analysis and the online/offline databases. The PanDA production and distributed analysis system provides also a global monitoring system with a web interface[38].

4.9 Readiness of ATLAS detector for LHC collisions

Prior to the start of data-taking, understanding of the expected performance of individual subsystems relied on beam test results, as well as on detailed `GEANT4` simulations, including the modeling of inactive material both in the detector components and in the detector services and support structure (see [13], Volume I). While extensive beam testing provided a great deal of information about the performance of the individual detector subsystems, a detailed understanding of the full detector could only be achieved after the system was in place so the physics signals could be used for performance studies and for validation or tuning of the simulation. During 2008 and 2009 ATLAS detector including all sub-detectors, data aqusition and trigger were commissioned using high statistics data samples of cosmic-ray events. Analysis of these events also enabled exercising of the infrastructure such as the data-handling system, reconstruction software, and tools for hardware and data-quality monitoring. The results are published in series of papers [39, 40, 41, 42, 43]. Here just some results relevant for the analysis in this thesis are outlined.

Inner Detector readiness. The final installation of the ATLAS Inner Detector in August 2008 was followed by commissioning and calibration. During this period ID took data with high efficiency with both LHC single beams and cosmic rays, and more than 98% of the ID was operational before data-taking with colliding beams. During 2008 calibration of the detector with synchronisation of all sub-detectors, as well measurement of efficiency and noise occupancy for each subdetector in combined operation[12] was performed. Testing of the reconstruction software and the tracking triggers on real data was carried out as well.

The cosmic-ray data were used to perform an initial detector alignment. The resolution of track parameters was measured by comparing two segments of a cosmic-ray track. The alignment proceeded in stages from larger structures to the individual module level. At each stage more degrees of freedom were introduced, with the expected sizes of the corrections decreasing. The cosmic-ray alignment significantly improved the track reconstruction and the track-parameter resolutions. The achieved level of precision, about 20 μm, ensured that track reconstruction efficiency with early LHC data was not significantly affected by residual misalignments. Local alignment with cosmic rays was statistically limited by the small acceptance of individual detector modules, especially in the endcap region. Therefore it was not possible to perform alignment at module-to-module level in the endcaps, and reduced set of degrees of freedom was used in the barrel region. Thus not all possible misalignments could be recovered using only cosmic-ray data which partially explains why the nominal Monte Carlo resolution was not achieved. This is ilustrated in Fig4.14, and in this asymptotic limit the relative momentum resolution was measured to be $\sigma_p/p = (4.83 \pm 0.16) \times 10^{-4}$ GeV$^{-1} \times p_T$. In order to reach the design granularity, a high statistics sample of tracks from pp collisions is needed. When this has been collected, all 1744 and 4088 Pixel Detector and SCT modules will be aligned with the full set of degrees of freedom.

Calorimeters. The LAr and Tile hadronic calorimeter underwent extensive testing during its commissioning and cosmic muon data-taking periods. In the EM, detailed studies with of the signal shape predictions allowed to check there was no extra contribution to the dominant contributions to the intrinsic constant term of the energy resolution. This indicated that the reach of a global constant term of 0.7% was achievable. The nonuniformity of the barrel EM response to cosmic muons is consistent at the percent level with the simulated response.

The noise in the Tile had been proven to be within the expectations and requirements, with a non-Gaussian component which was taken into account in the reconstruction of clusters and physics objects. The electromagnetic energy scale was been transferred from 11% of modules

[12]Combined ATLAS cosmic-ray run means that data were taken by the full ATLAS detector with different magnetic field combinations, toroid and solenoid switched on and off independently.

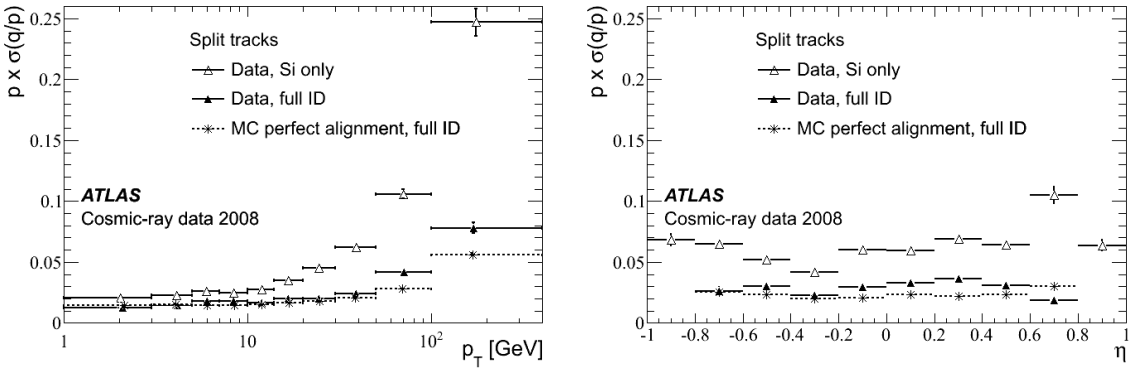

Figure 4.14: The relative momentum resolution $p \times (\sigma/p)$ as a function of p_T and η of the track. The resolution has the expected degradation at higher transverse momenta. The resolutions are shown for full ID tracks (solid triangles), silicon-only tracks (open triangles) and simulated full ID tracks (stars), [40].

calibrated at testbeam to the full Tile Calorimeter in the ATLAS cavern setting by means of the TileCal calibration systems. The precision of all calibration systems is remarkable and has proven to follow the systems design requirements. The separation between signal and noise was very good, with an S/N ratio of $\sim$29 for the sum of the three radial layers. The measurements with cosmic ray muons were compatible with a successful propagation of the EM scale factor from testbeam to the full ATLAS configuration.

As is the case of running with pp collisions, during cosmic-ray data-taking randomly triggered events are also recorded. The large sample of such events collected during the global cosmic-ray running allowed investigations of the detector performance for the measurement of missing transverse energy. No energy imbalance was expected in these events. However, global quantities such as missing transverse energy ($\not\!\!E_T$) and scalar sum of energy in the calorimeter ($\sum E_T$), result from the sum of energy deposits in calorimeter channels, each with its own electronic noise. A proper determination of these quantities relies on a good understanding of the cell-level noise in all calorimeter channels, and, in particular, a proper treatment of a few very noisy cells and cells having nonnominal high-voltage. More details of calculation of $\not\!\!E_T$ and $\sum E_T$, and two methods used to supress the electronic noise, are given in the next section. Fig 4.15 shows the results of both calculations applied to the random triggers recorded during a 2008 cosmic-ray run, illustrating the superior noise suppression of the method using the so called topological clustering. Tails in the distribution (beyond 8 GeV for topological-cluster-based, and 16 GeV for cell-based definition), contributing less than 0.1% of events, are due to coherent noise in a specific region of the LAr presampler which has since been repaired. The time stability of the $\not\!\!E_T$ calculation was also investigated and found to be very good. For the

method based on topological clusters, which provides the best resolution, the mean and width of the distributions of the x and y components of $\not\!\!E_T$ were stable to within about 100 MeV over the 45 days of data-taking.

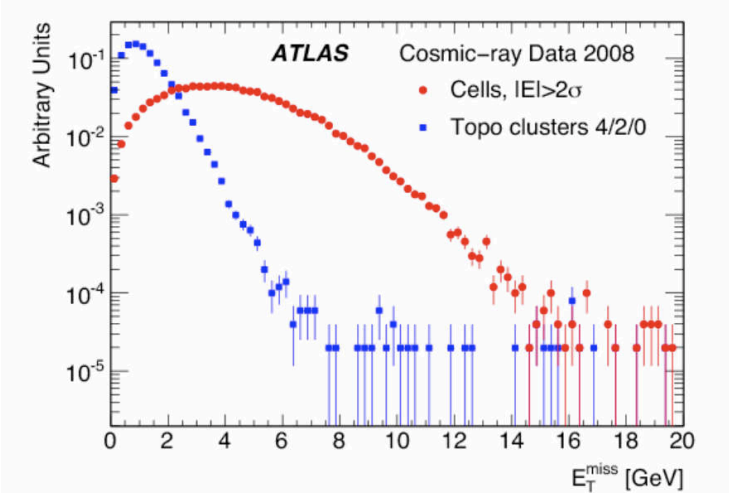

Figure 4.15: Distribution of $\not\!\!E_T$ from analysis of random triggers recorded during the 2008 global cosmic-ray running, for the two methods described in the text, [43]

Muon Spectrometer Commissioning and Performance with Cosmics. About 60 M events collected during the 2008-2009 cosmic ray runs have been analyzed to assess the performance of the Muon Spectrometer after its installation in the ATLAS experiment. Parts of the MS, the Small Wheels in front of the end-cap toroids, were installed during the runs and the commissioning of the many detectors was proceeding while debugging the data acquisition and the data control systems. The detector coverage during most of the run period was higher than 99%, with the exception of the RPC chambers which were still under commissioning, reaching 95% efficiency in Spring of 2009. Most of the cosmic rays reach the underground detectors via the two big shafts, hence they have incident angles close to the vertical axis and they are mainly triggered by the RPCs.

Several aspects of the MS performance have been studied: detector coverage, efficiency, resolution and relative timing of trigger and precision tracking chambers, track reconstruction, calibration, alignment and data quality. Finally, with data collected when the magnetic field was on, a first estimate of the spectrometer momentum resolution was obtained. The trigger chamber timing has been adjusted with enough precision to guarantee that the interaction bunch crossing can be identified with a minimal number of failures.

The design transverse momentum resolution of 10% for TeV tracks, requires a sagitta resolution of 50 μm. The intrinsic resolution of MDT chambers contributes a 40 μm uncertainty to

the track sagitta, hence other systematic uncertainties (alignment and calibration) should be kept at the level of 30 μm or smaller. The performance of the end-cap and barrel optical alignment systems have been measured using cosmic muon tracks with no magnetic field. The results demonstrate that the end-cap optical system is able to provide the required precision for chamber alignment. The result from the optical alignment system is shown in Fig.4.16. The small sectors have a significantly worse alignment than the large sectors. Conservatively, performance of the optical system, in terms of sagitta precision, is $\sim$200 μm for the large sectors, and $\sim$1 mm for the small sectors. The design of the alignment system in the barrel required additional constraints provided by straight tracks. The track alignment algorithm had been tested with MC simulations and with cosmic ray data. The simulation studies show that 10^5 tracks with a momentum greater than 20 GeV and pointing to the IP are needed to align the large sectors with a precision of 30 μm. Small sectors require five times more tracks than large sectors, due to the multiple scattering in the toroid coils. Using straight cosmic muon tracks a set of alignment constants had been produced. A total of 10^7 events were used corresponding to about 3×10^5 cosmic muon tracks in each of the most illuminated barrel sectors. The statistical uncertainty of the sagitta using this track alignment procedure was estimated to be 30 μm for large sectors.

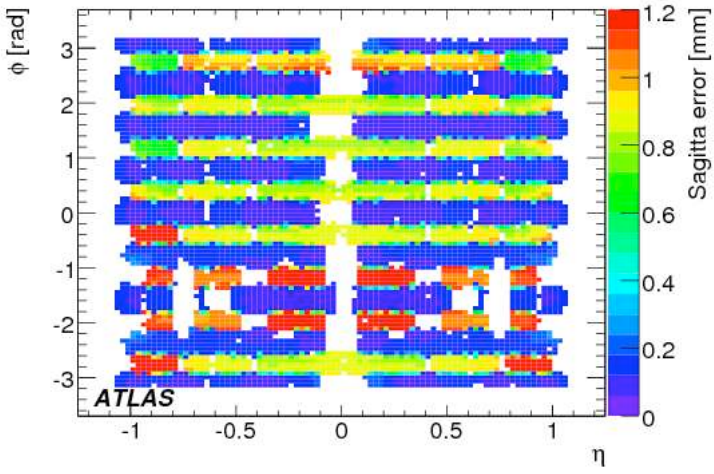

Figure 4.16: $\eta - \phi$ map of the contribution to the sagitta error due to alignment, as estimated with the method described in the text. As expected from the system design, the small sectors (even sector numbers) are aligned with significantly less precision than the large sectors (odd sector numbers), [42]

Algorithms for track reconstruction in the MS have been optimized to reconstruct muon tracks originating from the IP. To cope with the different topology of cosmic ray muons they had to be slightly modified. To mimic muons in collision events, the tracks were split at their perigee (point of closest approach to the beam axis), giving, usually, two reconstructed tracks:

one in the upper part of the MS and one in the lower part. Performance of the MS in terms of resolution reported in [42] was established with 19K top-bottom track pairs. The results are improved with higher statistics sample collected during 2009. Beside standalone, also combined (ID+MS, denoted bellow as CB) tracking performance was investigated, and the results are reported in [43].

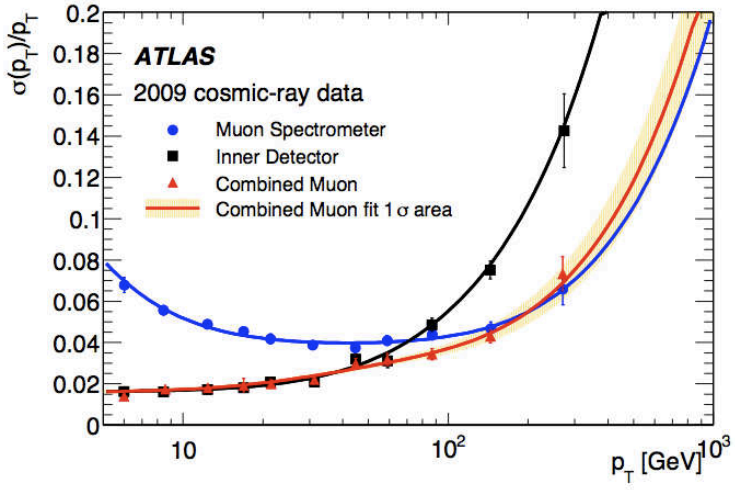

Figure 4.17: Transverse momentum resolution evaluated with the top-bottom method resolution on relative p_T as a function of p_T for ID and MS standalone tracks, and for CB tracks. The results are for barrel only, ($|\eta|$ <1.1), both Small and large sectors. The shaded region show the $\pm 1\sigma$ of the fit to the resolution curve for the CB tracks, [43].

Fig. 4.17 shows the relative p_T resolution for ID, MS and CB tracks as a function of p_T . For each pair of upper/lower tracks, the value of the transverse momentum was evaluated at the perigee. The difference between the values obtained from the upper and lower parts of the detector, divided by their average

$$\frac{\Delta p_T}{pT} = 2\frac{p_{Tup} - p_{Tdown}}{p_{Tup} + p_{Tdown}} \tag{4.3}$$

was measured and plotted in eleven bins of p_T . Since the cosmic muon momentum distribution is a steep function, the p_T value of each bin was taken as the mean value of the distribution in that bin. The highest bin was 200-400 GeV. The results of this procedure have been fitted to parametrizations appropriate to each particular track class: MS, ID, and CB. The resolution function for MS is fitted with the sum in quadrature of three terms, the uncertainty on the energy

loss corrections p_0, the multiple scattering term p_1, and the intrinsic resolution p_2:

$$\frac{\sigma p_T}{p_T} = \frac{p_0}{p_T} \oplus p_1 \oplus p_2 \times p_T \tag{4.4}$$

For ID, energy loss factor is dropped, and for CB a more complex function was used(see [43]). Table 4.3 compares the fitted sizes of the multiple scattering and intrinsic resolution terms for

Table 4.3: Fitted values of the multiple scattering and intrinsic momentum resolution terms (as described in the text) for ID, MS and CB tracks.

Fitted resolution	p_1	p_2
ID	$1.6 \pm 0.1\%$	$(53 \pm 2) \times 10^{-5} GeV^{-1}$
MS	$3.8 \pm 0.1\%$	$(20 \pm 3) \times 10^{-5} GeV^{-1}$
CB	$1.6 \pm 0.1\%$	$(23 \pm 3) \times 10^{-5} GeV^{-1}$

the ID, MS and CB tracks. For the CB tracks the multiple scattering term is determined mainly by the ID contribution while the intrinsic high-energy resolution comes mainly from the MS measurement. Extrapolation of the fit result yields an ID momentum resolution of about 1.6% at low momenta and of about 50% at 1 TeV. The MS standalone results gives the resolution extrapolated to 1 TeV is about 20%. As expected, the ID and MS systems dominate the resolution at low and high-p_T , respectively. The value of the energy loss term is $p_0 \sim 0.29$ GeV, but this term is not relevant for the performance of high-p_T muons that could come from W' decays.

As the rate of production of high-p_T muons in pp collision events is rather low, the cosmic-ray data will continue to be relevant to the MS commissioning, until a sufficient number of high-p_T muons from the collisions is accumulated.

Bibliography

[1] LHC Study Group, The Large Hadron Collider: conceptual design, CERN-AC-95-05-LHC (1995).

[2] L. Evans (ed.), P. Bryant (ed.), LHC Machine, JINST **1** S08003 (2008).

[3] ATLAS Collaboration, JINST **1** S08003 (2008).

[4] CMS Collaboration, JINST **4** S08004 (2008).

[5] ALICE Collaboration, JINST **2** S08002 (2008).

[6] LHCb Collaboration, JINST, **5** S08005 (2008).

[7] TOTEM Collaboration, JINST, **7** S08007 (2008).

[8] LHCf Collaboration, JINST, **6** S08006 (2008).

[9] `https://edms.cern.ch/file/973073/1/Report_on_080919_incident_at_LHC_2_.pdf`

[10] `https://twiki.cern.ch/twiki/bin/view/AtlasPublic/RunStatsPublicResults2010`

[11] `http://atlas-runquery.cern.ch/`

[12] ATLAS collaboration, Detector and physics performance technical design report, Vol I CERN/LHCC/99-014, Vol II, CERN/LHCC/99-015 (1999).

[13] Expected Performance of the ATLAS Experiment - Detector, Trigger and Physics, The ATLAS Collaboration, CERN-OPEN-2008-020, arXiv:0901.0512v4 [hep-ex] (2009).

[14] ATLAS Collaboration, ATLAS computing technical design report. ATLAS-TDR-017, CERN-LHCC-2005-022 (2005).

[15] N. Corso-Radu, H. Hadavand, M. Hauschild, R. Kehoe, and S. Kolos. Data Quality Monitoring Framework for the ATLAS Experiment at the LHC. IEEE Transactions on Nuclear Science, 55:417420 (2008).

[16] ATLAS Collaboration, Inner Detector Technical Design Report vol I, CERN/LHCC/97-16 (1997).
Inner Detector Technical Design Report vol II, CERN/LHCC/97-17 (1997).

[17] ATLAS Collaboration, Liquid Argon Technical Design Report, CERN/LHCC/96-41 (1996).

[18] ATLAS Collaboration, Tile Calorimeter Technical Design Report, CERN-LHCC-96-12 (1996).

[19] ATLAS muon spectrometer: Technical Design Report. CERN, Geneva (1997).

[20] ATLAS Collaboration, Level 1 Trigger Technical Design Report, CERN/LHCC/98-14 (1998).

[21] ATLAS Collaboration, ATLAS DAQ, EF, LVL2 and DCS Technical Progress Report, CERN/LHCC/98-16 (1998).

[22] P. Jenni et al., High Level Trigger, Data Acquisition and Controls, CERN/LHCC/2003-22 (2003).

[23] A. Barriuso Poy et al., The detector control system of the ATLAS experiment, JINST 3 P05006 (2008).

[24] N. Corso-Radu, H. Hadavand, M. Hauschild, R. Kehoe, and S. Kolos. Data Quality Monitoring Framework for the ATLAS Experiment at the LHC. IEEE Transactions on Nuclear Science, 55:417420 (2008).

[25] ATLAS Collaboration, G. Aad et al., The ATLAS Simulation Infrastructure, Eur.Phys.J. C70, 823-874, arXiv:1005.4568 [physics.ins-det] (2010)

[26] I. Bird et al. (eds.), LHC computing Grid. Technical design report, CERN-LHCC-2005-024. `http://lcg.web.cern.ch/lcg/`

[27] `http://atlas-computing.web.cern.ch/atlas-computing/packages/athenaCore/athenaCore.php`

[28] S. Agostinelli et al., Geant4a simulation toolkit. Nucl. Instrum. Methods Phys. Res. A 506, 250303 (2003).

[29] J. Allison et al., Geant4 developments and applications. IEEE Trans. Nucl. Sci. 53, 270278 (2006).

[30] V. Boisvert et al., Final report of the ATLAS reconstruction task force. ATL-SOFT-2003-010 (2003).

[31] R. Brun, F. Rademakers, ROOT - an object oriented data analysis framework, Nuclear Instruments and Methods in Physics Research Section A 389, no. 1-2 81 86 (1997). New Computing Techniques in Physics Research.

[32] E. Richter-Was, D. Froidevaux, L. Poggioli, ATLFAST 2.0 a fast simulation package for ATLAS. CERN-ATL-PHYS-98-131 (1998).

[33] K. Edmonds et al., TheFast ATLAS track simulation (FATRAS) ATL-SOFT-PUB-2008-01 (2008).

[34] ATLAS DDM
`https://twiki.cern.ch/twiki/bin/view/Atlas/DistributedDataManagement`

[35] M. Lassnig et. al., Managing ATLAS data on a petabyte-scale with DQ2, in Journal of Physics: Conference Series, (Bristol, England), Institute of Physics Publishing, September.

[36] T. Maeno, PanDA: distributed production and distributed analysis system for ATLAS, Journal of Physics: Conference Series 119, no. 6 062036 (4pp) (2008) `https://twiki.cern.ch/twiki/bin/view/Atlas/PanDA`

[37] J. T. Moscicki, et al. Ganga: A tool for computational-task management and easy access to grid resources., Computer Physics Communications 180, no. 11 23032316, arXiv:0902.2685v2 (2009)

[38] PanDA production monitor
`http://panda.cern.ch:25880/server/pandamon/query?dash=prod`

[39] ATLAS Collaboration, Readiness of the ATLAS Liquid Argon Calorimeter for LHC Collisions, EPJC 70, 723, arXiv:0912.2642v4 [physics.ins-det], (2010).

[40] ATLAS Collaboration, The ATLAS Inner Detector commissioning and calibration, EPJC 70, 787, arXiv:1004.5293v2 [physics.ins-det], (2010).

[41] ATLAS Collaboration, Readiness of the ATLAS tile calorimeter for LHC collisions, EPJC 70, 1193, arXiv:1007.5423v2 [physics.ins-det], (2010).

[42] ATLAS Collaboration, Commissioning of the ATLAS Muon Spectrometer with Cosmic Rays, EPJC 70, 875, arXiv:1006.4384v2 [physics.ins-det], (2010).

[43] ATLAS Collaboration, Studies of the performance of the ATLAS detector using cosmic-ray muons, EPJC 71, 1593, arXiv:1011.6665v1 [physics.ins-det], (2011).

Chapter 5

Event Selection

5.1 Object reconstruction

5.1.1 Muon reconstruction at ATLAS

Different strategies, corresponding to different ways of combining data from more ATLAS subdetectors, have been developed so far to measure and identify muon candidates. Three main strategies used to reconstruct different types of muons are:

- Standalone muon reconstruction. Standalone muons are reconstructed using only the Muon Spectrometer exploiting its toroid magnetic field and full coverage up to $|\eta| < 2.7$. The tracks are extrapolated to the beam region at the perigee of the track. During the extrapolation to the beam line the material effects, namely energy loss and multiple scattering, are taken into account. However, performance of Standalone muons must be carefully studied with collision data before they are included in physics analysis.

- Combined muon reconstruction. Combined muons are formed by matching Inner Detector tracks with Muon Spectrometer tracks. The track matching is based on the χ^2 defined as:
  $\chi^2_{match} = (\mathbf{p}_{MS} - \mathbf{p}_{ID})^T (V_{ID} + V_{MS})^{-1} (\mathbf{p}_{MS} - \mathbf{p}_{ID})$,
  where $\mathbf{p}^T = (d_0, z_0, \phi, \theta, q/p)$ is the vector of 5 track parameters and V is the corresponding covariance matrix. Track parameters (expressed at the perigee) are: transverse distance of closest approach (d_0), the position along the beam axis (z_0), azimuthal and polar angles (ϕ and θ), and signed inverse momentum of the track (q/p). The subscript MS refers to the standalone muon, while ID refers to the Inner Detector track. The combination of the MS and ID measurements provides efficient muon reconstruction (with

matching efficiency above 95% for muons with p_T $\sim$50 GeV) and best momentum resolution. Further it suppresses the rate of fake muons[1].

- Tagged muons are Inner Detector tracks that are identified as muons by using either hits and segments in the MS, or the energy depositions in the calorimeters. Tagging algorithms were developed to recover the efficiency gaps left by low momentum particles that cannot reach the outer stations of the MS, or regions where MS is not fully instrumented yet (for example at $|\eta|$ = 1.3 where the installation of some chambers in the innermost station has been staged).

A set of algorithms used to identify and reconstruct each of the muon types are present in the ATLAS offline software framework. The algorithms are usually classified into two families, `STACO`[1] and `MUID`[2]. The different algorithms in these two families are listed in Table 5.1.

Table 5.1: A summary of the muon reconstruction families `STACO` and `MUID`.

Muon type	`STACO`	`MUID`
Standalone	`Muonboy`	`Moore`
Combined	`Staco Combined`	`Muid Combined`
Tagged	`MuTag`	`MuGirl, MuTagIMO`

It should be mentioned that two additional algorithms based on the pattern of the energy depositions in the calorimeter are developed for the muon identification: `CaloMuonTag` and `CaloMuonLikelihoodTool` [3]. These algorithms aim mainly to the improvement of the muon identification efficiency around η = 0. However, there is a caveat of possible increase in the backgrounds coming from "fake" muons.

There are several differences among algorithms of `STACO` and `MUID` families, but two are outlined here: measurement of the track parameters of the combined track, and estimation of energy loss in the track extrapolation from MS to the beam line. To obtain the track parameters of the combined track `Staco Combined` does a statistical combination of the ID and MS track parameters to calculate the combined track parameters:

$$\mathbf{p} = (V_{ID}^{-1} + V_{MS}^{-1})^{-1}(V_{ID}^{-1}\mathbf{p}_{ID} + V_{MS}^{-1}\mathbf{p}_{MS}) \tag{5.1}$$

On the other hand, in `Muid Combined` ID tracks are extrapolated to the first measurement on the MS track. A position match and a momentum balance check decides whether the ID track

[1] Fake muon here is defined as a track not corresponding to any true muon at the interaction vertex.

matches with the MS track. To obtain the combined track parameters, `Muid` performs a refit of the Inner Detector and Muon Spectrometer measurements. For energy loss, `Muonboy` is implementing a parametrisation of the muon energy loss, while `Moore` combines information from the calorimeter and parametrisations to correct for the Landau tails of the energy loss distribution.

In Fig. 5.1 the p_T resolution of the standalone spectrometer measurement obtained with `STACO` and `MUID` is presented as a function of the muon p_T using W'events ($m_{W'}$= 1 TeV). According to the simulation, both algorithms have comparable performance. It should be noted however, that the resolution in data was worse with respect to the one in Monte Carlo. This will be discussed in Section 5.2.4. In Fig. 5.2 `STACO` and `MUID` efficiency as a function of p_T and η respectively are presented. The resulst are also comparable for the two algorithms. The degradation of efficiencies as a function of p_T is contributed to the due to increasing radiative energy loss in the MS. As a consequence of the increasing radiative energy loss, tracking algorithm fails to reconstruct the track due to multiple hits around the true muon.

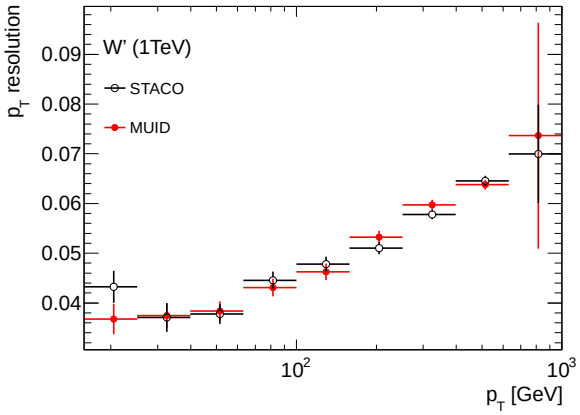

Figure 5.1: Muon p_T resolution of the spectrometer only measurement as a function of the reconstructed p_T for `STACO` and `MUID` combined muons in W' MC sample, $m_{W'}$= 1 TeV. Resolution is defined as $(1/p_{T,r} - 1/p_{T,t})/(1/p_{T,t})$, where $p_{T,r}$ is transverse momentum of the reconstructed muon matched with true muon with transverse momentum $p_{T,t}$.

Results presented in this thesis are obtained using `STACO`. Only combined tracks are used, and the direction and position (at closest point to the primary vertex) of the muon are taken from the combined measurement. As discussed before (cf. Section 4.9) prior to pp collisions Inner Detector was commissioned with cosmic rays, and its alignment was not known at the sufficient level. To avoid biases from systematic misalignments of the ID, the value of the muon transverse momentum in the following analysis is taken from standalone measurement. This approach is not completely independent from the momentum measurement in the ID, since track matching

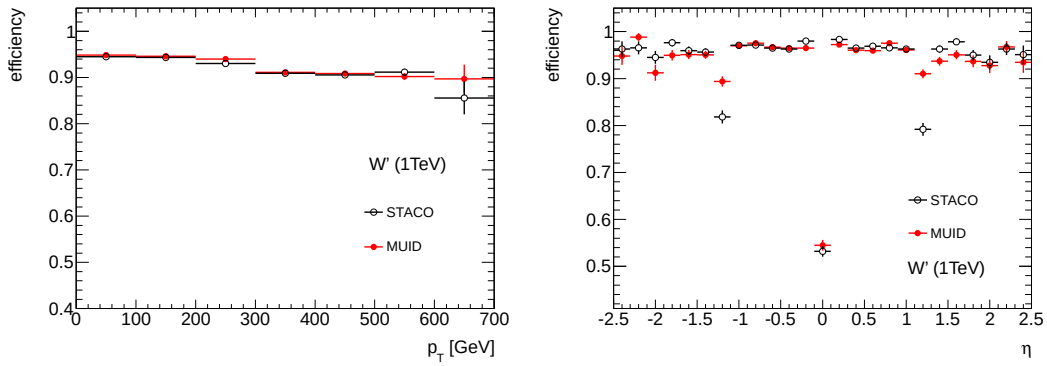

Figure 5.2: Muon reconstruction efficiency as a function of the reconstructed p_T and η for STACO and MUID combined muons in W'MC sample, with $m_{W'}$= 1 TeV. Efficiency is defined as a fraction of true muons matched with reconstructed muons in ΔR <0.1. Overal efficiencies are (91.9±0.2)% and (92.1±0.2)% for STACO and MUID respectively.

requires tracks to be independently reconstructed in the ID and MS and then statistically combined, weighted with their error matrices. Though difference in measured momenta in the MS and ID could be quite high, this matching is fairly loose, and possible efficiency loss caused by the tracks failing combination is assumed to be marginal. On the other hand, as explained above, the track matching requirement aids in the identification and rejection of cosmic rays, secondary muons produced in the decay of hadrons, and hadron jets that punch through the calorimeter.

This initial W'search with 2010 data is restricted to muons detected in the barrel of the MS ($|\eta|$ <1.05) where the momentum resolution (with sufficient high p_T) has been measured with cosmic rays. Discrimination against backgrounds is improved by imposing tight requirements on the hit multiplicities of both ID and MS. The requirement on the latter also ensures a precise and reliable measurement of the muon momentum. These requirements are discussed in detail in Section 5.3.

5.1.2 Measurement of $\not{E}_T$ at ATLAS

Measurement of the transverse missing energy ($\not{E}_T$) in ATLAS is performed from energy deposits in the calorimeter and reconstructed muon tracks [4]. Apart from the hard scattering process of interest, many other sources, such as the underlying event, multiple interactions, pile-up and coherent electronics noise, lead to energy deposits and/or muon tracks. In addition, the loss of energy in dead regions and readout channels contribute to the $\not{E}_T$ measurement.

The calorimeter plays a crucial role in the $\not{E}_T$ measurement: the electronics noise alone

in the ≈200k readout channels of the ATLAS calorimeter contributes about 13 GeV to the width of the $\not\!\!E_T$ distribution, hence the noise suppression is of crucial importance. Two noise suppression methods have been studied so far: standard noise suppression and noise suppression using topological clusters. Both require knowledge of the width of the noise distribution, σ_{noise}, which can be either purely electronics noise or a combination of electronics and pile-up noise.

Standard noise suppression is based on only using calorimeter cells with energies larger than a threshold, generally corresponding to a certain number of σ_{noise}. The threshold is optimized for $\not\!\!E_T$ resolution, the scale of $\not\!\!E_T$, the total transverse energy in the calorimeters, $\sum E_T$, and for the highest p_T jet to be close to the case without noise simulation. For the noise suppression, a symmetric threshold ($|E_{cell}| > 2 \times \sigma_{noise}$) is generally used.

The second method uses cells in 3-dimensional topological calorimeter clusters called TopoClusters. A TopoCluster is reconstructed starting from a seed cell with an absolute energy value $|E_{cell}| > 4 \times \sigma_{noise}$ to which neighbors with $|E_{cell}| > 2 \times \sigma_{noise}$ are added. Finally the cells at the boundary are required to have $|E_{cell}| > 0 \times \sigma_{noise}$. The cells that constitute the TopoCluster are called TopoCells. This set of thresholds, referred to as 4/2/0, is optimized to suppress electronics noise as well as pile-up from minimum bias events, while keeping the single pion efficiency as high as possible.

$\not\!\!E_T$ calculated from TopoCells with the electromagnetic calibration applied to all cells, gives a large shift in the $\not\!\!E_T$ scale of about 30% with respect to true $\not\!\!E_T$. Thus a dedicated calibration scheme is needed to reduce the systematic shift of the $\not\!\!E_T$ scale and optimize its resolution. This goal is achieved in several steps according to the cell classification. The classification depends on whether the energy deposits in the calorimeter are electromagnetic or hadronic in nature and whether they are associated with high p_T particles. To classify energy deposits, schemes to calibrate hadronic showers such as H1-like calibration or Local-Hadronic calibration [5] utilize the energy density in a cell. Electromagnetic showers tend to have higher energy densities as compared to hadronic showers. The Local-Hadronic calibration scheme uses further information related to shape and depth of the calorimetric shower to classify a TopoCluster. The next step in the cell-based $\not\!\!E_T$ reconstruction is to globally calibrate all calorimeter cells using the H1-like or Local-Hadronic calibration schemes. This procedure is robust already at initial data taking because it does not rely on other reconstructed objects. In a subsequent step, the cells can be calibrated according to the reconstructed object they are assigned to. Calorimeter cells are associated with a parent reconstructed and identified high-p_T objects: electrons, photons, muons, hadronically decaying τ-leptons, b-jets and light jets.

In W' analysis described in this chapter, the calorimeter part of $\not\!\!E_T$ is obtained from the

topological clusters with local hadronic calibration (MET_LocHadTopo):

$$\not{E}_{T_x}^{calo} = -\sum E cos(\phi)/cosh(\eta), \tag{5.2}$$

$$\not{E}_{T_y}^{calo} = -\sum E sin(\phi)/cosh(\eta). \tag{5.3}$$

This term already includes correction for the energy loss in cryostat[4]. The value of the muon momentum excluding the energy muon deposited in the calorimeter is added to the calorimeter estimate of the $\not{E}_T$:

$$\not{E}_{T_x} = \not{E}_{T_x}^{calo} - p_x^{\mu} + E_{loss}^{\mu} cos(\phi)/cosh(\eta), \tag{5.4}$$

$$\not{E}_{T_y} = \not{E}_{T_y}^{calo} - p_y^{\mu} + E_{loss}^{\mu} sin(\phi)/cosh(\eta). \tag{5.5}$$

The last term, E_{loss}^{μ}, is the energy loss calculated by the muon reconstruction algorithm accounting for the amount material crossed by the muon, and is included to avoid double counting of the energy deposited by the muon in the calorimeter. In $W' \to e\nu$ search, only 5.2 and 5.3 are used.

5.1.3 Performance using first collision data

Performance of the ATLAS detector was tested with data taken in pp collisions at 900 GeV and 2.36 TeV. These data sets do not contain very many high-p_T objects, and therefore do not correspond to the environment for which ATLAS is designed. However, this was an important step towards succesfull operation and data taking at 7 TeV. The details of the performed analysis can be found in [4].

The data sample at 900 GeV contains nearly 400 000 events recorded with high-quality calorimeter and tracking information. About 36 000 events of data were taken at 2.36 TeV, but they were used only for calorimeter studies. Events included in this analysis were required to pass Good Run List, which means stable beams request, and SCT, RPCs, TGCs and MDTs were operational (”green“ DQ flags). CSC chambers were not taking data during this period. One of the selection criteria was that the solenoid and toroid fields were at the nominal values. This lead to a somewhat smaller data set (264 000 events) since the toroid system was not always fully operational. Analyzed runs were those with run numbers 142174, 142189, 142191, 142193, 142195, and 142383.

In order to suppress cosmics and other non collision backgrounds, the event selection was based on the timing difference of signals detected on both sides A and C, of the ATLAS detector. Coincident signals were required, within a time window of 5 ns or 10 ns from either

the electromagnetic (end-cap or forward) calorimeters or from the two MBTS wheels, respectively. In addition the events were triggered with Minimum Bias Trigger Scintillator trigger (L1_MBTS_1_1) mentioned in the previous Chapter. In case no timing coincidence is found, a two hit MBTS trigger with at least one hit per side is required.

For the selection of muon candidates, events were required to have at least 3 tracks in the ID, each with at least 1 Pixel and 5 SCT hits to supress cosmic events. At least 1 ID track was required to have momentum p>4 GeV in order to insure there is a muon candidate in the event with sufficient energy to reach MS. All muons were required to have at least 1 trigger hit in any muon trigger chamber. Further, algorithm specific cuts for muons from `STACO` and `MUID` famailies were applied. These criteria were the following:

- `Staco Combined`: χ^2_{match} <50;
- `MuTag`: ID track - segment matching $< 3\sigma$;
- `Muid Combined` and standalone: at least 2 hits in RPCϕ layer;
- `MuGirl`: at least 6 SCT hits, and at least 2 segments in MS associated with the muon.

No specific requirements were imposed for `STACO` standalone muons. For the final results, only muons satisfying the following kinematic requirements were considered: p_T >2.5 GeV, $|\eta| < 2.5$, and p>4 GeV. Results obtained with muons passing above criteria were com-

Table 5.2: Number of muon candidates selected with each algorithm, with results from `MUID` family in the brackets. Numbers from MC are obtained using the normalization explained in the text. Total number of events after event selection cuts is given in the first three rows.

Selection	Data No p_T ,η and p cuts	MC	Data With p_T ,η and p cuts	MC
Collision candidates	252920			
Number of ID tracks>2	231139			
p ID track >4 GeV	163628			
Number of muon candidates	268	∼203	101	∼79
Trigger hit >0	228	∼198	90	∼78
Number of muons after algorithm cut	190(166)	∼194(∼177)	64(52)	∼75(∼67)
Combined	69 (71)	∼60 (∼65)	24 (34)	∼37 (∼45)
Standalone	85 (23)	∼97 (∼50)	12 (6)	∼6 (∼8)
Tagged	36 (72)	∼37 (∼61)	28 (12)	∼32 (∼14)

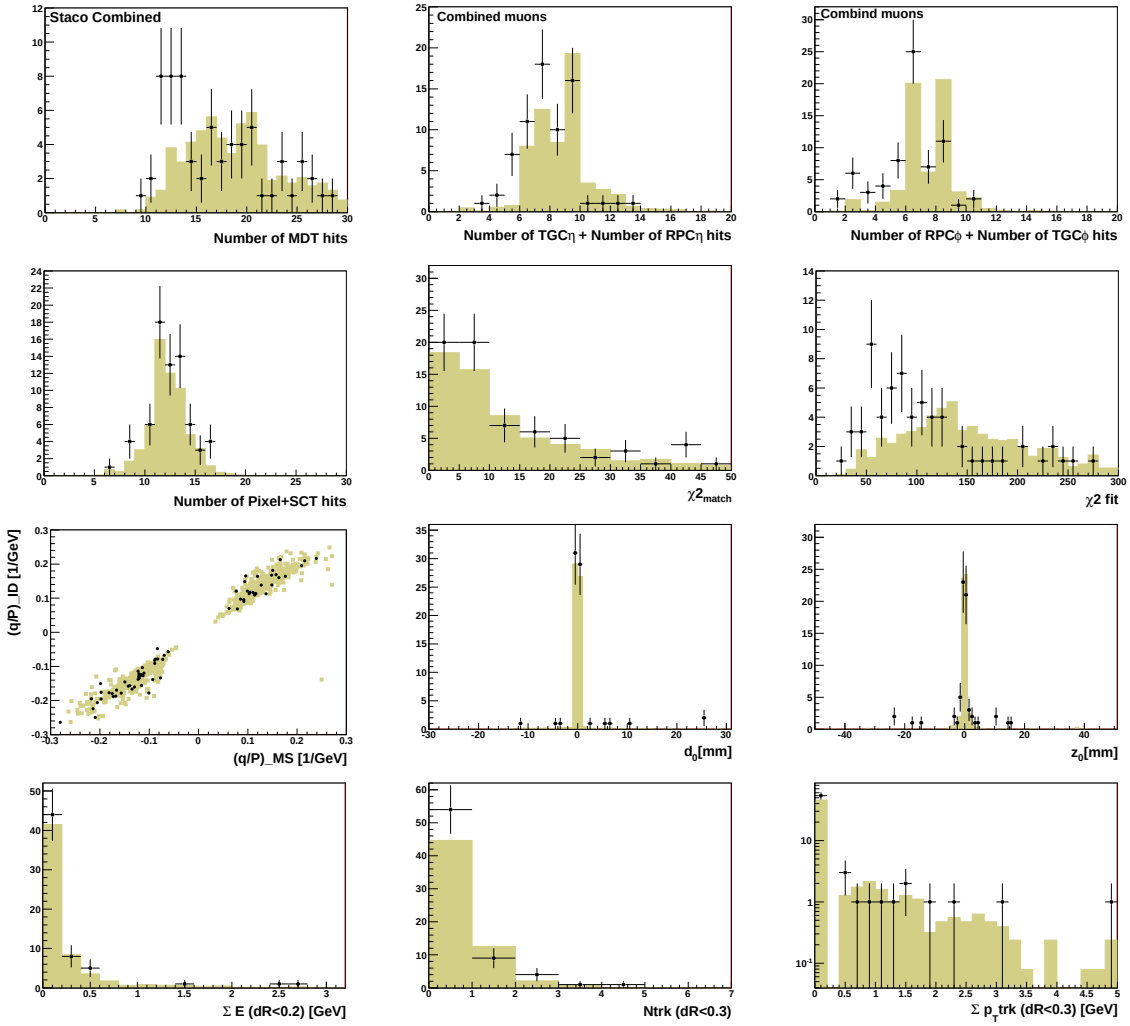

Figure 5.3: Some basic distributions for the `Staco Combined` candidates, data is represented with dots and MC with shaded histograms. Normalization of MC histograms is explained in the text. Kinematic cuts for final selections are not applied in order to have higher statistics.

pared with Monte Carlo expectations. Monte Carlo minimum bias samples were produced with the `PYTHIA`, 6.4.21[5] event generator. Various samples were generated for single-diffractive, double-diffractive and non-diffractive processes in pp collisions. The different contributions in the generated samples were mixed according to the cross-sections calculated by the generator. All the events were passed through the full simulation of ATLAS detector, with nominal alignment for the MS geometry. The data and MC samples used in this analysis have been reprocessed after the first reconstruction, with reprocessing implemented a number of software improvements mainly in tracking and muon reconstruction.

The results from Data and MC are presented in Table5.2. Results from MC were normalized to the number of events in data after the requirement there is at least 1 ID track with p>4 GeV.

Some basic distributions for the `Staco Combined` candidates are presented in Fig.5.3, with similar results obtained for `Muid Combined`. Comparison in number of hits in the muon precisions and trigger chambers, as well as number of hits in silicon detectors (Pixel and SCT), is good between data and MC. This is also true for χ^2_{match} distribution, while for χ^2_{fit} there is some difference. Momenta of MS and ID tracks are correlated, with no sign missmatch. The comparison between data and MC for impact parameters, calculated with respect to the reconstructed vertex, is good, though there are some additional tails possibly due to cosmic background and fakes which can be associated to pions or kaons. Isolation variables are also shown: energy deposited by the muon in the calorimeter in cone ΔR <0.2 around the position of the muon track, and number of tracks and scalar sum p_T tracks in ΔR <0.3 in the ID. Tracks that are allowed in the sum are required to have a minimum p_T of 1.0 GeV and given the soft spectrum of tracks in the 900 GeV collisions, only a few muon candidates have such ID tracks close to the muon candidate. MC/data agreement is good for tested isolation variables.

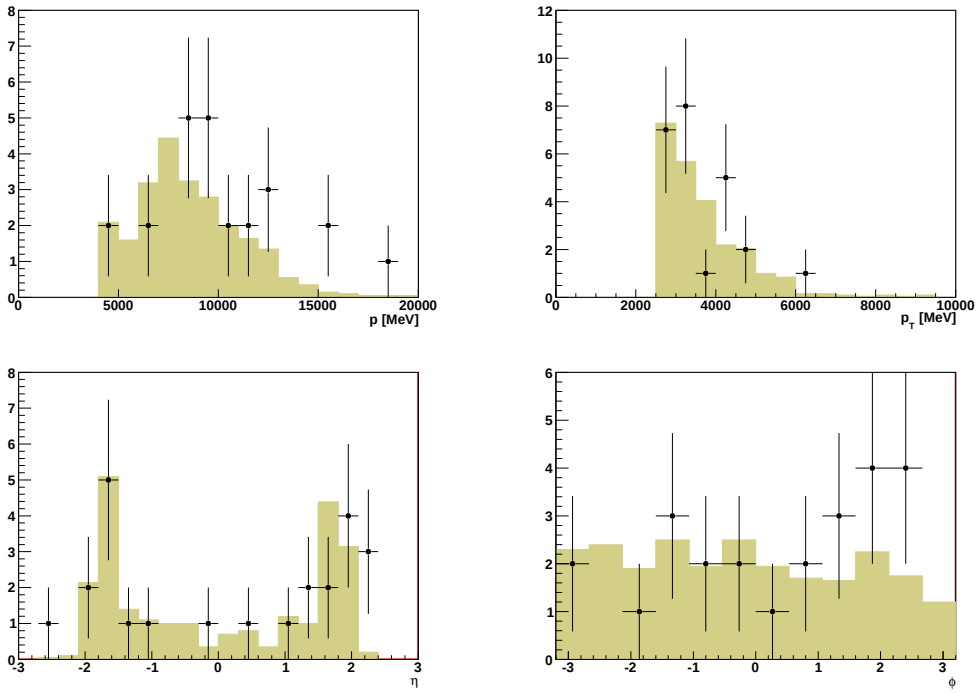

Figure 5.4: The distribution of p,p_T ,η and ϕ of reconstructed combined muons in the 900 GeV data. Kinematic cuts p_T >2.5 GeV, $|\eta| < 2.5$, and p>4 GeV, are applied for selection of muon candidates.

Raw distributions of p,p_T ,η and ϕ for the combined tracks after kinematic requirements are shown in Fig5.4. The muons studied were of relatively low p_T . The observed spectrum was soft and strongly peaked in the forward direction, where the momentum of the muons more

often exceeds the 3.2 GeV needed to penetrate through the forward calorimeter.

In conclusion, the Muon Spectrometer was not extensively tested with this data set, but good agreement is found between data and simulation indicating a reasonable understanding of the initial performance of the MS.

5.2 Data and Monte Carlo Samples

5.2.1 Collision data

The results in this thesis are based on the full 2010 datasample of $\sqrt{s}$ =7 TeV pp collisions collected from April to November. These datasets are divided according to the beam conditions and trigger configuration in periods labeled 'A' to 'I' [8], and go from run 152844 to run 167844. The analysed data is processed with `Athena` release 15, i.e. come from the "May Reprocessing"[9].

To ensure the relevant parts of the detector were operational, data quality flags set by the relevant combined performance groups are used to exclude problematic luminosity blocks. In addition, a few runs were excluded for problems not covered by the data quality flags. Good data quality can be summarized first as having all tracking (pixel, SCT and TRT) and calorimeter (EM, HEC, FCAL and TILE) subdetectors performing well. As only muons in the barrel region are used, the muon subdetectors in the barrel region: RPC and MDT chambers, and muon trigger must be also performing adequately. The toroids and the solenoid must be operating at their nominal current for precise muon momentum measurements. The LHC beams must be stable and operate at 3.5 TeV each and the luminosity calculations must be reliable. The list of requirements used in the Good Run List query are as follows[2]:

- Run range: 152844-167844
- Beam status: `ptag data10_7TeV and lhc stablebeams`
- Data requirements: partition ATLAS and db DATA
- Detector related quality requirements: `atlgl, atltor, atlsol, l1ctp, GLOBAL_ALL_ID_GL_AL, GLOBAL_ALL_MAG, MDTBA, MDTBC, RPCBA, RPCBC, CP_MET_METCALO, L1MUB, TRMUO, and lumi.`
- Database tag: `DetStatus-v03-pass1-analysis-2010`

The integrated luminosity satisfying GRL criteria summed over all datasets is $\mathscr{L}_{\text{int}}$ = 36.35

[2]For the definition of the flags, see [10].

pb^{-1} for an unprescaled trigger. Trigger is described in detail in section 5.3. Integrated luminosity was measured with the standard luminosity measurement at that time (`OflLumi-7TeV_002`).

5.2.2 Signal and Background Monte Carlo Samples

ATLAS Monte Carlo samples are used to calculate acceptances and to model the properties of the signal and Standard Model background processes. Events are generated using `PYTHIA`[5], `HERWIG`[11], and `MC@NLO`[6] generators. W^* samples are generated with `COMPHEP`[13] program followed by `PYTHIA`, as explained bellow. All generators are interfaced to `PHOTOS`[9] to describe the effect of final state QED radiation. The MRST LO*[6] parton distribution functions are used for the `PYTHIA` and `HERWIG` samples. All samples, signal and background, are generated and fully simulated in the ATLAS `MC09` framework [7], consistent with the "May reprocessing". Generated events are passed through the `GEANT`-based simulation of ATLAS detector, as described in the section 4.8, within `Athena` release 15.6.3.10, and then digitized and reconstructed with release 15.6.9.8 (which corresponds to the reconstruction tags `r1302` or `r1306`). Dedicated samples, reconstructed within `Athena` release 15.6.10.4 (`r1388`), are used to model effect of pileup. In these samples minimum bias events are overlaid over the original hard-scattering event. The `GEANT` simulation is the same as for non-pileup production and the pileup interactions are added as part of the digitization.

Signal samples $W' \to \ell\nu$ ($\ell = e, \mu, \tau$) and $W^* \to \ell\nu$ (ℓ or e, or μ) are described in Sections 3.2 and 3.4 respectively. $W^* \to \ell\nu$ samples are generated with kinematic cuts $p_T(l) > 25$ GeV, $|\eta(lep) < |2.5$ and $p_T(\nu) > 25$ GeV. Some information of the samples is listed in Tables 5.3 and 5.4. Statistics of these samples is sufficient for the analysis of the data collected during 2010.

Background samples that are used or considered for the analysis are presented in the table 5.5.

The W/Z samples are generated with `PYTHIA` covering all leptonic decay modes. Sample used for $W \to \mu\nu$ covers the full W mass range, and for $Z \to \mu\mu$ mass above 60 GeV. A sample of $W \to \tau\nu$ with τ decaying leptonically is also used. To ensure adequate statistics at high transverse mass, separate samples are generated in mass bins and the events from these are used instead of the ones in inclusive W/Z samples. Also, pileup samples with about 7 times less reconstructed events, are available for the inclusive $W \to \mu\nu$ and for $Z \to \mu\mu$ processes. There are no dedicated pileup samples for the binned datasets, nor for the signal samples. Diboson samples (WW, WZ and ZZ) are generated with `HERWIG` [11] with a filter requiring at least one lepton. The $t\bar{t}$ background is generated with `MC@NLO`[6] in conjuction with programs `HERWIG`

Table 5.3: Monte Carlo W' and samples. ATLAS MC run number is followed by the cross section time branching fraction for $W' \to e\nu$ process. Higher order corrections are explained in section 3.3. The last columns give the number of generated events (including the μ and τ channels) and the corresponding integrated luminosity $\mathscr{L}_{\text{int}} = N_{\text{evt}}/(\sigma B)$ (with respect to the NNLO cross sections).

Mass	Run	σB [pb]			
[GeV]	number	LO	NNLO	N_{evt} [k]	$\mathscr{L}_{\text{int}}$ [pb^{-1}]
500	100000	15.55	17.25	60	1160.
750	115373	2.931	3.200	60	6251.
1000	105610	0.7792	0.8366	60	24000.
1250	105277	0.2555	0.2606	40	51456.
1500	105626	0.09257	0.08870	30	113507.
1750	105278	0.03622	0.03246	30	308008.

Table 5.4: Monte Carlo W^* samples. ATLAS MC run number is followed by the cross section time branching fraction for $W^* \to e\nu$ process. The column for the cross section is given without cuts, and with kinematic cuts $p_T(l) > 25$ GeV, $|\eta(lep)|$ <2.5 and $p_T(\nu) > 25$ GeV. The last columns give the number of generated events and the corresponding integrated luminosity $\mathscr{L}_{\text{int}} = N_{\text{evt}}/(\sigma B)$.

Mass	Run number		σB [pb]		N_{evt}	$\mathscr{L}_{\text{int}}$
[GeV]	$e\nu$	$\mu\nu$	no cuts	with cuts	[k]	[pb^{-1}]
500	115525	115523	12.590	10.798	20	1850
750	105150	115524	2.339	2,095	20	9550
1000	105262	105266	0.6098	0.5587	20	35800
1250	105559	105388	0.1884	0.1751	20	114500
1500	105263	105267	0.0636	0.0595	20	336000
1750	105566	105389	0.0226	0.0212	20	942000

and JIMMY[18]. MC@NLO is used to generate matrix elements, while HERWIG is used to simulate parton showers and underlying event with multiple parton interactions described with JIMMY. CTEQ6.6 [19] parton distribution functions are used for $t\bar{t}$ simulation. The top mass is set to 172.5 GeV. A filter is applied at the generator level to retain only events where a lepton (e, μ or τ) is produced. The sample has negative weights for 11.3% of the events and the luminosity in Table 5.5 accounts for this.

The QCD background (sometimes denoted as dijet background) is simulated using PYTHIA hard-QCD processes, i.e. quark-quark, quark-gluon and gluon-gluon scatters. These samples are denoted by $jj(p_1, p_2) \to \mu X$, where the arguments indicate the allowed range of the trans-

Table 5.5: Monte Carlo background samples. Sources for the cross-sections are discussed in the text. Filtering efficiency is included in the cross section.

MC Sample	Run number	σB [pb] Leading Order	Higher Order	N_{evt} [k]	$\mathscr{L}_{\text{int}}$ [pb^{-1}]
$W \to \mu\nu$	106044	8939	10460	7000	670
$W \to \mu\nu$ (pileup sample)	106044	8939	10460	1000	95
$W \to \tau\nu$ ($\lvert\eta_\tau\rvert < 2.8$))	106022	7804	9134	1000	109
$W(200,500) \to \ell\nu$	106604	8.90	10.42	60	5760
$W(500,1500) \to \ell\nu$	105274	0.242	0.283	60	212000
$W(1500,2500) \to \ell\nu$	105275	0.00079	0.00092	60	6540000
$Z \to \mu\mu$	106047	856	989	5300	5360
$Z \to \mu\mu$ (pileup sample)	106047	856	989	1000	1011
$Z \to \tau\tau$	106052	856	989	2000	2022
$Z(250,400) \to \mu\mu$	105479	0.416	0.480	20	42
$Z(400,600) \to \mu\mu$	105480	0.0672	0.0777	20	257
$Z(600,800) \to \mu\mu$	105481	0.0112	0.0129	20	1550
$Z(800,1000) \to \mu\mu$	105482	0.00274	0.0032	20	6250
$Z(1000,1250) \to \mu\mu$	105483	0.000918	0.00106	20	18867
$Z(1250,1500) \to \mu\mu$	105484	0.000249	0.00029	20	68695
$t\bar{t} \to \ell X$	105200	80.2	89.4	1000	8650
WW	105985	11.49	17.82	250	14000
WZ	105987	3.481	6.07	250	41200
ZZ	105986	0.976	1.387	250	180000
$jj(8,17) \to \mu X$	109276	844000		2500	2.96
$jj(17,35) \to \mu X$	109277	821000		2500	3.05
$jj(35,70) \to \mu X$	109278	222000		500	2.25
$jj(70,140) \to \mu X$	109279	28600		500	17.5
$jj(140,280) \to \mu X$	109280	1960		500	255
$jj(280,560) \to \mu X$	109281	71.0		500	7040
$jj(560,1120) \to \mu X$	209435	1.15		10	8740
$c\bar{c} \to \mu X$	106059	28400		1500	52.8
$b\bar{b} \to \mu X$	108405	73900		4500	60.9

verse momentum of the hard scatter: $p_1 < \hat{p}_T < p_2$. Dijet events are filtered with requiring a muon with p_T >8 GeV. The filter was used after verifying that most of the muon rate is due to heavy flavor decays and so is included in these samples.

In the table 5.5 primary cross sections are computed with generator used to simulate events of a given sample. However, higher order cross sections are used to normalize predicted event counts for the various samples. The exception is for QCD background where listed cross-section are computed using PYTHIA. Higher order cross sections are obtained as follows.

The W/Z cross-sections, including binned samples, are initially normalized to the NNLO cross-sections as provided by the FEWZ program [2, 3] ($\sigma_{W\to\ell\nu}$ =10.46 pb, and $\sigma_{Z\to\ell\ell}(\sqrt{\hat{s}}>$ 60GeV) =989 pb). The details of NNLO computation are given elsewhere[22], but it should be noted that the input parameters are quite similar to the ones listed in the section 1.4 used for W' cross section calculation at NNLO. The total uncertainty of these NNLO cross sections is conservatively estimated to be about 5%, dominated by uncertainty from the choice of PDF. Although W/Z are normalized using NNLO cross section calculations, the raw background level in the high-m_{T} bins used in this analysis is significantly overestimated due to the different mass dependence of the cross section at leading and higher orders. Thus, additional correction factors are needed to account for both QCD and electroweak corrections. These corrections and theoretical uncertainties specific for the high-m_{T} regions are described in detail in the next chapter.

NLO cross sections for diboson samples are estimated using MC@NLO program as described in [22]. Since these processes represent small fraction of the total background, no attempt was made to estimate their NNLO cross sections. NNLO $t\bar{t}$ cross-section is 161 pb, taken from [23]. The uncertainty is 6% added in quadrature to the PDF uncertainty.

5.2.3 Pileup

Increased instantaneous luminosity at the LHC leads to additional pp interactions occurring in the same and previous bunch crossings. This is referred to as in-time and out-of-time pileup, respectively. The in-time pileup result in additional reconstructed primary vertexes. The increased average number of vertices can influence the efficiency of event selection through the effect of additional tracks in lepton isolation and also affects $\not\!\!E_T$ distribution. To model the pileup effects on the selection efficiency, simulated MC samples with the so called bunch train pileup-setup are used. As explained before, simulated minimum bias interactions are overlaid on top of the hard-scattering event. Individual bunches are separated by 150 ns and contained in trains of eight bunches length. A second bunch train follows with a time separation equal to 225

ns, followed by a longer pause before the next bunch train. The average amount of simulated additional minimum bias interactions per bunch crossing is chosen to be Poisson distributed with the expectation value $\mu = 2.2$. No out-of-time contributions is considered.

In order to match the data, Monte Carlo events in the pileup samples, are weighted according to the number of primary vertices in data. To calculate the number of vertices, W' preselection requirements described in the next sections are applied in order to reduce the influence of non-collision backgrounds such as cosmic rays. This is particularly important for the number of events with zero vertices. When counting the vertices, only those with at least 3 tracks and $|z_{\text{vtx}}| < 15$ cm are taken into account. In the calculation of the event weights, the zero vertex bin is excluded, and the weight is set to one.

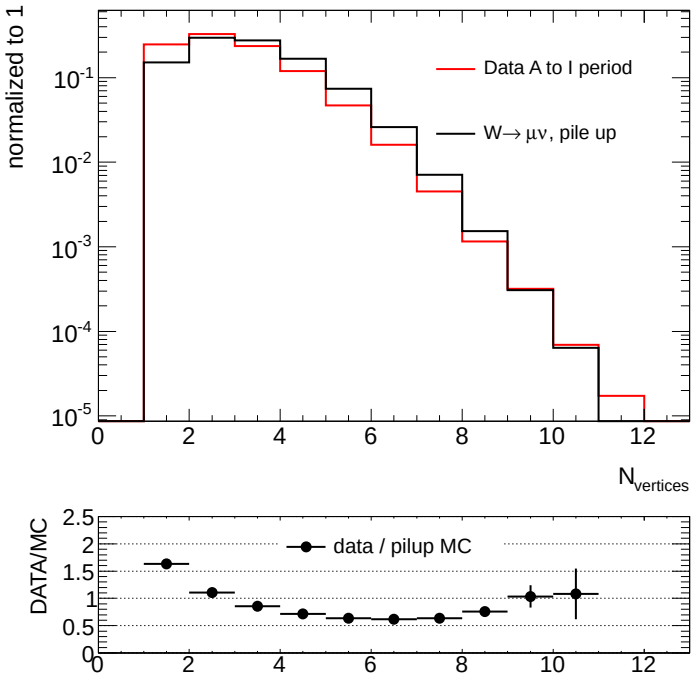

Figure 5.5: Number of vertices in data and the Monte Carlo $W \to \mu\nu$ sample with pileup.

Table 5.6 gives the fraction of events with each vertex multiplicity for data and unweighted $W \to \mu\nu$ Monte Carlo as well as the derived Monte Carlo weights. The normalized number of vertices in data and pileup MC, as well the ratio of the two, is shown in Fig 5.5.

It should be mentioned however, that the difference of the selection efficiency obtained with reweighted and unreweighted $W \to \mu\nu$ pileup sample is 0.2%. This suggests that the systematic uncertainty from the Monte Carlo pileup reweighting procedure is negligible. As the instantaneous luminosity of the LHC increases in the future, correctly accounting for pileup will become clearly a more important effect.

Table 5.6: Events weights for the $W \to \mu\nu$ pileup sample. The first column is the number of reconstructed vertices and the next two are the fraction of events with that multiplicity in data and in the $W \to \mu\nu$ pileup sample. The last column is the weight assigned to events in the pileup samples.

N_{vtx}	f_{data}	f_{MC}	Event weight
0	0	0	1
1	0.246599	0.151054	1.63252
2	0.328767	0.2972	1.10622
3	0.235981	0.275637	0.856129
4	0.119392	0.16721	0.714022
5	0.0470739	0.07381	0.637771
6	0.0160969	0.0260949	0.616862
7	0.00452744	0.00709184	0.638402
8	0.00115926	0.00152561	0.759866
9	0.000317209	0.000306398	1.03529
10	6.92093e-05	6.38329e-05	1.08423
11	1.73023e-05	6.38329e-06	2.71057

5.2.4 Muon momentum scaling and smearing

Measurements of the muon momentum resolution of both the ID and MS, performed with cosmic rays and collision data, indicate that the resolution is significantly worse than in the MC09 simulation [24]. This has the effect of the broadening W' peak in the m_{T} distribution, and increasing the level of background. To account for this, muon momentum is smeared for kinematic distributions and estimation of the signal event selection efficiency and expected number of background events from MC samples.

In principle, the smearing is a function of direction (θ and φ) and momentum. However, the p_T resolution varies slowly as a function of θ, hence the smearing is constant as a function of p_T rather than momentum magnitude p . The trajectory deviations measured by the tracking detectors are proportional to the inverse of the signed momentum, and so the intrinsic resolution, arising from uncertainties in position measurements (including alignment), is constant for q/p . Thus, q/p has been chosen as the smearing variable.

The smearing is applied randomly for each muon in the event. The final value of q/p is calculated from the initial value, $(q/p)_{\text{ini}}$ as:

$$q/p = [(q/p)_{\text{ini}} + S_1 g_1 (q/p)_{\text{ini}} + S_2 g_2 \sin\theta]/S_p + S_o. \tag{5.6}$$

Here g_1 and g_2 are random variables selected from a Gaussian distribution with RMS = 1, S_p is the momentum scale, S_o is the q/p bias (curvature offset), and S_1 and S_2 are the smearing pa-

rameters. S_1 is the scale coefficient and S_2 is the intrinsic resolution coefficient (cf. Section 4.9). The $\sin\theta$ dependence of the intrinsic resolution term ensures the q/p_T smearing is constant as function of θ. The values of the smearing parameters used in this thesis are:

$$S_1 = 0.023 \pm 0.03, \quad \text{and}$$
$$S_2 = (0.18 \pm 0.04)\ \text{TeV}^{-1}.$$

The values for the scale and bias are $S_p = 1 \pm 0.001$ (corresponding to no scaling) and $S_o = (0.0 \pm 0.071)\ \text{TeV}^{-1}$ (no bias). The uncertainties on these values lead to systematic uncertainties on the signal selection efficiencies and background counts. These are discussed in the next Chapter.

5.2.5 $\not\!\!E_T$ scaling and smearing

Studies with data and MC from "May Reprocessing" show that the resolution of the calorimeter part of $\not\!\!E_T$ (equations 5.2,5.3)[3] is underestimated, mostly because of pileup. The agreement between data and Monte Carlo shapes of $\not\!\!E_T$ and m_{T} is significantly improved when pileup is included. This is illustrated in Fig 5.6. The pileup has little impact on the shape of muon p_T distribution. However, the statistics available in the W/Z pileup samples are about seven times smaller than those in the non-pileup samples. Due to the resolution of the standalone measurement of the muon p_T , events from these samples propagate to the high-m_{T} region of interest for $W' \to \mu\nu$ search. Pileup samples are not available for the other relevant backgrounds including the W and Z high-mass binned samples, nor for the W' and W^* signal samples. Consequently, the signal efficiency and background level estimates are done with non-pileup samples with $\not\!\!E_T{}^{calo}$ smeared in order to make MC distributions match the data. Beside the smearing, additional scaling of the $\not\!\!E_T{}^{calo}$ is considered since the studies indicated that the reconstructed calorimeter part of $\not\!\!E_T$ is biased and that the bias is different in data and MC.

The Monte Carlo non-pileup samples are corrected as follows. The hadronic recoil as measured in the calorimeter is separated into a component parallel ($E_\parallel$) and perpendicular ($E_\perp$) to the direction of the leading muon in the event. The smearing and scaling function has two parameters in both directions. Each component of $E_\parallel$, and $E_\perp$ is obtained from the initial value $E_{\parallel(\perp),ini}$ according to the equation:

$$E_{\parallel(\perp)} = S_m(E_{\parallel(\perp),ini}) + S_r g, \tag{5.7}$$

[3]Calorimeter part of $\not\!\!E_T$ without lepton contribution (which is trivial for $W \to \mu\nu$like processes) is sometimes referred to as hadronic recoil.

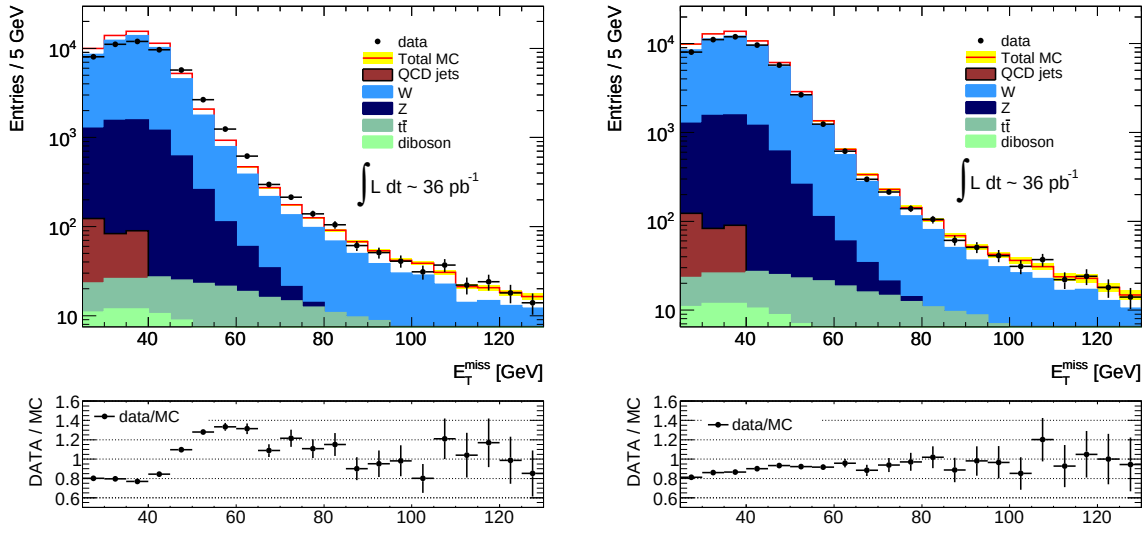

Figure 5.6: $\not\!\!E_T$ distribution in data and Monte Carlo plotted after all selection cuts described later in this Chapter. On the left plot standard Monte Carlo W/Z samples are used, while the right plot is obtained using pileup samples. The pileup samples are reweighted according to the procedure explained in section 5.2.3. The ratio of data to the total MC is shown below each distribution.

where g is a random variable selected from a Gaussian distribution with RMS = 1, and the scale and smearing parameters S_m and S_r adjusted to reproduce observations with data.

The values of S_m and S_r are obtained from studies of $Z \to \mu\mu$ and $W \to \mu\nu$ with 36 pb^{-1} of data. These studies were performed by other groups, and full explanation can be found in the W' search supporting note [25]. Briefly, smearing parameter is obtained from $Z \to \mu\mu$ studies by fitting component of hadronic recoil perpendicular to the direction of the dimuon in data and Monte Carlo, while scaling parameter is obtained using the $Z \to \mu\mu$ component of $\not\!\!E_T$ to the direction of the dimuon and comparing data to MC. In $W \to \mu\nu$ study, the smearing parameters are obtained by minimizing the χ^2 of the data and MC comparison of $E_\parallel$ and $E_\perp$ in the core ($\pm$50 GeV) and the scaling parameter in the tail region (>50 GeV) of the $\not\!\!E_T$ distributions.

Combining these two approaches, S_m and S_r are obtained. The values of the parameters are are:

$$S_r = (4.0 \pm 0.4)\ \text{GeV} \quad \text{and}$$
$$S_m = (1.0 \pm 0.2),$$

and are same for $E_\parallel$ and $E_\perp$.

In order to validate this procedure, and values obtained from $Z \to \mu\mu$ and $W \to \mu\nu$ studies, the comparison of some distributions in the standard $W \to \mu\nu$ sample with and without smear-

ing to those obtained from the pileup samples is performed. Figure 5.7 shows the longitudinal and perpendicular component of the hadronic part of $\not\!\!E_T$ for these three cases after preselection plus the isolation requirement (section 5.4). Figure 5.8 shows the distributions of $\not\!\!E_T$ after isolation requirement, and m_{T} after all selection cuts. The agreement between the pileup and smeared samples is very good.

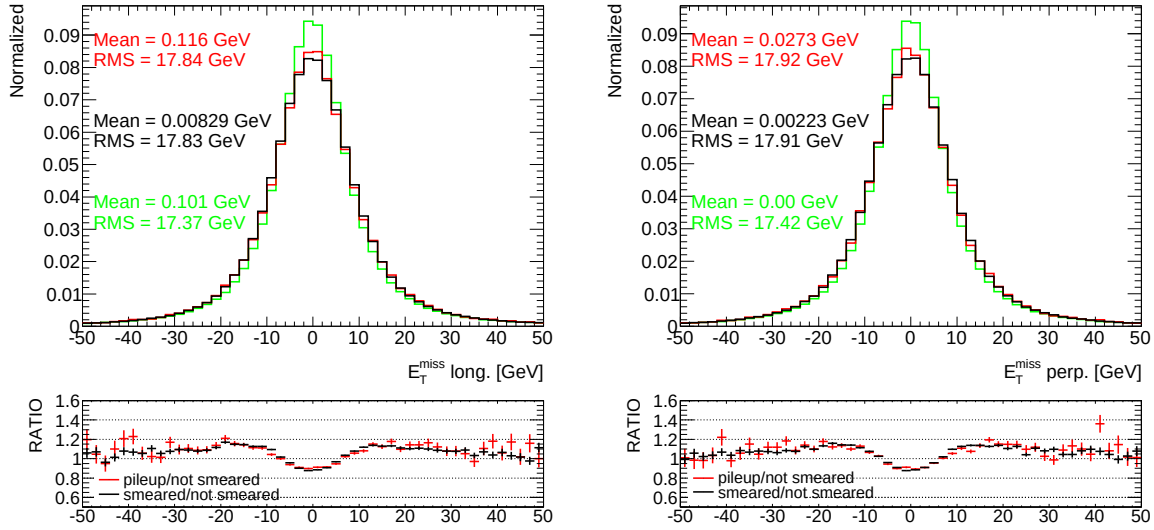

Figure 5.7: Longitudinal and perpendicular component of non-leptonic $\not\!\!E_T$ calculated with respect to the direction of the muon, in standard $W \to \mu\nu$ sample without (green) and with (red) smearing applied, and in pileup sample (black line). All selection cuts including $\not\!\!E_T > 25$ GeV are applied. The distributions are normalized to have the same area.

5.3 Preselection

Events are selected with the goal of maintaining a high efficiency for signal events while keeping the statistical and systematic uncertainties in the backgrounds at levels that do not significantly degrade discovery potential/exclusion limit.

This section describes the event selection used to preselect collision events. The event selection comprise trigger requirement, vertex cut, and $\not\!\!E_T$ cleaning cuts. The following sections (5.4 and 5.5) describe the cuts specific to the selection of muon candidates, and further selection cuts introduced mainly to suppress backgrounds arising from QCD jet production and $t\bar{t}$.

For the selection of candidate events for W' search, low-p_T single muon unprescaled trigger is used. This choice is made in order to pick up enough events that would allow reconstruction of the W boson Jacobian peak in the m_{T} distribution. Due to the rapidly changing conditions

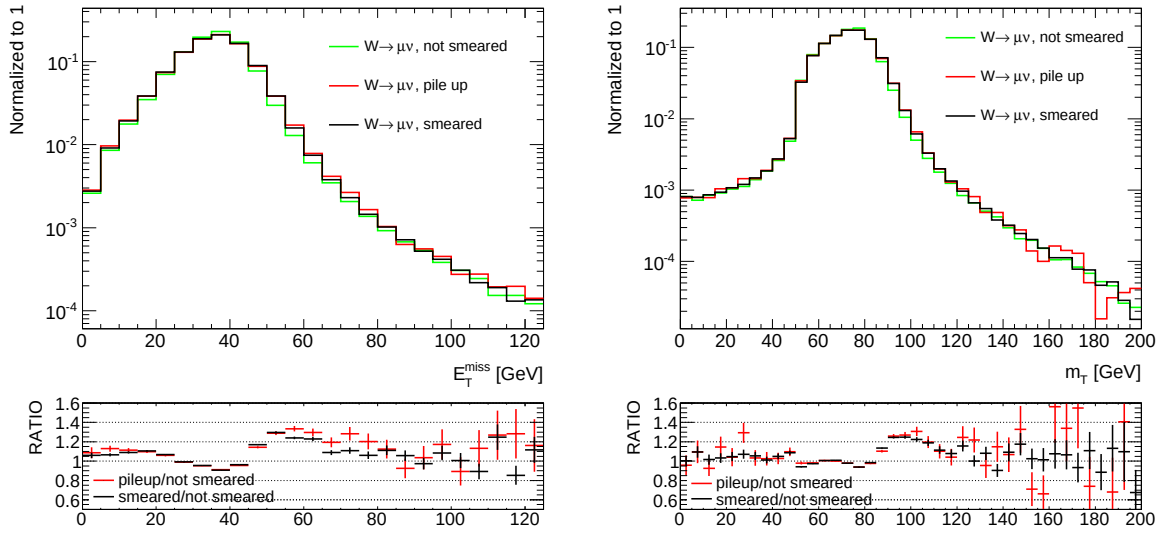

Figure 5.8: Distribution of $\not{E}_T$ after isolation requirement, and m_T after all selection cuts.

(instantaneous luminosity) of LHC operation during 2010 data taking, trigger menu has been evolving rapidly. Hence, the trigger used to select data has been changing. Data for the muon channel are selected with the muon triggers listed in table 5.7. Integrated luminosities corresponding to the periods in the table are calculated using LumiCalc tool[26]. For the first trigger period (periods A1 to E3), due to commissioning purpose, the muon trigger signals are stretched to have an acceptance of 3 BC for a L1 trigger signal ($3BC < T_{L1\_MU} - T_{MBTS} < 1BC$), but the fraction of events with positive BC difference were not collected by the data acquisition system. This is fixed with the trigger match requirement in the muon selection described later. In order to avoid bias coming from ID momentum measurement, triggers with momentum measured only in the MS are used in "OR" with `EF_mu20` for periods from G5 to I2.

Table 5.7: Triggers used to select data for $W' \to \mu\nu$ search, and corresponding integrated luminosities.

Run periods	Run numbers	Trigger	$\mathscr{L}_{\text{int}}$ [pb^{-1}]
A1-E3	152844-160879	`L1_MU0`	0.76
E4-G5	160899-165956	`EF_mu20_MSonly`	5.76
G5-I2	166094-167844	`EF_mu20`, `EF_mu30_MSonly`, `EF_mu40_MSonly`	29.83
A1-I2	152844-167844		36.35

Because of the arrangement of detector services in the Muon Spectrometer, the feet of the detector, as well as support for the toroid coils, the real coverage of the barrel trigger is 80% of

the region -1.05< η <1.05, as illustrated in Figure 5.9. The figure shows trigger efficiency in η -ϕ space in W' ($m_{W'} = 1$TeV) MC sample with respect to the true muon with p_T >10 GeV . To account for this loss of efficiency in the analysis, the MC is processed requiring `L1_MU10` to be passed. Since different triggers are used in data, correction factors are needed to account for discrepancy in the trigger efficiency between data and MC.

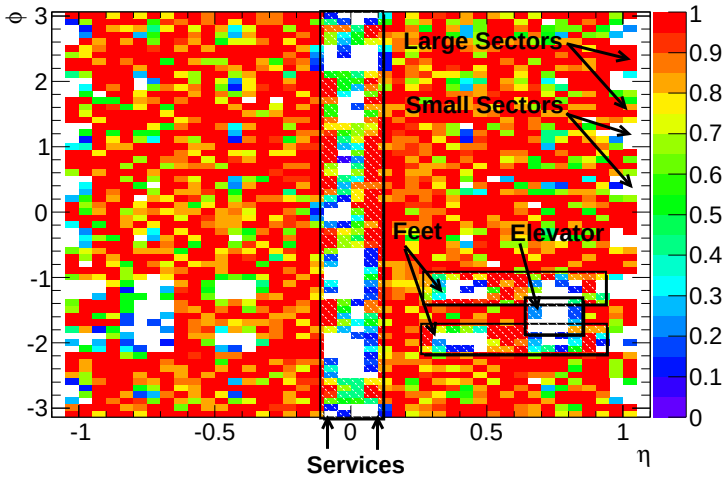

Figure 5.9: Map of the RPC trigger coverage in η - ϕ space W' ($m_{W'} = 1$TeV) MC with respect to the true muon with p_T >10 GeV.

To ensure the muon that triggered an event was produced in a pp collision, the event is required to have a primary vertex with at least three tracks (with p_T >150 MeV) and z-position within 15 cm of the center of the IP. Events often have multiple vertices due to collisions from other protons in the bunches. The primary vertex is taken to be the one with the highest sum of squared transverse momenta of the ID tracks.

$\not{E}_T$ cleaning cuts are used in order to reject events where unphysical jets produced by instrumental effects affect the measured missing transverse energy[27]. Typically such effects are due to:

- Noise burst in the hadronic endcap calorimeter resulting in energy deposits localised almost completely in a single HEC cell with a low energy deposit in the EM calorimeter.
- Noise in the EM calorimeter resulting in a large fraction of the jet energy deposited in the EM calorimeter compared to the total jet energy.
- Out-of-time energy depositions in the calorimeter compared to the time of the event.

To clean $\not{E}_T$, a set of requirements are applied to the jets in the event. Jets are reconstructed with `AntiKtTopo` algorithm[28] and distance parameter of R = 0.4. Only jets with calibrated transverse momentum greater than 20 GeV are considered. The calibrated transverse momentum of a jet is evaluated at electromagnetic scale[4] and corrected for calorimeter non-compensation, upstream material and other effects using p_T and η dependent calibration factors obtained from Monte Carlo and validated with extensive test-beam and collision data studies [29]. If 'bad' jet in the event is present, whole event is discarded. The jet is considered as bad if satisfies at least one of the following requirements:

- electromagnetic fraction is >0.95 and absolute value of jet quality >0.8;
- energy fraction in the HEC >0.8 and minimum number of cells containing at least 90% of the jet energy <=5;
- energy fraction in the HEC >0.5 and absolute value of jet quality >0.5;
- absolute value of jet time computed as the energy squared cells mean time>25 ns;
- electromagnetic fraction <0.05;
- maximum energy fraction in one calorimeter layer >0.99 and $|\eta(jet)|$ <2.

The calorimeter quality is a measure of the difference in the sampling of the measured pulse and the reference pulse shape that is used to reconstruct the cell energy. In order to deal with jets that have a large portion of their energy accounted for by coherent noise, the variable jet quality is defined, which is the fraction of jet energy from bad-quality calorimeter cells.

Described requirements correspond to the "loose" cleaning, which is evaluated to be sufficient for $W \to e\nu$ and $W \to \mu\nu$ studies. The effect of $\not{E}_T$ cleaning cuts is of the order of 0.05% for $W \to \mu\nu$ events and well described in the MC simulation. For $W' \to \mu\nu$ signal events, the efficiency of the cleaning cuts is 98.5%-96.5% with respect to the vertex cut, for W' masses 500 GeV - 1750 GeV . This drop in efficiency is entirely due to requirement of electromagnetic fraction <0.05. Highly energetic muon from W' decays deposits more energy in the calorimeter than muon from W process, and this deposition is then recognizes as a jet by the jet algorithm. Since most of this energy is deposited in the hadronic calorimeter, jet with electromagnetic fraction <0.05 is found in the event. For the time being, this cut is not dropped from the selection, but all cuts should be reevaluated in future searches.

[4]The electromagnetic scale is the energy scale defined by electromagnetic processes in the calorimeter. It reconstructs the energy deposited in electromagnetic showers, but does not correct for the lower hadron response.

5.4 Muon event selection

Basic kinematic cuts. Events included in the $W' \to \mu\nu$ and $W^* \to \mu\nu$ searches are required to satisfy selection criteria in addition to the vertex and cleaning cuts and the trigger listed in the previous section. In order to select muon candidates from W' or W^* decays, basic kinematic cuts are applied: $p_T > 25$ GeV and $|\eta| < 1.05$. Muons are required to be combined. Cut on the muon p_T is chosen to suppress the contamination from π/K decays, high-rate low mass SM processes, cosmics and other non-collision backgrounds, while retaining very high signal efficiency. As explained in the Section 5.2.1, due to alignment uncertainties in the endcap, only barrel muon candidates are considered. Major fraction of muons from W' decays are emitted into the central detector region, particularly for W' bosons with higher masses. Muons from W^* , have different kinematics, and the selection is more affected with the barrel constraint. Fig 5.10 and 5.11 show η distribition of true muons versus true transverse mass of the muon neutrino system in W' and W^* cases respectively.

The region of lower transverse masses ($m_{\mathrm{T}} < \frac{1}{2}m_{W'}$) has some fraction of muons outside barrel (decreasing with mass of W' particle), but for final results this kinematic region is rejected due to low signal-to-background ratio. In this region the overwhelming background from Standard Model W production can not be reduced. Table 5.8 shows the fraction of events with $|\eta| < 1.05$ with respect the whole η , without and with $m_{\mathrm{T}} > \frac{1}{2}m_{W'(W^*)}$ requirement. Fraction of events that have $m_{\mathrm{T}} > \frac{1}{2}m_{W'}$ with muon emmited in $|\eta| < 1.05$ is ranging from 0.6790-0.8963 for W' masses 500-1750 GeV Ḟor W^* this fraction is lower, and in range 0.5910-0.6732.

Table 5.8: Fraction of events with muon from W' and W^* decay emmited in $|\eta| <$1.05 region. Numbers show the fraction of events without cut on true m_{T} , and with cut $m_{\mathrm{T}} > \frac{1}{2}m_{W'(W^*)}$.

Mass	$W' \to \mu\nu$		$W^* \to \mu\nu$	
[GeV]	no m_{T} -cut	$m_{\mathrm{T}} > \frac{1}{2}m_{W'}$	no m_{T} -cut	$m_{\mathrm{T}} > \frac{1}{2}m_{W^*}$
500	0.6264 ± 0.0056	0.6790 ± 0.0066	0.5432 ± 0.0053	0.5910 ± 0.0064
750	0.6799 ± 0.0059	0.7622 ± 0.0071	0.5215 ± 0.0051	0.6005 ± 0.0065
1000	0.7143 ± 0.0060	0.8210 ± 0.0074	0.5336 ± 0.0051	0.6382 ± 0.0068
1250	0.7327 ± 0.0074	0.8597 ± 0.0094	0.5164 ± 0.0051	0.6434 ± 0.0069
1500	0.7417 ± 0.0087	0.8771 ± 0.0111	0.5149 ± 0.0051	0.6607 ± 0.0070
1750	0.7335 ± 0.0087	0.8963 ± 0.0117	0.5111 ± 0.0051	0.6733 ± 0.0072

Inner Detector hits. In order to suppress muons from decay in flight, and fakes from punch-throughs of jets into the Muon Spectrometer, muon candidates are required to have some minimal number of hits in the ID. These loose requirements are:

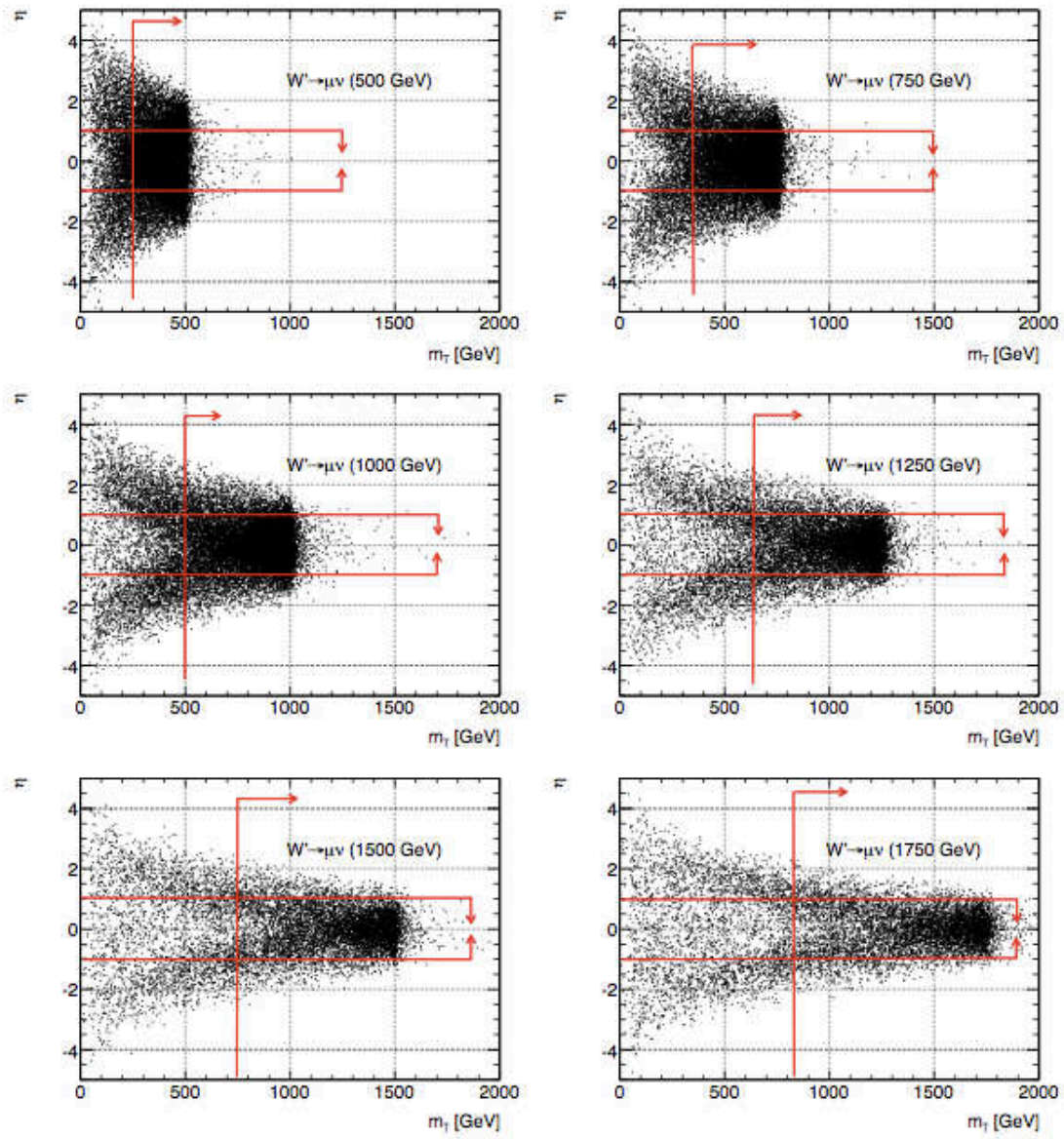

Figure 5.10: True η distribution as a function of the true transverse mass m_{T} for various masses of the W' boson $m_{W'}$. No other cuts are applied, except $p_T > 25$ GeV. The red line indicate analysis cuts $|\eta| < 1.05$ and $m_{\mathrm{T}} > \frac{1}{2} m_{W'}$.

- $N_{hit}^{pixel} > 0$, where N_{hit}^{pixel} is the number of hits in the Pixel detector,
- $N_{hit}^{SCT} > 3$, where N_{hit}^{SCT} is the number of SCT hits, and
- $N_{hit}^{pixel} + N_{hit}^{SCT} > 5$.

Multiplicity of Pixel, SCT, and silicon hits (Pixel and SCT together) in data is shown in

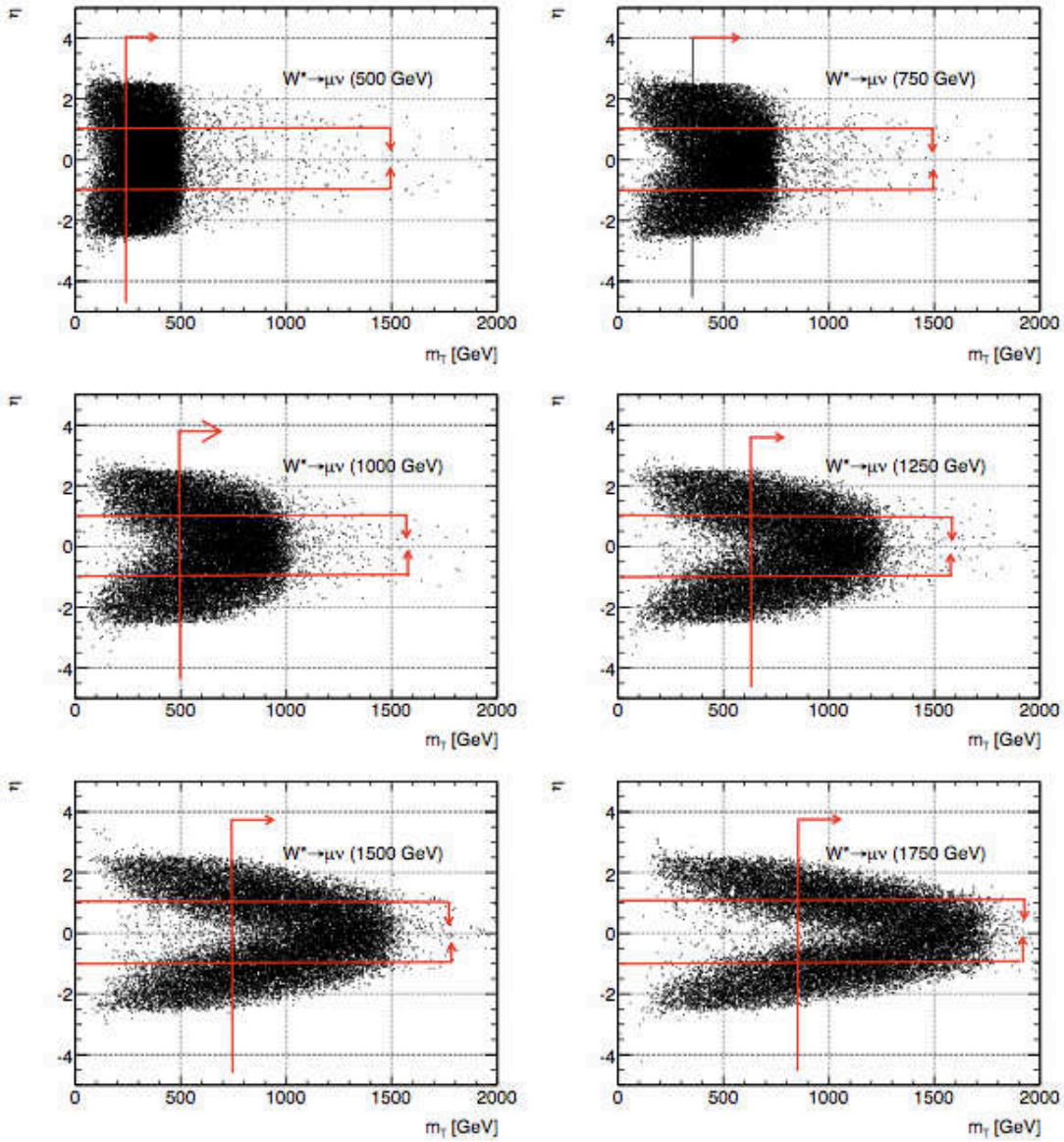

Figure 5.11: True η distribution as a function of the true transverse mass m_{T} for various masses of the W^* boson m_{W^*}. No other cuts are applied, except $p_T > 25$ GeV. The red line indicate analysis cuts $|\eta| < 1.05$ and $m_{\mathrm{T}} > \frac{1}{2} m_{W'}$.

Fig5.4. Effect of these cuts on data and MC is small reflecting high efficiency of the ID. For the analysis performed within `Athena` release 15, ATLAS Muon Combined Performance group (MCP) recomended that muon candidates have a successful TRT extension in the η acceptance of the TRT [30]. An unsuccessful extension corresponds to either no TRT hit associated, or a set of TRT hits associated as outliers. The recommendation of MCP group was to reject muon in $|\eta|$ <1.9 that have:

- $n = N_{hits}^{TRT} + N_{outliers}^{TRT}$ <6, or
- $N_{outliers}^{TRT} >= 0.9n$

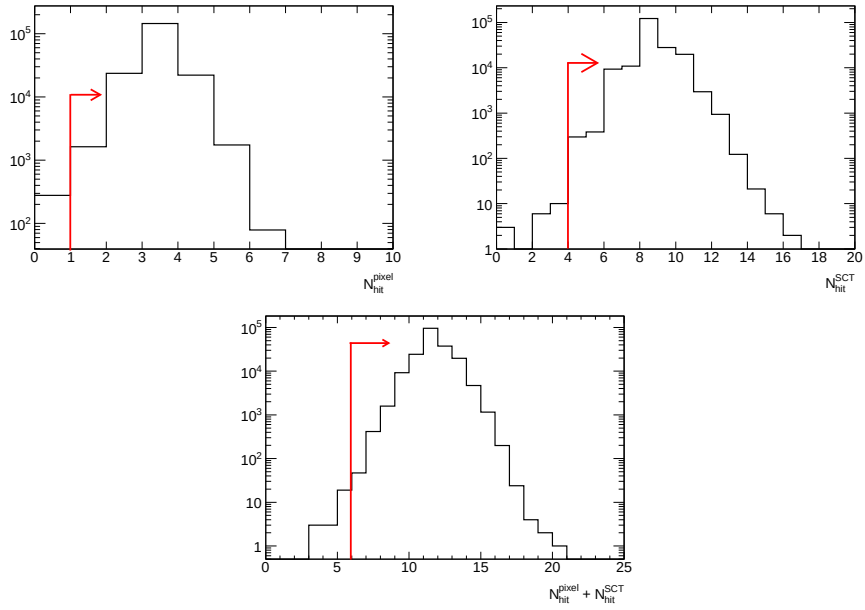

Figure 5.12: Multiplicity of Pixel, SCT, and silicon hits (Pixel and SCT together) in events that pass preselection and have at least 1 combined muon with $p_T > 25$ GeV and $|\eta| < 1.05$.

Multiplicity of $N_{hits}^{TRT} + N_{outliers}^{TRT}$, and $N_{outliers}^{TRT}$ normalized to n are shown in Fig 5.13. Fraction of muons that fail this criteria is small, and non of the discarded muon has high-p_T , or high-m_{T} hence this requirement is omitted.

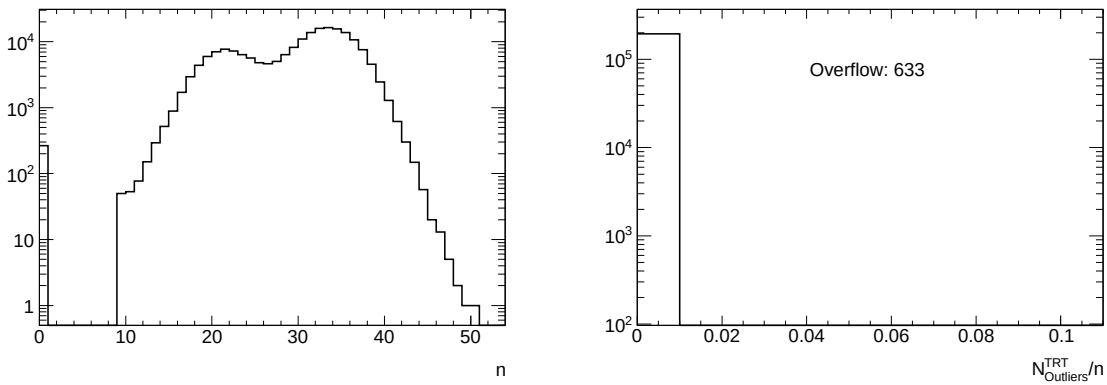

Figure 5.13: $n = N_{hits}^{TRT} + N_{outliers}^{TRT}$, and $N_{outliers}^{TRT}/n$ in events that pass preselection and have at least 1 combined muon with $p_T > 25$ GeV and $|\eta| < 1.05$, and muons pass minimal number of silicon hits listed in the text.

Impact parameter cuts. In order to suppress muons from cosmic backgrounds, and further suppress muons from QCD backgrounds, especially the ones from decays of heavy flavor mesons (produced in $c\bar{c} \to \mu X$ and $b\bar{b} \to \mu X$ processes), additional cuts are imposed. These cuts are the position along the beam axis (measured with respect the position of the primary vertex) $|z_0| < 5$ mm, and the transverse distance of closest approach (also measured with respect to the same distance of the primary vertex) $|d_0|$ <1 mm. If there are more vertices in the event, the most energetic one (highest sum p_T^2) is chosen for the calculation. The distributions of d_0 and z_0 in data and MC are shown in Fig5.4. MC is normalized to the expected number of events, using the cross sections from Table 5.5. Distributions in Fig5.4 show the following:

- Impact of d_0/z_0 cuts on SM backgrounds from $W \to \ell\nu$ and $Z \to \ell\ell$ is small, which is also true for the signal. Hence, chosen values of the cuts, especially d_0 , are loose, and could be tightened if necessary.

- The large tails in data indicate significant number of muons from non-collision backgrounds, especially cosmics. Variables d_0 and z_0 could be used to estimate these backgrounds from data (cf. next chapter).

- Cross section calculation of QCD jet production is not reliable, and this background should be estimated from data, rather than MC.

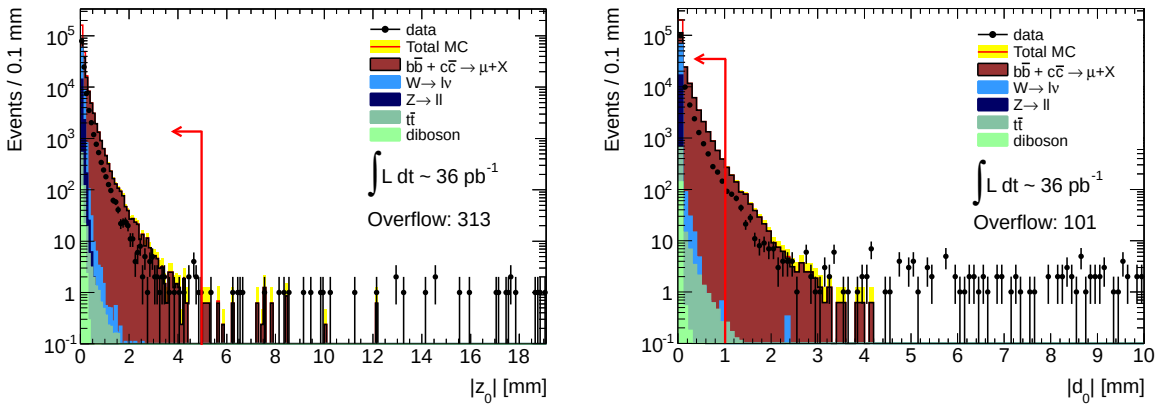

Figure 5.14: Distributions of the muon position along the beam axis $|z_0|$, and the transverse distance of closest approach $|d_0|$. Muons pass preselection and requirements $p_T > 25$ GeV and $|\eta| < 1.05$ and have sufficient number of hits in the ID. Distributions are normalized to the luminosity according to the cross sections from Table 5.5. The red line indicate analysis cuts $|z_0| < 5$ mm, and $|d_0|$ <1 mm.

Hits in the Muon Spectrometer. Because of very high p_T of the muon that would come from $W' \to \mu\nu$ process, and relatively small number of events needed to establish a signal, muon

resolution represents a critical part of the $W' \to \mu\nu$ search. The best resolution is obtained by the combination of momentum measurement in the ID and MS, when both systems are fully commissioned and alignment. Since ID was not aligned with sufficient precision, momentum measurement of the combined track is not used. For the same reason, momentum from ID cannot be used in combination with momentum measured in MS as a quality cut, as it was recommended by the MCP group [30]. In order to improve resolution of standalone measurement, additional quality cuts based only on the information from the spectrometer are investigated. The investigated cuts are:

- number of φ hits in RPC layers;
- number of hits in in each of the three barrel stations: inner, middle and outer;
- dropping the muons that cross more than 1 sector in the barrel;
- dropping the muons that are reconstructed in the feet region;[5]
- dropping the muons that have MDT holes on the track.

The histograms that represent p_T and m_{T} distributions for muons passing preselections, basic kinematic cuts, ID hits cut as well as impact parameter cuts are shown in Figures 5.4,5.4. The distribution are obtained from $W \to \mu\nu$ MC sample, with muon momentum and $\not{E}_T$ smearing applied. Full histograms are without any additional quality cuts, while shaded histograms are obtained with a quality cut indicated on the plot.

The requirement of $N_{layer}^{RPC\varphi} > 1$ (at least one φ hit in each of at least two of the three RPC layers) has small impact on the tails p_T and m_{T} distributions, and negligible effect ($\sim$0.1-0.2%) on the muon efficiency, since this is also required by the trigger. This particular cut is introduced to allow measurement of the track in the φ-direction. Requirements of at least 2, 3 or 4 hits in each barrel inner (BI), middle (BM), and outer station (BO), remove the tails in the p_T and m_{T} distributions, indicating improvement of the resolution. Similar, but less pronounced effect have requirements that muon crosses only 1 sector of MDT barrel chambers, or there are no holes on the muon track in the barrel chambers. The effect of removing muons from the feet region is marginal.

The effect of the MS hits requirements on the possible W' signal is shown in Table 5.9. Table shows fractions of muons that pass particular quality criteria with respect to the previous cut ($|d_0|$ <1 mm and $|z_0| < 5$ mm). From this table it is obvious that requirement of only 1

[5]"Feet" is defined by the following constraints: $-2.1 < \varphi < -1.9$ or $-1.2 < \varphi < -1.0$ and $0.3 < |\eta| < 0.5$; $-2.1 < \varphi < -1.0$ and $0.65 < |\eta| < 0.85$.

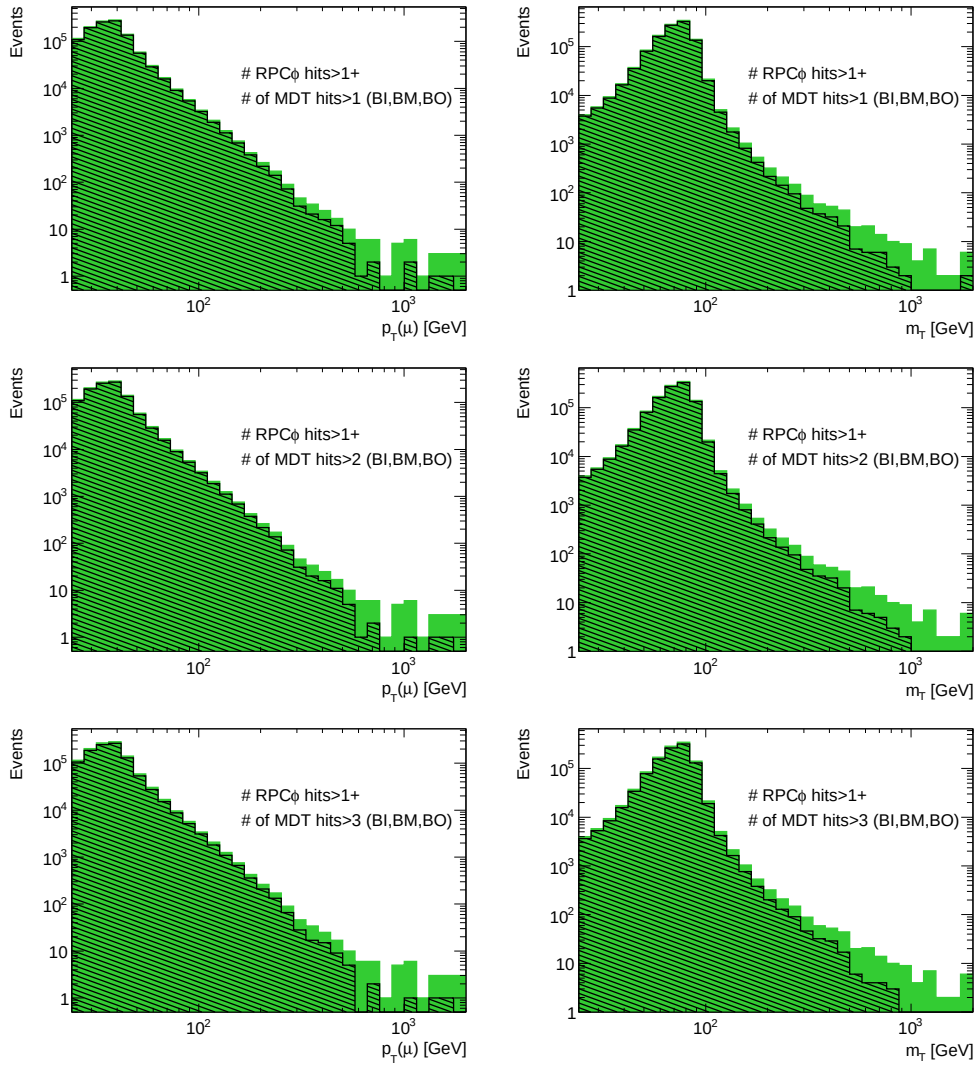

Figure 5.15: Distributions of p_T , and m_{T} in $W \to \mu\nu$ MC sample. Muons pass preselection, kinematic cuts, have ID hits and impact parameter cuts. Full histograms are without any additional quality cuts, while shaded histograms are obtained with a quality cut indicated on the plot. Smearing of the muon p_T and hadronic part of the $\not{E}_T$ are applied.

barrel sector has the largest impact on the signal efficiency (∼13%), while requirements on feet exclusion or number of $N_{layer}^{RPC\varphi}$hits have marginal. The difference in signal efficiency in requirements of at lest 2 or 3 hits in MDT stations is small. Fig. 5.17 shows muon p_T resolution in $W \to \mu\nu$ and W' events without and with requirements of at lest 3 hits in each of the three barrel stations. The improvement of the resolution is obvious for $W \to \mu\nu$ which is emphasized on the third plot that shows p_T resolutions versus reconstructed p_T in $W \to \mu\nu$ sample. The effect of the requirement of at least 3 hist in each of the chambers on p_T and m_{T} distributions obtained from data is demonstrated in Fig5.4. Data plot is consistant with plots obtained from

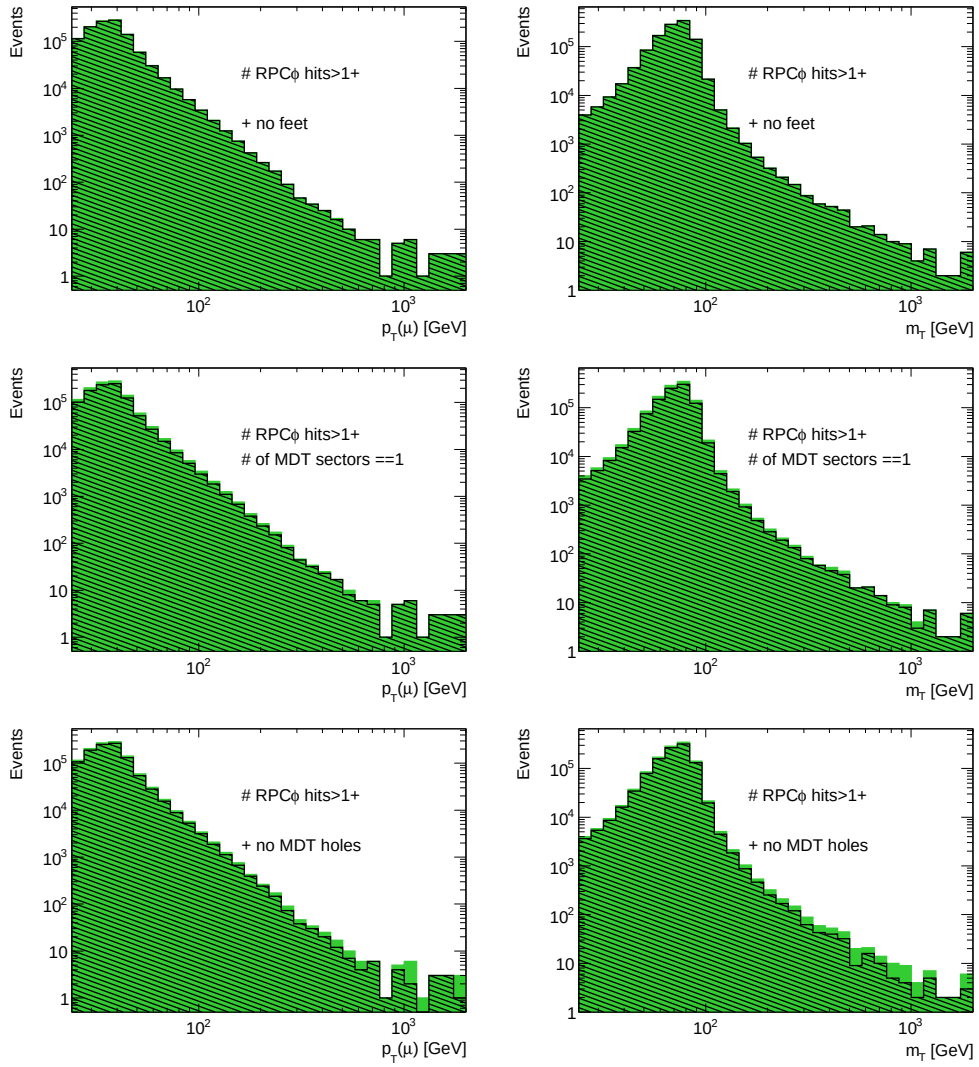

Figure 5.16: Distributions of p_T , and m_{T} in $W \to \mu\nu$ MC sample. Muons pass preselection, kinematic cuts, have ID hits and impact parameter cuts. Full histograms are without any additional quality cuts, while shaded histograms are obtained with a quality cut indicated on the plot. Smearing of the muon p_T and hadronic part of the $\not{E}_T$ are applied.

MC samples.

The requirements on the number of hits in the ID, as well as the requirement of hits in three stations in the MS, selects tracks with good resolution and whose properties are well-modelled by the simulation. In particular the 3-station MS measurement is giving the best muon resolution estimation.

To remove possible badly measured muons, muon candidates are rejected if they pick up hits from the at the time not-at-the-time-aligned BIS7 and BIS8 chambers that are just outside the nominal acceptance. The effect of this cut is small, and removes 694 muon candidates out

Table 5.9: Fraction of muons passing each of the cuts on MS hits with respect to the d_0/z_0cut.

Mass [GeV]	$N_{layer}^{RPC\varphi} > 1$	$N_{hit}^{MDT} > 1$	$N_{hit}^{MDT} > 2$	$N_{hit}^{MDT} > 3$	exclude feet	only 1 barrel sector	no MDT holes
500	0.996	0.950	0.941	0.912	0.990	0.869	0.920
750	0.997	0.944	0.936	0.904	0.989	0.869	0.921
1000	0.996	0.942	0.933	0.900	0.991	0.870	0.922
1250	0.996	0.946	0.937	0.905	0.990	0.867	0.922
1500	0.996	0.945	0.932	0.902	0.990	0.869	0.920
1750	0.996	0.945	0.934	0.900	0.992	0.870	0.918

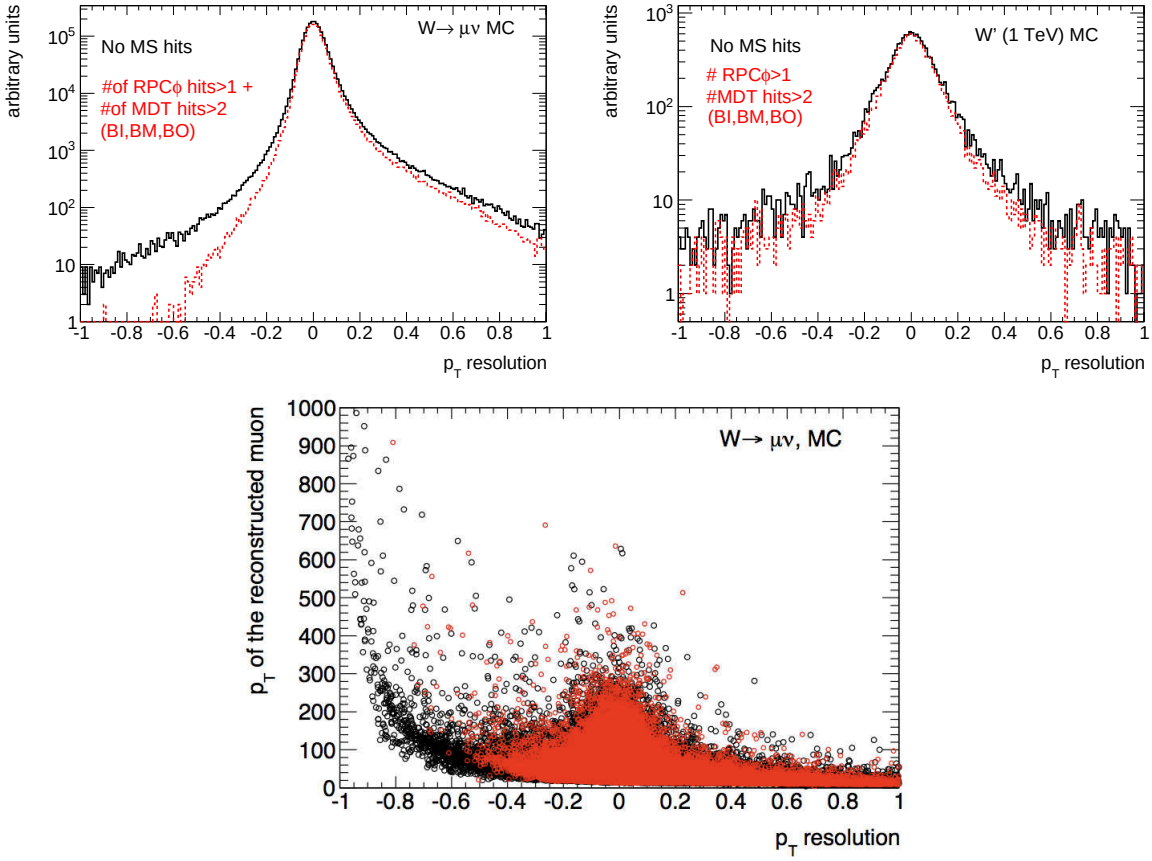

Figure 5.17: Resolution on $W \to \mu\nu$ and W' MC events without and with requirements of at least 3 hits in each of 3 MDT stations. Resolution is defined as $(1/p_{T,r} - 1/p_{T,t})/(1/p_{T,t})$, where $p_{T,r}$ is transverse momentum of the reconstructed muon matched with true muon with transverse momentum $p_{T,t}$. The third plots shows p_T resolutions versus reconstructed p_T in $W \to \mu\nu$ sample without 3 hit requirement (black dots) and with 3 hit requirement (red dots).

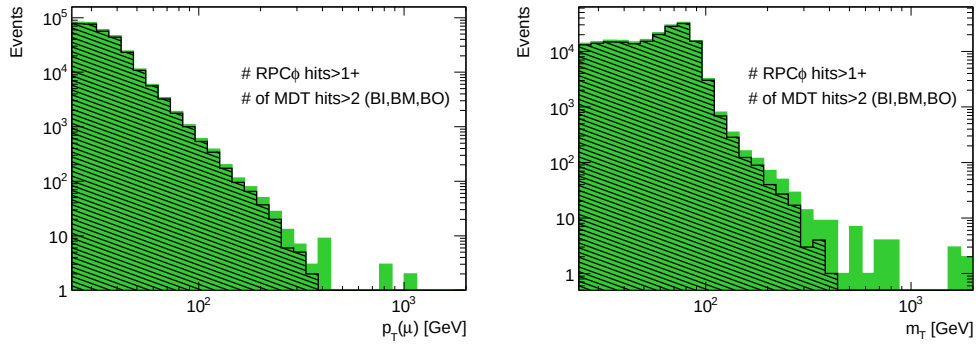

Figure 5.18: Distributions of p_T , and m_{T} in the whole 2010 dataset. Muons pass preselection, kinematic cuts, have ID hits and pass impact parameter cuts. Full histograms are without any additional quality cuts, while shaded histograms are obtained with requirement that muon candidated have at least 3 hits in each of 3 MDT stations.

of 288247.

Trigger matching. The "trigger-matchig" cut ensures that the muon that tags the event, is the one that actually fired the trigger. In order to do so, muons are required to have $\Delta R_{trig} < 0.1$, where ΔR_{trig} is the η - φ distance between the reconstructed muon and the nearest passing trigger muon. This requirement is motivated by the measurement of the trigger efficiency from data where probability of an offline muon, matched to a trigger object, passing the trigger is measured. The correction and systematic uncertainty derived from this measurement (which are the functions of p_T , η and φ) could not be applied to the wrong muon, i.e. to the one that would had not fired the trigger. However, this bias is expected to be small since trigger efficiency is high. Nevertheless, trigger matching cut is applied.

Summary. In order to select good $W' \to \mu\nu$ ($W^* \to \mu\nu$) candidates in data, events passing the preselection are required to have exactly one combined muon satisfying the following criteria:

- $|\eta| < 1.05$;
- $p_T > 25$ GeV;
- $N_{hit}^{pixel} > 0$;
- $N_{hit}^{SCT} > 3$;
- $N_{hit}^{pixel} + N_{hit}^{SCT} > 5$;
- $N_{layer}^{RPC\varphi} > 1$ (at least one phi hit in each of at least two of the three RPC layers);
- $N_{hit}^{MDT} > 2$ in each of the three barrel stations;
- muons are rejected if they pick up hits from BIS7 and BIS8 chambers;
- $|d_0|$ <1 mm and $|z_0| < 5$ mm, and

- $\Delta R_{trig} < 0.1$.

Basic kinematic distributions of muon p_T ,η ,φ, as well as $\not{E}_T$ and m_{T} distributions after muon selection are shown in Fig5.4. QCD MC is normalized according to cross section, and scaled by factor 0.5. This factors is ad-hoc introduced in order to match data and MC in low-m_{T} region where QCD dominates. This procedure however is not realistic estimation of QCD background from data. For each distribution, ratio between data and MC is shown. Muon kinematic distributions show very good agreement in shape between data and MC. $\not{E}_T$ distribution show some discrepancy in shape, which is then propagated to the m_{T} distribution.

5.5 Isolation and $\not{E}_T$ cut

The above requirements are fairly effective in guaranteeing the muon momentum is well measured and in discriminating against background from sources other than W/Z production. To further suppress QCD background and muons from heavy flavor decays and $t\bar{t}$ production, the muon is required to be isolated and events to have $\not{E}_T$ above some threshold.

Isolation. Muons from W' decay are expected to be isolated from other tracks and in particular from jets, in contrast to some of the main background sources due to heavy-hadrons decays. Moreover background muons can come from in-flight decays of pions and kaons. In order to reject these sources of background, it is possible to require that muon track is isolated from other tracks in the ID, or/and the energy around the direction of the muon track in the calorimeter to be small. Isolation variable based on ID information is constructed from the sum of p_T of ID tracks picked up within some cone ΔR around the muon track (excluding muon track itself). ID tracks are required to have $p_T > 1$ GeV and that are coming from the primary vertex. Calorimeter isolation variable is obtained by summing up energy in the calorimeter cells in some cone around the direction of the muon. For W' searches, it is useful to scale isolation variable with lepton p_T :

$$\sum p_T(trk)/p_T(\mu), \quad \sum E_T/p_T(\mu) \tag{5.8}$$

The scaling of the isolation variable with the muon p_T reduces efficiency losses due to radiation from the muon at high p_T .

Fig 5.20(a) and 5.20(b) show the distributions of relative isolation variables in $W \to \mu\nu$ MC samples. The quantities are plotted for different values of the surrounding cones ($\Delta R < 0.3$ and $\Delta R < 0.4$) and in MC samples without, and with additional interactions due to pileup. Distributions demonstrate that isolation based on calorimeter information is much more sensitive to the effect of pileup then isolation based on ID information, irrespective of the cone size. In this

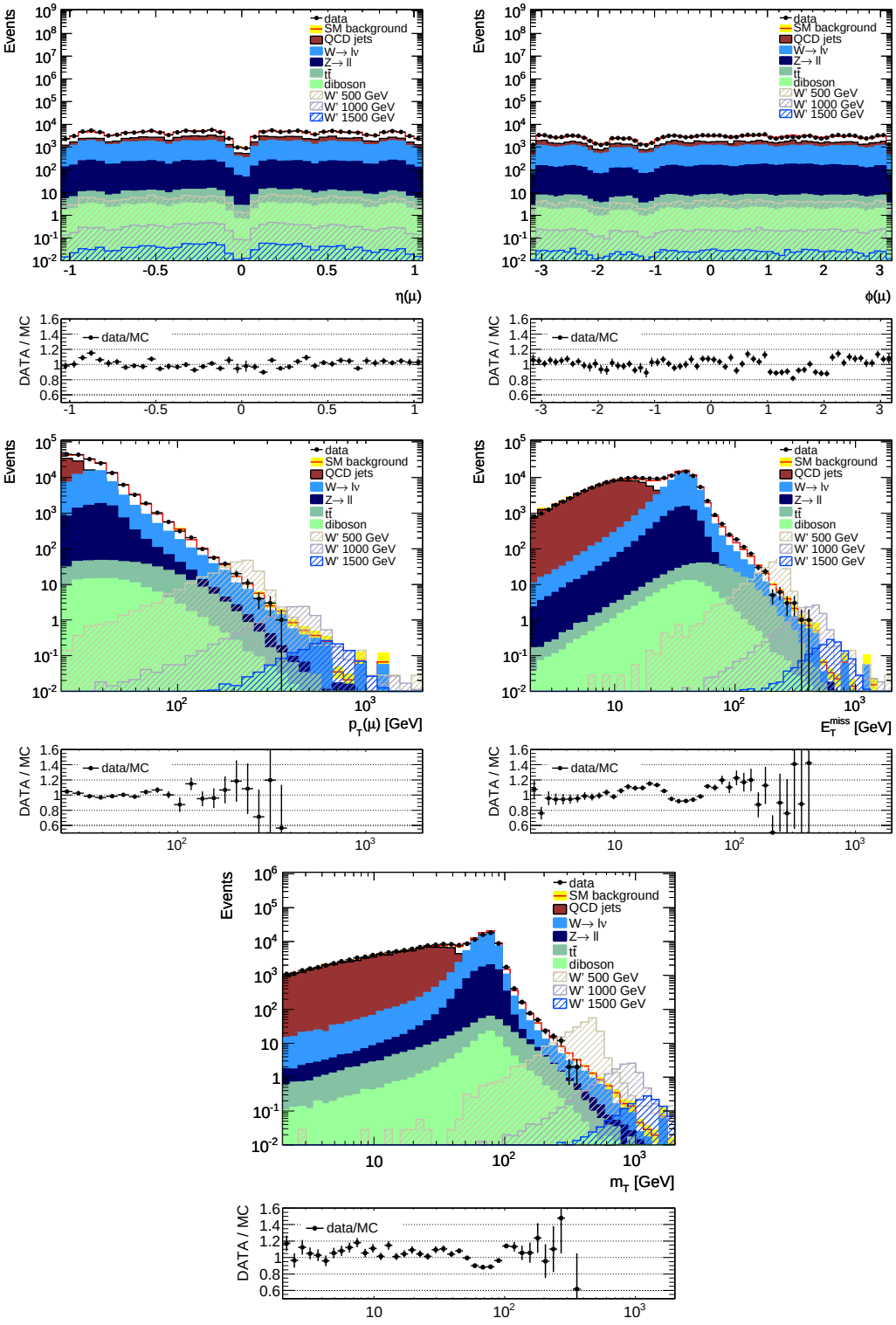

Figure 5.19: Muon p_T ,η ,φ ,$\not{E}_T$ and m_{T} distributions after muon selection.

analysis relative track isolation is used.

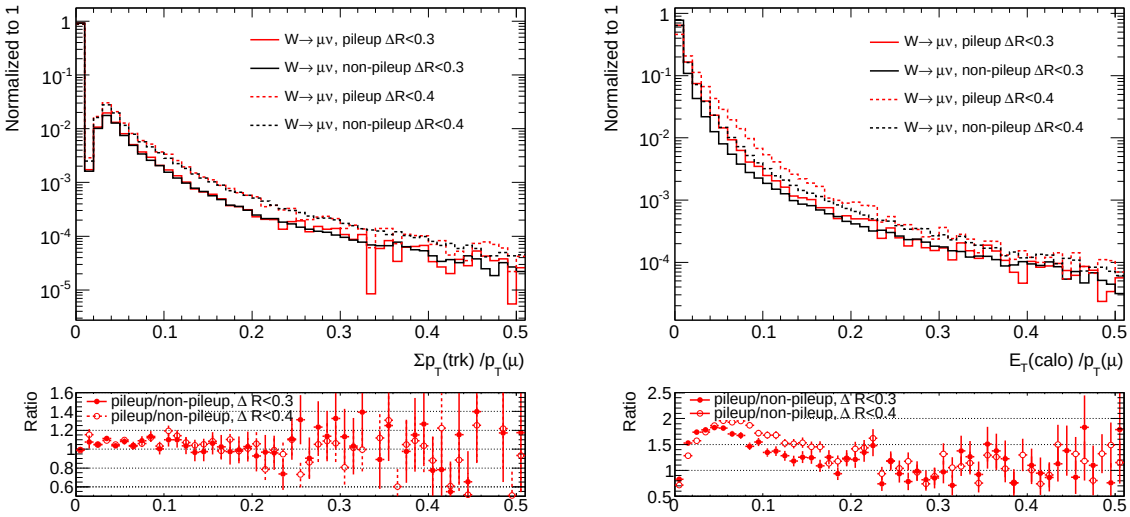

(a) (b)

Figure 5.20: (a) Distributions of relative track isolation in $W \to \mu\nu$ MC pileup and non-pileup samples obtained for two cones: $\Delta R < 0.3$ and $\Delta R < 0.4$. (b) Distributions of relative calorimeter isolation in $W \to \mu\nu$ MC pileup and non-pileup samples obtained for two cones: $\Delta R < 0.3$ and $\Delta R < 0.4$.

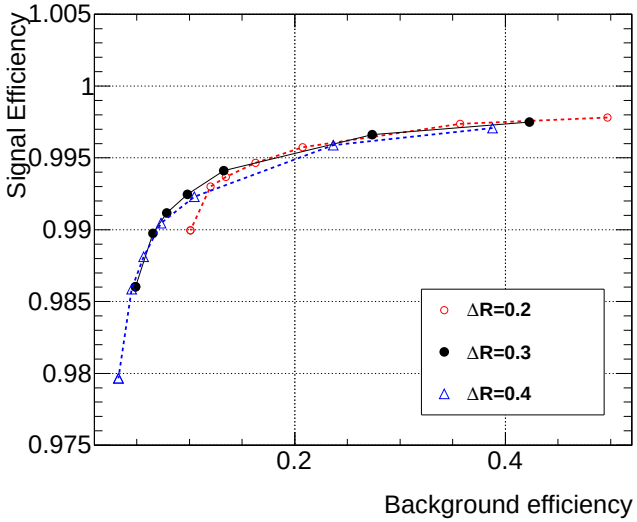

Figure 5.21: Background versus signal efficiency for different tuning of the isolation cut.

The cone size is chosen by utilizing the rejection of muons from non-prompt sources compared to the efficiency of muons from $W' \to \mu\nu$ decays. The sample with mass of W' of 1 TeV is used for this study. Efficiency of the MC signal sample is compared to the efficiency of QCD background sample for different cones and different values of the relative isolation

quantity $\sum p_T/p_T$. These studies on the isolation cut are illustrated by the plot in Fig5.5. A cone value of 0.2 clearly does not provide enough background rejection power, while 0.3 and 0.4 show similar performances. The cone value of $\Delta R < 0.3$ with cut value $\sum p_T/p_T < 0.05$ is chosen due to slightly higher signal efficiency with respect the value of the cone 0.4. Signal efficiency of this requirement is >98.5%, and basically independent of W' mass. Distributions of the isolation quantity for data and SM backgrounds is shown in Fig5.22(a) , and normalized distributions in three signal MC samples are shown in Fig5.22(b).

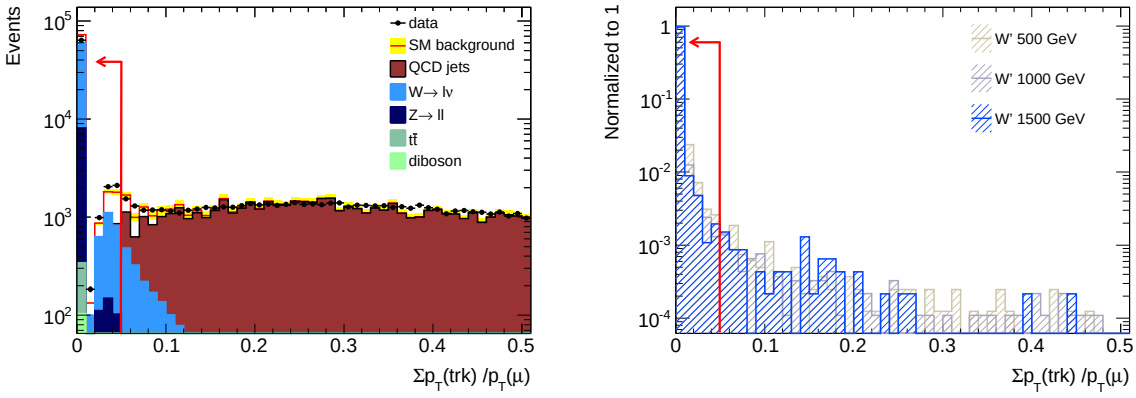

(a) (b)

Figure 5.22: (a) Muon isolation variable after preselection. QCD MC is normalized using theoretical cross section scaled by 0.5. (b) Isolation variable in three W' MC samples. Distribution is normalized to unity.

$\not{E}_T$ **cut.** The QCD background includes both real leptons from heavy flavor decay and jets that can fake muons. In both cases, the $\not{E}_T$ is typically small in contrast to W' (and majority of standard model W) events where the $\not{E}_T$ roughly balances the lepton transverse momentum. Effective discriminant is a fixed $\not{E}_T$ threshold:

$$\not{E}_T > 25 \text{ GeV} \tag{5.9}$$

Efficiency of this cut in the W' signal is almost 100%. Fig5.23(a) and 5.23(b) show the distributions of $\not{E}_T$ vs. muon transverse momentum, and $\not{E}_T$ vs. m_{T} in the events that pass isolation requirement. The value of the $\not{E}_T$ cut is indicated on the figures. The chosen value of the $\not{E}_T$ cut ensures effective suppression of QCD, mainly concentrated in low-$\not{E}_T$ and low-m_{T} region. Although it is possible to raise the value ($\not{E}_T$ >50 GeV have been used in the prospect studies [31]) keeping still high signal efficiency, this would affect mostly W background reducing number of events on the m_{T} peak.

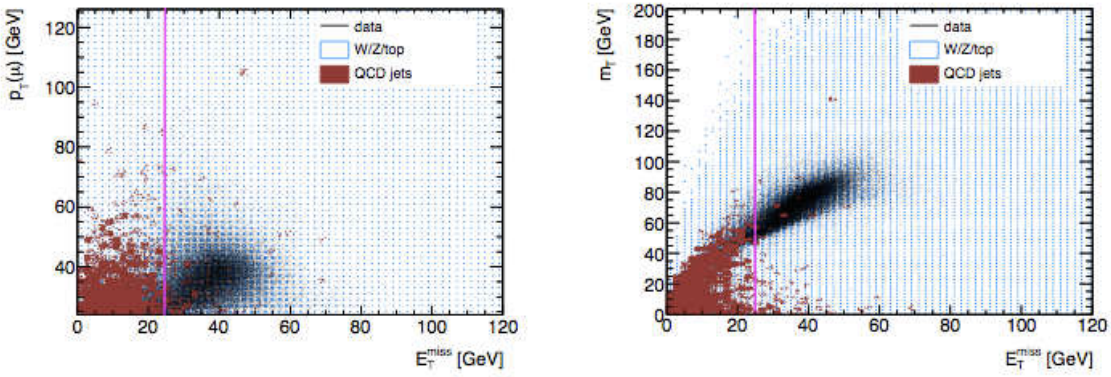

(a) (b)

Figure 5.23: Events passing muon selection and isolation requirement. (a) $\not{E}_T$ vs. muon transverse momentum (b) $\not{E}_T$ vs. m_{T} .

5.6 Initial results

5.6.1 Cut flows

Table 5.10: Cut flow of events in collision data.

Selection requirement	Number of events
GRL	178238511
Trigger	15359321
Vertex cut	14609571
Jet cleaning	14601355
At least 1 combined μ	2925624
Muon $\lvert\eta\rvert < 1.05$	1705345
Muon p_T >25 GeV	190843
ID hits	190593
MS hits	178340
Impact par. cuts	177326
Trigger match	175676
Exactly 1 μ (above sel.)	173279
Isolation	69002
$\not{E}_T > 25$GeV	52096

The cut flow for the sample of collision data corresponding to integrated luminosity of 36.35 pb^{-1} is presented in Table 5.10. The cut flows for used Monte Carlo samples are presented after that in Tables 5.11,5.12, and 5.13. Events that would come from $W' \to \tau\nu$ processe, where τ-lepton would decay into a muon and corresponding neutrinos, are filtered out before event selection is applied. This contribution to the signal is completely ignored.

Table 5.11: Cut flow of events in W' and W^* MC signal samples. Numbers in the table represent fraction of events satisfying a particular selection requirement calculated with respect to the previous requirement. Before selection requirements are applied, events from $W' \to \tau\nu$ and $W' \to e\nu$ processes are filtered out from the samples. Generator cut corresponds to the fraction of $W' \to \mu\nu$ events. Quoted uncertainties are statistical.

MC sample	W'(500 GeV)	W'(750 GeV)	W'(1000 GeV)	W'(1250 GeV)	W'(1500 GeV)	W'(1750 GeV)
Generator cut	0.3332±0.0024	0.3316±0.0026	0.3339±0.0024	0.3362±0.0029	0.3321±0.0033	0.3301±0.0033
Trigger	0.7773±0.0021	0.7795±0.0021	0.7815±0.0021	0.7857±0.0026	0.7814±0.0030	0.7770±0.0030
Vertex cut	0.9859±0.0021	0.9866±0.0021	0.9875±0.0021	0.9858±0.0026	0.9868±0.0029	0.9871±0.0029
Jet cleaning	0.9857±0.0020	0.9805±0.0020	0.9742±0.0020	0.9703±0.0025	0.9677±0.0029	0.9658±0.0029
comb. μ, $\lvert\eta\rvert$ <1.05	0.5746±0.0016	0.6265±0.0016	0.6595±0.0017	0.6747±0.0021	0.6793±0.0024	0.6734±0.0023
p_T >25 GeV	0.9912±0.0015	0.9909±0.0016	0.9911±0.0017	0.9915±0.0021	0.9889±0.0024	0.9854±0.0023
ID hits	1.0000±0.0015	0.9998±0.0016	0.9999±0.0017	1.0000±0.0021	0.9998±0.0024	0.9996±0.0023
MS hits	0.9410±0.0015	0.9362±0.0015	0.9328±0.0016	0.9364±0.0020	0.9288±0.0023	0.9338±0.0022
Impact par. cuts	1.0000±0.0015	1.0000±0.0015	1.0000±0.0016	1.0000±0.0020	1.0000±0.0023	1.0000±0.0022
Trigger match	0.9985±0.0015	0.9983±0.0015	0.9985±0.0016	0.9989±0.0020	0.9983±0.0023	0.9982±0.0022
Exactly 1 μ	0.9999±0.0015	0.9998±0.0015	1.0000±0.0016	0.9995±0.0020	0.9994±0.0023	0.9998±0.0022
Isolation	0.9868±0.0015	0.9883±0.0015	0.9891±0.0016	0.9864±0.0020	0.9890±0.0023	0.9898±0.0022
$\not{E}_T > 25$GeV	0.9980±0.0015	0.9992±0.0015	0.9995±0.0016	0.9994±0.0020	0.9991±0.0023	0.9989±0.0022
Overall	0.1326±0.0015	0.1412±0.0015	0.1511±0.0016	0.1558±0.0016	0.1523±0.0020	0.1495±0.0022

MC sample	W^*(500 GeV)	W^*(750 GeV)	W^*(1000 GeV)	W^*(1250 GeV)	W^*(1500 GeV)	W^*(1750 GeV)
Trigger	0.8267±0.0064	0.8270±0.0064	0.8332±0.0064	0.8332±0.0064	0.8331±0.0064	0.8403±0.0064
Vertex cut	0.9857±0.0064	0.9858±0.0064	0.9869±0.0064	0.9862±0.0064	0.9855±0.0064	0.9862±0.0064
Jet cleaning	0.9871±0.0063	0.9820±0.0063	0.9796±0.0063	0.9723±0.0063	0.9711±0.0063	0.9671±0.0063
comb. μ, $\lvert\eta\rvert$ <1.05	0.4710±0.0043	0.4489±0.0042	0.4553±0.0042	0.4346±0.0041	0.4308±0.0041	0.4299±0.0041
p_T >25 GeV	0.9939±0.0043	0.9938±0.0042	0.9927±0.0042	0.9941±0.0041	0.9905±0.0041	0.9915±0.0041
ID hits	0.9998±0.0043	0.9997±0.0041	0.9997±0.0042	0.9997±0.0042	0.9997±0.0041	0.9995±0.0041
MS hits	0.9394±0.0042	0.9360±0.0040	0.9335±0.0041	0.9398±0.0040	0.9311±0.0039	0.9303±0.0039
Impact par. cuts	1.0000±0.0042	1.0000±0.0042	1.0000±0.0042	1.0000±0.0042	1.0000±0.0042	1.0000±0.0042
Trigger match	0.9994±0.0042	0.9994±0.0040	0.9989±0.0041	0.9995±0.0040	0.9993±0.0039	0.9988±0.0039
Exactly 1 μ	0.9998±0.0042	1.0000±0.0040	0.9997±0.0041	1.0000±0.0040	0.9997±0.0041	0.9994±0.0041
Isolation	0.9909±0.0041	0.9905±0.0040	0.9843±0.0040	0.9836±0.0040	0.9811±0.0039	0.9829±0.0039
$\not{E}_T > 25$GeV	0.9987±0.0041	0.9987±0.0040	0.9997±0.0040	0.9998±0.0040	0.9999±0.0039	0.9984±0.0039
Overall	0.3498± 0.0041	0.3309±0.0043	0.3342±0.0040	0.3189± 0.0040	0.3105± 0.0039	0.3120±0.0039

Table 5.12: Cut flow of events in W/Z MC background samples. Events with $M(W) >200$ GeV and $M(Z) >250$ GeV are filtered out from the inclusive $W \to \mu\nu$, $W \to \tau\nu$, and $Z \to \mu\mu$ samples. Generator cuts correspond to the fraction of events that pass true mass requirements.

MC sample	$W \to \mu\nu$	$W \to \tau\nu$	W200M500	W500M1500	W1500M2500
Generator cut	0.99967 ± 0.00038	0.99967 ± 0.00050	1.0000 ± 0.0000	1.0000 ± 0.0000	1.0000 ± 0.0000
Trigger	0.62160 ± 0.00030	0.23810 ± 0.00049	0.2955 ± 0.0022	0.3122 ± 0.0023	0.3243 ± 0.0023
Vertex cut	0.98562 ± 0.00030	0.98547 ± 0.00048	0.9857 ± 0.0022	0.9860 ± 0.0023	0.9872 ± 0.0023
Jet cleaning	0.99687 ± 0.00030	0.99878 ± 0.00048	0.9903 ± 0.0022	0.9822 ± 0.0022	0.9606 ± 0.0023
comb. μ, $\|\eta\|$ <1.05	0.39309 ± 0.00019	0.41822 ± 0.00031	0.4782 ± 0.0015	0.5956 ± 0.0017	0.6990 ± 0.0019
p_T >25 GeV	0.69422 ± 0.00016	0.16786 ± 0.00012	0.9212 ± 0.0015	0.9627 ± 0.0017	0.9666 ± 0.0019
ID hits	0.99986 ± 0.00015	0.99982 ± 0.00012	0.9999 ± 0.0015	0.9994 ± 0.0017	0.9933 ± 0.0019
MS hits	0.93974 ± 0.00015	0.93930 ± 0.00012	0.9382 ± 0.0014	0.9395 ± 0.0017	0.9289 ± 0.0018
Impact par. cuts	1.00000 ± 0.00015	0.99994 ± 0.00012	0.9997 ± 0.0014	0.9992 ± 0.0017	0.9981 ± 0.0018
Trigger match	0.99921 ± 0.00015	0.99929 ± 0.00012	0.9997 ± 0.0014	0.9985 ± 0.0016	0.9985 ± 0.0018
Exactly 1 μ	1.00000 ± 0.00015	0.99987 ± 0.00012	1.0000 ± 0.0014	0.9998 ± 0.0016	0.9997 ± 0.0018
Isolation	0.96902 ± 0.00015	0.96423 ± 0.00012	0.9814 ± 0.0014	0.9849 ± 0.0016	0.9850 ± 0.0018
$\not{E}_T >$ 25GeV	0.85416 ± 0.00014	0.62354 ± 0.00010	0.9820 ± 0.0014	0.9961 ± 0.0016	0.9994 ± 0.0018
Overall	0.12947 ± 0.00014	0.00927 ± 0.00010	0.1148 ± 0.0014	0.1593 ± 0.0016	0.1880 ± 0.0018

MC sample	$Z \to \mu\mu$	$Z \to \tau\tau$	$Z\mu\mu$250M400	$Z\mu\mu$400M600	$Z\mu\mu$600M8000	$Z\mu\mu$800M1000	$Z\mu\mu$1000M1250	$Z\mu\mu$1250M1500
Generator cut	0.99944 ± 0.00045	1.00000 ± 0.0000	1.0000 ± 0.0000	1.0000 ± 0.0000	1.0000 ± 0.0000	1.0000 ± 0.0000	1.0000 ± 0.0000	1.0000 ±0.00000
Trigger	0.84998 ± 0.00041	0.14450 ± 0.0003	0.9292 ± 0.0068	0.9436 ± 0.0069	0.9455 ± 0.0069	0.9501 ± 0.0069	0.9515 ± 0.0069	0.9504 ± 0.0069
Vertex cut	0.98660 ± 0.00041	0.98660 ± 0.0019	0.9872 ± 0.0073	0.9875 ± 0.0072	0.9875 ± 0.0072	0.9873 ± 0.0068	0.9871 ± 0.0068	0.9875 ± 0.0068
Jet cleaning	0.99297 ± 0.00041	0.98819 ± 0.0019	0.9808 ± 0.0073	0.9728 ± 0.0072	0.9629 ± 0.0072	0.9547 ± 0.0067	0.9445 ± 0.0067	0.9316 ± 0.0066
comb. μ, $\|\eta\|$ <1.05	0.56961 ± 0.00031	0.45447 ± 0.0013	0.6864 ± 0.0062	0.7496 ± 0.0064	0.7907 ± 0.0066	0.8191 ± 0.0060	0.8252 ± 0.0060	0.8136 ± 0.0060
p_T >25 GeV	0.76112 ± 0.00027	0.18724 ± 0.0012	0.9895 ± 0.0089	0.9957 ± 0.0086	0.9964 ± 0.0084	0.9966 ± 0.0060	0.9967 ± 0.0060	0.9961 ± 0.0059
ID hits	0.99999 ± 0.00027	0.99975 ± 0.0064	0.9998 ± 0.0090	0.9999 ± 0.0086	0.9998 ± 0.0084	0.9999 ± 0.0060	0.9999 ± 0.0060	0.9999 ± 0.0059
MS hits	0.91035 ± 0.00026	0.92933 ± 0.0062	0.9121 ± 0.0086	0.9130 ± 0.0082	0.9125 ± 0.0082	0.9158 ± 0.0057	0.9200 ± 0.0058	0.9999 ± 0.0059
Impact par. cuts	1.00000 ± 0.00026	0.99982 ± 0.0067	1.0000 ± 0.0094	1.0000 ± 0.0090	1.0000 ± 0.0088	1.0000 ± 0.0058	1.0000 ± 0.0058	1.0000 ± 0.0057
Trigger match	0.92709 ± 0.00027	0.98535 ± 0.0066	0.9302 ± 0.0091	0.9321 ± 0.0088	0.9337 ± 0.0085	0.9367 ± 0.0060	0.9368 ± 0.0060	0.9459 ± 0.0059
Exactly 1 μ	0.79940 ± 0.00072	0.99093 ± 0.0067	0.9302 ± 0.0091	0.8113 ± 0.0087	0.7842 ± 0.0082	0.7646 ± 0.0049	0.7425 ± 0.0048	0.7078 ± 0.0047
Isolation	0.97043 ± 0.00022	0.96153 ± 0.0066	0.8222 ± 0.0089	0.9850 ± 0.0100	0.9874 ± 0.0102	0.9893 ± 0.0049	0.9853 ± 0.0048	0.9887 ± 0.0047
$\not{E}_T >$ 25GeV	0.78418 ± 0.00019	0.27696 ± 0.0036	0.9813 ± 0.0107	0.9935 ± 0.0100	0.9972 ± 0.0103	0.9970 ± 0.0049	0.9988 ± 0.0048	0.9989 ± 0.0046
Overall	0.18524 ± 0.00019	0.002896± 0.00004	0.9819 ± 0.0108	0.4571 ±0.0048	0.4659 ±0.0048	0.4729 ± 0.0049	0.4594 ± 0.0048	0.4344 ± 0.0046

Table 5.13: Cut flow of events in $t\bar{t}$, diboson and QCD background samples.

MC sample	$t\bar{t}$	WW	WZ	ZZ
Generator cut	1.0000 ± 0.0000	1.0000 ± 0.0000	1.0000 ± 0.0000	1.0000 ± 0.0000
Trigger	0.4334 ± 0.0007	0.4330 ± 0.0013	0.4409 ± 0.0013	0.4724 ± 0.0014
Vertex cut	0.9872 ± 0.0017	0.9874 ± 0.0031	0.9877 ± 0.0030	0.9873 ± 0.0029
Jet cleaning	0.9925 ± 0.0018	0.9940 ± 0.0031	0.9919 ± 0.0030	0.9908 ± 0.0029
comb. μ, $\|\eta\|$ <1.05	0.6432 ± 0.0014	0.4628 ± 0.0021	0.5264 ± 0.0022	0.6047 ± 0.0023
p_T >25 GeV	0.5736 ± 0.0017	0.7006 ± 0.0038	0.6729 ± 0.0035	0.6503 ± 0.0030
ID hits	0.9997 ± 0.0029	0.9998 ± 0.0054	1.0000 ± 0.0056	0.9998 ± 0.0047
MS hits	0.9249 ± 0.0028	0.9327 ± 0.0052	0.9254 ± 0.0049	0.9142 ± 0.0045
Impact par. cuts	0.9985 ± 0.0030	1.0000 ± 0.0056	0.9999 ± 0.0051	0.9995 ± 0.0050
Trigger match	0.9707 ± 0.0030	0.9880 ± 0.0056	0.9996 ± 0.0053	0.9341 ± 0.0047
Exactly 1 μ	0.9677 ± 0.0030	0.9847 ± 0.0056	0.9251 ± 0.0052	0.7999 ± 0.0045
Isolation	0.8411 ± 0.0029	0.9537 ± 0.0056	0.9434 ± 0.0055	0.9089 ± 0.0054
$\not{E}_T$ > 25GeV	0.8489 ± 0.0031	0.7864 ± 0.0051	0.7688 ± 0.0051	0.7347 ± 0.0051
Overall	0.0970 ± 0.0004	0.0935 ± 0.0006	0.0916 ± 0.0006	0.0828 ± 0.0006

MC sample	J0μ	J1μ	J2μ	J3μ	J4μ	J5μ	J6μ
Generator cut	1±0	1±0	1±0	1±0	1±0	1±0	1±0
Trigger	0.6848 ± 0.0012	0.7204 ± 0.0013	0.7553 ± 0.0012	0.7865 ± 0.0013	0.8050 ± 0.0013	0.8109 ± 0.0014	0.8156 ± 0.009041
Vertex cut	0.9875 ± 0.0017	0.9869 ± 0.0017	0.9870 ± 0.0016	0.9868 ± 0.0016	0.9866 ± 0.0016	0.9867 ± 0.0017	0.9850 ± 0.011
Jet cleaning	0.9997 ± 0.0017	0.9993 ± 0.0018	0.9986 ± 0.0016	0.9987 ± 0.0016	0.9981 ± 0.0016	0.9974 ± 0.0017	0.9968 ± 0.011
comb. μ, $\|\eta\|$ <1.05	0.4614 ± 0.0012	0.4719 ± 0.0012	0.4981 ± 0.0012	0.5484 ± 0.0012	0.6244 ± 0.0013	0.7172 ± 0.0015	0.8109 ± 0.011
p_T >25 GeV	0.00032 ± 4.5e-05	0.0026 ± 0.00013	0.0365 ± 0.0004	0.1501 ± 0.0008	0.2941 ± 0.0011	0.4113 ± 0.0013	0.4627 ± 0.008
ID hits	1 ± 0.14	1 ± 0.05032	0.9999 ± 0.012	0.9993 ± 0.0057	0.998 ± 0.0038	0.9904 ± 0.0032	0.9693 ± 0.018
MS hits	0.92 ± 0.14	0.8987 ± 0.0477	0.9316 ± 0.013	0.9335 ± 0.0055	0.9304 ± 0.0037	0.9285 ± 0.0031	0.9222 ± 0.018
Impact par. cuts	0.9565 ± 0.14	0.9972 ± 0.053	0.9973 ± 0.012	0.9931 ± 0.0058	0.9864 ± 0.0039	0.9801 ± 0.0031	0.9799 ± 0.019
Trigger Match	1 ± 0.15	1 ± 0.05315	0.9911 ± 0.012	0.9899 ± 0.0058	0.9875 ± 0.0040	0.9817 ± 0.0033	0.9787 ± 0.019
Exactly 1 μ	1 ± 0.15	1 ± 0.05315	0.9994 ± 0.0127	0.9973 ± 0.0059	0.9895 ± 0.0040	0.984 ± 0.0033	0.9787 ± 0.019
Isolation	0.2273 ± 0.071	0.1525 ± 0.02076	0.05941 ± 0.003	0.0172 ± 0.0008	0.006804 ± 0.00033	0.002499 ± 0.0017	0.9665 ± 0.019
$\not{E}_T$ > 25GeV	0.3 ± 0.17	0.0185 ± 0.01852	0.01351 ± 0.006	0.1623 ± 0.018	0.3486 ± 0.029	0.6179 ± 0.054	0.0016 ± 0.00081
Overall	6.0e-06 ± 3.0e-06	2.2e-06± 2.2e-06	1.0e-05 ± 4.476e-06	0.000163 ± 1.8e-05	0.00031±2.5-05	0.0003162 ± 2.7e-05	0.00041 ± 0.0002

5.6.2 Uncorrected results

Events passing preselection requirements and having exactly one isolated muon (passing muon selection and isolation cut defined before), and $\not\!\!E_T$ >25 GeV define "search" sample, i.e. dataset that might contain good W' candidates. In order to perform search for W' (or W^* like) particle, the observed transverse mass distribution is compared to the expectation of the SM backgrounds. Table 5.14 presents number of observed events in data, and expected number of events obtained from signal and background MC samples normalized to the integrated luminosity of $\mathscr{L}_{\text{int}}$=36.35 pb^{-1} . Events are counted after $\not\!\!E_T$ cut, and series of m_{T} cuts, each corresponding to the half mass of a W' mass point.

Expected signal and backgrounds, are evaluated with simulated samples and normalized with respect to one another using the highest-order available cross sections predictions listed in Tables 5.3 and 5.5, except for QCD background where LO cross sections are used. The shapes of distributions come from generators used in simulation, for example from `Pythia` for the dominant W/Z backgrounds. These results, however, should be corrected to account for the discrepancy between data and MC regarding muon trigger, identification and isolation efficiency. Also, theoretical corrections should be applied to account for m_{T}-dependence of the quantum chromodinamics higher order calculation with respect to Pythia LO* predictions. Higher order weak corrections (beyond the photon radiation included in the simulation by `PHOTOS`) are also mass (m_{T}) dependent, and are expected to be significantly higher with respect to the % effect at W pole. The description and evaluation of all corrections to be applied to MC expectations is done in the next chapter. Here, a preliminary, uncorrected results are presented. On top of this, as shown before, cross section of QCD background has high uncertainty. Thus this background should be estimated from data directly, rather than MC. Cosmic background should also be estimated, and added to all other backgrounds. Procedures for estimation of cosmic and QCD backgrounds from data will be presented in the next chapter as well.

Results presented the Table 5.14 confirm that data show no evidence for any excess above Standard Model expectation. SM $W \to \ell\nu$ production constitutes most of the background, while $Z \to \ell\ell$ process is 18-20% of the total SM background. The high fraction of $Z \to \ell\ell$ background is caused by the limited acceptance of the Muon Spectrometer used in the analysis and muon momentum resolution. Both give raise to the $\not\!\!E_T$ and m_{T} tails. Possible further suppression of the $Z \to \ell\ell$ background will be discussed in the section 5.7.1. $t\bar{t}$ process makes about 7% of the SM background, while diboson and QCD backgrounds are negligible according to the simulation results. High uncertainty in high-m_{T} tail is due to low statistics of the inclusive $W \to \mu\nu$ MC sample, in which some events with low true m_{T} are propagated to very high-m_{T}.

This is caused by non-Gaussian tails in muon resolution appearing as a consequence of the worsening of standalone resolution with muon p_T . Combined p_T of these muons has much better resolution, and events are not present in the high-m_{T} if the combined measurement would have been used[6].

Fig5.6.2 show p_T ,$\not\!\!E_T$, and m_{T} distributions after the $\not\!\!E_T > 25$ GeV cut applied. As after preselection, the agreement in shape between data and MC is good for p_T , but not perfect for $\not\!\!E_T$ and consequently m_{T} distributions.

The list of 16 events with highest m_{T}($m_{\mathrm{T}} > 250$GeV) which contains numbers of the runs, events and luminosity blocks, as well as some basic properties of these events, is presented in Tab5.15. The highest-m_{T} event has m_{T} =361 GeV and its display in the ATLAS detector is presented in 5.29.

Table 5.14: Number of observed events in data, and expected number of events obtained from background and W' signal MC samples normalized to the integrated luminosity of $\mathscr{L}_{\mathrm{int}}$=36.35 pb^{-1} . Highest-order available cross sections are used for signal and background calculation, expect for QCD where LO cross sections are used. The last six columns give the number of selected events after the indicated m_T cut is applied. Quoted uncertainties are statistical only.

	$\not\!\!E_T >$ 25 GeV	$m_{\mathrm{T}} >$ 250 GeV	$m_{\mathrm{T}} >$ 375 GeV	$m_{\mathrm{T}} >$ 500 GeV	$m_{\mathrm{T}} >$ 625 GeV	$m_{\mathrm{T}} >$ 750 GeV	$m_{\mathrm{T}} >$ 875 GeV
Data	52096	**16**	**0**	**0**	**0**	**0**	**0**
SM BG	59838 $\pm$215	**21.6 $\pm$ 0.5**	**5.90 $\pm$ 0.30**	**2.33 $\pm$ 0.22**	**1.18 $\pm$ 0.16**	**0.76 $\pm$ 0.13**	**0.61 $\pm$ 0.11**
$W \to \ell\nu$	52399 $\pm$55	14.0 $\pm$ 0.5	4.21 $\pm$ 0.29	1.66 $\pm$ 0.22	0.84 $\pm$ 0.17	0.54 $\pm$ 0.14	0.44 $\pm$ 0.10
$Z \to \ell\ell$	6678 $\pm$7	4.2 $\pm$ 0.1	1.07 $\pm$ 0.04	0.42 $\pm$ 0.03	0.21 $\pm$ 0.03	0.14 $\pm$ 0.02	0.11 $\pm$ 0.02
$t\bar{t}$	316 $\pm$1	2.8 $\pm$ 0.1	0.46 $\pm$ 0.05	0.17 $\pm$ 0.03	0.09 $\pm$ 0.02	0.05 $\pm$ 0.02	0.04 $\pm$ 0.00
diboson	85 $\pm$1	0.6 $\pm$ 0.0	0.14 $\pm$ 0.02	0.06 $\pm$ 0.00	0.03 $\pm$ 0.00	0.01 $\pm$ 0.00	0.01 $\pm$ 0.03
QCD	360 $\pm$208	0.02 $\pm$ 0.02	0.02 $\pm$ 0.02	0.02 $\pm$ 0.02	0.02 $\pm$ 0.02	0.02 $\pm$ 0.02	0.02 $\pm$ 0.02
W'(500)	225.2 $\pm$ 2.5	193.2 $\pm$ 2.3	-	-	-	-	-
W'(750)	49.26 $\pm$ 0.52	-	42.46 $\pm$ 0.45	-	-	-	-
W'(1000)	12.86 $\pm$ 0.14	-	-	10.98 $\pm$ 0.12	-	-	-
W'(1250)	4.34 $\pm$ 0.06	-	-	-	3.66 $\pm$ 0.05	-	-
W'(1500)	1.54 $\pm$ 0.02	-	-	-	-	1.275 $\pm$ 0.021	-
W'(1750)	0.53 $\pm$ 0.01	-	-	-	-	-	0.43 $\pm$ 0.04

Since no excess above SM is observed, the data and MC expectations are used to set limits on W' and W^* production cross sections. These limits, being a function of particle mass, are then converted into the mass limits of new gauge bosons. In order to set the limits, one needs to have selection efficiency comprising of efficiency due to geometrical acceptance of the detector, and efficiency of trigger, muon reconstruction, and specific selection cuts. Uncorrected event selection efficiencies for W' and W^* bosons are presented in Table5.16.

[6]Majority of the non-Gausian tails is not caused by the additional smearing of the muon momenta.

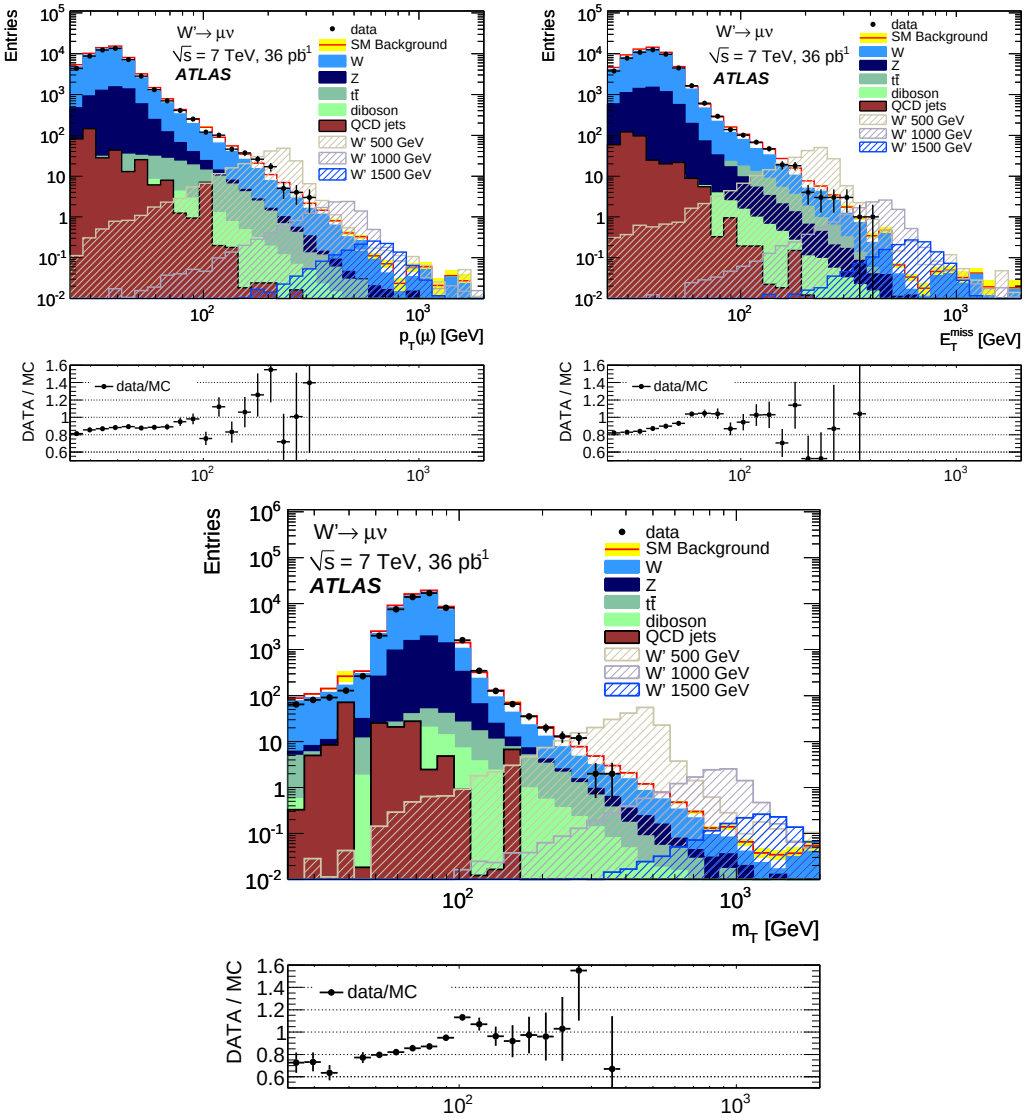

Figure 5.24: Uncorrected p_T , $\not{E}_T$ and m_{T} distributions after final selection. MC is normalized using theoretical cross sections, as explained in the text. Yellow uncertainty band is statistical only.

5.7 Possible additional cuts in muon channel

Event selection defined in the previous sections ensures clean data sample, suppression of reducible backgrounds such as QCD jets and $t\bar{t}$, and good control of irreducible W/Z backgrounds. The efficiency of signal is high, with main losses due to limited coverage of the trigger chambers, barrel constraint and requirement on number of hits in MDT chambers in the barrel (cf. Table5.11).

However, additional selection cuts could be considered, in order to remove events with

Table 5.15: List of high-m_{T} events in data, with event characteristics. Event with highest m_{T} is bolded.

Run	LB	Event	m_{T} [GeV]	p_T [GeV]	$\not{E}_T$ [GeV]	$\not{E}_T{}^{calo}$ [GeV]	$E^{\mu}_{T,loss}$ [GeV]	$\eta(\mu)$	$\phi(\mu)$
161520	174	6935488	267	311	59	251	5	-0.6898	2.961
162577	6	565990	266	140	130	43	3	-0.2007	2.086
166142	153	9662434	329	179	151	25	4	-0.9500	2.418
166786	301	14149879	279	148	131	14	4	0.8355	0.358
166924	**63**	**2790240**	**361**	**176**	**185**	**21**	**4**	**0.0394**	**-2.753**
167576	230	106038781	256	128	130	23	3	-0.5987	-0.838
167576	275	128061007	264	113	154	47	4	0.0311	0.566
167607	88	1083337	260	197	87	109	5	-0.5544	0.0181
167607	269	68183948	318	158	160	6	3	-0.8883	-2.700
167680	125	33368768	262	148	117	28	4	0.5697	2.743
167680	253	83253473	285	224	91	129	5	0.64511	0.282
167680	263	86704612	335	286	98	182	6	0.5835	0.441
167776	188	26738274	256	140	118	25	4	0.2748	1.704
167776	270	59634765	259	131	130	36	4	0.3095	0.611
167776	302	73803883	255	114	142	32	3	0.1502	-2.759
167776	425	129360643	255	128	127	11	4	-0.6327	-3.100

Table 5.16: Uncorrected event selection efficiencies, i.e. the fraction of Monte Carlo events that satisfy all event selection criteria and pass the m_{T} threshold equal to half of each W' mass. Results are shown for both $W' \to \mu\nu$ and $W^* \to \mu\nu$. The numbers in brackets represent signal efficiency of $W' \to \tau\nu$ process, which is latter ignored in the limit calculations. Uncertainties are statistical only.

mass	$\varepsilon^{\mathrm{MC}}_{\mathrm{sig}}$		
[GeV]	$W' \to \mu\nu$	$(W' \to \tau\nu)$	$W^* \to \mu\nu$
500	0.342 ± 0.004	(0.0133 ± 0.0008)	0.274 ± 0.004
750	0.365 ± 0.004	(0.0170 ± 0.0009)	0.266 ± 0.004
1000	0.386 ± 0.004	(0.0167 ± 0.0009)	0.273 ± 0.004
1250	0.390 ± 0.005	(0.0158 ± 0.0011)	0.264 ± 0.004
1500	0.380 ± 0.006	(0.0166 ± 0.0013)	0.260 ± 0.004
1750	0.361 ± 0.006	(0.0143 ± 0.0012)	0.262 ± 0.004

additional muons present, or to suppress events with high hadronic activity. Non of these requirement is critical to impose at this stage of the analysis. However, they are briefly discussed.

5.7.1 Vetoing additional muons in the event

Presence of additional muons in the event (in the endcap, but also in the barrel), are incompatible with the search signature that basically consists of "a muon and nothing else in the event". Nevertheless, this cut is not used in order to keep analysis as general as possible. To study the effect of this requirement on data and MC, in additions to the event selection defined before, events are discarded if there is at least one additional good muon in the event. This muon is required to be combined, with $p_T > 20$GeV, $|\eta| < 2.5$. Cut on p_T ensures avoiding fakes and low mass products as much as possible, as well as soft muons inside jets. Momentum measurement is taken from the combined track, and the search is not constrained on the barrel only. The bias of the ID misalignment to the momentum measurement is not relevant, since one is not interested to measure muon's p_T per se, just to establish if the muon is present. In order to suppress cosmics contamination, the muon is required to pass ID hits defined in section 5.4, and to have $|d_0|$ <1 mm and $|z_0|$ <5 mm.

The effect of vetoing additional muon on data and SM backgrounds is shown in Table5.17. The additional requirement of TGC chambers and endcap MDT and CSC chambers to be green in GRL removes negligible number of events in the preselection, corresponding to only 11 luminosity blocks. The effect on m_{T} distribution is shown in Fig5.25. This requirement mainly affects $Z \to \mu\mu$ background reducing it by about 50%, and has no impact on the signal efficiency.

Table 5.17: Number of observed events in data, and expected number of events for SM backgrounds with all selection cuts plus additional muon veto applied. The numbers are normalized to $\mathscr{L}_{\mathrm{int}}$=36.3p pb^{-1}

	second μ veto	$m_{\mathrm{T}}>$ 250 GeV	$m_{\mathrm{T}}>$ 375 GeV	$m_{\mathrm{T}}>$ 500 GeV	$m_{\mathrm{T}}>$ 625 GeV	$m_{\mathrm{T}}>$ 750 GeV	$m_{\mathrm{T}}>$ 875 GeV
Data	46344	11	0	0	0	0	0
SM BG	54251	18.04	5.09	1.94	0.94	0.65	0.51
$W \to \ell\nu$	52390	14.46	4.36	1.64	0.77	0.54	0.42
$Z \to \ell\ell$	1161	1.09	0.29	0.14	0.07	0.06	0.05
$t\bar{t}$	288	2.12	0.34	0.12	0.06	0.03	0.02
diboson	73	0.35	0.08	0.03	0.02	0.01	0.01
QCD	339	0.02	0.02	0.02	0.02	0.02	0.02

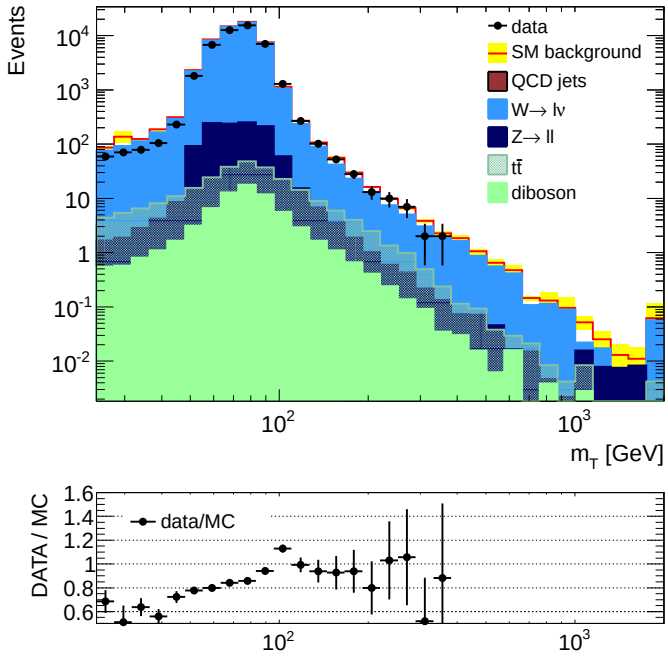

Figure 5.25: m_{T} distribution after all selection cuts plus additional muon veto applied.

5.7.2 $\not{E}_T\,/p_T$ cut

In addition to the cut on $\not{E}_T$, for W' search it could be useful to require cut on $\not{E}_T$ that scales with lepton p_T . For this purpose variable $\not{E}_T\,/p_T$ is introduced. In $W' \to \ell\nu$ process, lepton p_T is ballanced with $\not{E}_T$ which is in principle not the case in QCD and W+jets production. This is illustrated in Fig5.26(a), where $\not{E}_T\,/p_T$ is shown in the events with m_T >100 GeV. This selection requirement maybe more critical in $W' \to e\nu$ search (where it is actually introduced), where much higher fake rate in the high-m_{T} tail distribution is expected than in the muon channel. However, selection efficiency of this cut for signal is high, which is illustrated in Fig5.26(b). The effect of the selection requirement $\not{E}_T/p_T$ >0.6 in addition to the standard cut $\not{E}_T > 25$ GeV on data and SM backgrounds is presented in the Table5.18 and in Fig 5.7.2. Cut is chosen to be asymmetric in order to maximize signal efficiency since the background doesn't have high $\not{E}_T\,/p_T$. Signal efficiency 98-99% for W' mass range 500-1750 GeV.

5.7.3 Lepton fraction

Beside leptons and large $\not{E}_T$, events passing standard selection could contain large number of energetic jets. Thus, standard selection is not "safe" against contamination that might come from for example SUSY events. Also, when the energy of LHC is raised, cross section for

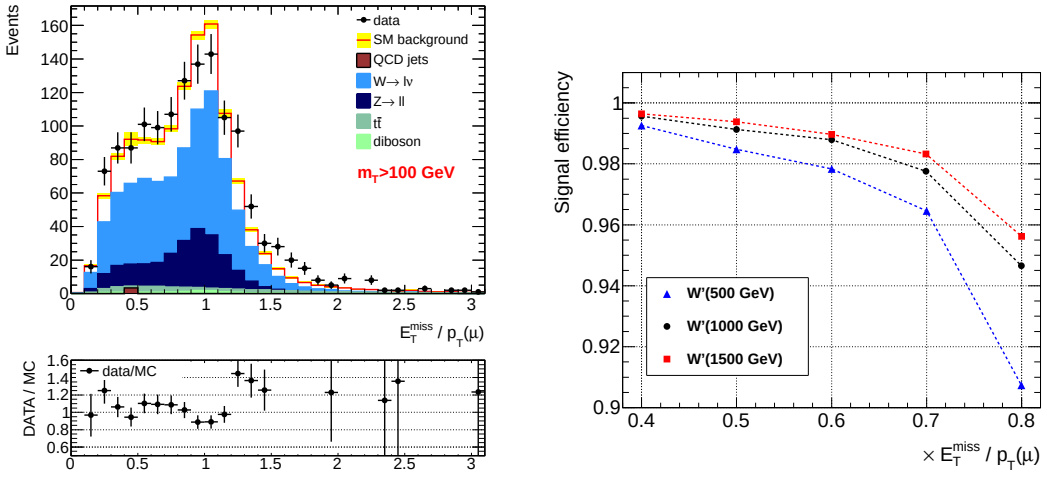

(a) (b)

Figure 5.26: (a)Distribution of $\not{E}_T/p_T$ in events with all selection cuts applied and m_T >100 GeV. (b) Selection efficiency as a function of the value of the cut on $\not{E}_T/p_T$ in three W' MC signal samples.

Table 5.18: Number of observed events in data, and expected number of events for SM backgrounds with all selection cuts plus $\not{E}_T/p_T$ >0.6 cut applied. The numbers are normalized to $\mathscr{L}_{\text{int}}$=36.3p pb^{-1}

	$\not{E}_T$ > 25 GeV	m_T > 250 GeV	m_T > 375 GeV	m_T > 500 GeV	m_T > 625 GeV	m_T > 750 GeV	m_T > 875 GeV
Data	49604	12	0	0	0	0	0
SM BG	57020	17.61	4.83	1.87	0.97	0.69	0.52
$W \to \ell\nu$	50179	11.19	3.36	1.29	0.66	0.49	0.36
$Z \to \ell\ell$	6253	3.61	0.94	0.39	0.19	0.12	0.09
$t\bar{t}$	254	2.30	0.41	0.14	0.09	0.05	0.05
diboson	70	0.50	0.11	0.05	0.03	0.01	0.01
QCD	263	0.01	0.01	0.01	0.01	0.01	0.01

$t\bar{t}$ production will grow fastly because of increase of the parton gluon density[7]. In order to suppress events with large hadronic activity, different variables have been considered in W' studies at ATLAS [31, 32]. One possible variable is so called "lepton fraction", defined as:

$$lf = \frac{p_T^\ell + \not{E}_T}{p_T^\ell + \not{E}_T + \Sigma p_T(jets)}, \tag{5.10}$$

where $\Sigma p_T(jets)$ is the scalar sum of p_T of jets above some threshold (typically above 20 GeV and $|\eta|$ <2.5). The distribution of the lepton fraction is shown in Fig5.28(a), with indicated

[7]In pp collisions at the LHC, $t\bar{t}$ is mainly produced via gg fussion.

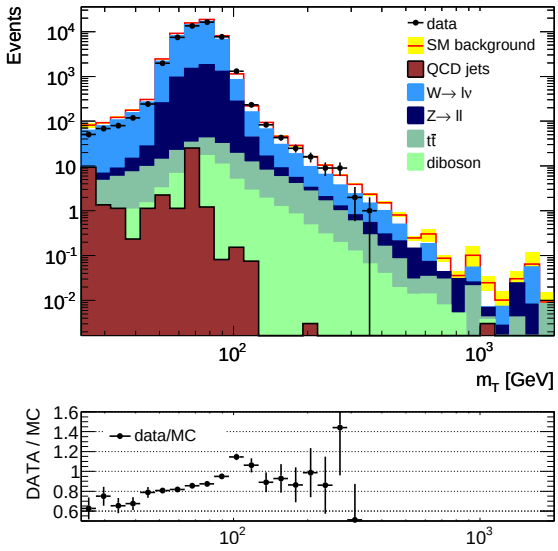

Figure 5.27: m_{T} distribution after all selection cuts plus $\not{E}_T / p_T$ applied.

value of the cut $lf > 0.5$. The effect of this cut (applied after $\not{E}_T$ cut) on the m_{T} distribution is illustrated in Fig5.28(b).

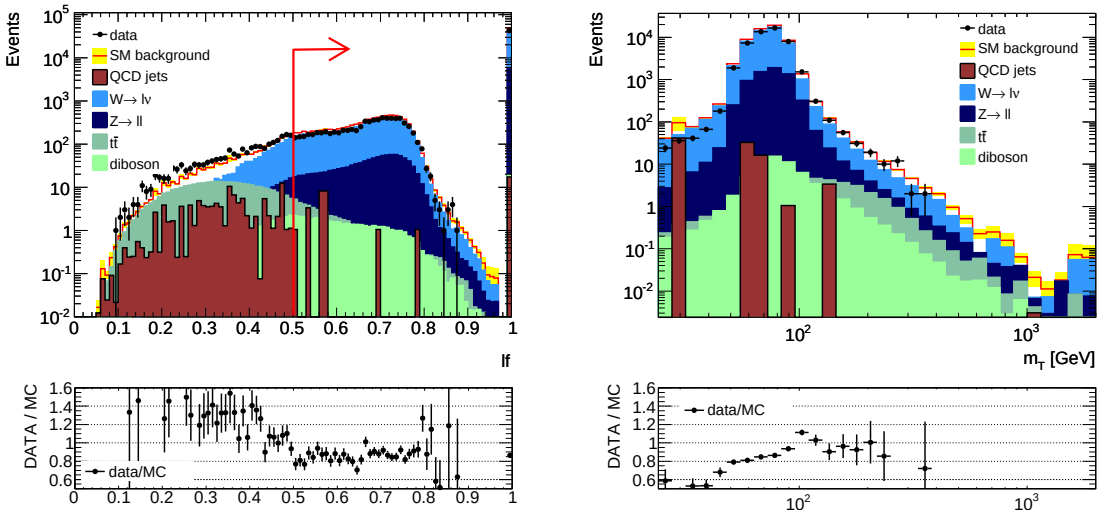

(a) (b)

Figure 5.28: (a) Distribution of lepton fraction variable as defined in text. All selection cuts are applied. (b) m_{T} distribution after all selection cuts plus lepton fraction cut applied.

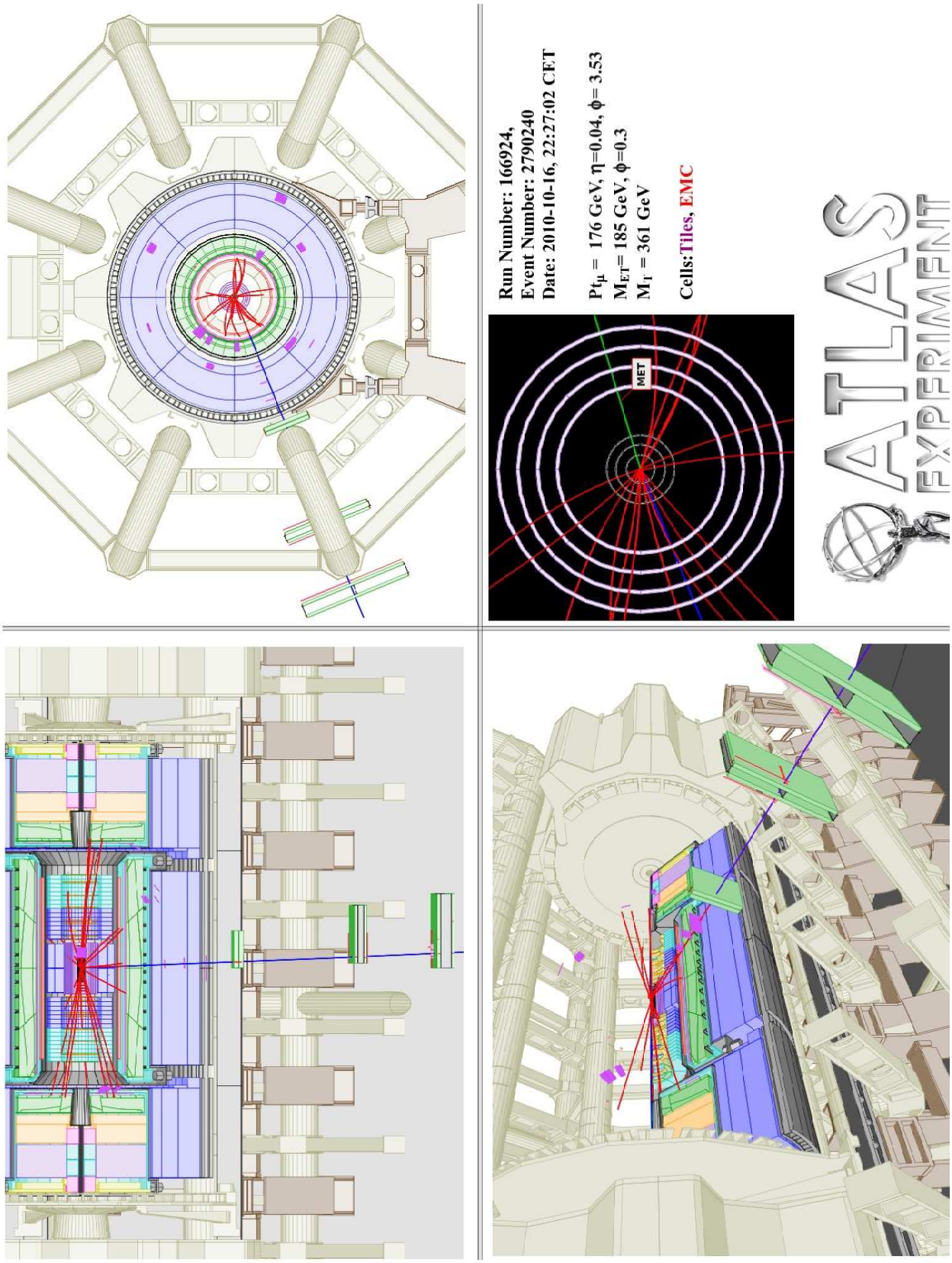

Figure 5.29: Event display of the event with the highest m_{T} (361 GeV) in 2010 dataset. Event passes all $W' \to \mu\nu$ selection criteria.

Bibliography

[1] S. Hassani, L. Chevalier, E. Lancon, J. F. Laporte, R. Nicolaidou and A. Ouraou, A muon identification and combined reconstruction procedure for the ATLAS detector at the LHC using the (MUONBOY,STACO, MuTag) reconstruction packages, Nucl. Instrum. Meth. A 572, 77 (2007).

[2] D. Adams et al., Track Reconstruction in the ATLAS Muon Spectrometer with Moore, ATLAS Internal Note, ATL-SOFT-2003-007 (2003).

[3] ATLAS Collaboration, Muons in the Calorimeters: Energy Loss Corrections and Muon Tagging, ATL-PHYS-PUB-2009-009 (part of CERN-OPEN-2008-020).

[4] ATLAS Collaboration, Measurement of Missing Tranverse Energy, ATL-PHYS-PUB-2009-016 (part of CERN-OPEN-2008-020).

[5] ATLAS Collaboration, Detector Level Jet Corrections ATL-PHYS-PUB-2009-013 (part of CERN-OPEN-2008-020).

[6] ATLAS Collaboration, Performance of the ATLAS Detector using First Collision Data, JHEP 09, 056 (2010).

[7] T. Sjostrand et al., JHEP 05, 026. 352 (2006).

[8] ATLAS Data Periods
`https://twiki.cern.ch/twiki/bin/view/AtlasProtected/DataPeriods`

[9] `https://twiki.cern.ch/twiki/bin/view/AtlasProtected/DataMCForAnalysis`

[10] `http://atlas-runquery.cern.ch/`

[11] M. Bahr et al., Eur. Phys. J. C58, 639707 (2008).

[12] S. Frixione et al., JHEP 08, 007.349 (2003)
S. Frixione et al., JHEP 06, 029 (2002).

[13] E. Boos et al. (CompHEP Collaboration), Nucl. Instr. Meth. A534, 250 (2004), hep-ph/0403113.

[14] P. Golonka and Z. Was, PHOTOS Monte Carlo: A Precision tool for QED corrections in Z and W decays, Eur. Phys. J. C45 (2006) 97107, hep-ph/0506026

[15] A. Sherstnev and R. S. Thorne, Parton Distributions for LO Generators, Eur. Phys. J. C55 (2008) 1296 553575, arXiv:hep-ph/0711.2473 [hep-ph].

[16] ATLAS Collaboration, ATLAS Monte Carlo tunes for MC09, ATL-PHYS-PUB-2010-002 `https://twiki.cern.ch/twiki/bin/view/AtlasProtected/McProductionCommonParameters09`

[17] J. Pumplin et al., JHEP 07, 012 (2002).

[18] J. M. Butterworth et al., Z. Phys. C72, 637646.357 (1996).

[19] P. M. Nadolsky et al., Implications of CTEQ global analysis for collider observables, Phys. Rev. D78 (2008).

[20] K. Melnikov, F. Petriello, Electroweak gauge boson production at hadron colliders through O(alpha(s)**2), Phys. Rev. **D74**, 114017, [hep-ph/0609070] (2006)

[21] R. Gavin, Y. Li, F. Petriello *et al.*, FEWZ 2.0: A code for hadronic Z production at next-to-next-to-leading order, [arXiv:1011.3540 [hep-ph]] (2010)

[22] J. M. Butterworth et al., Single and Diboson Production Cross Sections in pp collisions at $\sqrt{s}$ = 7 TeV, ATL-COM-PHYS-2010-695 (2010)

[23] U. Langenfeld, S. Moch, and P. Uwer. Measuring the running top-quark mass. Phys. Rev.,1849 D80:054009 (2009). `https://twiki.cern.ch/twiki/bin/view/AtlasProtected/TopMC2009.`

[24] ATLAS Collaboration, ATLAS Muon Momentum Resolution in the First Pass Reconstruction of the 2010 pp Collision Data at $\sqrt{s}$ =7 TeV, ATLAS-CONF-2011-046.

[25] D.L. Adams,...,D. Fassouliotis,...,C. Kourkoumelis,...,D.Popovic,..., N.Vranjes et al. Search for high-mass states with lepton plus missing transverse energy using the ATLAS Detector with 36 pb^{-1} of pp collisions at $\sqrt{s}$ = 7 TeV, ATL-COM-PHYS-2010-1073.

[26] Max Baak, LumiCalc. `https://atlas-datasummary.cern.ch/lumicalc/`

[27] https://twiki.cern.ch/twiki/bin/view/AtlasProtected/HowToCleanJets
See also ATLAS-CONF-2010-038.

[28] M. Cacciari, G.P. Salam, and G. Soyez, The anti-kT jet clustering algorithm, JHEP 04, 063 (2008).

[29] ATLAS Collaboration, Measurement of jet production in proton-proton collisions at 7 TeV centre-of-mass energy with the ATLAS Detector, ATLAS-CONF-2010-050 (2010).
E. Abat et al., Nucl. Instr. Meth. A621, 134 (2010).

[30] ATLAS Muon Combined Performance Group: Guidelines for Analysis in Release 15
https://twiki.cern.ch/twiki/bin/view/AtlasProtected/MCPAnalysisGuidelinesRel15

[31] ATLAS Collaboration, Lepton plus Missing Transverse Energy Signals at High Mass, ATL-PHYS-PUB-2009-071 (part of CERN-OPEN-2008-020).

[32] ATLAS Collaboration, ATLAS sensitivity prospects to W' and Z' at 7 TeV, ATL-PHYS-PUB-2010-007.

Chapter 6

Background Estimation, Corrections and Uncertainties

In this chapter the following items are addressed:

- estimation of the cosmics background and QCD background from data;
- theoretical corrections and related uncertainties for W/Z backgrounds;
- detector related corrections and uncertainties for signal selection efficiencies and background level.

After the cosmics and QCD backgrounds estimated, and all corrections applied and uncertainties properly evaluated, final results for $W' \to \mu\nu$ channel are presented.

6.1 Estimation of cosmic background

Cosmic rays background is suppressed by requiring the muons have small values of impact parameters: $|d_0| < 1$ mm and $|z_0| < 5$ mm. Since the reconstruction efficiency is flat or at least slowly-varying in the region immediately surrounding the selection, windows in the surrounding region are used to estimate the number cosmic events in the selection region.

Beside the cosmic background, events from SM backgrounds, particularly from heavy flavor decays, also have values of d_0 and z_0 in the surrounding region. Figure 6.1 shows the d_0 and z_0 distribution of events in data after muon selection (only one muon), then after isolation requirement and finally after $\not\!\!E_T > 25$GeV cut applied, but without any cut on impact parameters. The distributions demonstrate that isolation and then $\not\!\!E_T$ cut remove most of the events from $b\bar{b} \to \mu X$ and $c\bar{c} \to \mu X$ processes (cf. Fig5.4).

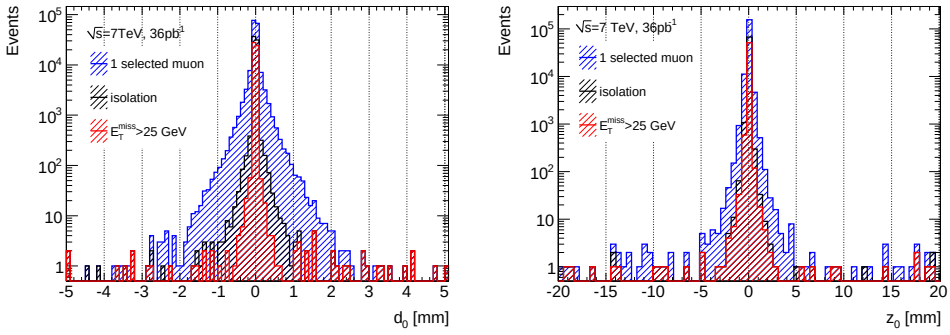

Figure 6.1: Distributions of d_0 and z_0 in data after muon selection, then after isolation requirement and finally after $\not{E}_T > 25$GeV cut applied. No cut is applied on impact parameters themselves.

Figure 6.2(a) shows the distribution of events in the r_0-z_0 plane with full $W' \to \mu\nu$ selection, except now the impact parameter cuts are reversed, i.e. muons are required to have $|d_0| > 1$ mm or $|z_0| > 5$ mm. Figure 6.2(b) shows the corresponding distributions for d_0 only. The excess of events near $d_0 = 0$, also seen in Monte Carlo, is primarily due to events with multiple vertices (pileup) where the muon comes from a vertex not identified as the primary. No such excess is observed z_0 distribution.

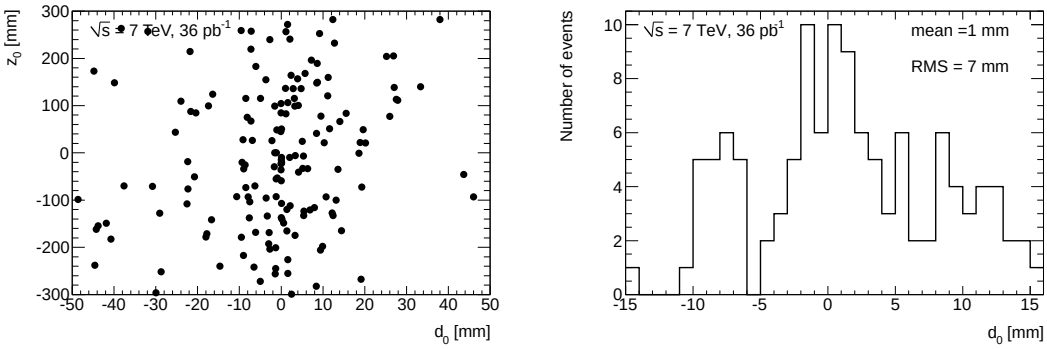

(a) (b)

Figure 6.2: (a) Distribution of z_0 vs. d_0 after all analysis cuts with inverted the impact parameter window. (b) Muon d_0 and distribution after all analysis cuts with inverted the impact parameter window.

Four r_0-z_0 regions are used to evaluate the expected cosmic background spectrum normalizing with the relative areas of the selection and evaluation regions. These estimates are summarized in table 6.1. The four results are consistent and the first, with the largest window, is used as the final estimate of the cosmic background, giving a total of 0.126 ± 0.018(stat) $\pm$ 0.034(syst) events. The largest deviation of the remaining three estimates is used to assign the

systematic uncertainty.

Table 6.1: Observed number of events in each cosmic evaluation region and the corresponding estimate for the number of cosmic background events in the $W' \to \mu\nu$ selection region.

Evaluation region	Evaluation	Selection
$2 < \|d_0\| < 15$ mm, $\|z_0\| < 150$ mm	46	0.126 ± 0.018
$5 < \|d_0\| < 15$ mm, $\|z_0\| < 150$ mm	35	0.125 ± 0.021
$2 < \|d_0\| < 15$ mm, $50 < \|z_0\| < 150$ mm	24	0.092 ± 0.019
$5 < \|d_0\| < 15$ mm, $50 < \|z_0\| < 150$ mm	24	0.120 ± 0.032

The transverse mass distribution of the background estimate is shown in Figure 6.3. The estimated number of events in each of the mass bins used to set the $W' \to \mu\nu$ limits are presented in Table 6.2. These numbers are small compared to the other backgrounds and the cosmic contamination is neglected in the final limit calculations.

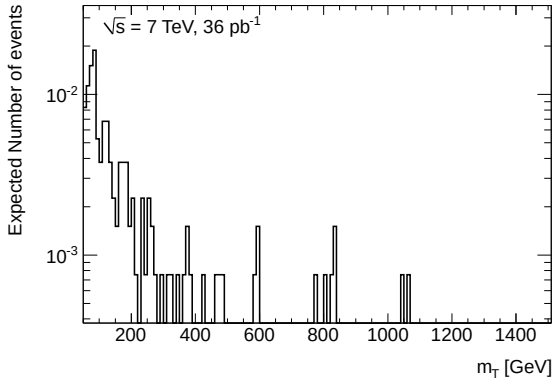

Figure 6.3: Distribution of transverse mass distribution for the events that satisfy all selection criteria except the impact parameter requirements.

Table 6.2: Expected number of cosmic background events above the m_{T} thresholds.

m_{Tmin} [GeV]	Expected Events
250	0.022 ± 0.007
750	0.013 ± 0.005
500	0.008 ± 0.004
625	0.006 ± 0.003
750	0.006 ± 0.003
875	0.002 ± 0.002

6.2 Estimation of QCD background

As stated before, theoretical cross section for QCD production has large uncertainty, and this quantity has not yet been measured in data with sufficient precision. Also, in spite of large statistics of MC multijet events, only a small fraction of these events pass the selection requirements. As can be observed from the Fig5.6.2, large statistical fluctuations are present in the histograms obtained from QCD MC samples, and there are no entries in the search region at very high-m_{T}.

This is the reason why QCD background is estimated from the data, as described bellow. The sensitivity of the data-driven estimate to the signal region is not so good, since the upper limit is comparable to the total background from other processes in the highest m_{T} bins. An extrapolation is performed to obtain a more precise estimate in the high-m_{T} region.

6.2.1 The method

Events from QCD processes pass selection criteria if there is a fake lepton in the event, or a real lepton from a heavy flavor quark decay. In the same event, there must be significant $\not{E}_T$ originating from the detector resolution or heavy flavor quark decay. The rate at which fake leptons are reconstructed are difficult to model reliably in Monte Carlo.

The QCD background is estimated by selecting a data sample with the same muon selection requirements as described in section 5.4, but with lepton isolation $0.2 < \sum p_T/p_T < 0.4$. Table6.3 shows number of observed events in data and expected number of events from $W \to \ell\nu$, $Z \to \ell\ell$, $t\bar{t}$ and diboson processes in the sample selected in this way. Contribution from non-dijet production is estimated to be less then one %, and from now on this sample will be referred to as "QCD-rich" sample. The sample with standard selection (i.e. isolation $\sum p_T/p_T < 0.05$) will be referred to as signal sample.

Table 6.3: Observed and expected number of events passing muon selection requirements and muon isolation requirement $0.2 < \sum p_T/p_T < 0.4$

source	Data	SM back.	$W \to \ell\nu$	$Z \to \ell\ell$	$t\bar{t}$	diboson
Numb. of events	26457	189.32	153.11	21.06	14.31	0.85

The events in QCD-rich sample are assumed to have kinematic distributions similar to the QCD contribution in the signal sample. $\not{E}_T$ distribution of these events is used as a template which is then combined with events from simulated W/Z, $t\bar{t}$ and diboson samples into one

reference distribution:

$$h_{ref} = C_1(W+Z+t\bar{t}+diboson)^{iso.} + C_2(template-(W+Z+t\bar{t}+diboson)^{noniso.}) \quad (6.1)$$

Label *iso* denotes simulated events passing standard isolation cut $\sum p_T/p_T < 0.05$, while *noniso* events passing inverted isolation cut $0.2 < \sum p_T/p_T < 0.4$. As can be seen from Table5.14 and Fig5.6.2 there is a discrepancy between data and MC expectations in the region $\not\!\!E_T >$ 25GeV. In order not to be biased in estimation of QCD from data due to this discrepancy, factor C_1 is introduced in order to make reference distribution agree with data in the region where W/Z, $t\bar{t}$ and diboson processes dominate (around $\not\!\!E_T$ peak). Factor C_2 is the scaling factor for the QCD sample.

A two-parameter binned maximum likelihood method is used to compare the data distribution in the signal sample to the reference distribution h_{ref}, and obtain C_1 and C_2. The observed number of events in each bin i of the $\not\!\!E_T$ distribution (n_i), can be described in terms of expected number of events in the bin s_i (from the reference distribution) using a Poisson probability:

$$P_i(n_i) = \frac{e^{-(s_i)}s_i^{n_i}}{n_i!} \quad (6.2)$$

The joint probability of all $\not\!\!E_T$ bins (assuming they are uncorrelated) is then:

$$P = \prod_i P_i \quad (6.3)$$

The log likelihood function of the joint probability is defined as:

$$\mathscr{L} = -\log P = -\sum_i [n_i \log(s_i) - s_i], \quad (6.4)$$

where the constant term $-\sum log(n!)$ is omitted. The best set of parameters C_1 and C_2 is obtained by minimizing the likelihood function 6.4. The procedure is performed on the $\not\!\!E_T$ distribution in range 0 GeV $< \not\!\!E_T <$ 100GeV, with 1GeV per bin. Only statistical contribution is considered for the calculation of the likelihood function. Obtained values of best parameters C_1 and C_2 are:

$$C_1 = 0.8548,\ C_2 = 0.2966.$$

Log likelihoods as a function of parameters C_1 and C_2 are shown in Fig6.4. The resulting $\not\!\!E_T$ distribution is shown in Fig6.5(a).

Subsequently the fraction of QCD events in the region with $\not\!\!E_T > 25$ GeV is determined.

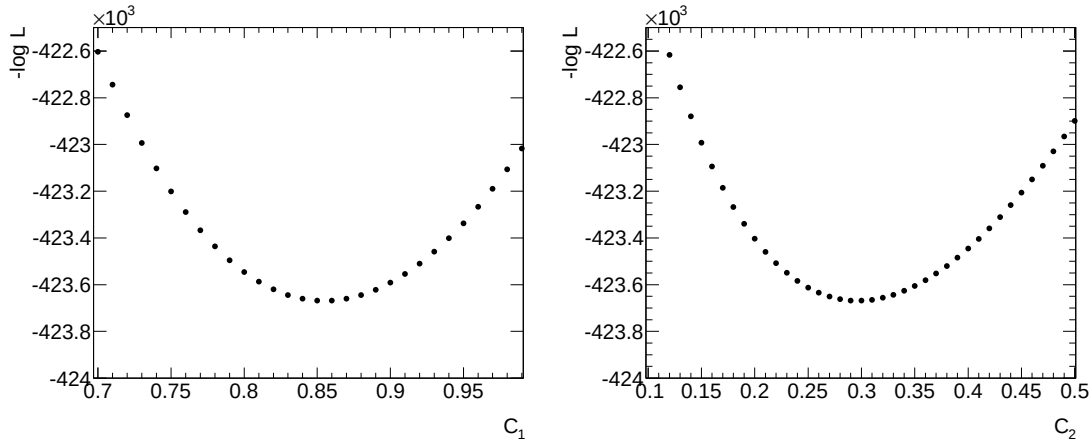

Figure 6.4: Negative log likelihoods as a function of parameters C_1 (left), and C_2 (right). The values of the likelihoods for each parameter are obtained while keeping the other one fixed. Only statistical contribution is considered.

isolation	C_1	C_2	N_{QCD}	fraction (%)
$0.10 < \sum p_T/p_T < 0.30$	0.861	0.302	603.25	1.16
$0.12 < \sum p_T/p_T < 0.32$	0.859	0.301	638.35	1.19
$0.14 < \sum p_T/p_T < 0.34$	0.857	0.295	638.35	1.23
$0.16 < \sum p_T/p_T < 0.36$	0.856	0.294	657.79	1.26
$0.18 < \sum p_T/p_T < 0.38$	0.856	0.295	675.85	1.30
$0.20 < \sum p_T/p_T < 0.40$	0.854	0.296	690.04	1.32
$0.22 < \sum p_T/p_T < 0.42$	0.854	0.302	714.25	1.37
$0.24 < \sum p_T/p_T < 0.44$	0.853	0.308	740.28	1.42
$0.26 < \sum p_T/p_T < 0.46$	0.853	0.315	736.56	1.47
$0.28 < \sum p_T/p_T < 0.48$	0.852	0.323	788.54	1.51
$0.30 < \sum p_T/p_T < 0.50$	0.851	0.334	822.30	1.58

Table 6.4: Number of estimated events from QCD passing $\not\!\!E_T > 25$GeV and their fraction in the total number of events for different isolation windows (first column).

The procedure described above yields 690.04 QCD events in this region. Since there are 52096 events in total, the fraction of QCD events with $\not\!\!E_T > 25$ GeV is estimated to be 1.3%. This is in perfect agreement with $1.3^{+0.3}_{-0.1}$ % reported in [11]. Result presented here has been corrected for contamination of events from other SM processes in the QCD side-band sample (estimated to be about 7% in total).

Uncertainties related to QCD estimation from data have been derived by varying the selection of the QCD background sample. Uncertainty that would come from range of $\not\!\!E_T$ distribution used to calculate likelihood function has been found to be negligible. Also, the size of the bin has no impact on the final result. To evaluate uncertainty, selection window is varied from

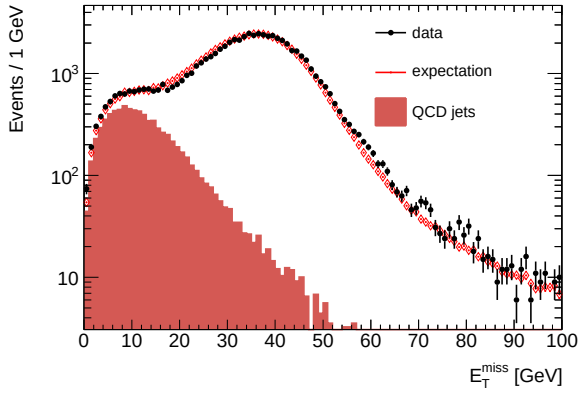

(a)

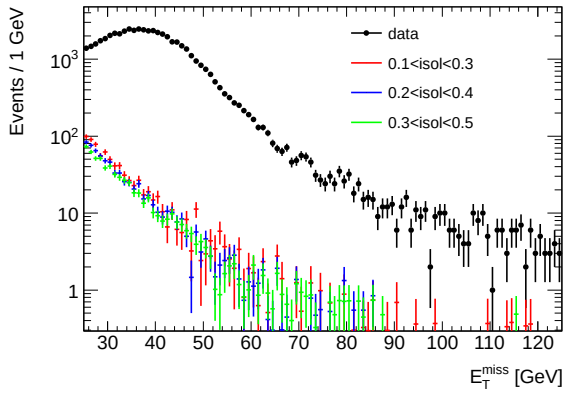

(b)

Figure 6.5: (a) $\not\!\!E_T$ distribution generated from data points and reference distribution as defined in 6.1 with C_1 =0.8548 and C_2 =0.2966. Estimated QCD contribution is shown separately. (b) $\not\!\!E_T$ distribution in data overlaid with QCD distributions obtained from three different sidebands as indicated on the legend.

$0.1 < \sum p_T/p_T < 0.3$ to $0.3 < \sum p_T/p_T < 0.5$ in steps of 0.02 as summarised in Table6.4. The variation of the QCD fraction in the data sample goes in range 1.15% to 1.58%. This confirms final results obtained in [11]. Figure6.5(b) shows the overlaid distributions of $\not\!\!E_T$ for data points and QCD contribution for three different sidebands. For m_{T} distribution, the highest positive entry is just below $m_{\mathrm{T}} = 250$ GeV and corresponds to 0.3 ± 0.3 events. From this, a conservative estimate of the background for any m_{T} range above this point would range from zero to around 0.3 events. However, this upper limit is comparable to the total background from other sources, and so an extrapolation is performed to obtain a more precise estimate in the high-m_{T} range.

6.2.2 Extrapolation to high m_{T}

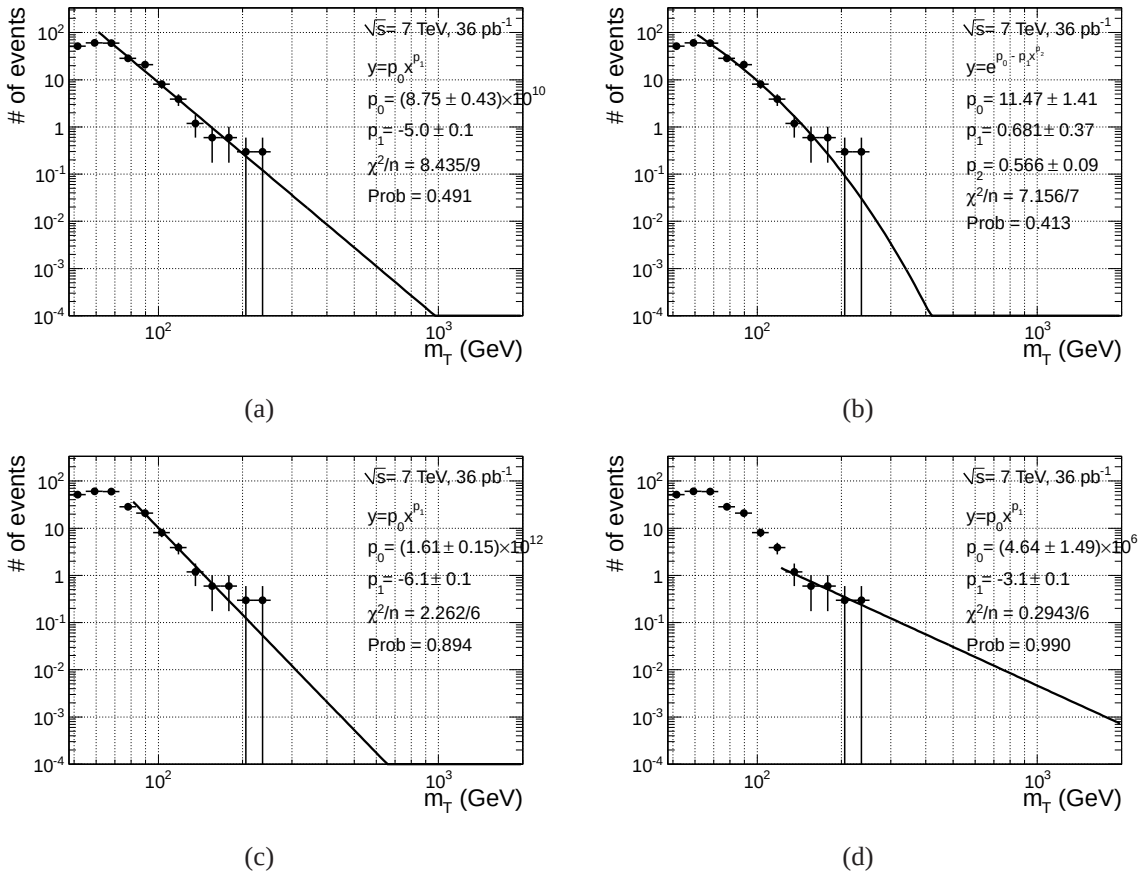

Figure 6.6: Fit of the shape of estimated QCD background with a power low (a) and a modified exponential function (b)(equation 6.5), both fitted for $m_{\mathrm{T}} > 60$ GeV. Power law function is also fitted for $m_{\mathrm{T}} > 80$ GeV (c) and $m_{\mathrm{T}} > 120$ GeV (d).

To estimate the QCD background in the high-m_T region several fits of experimental data are performed. The fits are performed on the m_{T} distribution obtained from QCD-reach sample as described in the previous subsection. The distribution is normalized to the number of events corresponding to 1.3% of the data from the signal sample. The expected contamination from other SM processes is estimated to be about 7% which is taken to have small effect, and no attempt has been made to do background subtraction.

First, two different functions are used to fit the data in range $m_{\mathrm{T}} > 60$ GeV, a power law, and a form of exponential function combined with a power law:

$$y = p_0 x^{p_1}, \quad y = e^{p_0 - p_1 x^{p_2}}. \tag{6.5}$$

The resulting fits are shown in Fig6.6 (a) and (b). Number of QCD background events for

the different values of m_{T} threshold obtained using the fits, are shown in the second and third column of the Table6.5. Because of the shape of the fitted m_{T} distribution, neither of the two functions can perform satisfactory fit for the lower range $m_{\mathrm{T}} < 50$ GeV. Both functions fit the data well, but exponential predicts less events in the high-m_{T} tail with respect to the power law function. In order to be conservative, QCD background is estimated using power law function. Further, examining the m_{T} spectrum, there is an indication that the shape of m_{T} distribution is changing once again above 80 GeV (available statistics is small, though). Thus, the fit starting at 60 GeV would underestimate the tail, so two different ranges are fitted as well, $m_{\mathrm{T}} > 80$ GeV, and $m_{\mathrm{T}} > 120$ GeV. The results are shown in Fig6.6 (c) and (d), and the last two columns of Table 6.5. The lower-m_{T}points suggest the result would be far from any reasonable expectation. A lower threshold would give a lower level and a a lower absolute uncertainty on that level. The final choice is to choose the fitting range $m_{\mathrm{T}} > 120$ GeV, which is felt to be the most conservative, reasonable one. It should be noted that the level of QCD background might be overestimated, and actually improves the observed limit a little bit in the lower mass range, with no effect for the higher masses.

Table 6.5: Estimated number of QCD background events for a serie of m_{T} thresholds, obtained from the fits described in the text.

	$y = e^{p_0 - p_1 x^{p_2}}$	$y = p_0 x^{p_1}$		
m_{Tmin} [GeV]	$m_T > 60$ GeV	$m_T > 60$ GeV	$m_T > 80$ GeV	$m_T > 120$ GeV
250	0.00379015	0.127363	0.04301629	$0.393819^{+0.360091}_{-0.209505}$
375	0.00007636	0.016606	0.00355000	$0.110670^{+0.106642}_{-0.0601852}$
500	0.00000258	0.003980	0.00061544	$0.0454955^{+0.0454254}_{-0.0251075}$
625	0.00000012	0.001236	0.00014859	$0.0214423^{+0.021996}_{-0.0119646}$
750	0.00000007	0.000516	0.00005069	$0.0124051^{+0.0129845}_{-0.00697871}$
875	0.00000001	0.000212	0.00001747	$0.0067751^{+0.0072196}_{-0.00383891}$

Uncertainty of this estimation is obtained by changing function parameters p_0, p_1 by their errors. Resulting uncertainties are presented in the last column of the above Table.

The results obtained here are close to the ones reported in [11]. However, estimated QCD background even with maximized error represents only a small fraction of the whole SM background, at the level of 4% at most (cf. Table5.14). Although relative error of the QCD background is large ($\sim$100%), it is much smaller compared to other systematic uncertainties of the SM background. These uncertainties will be described and evaluated in the next sections.

Future analysis will certainly benefit from increased statistics, providing a more solid extrapolation to high-m_{T} region of interest.

6.3 Theoretical corrections and uncertainties

Cross sections and related uncertainties for W' and W^* signal processes are described in the first chapter. W/Z background samples, as well as $t\bar{t}$ sample, are normalized to Next-to-next-to-leading order (NNLO) QCD cross section using a K-factors[1] which are taken to be uniform with respect to true invariant/transverse mass. This is described in 5.2.2, mentioning that the raw background level from W/Z processes in the high-m_{T} bins is significantly overestimated due to the different mass dependence of the cross section at leading and higher orders. In this section, W/Z background m_{T}-dependent higher order QCD corrections, as well as corrections due to Electroweak contributions, are evaluated together with proper systematic uncertainties.

6.3.1 Higher order QCD corrections and uncertainties

The Monte Carlo estimates for W/Z background levels are based on NNLO cross sections computed using `FEWZ` generator [2, 3]. On the other side, the shapes of the distributions come from `Pythia`, which is used to obtain selection efficiencies. Beside total, `FEWZ` generator allows also calculation of QCD differential distributions with the same accuracy. However, the current version of `FEWZ` is not optimized for events with invariant masses far away from W mass [4]. It appears that `Vegas` routine is not adapting the grid correctly for the values of high mass, and it is expected this problem is fixed in a new version of the program[2].

In order to estimate mass dependent K factors, and consequently, corrections to be applied to the estimated background level from Table5.14, a NLO generator should be used. One estimation is done using `MCFM` generator[5], as described in [11]. In this thesis, an independent estimate is performed using `MC@NLO` program[6], with the similar methodology as in the supporting note.

The procedure to obtain correction factors is as follows. Rather than weighting each event by the correction factor, a constant value for a particular m_{T}-threshold is obtained. Defining the K to be the ratio of NLO to `Pythia` cross section, the correction factor for the level of $W \to \ell\nu$ background $C^{W\to\ell\nu}_{\sigma,QCD}$ is defined as:

$$C^{W\to\ell\nu}_{\sigma,QCD} = K(m_{\mathrm{Tmin}})/K(m_W), \tag{6.6}$$

[1] The ratio of the higher order and leading order cross section is usually called K-factor. In principle K-factors are a function of the mass, rapidity, transverse momentum etc. of the produced particles and their decay products.

[2] This problem is not affecting estimation of W' NNLO QCD cross section, as described in section 3.3, since mass of W is set to W' mass in the program. It is probable that for higher masses of W' cross section is underestimated a bit due to off-shell production of the new heavy gauge boson. This will have to be verified with new version of `FEWZ`.

where $K(m)$ is the factor for the whole assessable mass range ($0 < m < 7000$ GeV), and $K(m_{\mathrm{Tmin}})$ is the K-factor calculated for a particular m_{T} threshold. It is fair to assume that correction factor that would be obtained with appropriate NNLO generator, be similar and there are no large differences in shapes of distributions between NNLO and NLO. The result of this procedure are not "absolute" K-factors that should be applied to the LO cross section, but correction factors to be applied to a NNLO cross section to account for different mass dependence of the cross section at leading and higher orders.

For the purpose of this analysis standalone `MC@NLO` code, version 3.1 is used. SM $W \to e\nu$ process is generated in several mass bins listed in Table6.6. For the input parameters, standard values from `MC09` production are used: $m_W = 80.403$ GeV, $\Gamma_W = 2.141$ GeV, $m_Z = 91.1876$ GeV, $\Gamma_Z = 2.4952$ GeV, $m_t = 172.5$ GeV. The other parameters can be found in [7]. Renormalization (μ_R) and factorization (μ_F) scales are set to be equal to the so-called reference scale ($\mu_R = \mu_F = \mu_0$), fixed in `MC@NLO` to:

$$\mu_0 = \sqrt{m_T^2(W^+) + m_T^2(W^-)}. \tag{6.7}$$

This basically sets renormalization scale to be equal (or very close) to the dynamic scale defined in [11] as the invariant mass of the lepton-neutrino system[3]. The value of the cross section beside choice of the renormalization scale depends also on the choice of the PDF, and K-factors are obtained with two different PDFs: `CTEQ66`, and `MRST2004nlo` (central value). For the K-factor calculation, rather then passing events through `Jimmy/Herwig` within `Athena` for the hadronization and fragmentation, and simulating m_{T} distribution, a fraction of events from each mass bin failing above each m_{T} threshold is used. These fractions are obtained from `Pythia` simulated samples.

Obtained cross sections are presented in Table6.6, and compared with `Pythia` results shown in the last column. Comparing cross section obtained with `MC@NLO` (`CTEQ66`) to the `Pythia` values, one can observe the K-factors change from $K(m_W) = 1.066$ for the whole mass range (but basically completely dominated by the W peak at $\sim$ 80GeV), to $K(m_W) = 0.85$ for the mass bin centered at 2.25 TeV. Further the differences in NLO cross section obtained with two different PDF sets are ranging from 0.3% at the W peak, to about 11% for very high mass. This is consistent with the result obtained for the signal processes.

The final results are obtained using `CTEQ66` as a central value. To evaluate systematic uncertainties arising from the choice of scale, results are obtained by setting renormalization scale

[3] `MC@NLO` basically doesn't have the feature as `MCFM` to set scales dynamically. This effect could be obtained by making mass bins smaller, but this is not worth the effort at this level of precision of the analysis.

Table 6.6: Cross sections for W boson production obtained with MC@NLO (NLO) with two different PDF sets, and with Pythia (LO) with MC09 default PDF.

Mass bin $[GeV]$	CTEQ66 σ_{NLO} [pb]	MRST2004nlo σ_{NLO} [pb]	MRST2007lomod σ_{LO} [pb]
0-7000	9534	9573	8940
200-500	3.291	3.344	2.961
500-750	0.0727	0.07569	0.06778
750-1000	0.010605	0.011083	0.010289
1000-1250	0.0022555	0.0023858	0.0022272
1250-1500	0.0005784	0.0006195	0.0006183
1500-2000	0.0002151	0.0002349	0.0002382
2000-2500	0.000020552	0.000023592	0.000024366

to be double or half of the reference scale. Further, to estimate PDF-related systematics, cross sections are computed varying CTEQ66 withing 44 eigenvector sets at the 90% C.L. limit, and calculating asymmetric deviation as for the signal:

$$\Delta\sigma^{+} = \sqrt{\sum_{i}[max(\sigma_i^{+} - \sigma_0, \sigma_i^{-} - \sigma_0, 0)]^2} \tag{6.8}$$

$$\Delta\sigma^{-} = \sqrt{\sum_{i}[max(\sigma_0 - \sigma_i^{+}, \sigma_0 - \sigma_i^{-}, 0)]^2} \tag{6.9}$$

The difference between cross sections obtained with CTEQ66 and MRST2004nlo central values is added in quadrature to the other sources of systematic in order to obtain final uncertainty on the K-factors. These results are presented in Table 6.7

Table 6.7: Systematic uncertainties for W NLO cross section arising from the choice of scale and PDF set.

Mass bin [GeV]	200-500	500-750	750-1000	1000-1250	1250-1500	1500-2000	2000-2500
Scale uncertainty							
$\mu_R = 2\mu_F$	-0.6%	-2.1%	-2.8%	-3.4%	-4.0%	-4.7%	-5.7%
$\mu_R = 0.5\mu_F$	+1.0%	+2.2%	+2.8%	+3.3%	+3.8%	+4.5%	+5.5%
PDF uncertainty							
asymmetric $\Delta\sigma^{+}$	$+3.1\%$	$+4.7\%$	$+5.8\%$	$+6.4\%$	$+8.3\%$	$+10.5\%$	$+16.6\%$
asymmetric $\Delta\sigma^{-}$	-3.3%	-4.9%	-6.2%	-8.0%	-8.4%	-10.0%	-14.3%
$CTEQ/MRST - 1$	-1.6%	-4.1%	-4.5%	-5.7%	-7.1%	-9.2%	-11.4%
Overall unc.	$\pm3.8\%$	$\pm6.8\%$	$\pm8.2\%$	$\pm10.4\%$	$\pm11.7\%$	$\pm14.7\%$	$\pm20.9\%$

K-factors as a function of the mass range are presented in Fig6.7, while in Fig6.8 K factors

are given as a function of the m_{T}-threshold. On both figures overall systematic uncertainty is presented. The uncertainty is dominated by the PDF uncertainty.

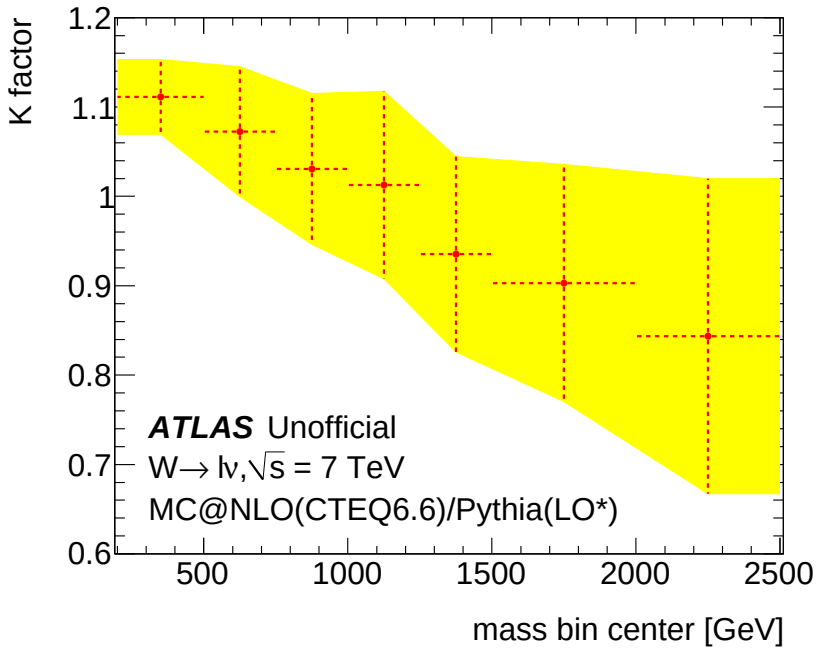

Figure 6.7: K-factors for W boson production as function of the mass bins used to calculate cross sections. Shaded area represents systematic uncertainty described in the text.

Final K-factors and correction factors with evaluated uncertainties are presented in Table 6.8. Although results are obtained for $W \to e\nu$ process, the same correction factors are applied to the $W \to \mu\nu$, although some differences may arise from the fact that muon channel is constrained to $|\eta|$ <1.05. It is assumed however, that at this level of precision, there is no need to investigate these differences. Also, the same correction factors are applied to the $Z \to \ell\ell$ since production mechanism and K-factors should be similar to the $W \to \ell\nu$ process.

Table 6.8: K-factors and correction above the m_{T} thresholds.

m_{Tmin} [GeV]	$K(m_{\mathrm{Tmin}})$	$C^{W\to\ell\nu}_{\sigma,QCD}$
250	1.106	$1.038 \pm 3.8\%$
750	1.090	$1.023 \pm 5.3\%$
500	1.059	$0.993 \pm 6.8\%$
625	1.040	$0.976 \pm 8.6\%$
750	1.012	$0.950 \pm 10.4\%$
875	0.995	$0.933 \pm 10.6\%$

Results presented in the third column of the Table 6.8 agree within the errors with the results

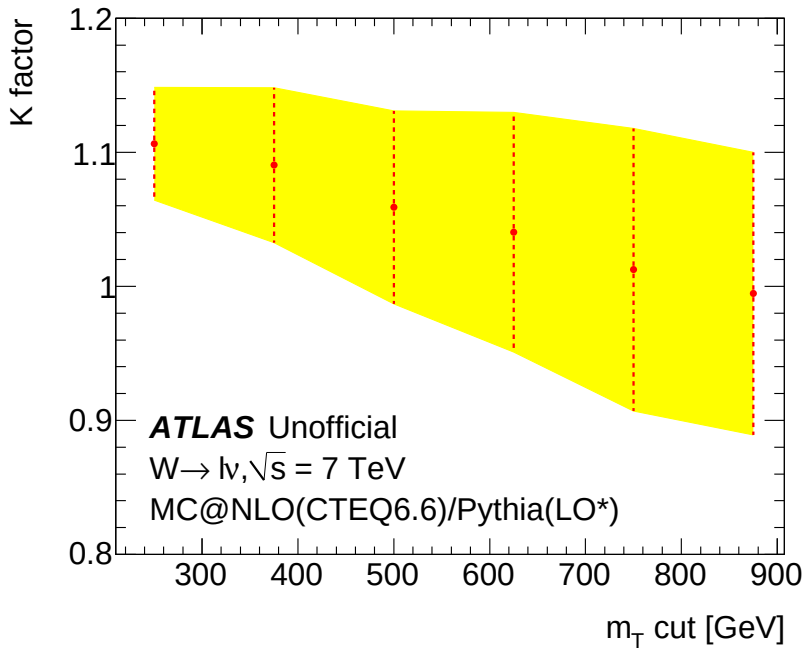

Figure 6.8: K-factors for W boson production as function of the m_{T}-threshold used to calculate cross sections. Shaded area represents systematic uncertainty described in the text.

presented in Table 9 of the 2010 analysis supporting note[11]. For the study described in the supporting note, correction factors are obtained by averaging results obtained with two different PDF sets `CTEQ66` and `MSTW2008nlo68cl`. This confirms that the results of the predicted W (and Z) cross section at high mass has large theoretical uncertainty, mainly due to limited knowledge of the proton PDF at such high x. In future these estimation will certainly benefit from the measurement of the high-m_{T} and high-$m_{\ell\ell}$ spectrum at the LHC.

6.3.2 Electroweak corrections and uncertainties

The $\mathscr{O}(\alpha)$ electroweak (EW) radiative corrections has been computed in the charged current channel (aka Wproduction) with the results presented in several papers [8]. It has been shown that $\mathscr{O}(\alpha)$ EW contributions give large corrections to the tails of the transverse mass and lepton transverse momentum distributions, because of the presence of large EW Sudakov logarithms. Thus, in addition to higher order QCD corrections, electroweak corrections to the $W \to \ell\nu$ cross sections need to be considered.

The electroweak corrections include contributions from final state photon radiation, electroweak loop corrections (”pure weak corrections”) and processes with initial photons which are part of the proton structure. Since in MC samples final state photon radiation (real QED emission) is accurately simulated using `Photos` [9] and a full detector simulation, this contri-

bution is excluded from an additional electroweak correction factor.

The electroweak corrections are evaluated using the Horace event generator, version 3.1 [10]. The same input parameters are used as in mentioned reference, with kinematic cuts applied $p_T^\ell > 25\,\text{GeV}$, $p_T^\nu > 25\,\text{GeV}$, and $|\eta_e| < 2.4$, or $|\eta_\mu| < 1.05$, for $W \to e\nu$ and $W \to \mu\nu$ respectively. For EW corrections (contrary to the previous subsection) different lepton kinematic selections used for two channels are taken into account. MRST2004QED PDF set [11] is used.

Correction factor is defined as a function of $\ell\nu$ invariant mass as the ratio of the differential cross section prediction including the exact $\mathcal{O}(\alpha)$ calculation matched with higher order contributions over the prediction including only final state QED radiation in the parton shower approximation. As for higher order QCD corrections, EW correction factors are obtained by integrated above m_T threshold for each mass bin:

$$C_{\sigma,EW}^{W\to\ell\nu} = \int_{m_\text{T}}^{\infty} \frac{\text{d}\sigma^{EW}}{\text{d}m_\text{T}}\text{d}m_\text{T} \Big/ \int_{m_\text{T}}^{\infty} \frac{\text{d}\sigma^{noEW}}{\text{d}m_\text{T}}\text{d}m_\text{T} \tag{6.10}$$

The corrections are not applied event by event, but as constant factors above particular threshold. The results are shown in Fig6.9 for electron and muon final states, respectively.

In contrast to neutral current Drell-Yan production [12], for the charged current process the additional contribution from processes involving initial photons are small. Using the MRST2004QED PDF set, this contribution is estimated to be below 1% for m_T<3 TeV.

The electroweak loop corrections are only partly canceled by the radiation of real W and Z bosons off the final state leptons. It is estimated that these contribution are at the level of one % [11], which is consistent with the fact that events with additional leptons in the event are vetoed.

The systematic uncertainty on the electroweak corrections is estimated to be 3% for all mass range. This takes into account uncertainties in the calculation of real boson radiation (1%) potential contributions from initial photons (1%), $\mathcal{O}(\alpha\alpha_s)$ corrections (1%) [10], and higher order electroweak corrections (1.5%) [13]. As the correction factor is defined with respect to the predicted cross section including FSR QED contributions, an additional uncertainty may arise if these contributions modify the total integrated W cross section. Since the so-called G_μ electroweak scheme is used to calculate the NNLO QCD cross section predictions, which minimizes the correction at low masses [14], this additional uncertainty can be neglected for W production. The final EW corrections and associated uncertainties are presented in Table 6.9. Since the results for the electron and muon channel are comparable, common correction factors are used for both channels.

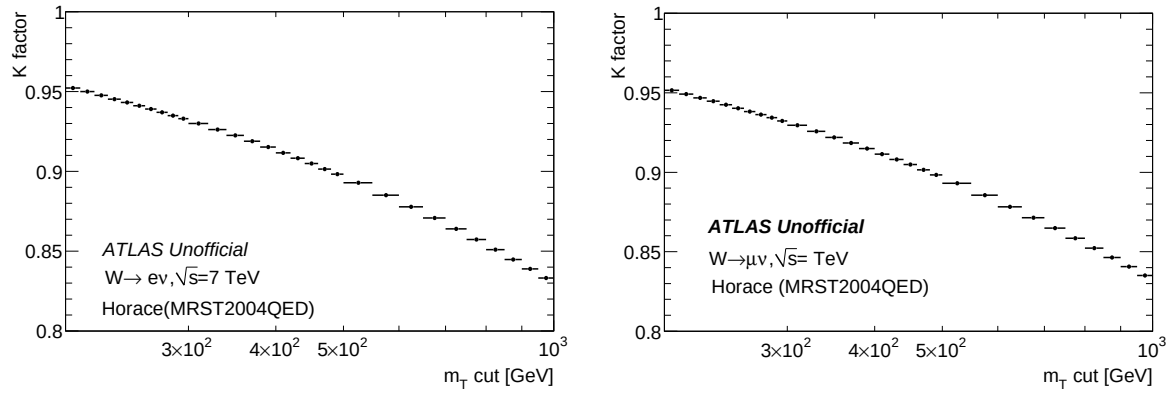

(a) (b)

Figure 6.9: The $\mathcal{O}(\alpha)$ electroweak radiative correction factors for $W \to e\nu$ (a), and $W \to \mu\nu$ (b) processes as a function of the m_{T} threshold.

6.3.3 Combination

Table 6.9 lists, for each value of m_{T} threshold, higher order QCD correction, electroweak correction, and the overall theoretical correction which is the product of the two:

$$C_{\sigma,th}^{W\to\ell\nu} = C_{\sigma,QCD}^{W\to\ell\nu} \times C_{\sigma,EW}^{W\to\ell\nu} \tag{6.11}$$

The corrections are derived for $W \to \ell\nu$, but are used for all W/Z processes. For $t\bar{t}$ and diboson processes no additional corrections are imposed since these backgrounds make only about 10% of the total background. A conservative uncertainty of 9.5% is assigned to $t\bar{t}$ cross section.

Table 6.9: W/Z corrections. The results in the last column are the overall cross section correction factors with systematic uncertainties explained in the text.

m_{Tmin} $[GeV]$	$C_{\sigma,QCD}^{W\to\ell\nu}$	$C_{\sigma,EW}^{W\to\ell\nu}$	$C_{\sigma,th}^{W\to\ell\nu}$
250	$1.038 \pm 3.8\%$	$0.954 \pm 3.0\%$	$0.990 \pm 4.8\%$
375	$1.023 \pm 5.3\%$	$0.937 \pm 3.0\%$	$0.958 \pm 6.1\%$
500	$0.993 \pm 6.8\%$	$0.918 \pm 3.0\%$	$0.912 \pm 7.4\%$
625	$0.976 \pm 8.6\%$	$0.901 \pm 3.0\%$	$0.879 \pm 9.1\%$
750	$0.950 \pm 10.4\%$	$0.889 \pm 3.0\%$	$0.844 \pm 10.8\%$
875	$0.933 \pm 10.6\%$	$0.875 \pm 3.0\%$	$0.816 \pm 11.0\%$

6.4 Detector related corrections and uncertainties

Detector related corrections and associated uncertainties are presented in this section. Unless stated otherwise, the details about the estimation of the muon and $\not{E}_T$ corrections and uncertainties are presented in 2010 supporting note[11].

Luminosity. Accurate determination of the luminosity delivered to ATLAS is needed for calculation of the limits, since majority of the background (except QCD) is determined using theoretical cross sections. As stated in section 5.2.1 the data in $W' \to \mu\nu$ search correspond to the integrated luminosity of 36.4pb^{-1} . The uncertainty on the value of absolute luminosity has been determined and publicly available[15] when this analysis was performed. The uncertainty has been estimated to be $\pm$11%, and was dominated by the determination of the so-called bunch charge product (number of protons in a bunch, N_b, equation 5.2), which was $\pm$10%. After W' analysis with 2010 data has been finalized, ATLAS has published an update of the estimation of the integrated luminosity[16]. Due to improvement in bunch charge product determination, the central value of the ATLAS luminosity scale is found to be 3.6% lower than the previous result, while the uncertainty on the luminosity scale determined to be $\pm$3.4%. Since uncertainty on the luminosity is one of the dominant uncertainties, and in order to stay consistent with ATLAS published result, the uncertainty of the luminosity in this thesis is kept at the level of $\pm$11%, with unchanged central value of 36.4pb^{-1} .

Trigger efficiency. The determination of the muon trigger efficiency is performed relative to reconstruction and it is found to be higher then the measured by the muon trigger slice group. This is explained by the fact that W' muon identification requires MDT hits in all three stations and an RPC hit in at least two of the three doublet layers. Two independent measurements are made: one using $Z \to \mu\mu$ data collected with muon trigger, and the other with events collected with an orthogonal jet trigger. The two results are found to be consistent with each other, and the final correction factor with associated uncertainty is:

$$C^{\mu}_{trig} = \varepsilon_{data}/\varepsilon_{MC} = 0.969 \pm 0.007. \tag{6.12}$$

This is a correction factor for both the signal and background event selection efficiency.

Muon reconstruction and isolation efficiency. Muon reconstruction, identification and isolation efficiencies are measured from data using famous tag& probe technique. The results are found to be consistent between data and MC, thus no correction is applied to MC.

For high-p_T muons, with momentum in excess of 100 GeV, additional loss of efficiency is expected due to radiative effects. This degradation is observed in Monte Carlo by comparing reconstruction efficiency for muons from W' with those from the standard model W. To account

for the possibility that the Monte Carlo might underestimate this effect, systematic uncertainty equal to this degradation is assigned:

$$R(p_T) = 1 - \frac{\varepsilon^{\mu}_{W',reco}(p_T)}{\varepsilon^{\mu}_{W',reco}(p_T = 0)}. \tag{6.13}$$

Pseudorapidity of muons from W' decays changes with mass of W' in a way that muons are produced in more central region with increase of the mass. As a consequence, efficiency losses are partly caused from the migration of the muons to the poorly covered region of the muon spectrometer at $|\eta| \sim 0$. In order to separate efficiency degradation caused by radiative effects from the loss due to acceptance, parametrization of the muon reconstruction efficiency as function of its momentum is performed in the range $0.1 < |\eta| < 1.05$. Parametrization of the efficiency is done with simple linear function with slope -2.6(4)%/TeV, and the result is shown in Fig 6.10. The main cause in the drop in efficiency of combined muon is due to requirement of at least 3 hits in the muon spectrometer. This requirement, however, does not change the slope of the linear function. The efficiency drop as a function of p_T is then convoluted with the muon p_T distribution for each signal hypothesis. The results of the evaluation of the muon reconstruction uncertainty for different mass points (different values of the m_{T} threshold) for W', W^*, and background are presented in Tables 6.12, 6.13 and 6.14 respectively.

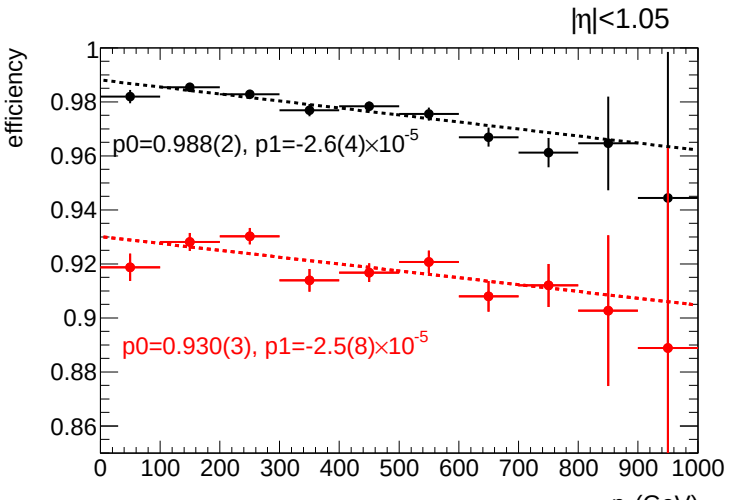

Figure 6.10: Reconstruction efficiency as a function of muon p_T. Upper curve is parametrization of the reconstruction efficiency of combined muons, while the lower curve is for combined muons with all selection requirements applied. The main drop in efficiency is due to requirement of at least 3 hits in each MDT station.

Muon momentum resolution. As discussed before, the muon momentum resolution observed in cosmic-ray and collision data is significantly worse with respect to the one in MC09

Monte Carlo. This is accounted for by smearing the momentum using equation 5.6. The smearing parameters are tuned according the position of the Z peak in data ($S_1 = 0.023 \pm 0.003$), and resolution from cosmic-ray data $S_2 = 0.18 \pm 0.04$ TeV^{-1}. These values and uncertainties have been measured by the ATLAS Muon Combined Performance group [17].

The uncertainties of the smearing parameters are used to estimate systematic uncertainty on signal efficiency and background level arising from muon momentum resolution. The signal efficiency and background level are recalculated with each parameter shifted up and down by its uncertainty while the other parameter is held at the central value. The uncertainty associated with each smearing parameter is taken to be the half of difference between the up and down values. The total resolution uncertainty is obtained by adding the uncertainties for the two smearing parameters in quadrature. Results for signals and background are presented in6.12, 6.13 and 6.14

Muon momentum scale. The value and uncertainty for the muon momentum scale (parameter S_p in equation 5.6) is evaluated from measurements of the magnetic field and the position of the Z-boson mass peak. All are consistent with unity and so $S_p = 1$ is taken as the central value. The effect of the uncertainty of muon scale on the $W' \to \mu\nu$ event selection efficiency is calculated using the maximum 1-sigma deviation of the most precise measurement: $S_p = 0.9996 \pm 0.0010$, i.e a decrease of 0.14%.

Muon curvature offsets. Detector misalignment in a particular region results in an offset in the curvature measured in that region, i.e. an offset in q/p_T. If the misalignments vary randomly with location in the the detector (with η and ϕ), then the effect is to smear the resolution additionally. This leads to the contribution to the S_2 term in equation 5.6. However, if there is residual correlation between regions, there will be a global bias, S_o in equation 5.6, that shifts the momentum magnitude of positive and negative muons in opposite directions. The width of a neutral dimuon resonance like the Z boson is not affected to first order, and the variable used to estimate the curvature offset is the q/p_T asymmetry of the Z:

$$A_{q/p_T} = [(q/p_T)^+ + (q/p_T)^-]/2 \tag{6.14}$$

The mean value of the asymmetry provides a direct measure of the offset and giving the value $S_o = 0 \pm 0.071$ TeV^{-1}. Assuming no correlation exists between the Inner Detector and the Muon Spectrometer alignments, a stronger limit may be put on the difference of the offsets in the two systems by comparing their momentum measurements. This was estimated to be $\Delta S_o = 0 \pm 0.024$ TeV^{-1}. However, the former is sufficient for this measurement and was adopted to avoid making any assumptions about the Inner Detector.

The corresponding uncertainties in the event selection efficiency and Monte Carlo background level are estimated by varying S_o by plus or minus its uncertainty. Results are given in the Tables 6.12, 6.13 and 6.14.

Muon vertex finding and impact parameter. Event selection requires that a primary vertex is reconstructed close to the center of the interaction region and that muon passes close to that vertex. The same selection requirements are imposed in data and Monte Carlo. The ratio of the efficiencies and its uncertainty of this selection requirement is assessed here. The efficiency to find a vertex (at the expected location) is evaluated as the ratio of the number events passing final selection to those passing final selection without the primary vertex requirement: $|z_{vtx}| < 15$ cm. The measured efficiencies for both data and Monte Carlo are presented in table 6.10. The Monte Carlo includes one of the $W' \to \mu\nu$ reference samples, the main background $W' \to \mu\nu$ and this background with luminosity-weighted pileup. The non-pileup background is used in the limit calculations and is most relevant here. The signal and background samples give consistent results indicating a small bias in the Monte Carlo that is largely explained by pileup.

Table 6.10: Vertex finding efficiency for muons. The last column is the ratio of the efficiency to that obtained in data.

Sample	Efficiency	Data/MC
Data (36 pb^{-1})	0.9909 ± 0.0004	1
$W' \to \mu\nu$ ($m_{W'} = 1$ TeV)	0.9888 ± 0.0011	1.0030 ± 0.0012
$W \to \mu\nu$	0.9862 ± 0.0001	1.0049 ± 0.0004
$W \to \mu\nu$ (with pileup)	0.9900 ± 0.0003	1.0010 ± 0.0005

The efficiency to both find a vertex and have the muon pass nearby is evaluated in a similar way, as the ratio of the number events passing final selection to the number passing final selection without either the impact parameter or vertex requirements. These results are in table 6.11. Since the data data includes a small contribution from cosmic muons, the measurement is expected to biased a bit. The efficiency for data is presented both without and with a correction for this contribution. The signal and non-pileup background samples give consistent results indicating a small bias. The bias is similar to that seen for the vertex efficiency suggesting the impact parameter efficiency is well-modeled by the Monte Carlo. However, the efficiency measured with the pileup sample is even further from the data, opposite to the result obtained for the vertex efficiency. Although this is not directly relevant to the $W' \to \mu\nu$ limits which are evaluated without use of the pileup samples, the efficiency change observed when pileup is added is

conservatively used to set the systematic uncertainty in the impact parameter correction factor. The correction factor to account for Monte Carlo bias in efficiency for both vertex finding and impact parameter is taken to be the same for signal and background: $C_{\text{vtx}} = 1.004 \pm 0.3\%$.

Table 6.11: Vertex finding plus impact parameter efficiency for muons. The last column is the ratio of the efficiency to that obtained in data with the correction for cosmic contamination.

Sample	Efficiency	Data/MC
Data (36 pb^{-1})	0.9864 ± 0.0004	1.0031 ± 0.0012
Data (36 pb^{-1} , cosmics removed)	0.9895 ± 0.0004	1
$W' \to \mu\nu$ MC ($m_{W'} = 1$ TeV)	0.9864 ± 0.0011	1.0031 ± 0.0012
$W \to \mu\nu$	0.9855 ± 0.0001	1.0041 ± 0.0004
$W \to \mu\nu$ (with pileup)	0.9832 ± 0.0004	1.0064 ± 0.0005

$\not\!\!E_T$ **scale and resolution.** Most of the $\not\!\!E_T$ in $W' \to \ell\nu$ candidate events comes from the lepton and that contribution is strongly correlated with the lepton p_T measurement. The leptonic contribution is therefore handled separately from the non-leptonic contribution obtained by summing energy from the calorimeter.

Most of the systematic correction and uncertainty arising from the leptonic contribution to the $\not\!\!E_T$ is included in the p_T systematics. For example, to properly account for this contribution and the correlation, the $\not\!\!E_T$ is varied along with that of the p_T when the latter varied to study the effect of changing the momentum scale or resolution. However, there can be residual effects because the p_T correction is not exactly the same as the $\not\!\!E_T$ calculation in the region around the lepton. The energy deposited by the muon in the calorimeter and the correction for this energy loss is an example of such residual effect. Since these are only a few GeV and mostly cancel one another, no systematic correction or uncertainty is assigned for residual effects.

To account for discrepancy in the $\not\!\!E_T$ resolution in data and MC (for the calorimeter part), pileup samples could be used with weighting events in order to match multiplicities of reconstructed vertices in data and MC. Instead of reweighted pileup samples, non-pileup samples are used with smearing of their calorimeter part of $\not\!\!E_T$ (cf. section 5.2.3, equation 5.7). As it is shown, these two options are equivalent, and the latter is used in this thesis. The uncertainty of the smearing parameter value $S_r = 4.0 \pm 0.4$ GeV is used to estimate uncertainty arising from the calorimeter resolution. Since the smearing is included for all non-pileup samples in the evaluation of the event selection efficiencies and background levels, there is no need to introduce a correction factor.

The effect of the uncertainty in the resolution on these quantities is assessed by varying the smearing parameter by its uncertainty and observing the change in signal efficiency and

background level. Results are presented in the Tables bellow, and the effect is found to be quite small.

There is some indication of a few percent difference between the $\not\!\!E_T$ scale in Monte Carlo and data but the variation as function of $\not\!\!E_T$ is not established and may be different for the W' m_{T} bins. It is assumed that $S_m = 1.0 \pm 0.1$ based on the observed variation with $\not\!\!E_T$. Again, there is no correction factor and uncertainties on the signal efficiency and background level are obtained by varying the scale by its uncertainty.

6.5 Final results and uncertainties for the muon search

As data show no evidence for any excess above SM expectations, limits on the production of new gauge bosons have to be set. In order to do so[4], systematic uncertainties on signal efficiency and level of background are evaluated in this chapter, as well as correction factors to account for difference in data and MC, and change in theoretical higher order calculation with mass. For W^*, kinematic cuts imposed at the generator level are accounted for. Also, QCD and cosmic contamination are evaluated from data itself, with uncertainties on these estimations treated as systematic uncertainties of the background level.

All systematic uncertainties, except for luminosity uncertainty stated to be $\pm$11% for all cases, for W' and W^* signal samples, along with systematic uncertainties of the background are presented in Tables 6.12, 6.13 and 6.14 respectively. Experimental (detector related) systematic uncertainties for the signal are dominated by the uncertainty of the extrapolation of muon reconstruction to high-p_T and uncertainty on trigger efficiency. The uncertainty arising from limited MC statistics of the signal W'/W^* MC samples is treated separately and added in quadrature with the other uncertainties. For W', there is a correction to account for the difference in kinematical distributions at NNLO and in the LO simulation. These are given in the last line in Table 3.2, and uncertainty of this correction is taken to be 0.7% for all masses. Systematic uncertainties for the background are dominated by theoretical uncertainties, and systematic uncertainty arising from limited MC statistics. The latter is high due to the muon momentum resolution which causes small number of events from offshell W production propagate to the high m_{T}-tail. Experimental uncertainties of the background range 1.4-4.8% depending on the m_{T}-threshold.

The expected number of signal events and selection efficiency is obtained by correcting

[4]The inputs to the σB limit calculations are the event selection efficiency, $\varepsilon_{\mathrm{sig}}$, the expected number of background events, N_{bg}, the uncertainties in these quantities, and the number of observed events, N_{obs}, and the integrated luminosity and its uncertainty. The predicted number of signal events, N_{sig}, is useful for understanding sensitivity to the σB of a specific model.

Table 6.12: $W' \to \mu\nu$ systematic uncertainties.

	m_{Tmin} [GeV]					
Source	250	375	500	625	750	875
Missing E_T resolution	0.1%	0.2%	0.1%	0.1%	0.1%	0.2%
Missing E_T scale	0.1%	0.1%	0.1%	0.1%	0.1%	0.1%
Trigger efficiency	0.7%	0.7%	0.7%	0.7%	0.7%	0.7%
Reconstruction efficiency	1.0%	1.1%	1.3%	1.5%	1.6%	1.9%
Momentum resolution	0.1%	0.1%	0.2%	0.3%	0.4%	0.5%
Momentum scale	0.1%	0.2%	0.1%	0.1%	0.1%	0.2%
Curvature offset	0.4%	0.3%	0.5%	0.5%	0.6%	0.9%
Vertex efficiency	0.3%	0.3%	0.3%	0.3%	0.3%	0.3%
All experimental	1.3%	1.4%	1.6%	1.8%	2.0%	2.3%
Monte Carlo statistics	1.2%	1.2%	1.1%	1.4%	1.6%	1.7%
NNLO	0.7%	0.7%	0.7%	0.7%	0.7%	0.7%
All	1.9%	2.0%	2.1%	2.4%	2.7%	3.0%

Table 6.13: $W^* \to \mu\nu$ systematic uncertainties.

	m_{Tmin} [GeV]					
Source	250	375	500	625	750	875
Missing E_T resolution	0.1%	0.1%	0.1%	0.1%	0.1%	0.1%
Missing E_T scale	0.2%	0.1%	0.4%	0.3%	0.1%	0.2%
Trigger efficiency	0.7%	0.7%	0.7%	0.7%	0.7%	0.7%
Reconstruction efficiency	0.9%	1.1%	1.2%	1.4%	1.6%	1.8%
Momentum resolution	0.2%	0.3%	0.3%	0.4%	0.4%	0.4%
Momentum scale	0.1%	0.1%	0.1%	0.1%	0.1%	0.1%
Curvature offset	0.2%	0.3%	0.2%	0.3%	0.8%	0.3%
Vertex efficiency	0.3%	0.3%	0.3%	0.3%	0.3%	0.3%
All experimental	1.3%	1.4%	1.6%	1.7%	2.0%	2.0%
Monte Carlo statistics	1.3%	1.4%	1.5%	1.5%	1.5%	1.5%
All	1.9%	2.0%	2.2%	2.3%	2.5%	2.6%

numbers from Table5.16 with trigger correction and NNLO/LO acceptance correction. The expected number of background events is obtained from Table5.14 using the correction factors from the last column of Table 6.9 for W/Z multiplied by trigger correction factor from equation (5.9). For $t\bar{t}$ and diboson contribution only trigger correction is applied. Numbers for QCD background are not corrected since these are obtained from data without background (i.e. W/Z, $t\bar{t}$, and diboson) subtraction. The same is for the cosmic contamination. The final m_{T} distribu-

Table 6.14: Background systematic uncertainties.

	m_{Tmin} [GeV]					
Source	250	375	500	625	750	875
Missing E_T resolution	0.2%	0.2%	0.4%	0.1%	0.1%	0.1%
Missing E_T scale	0.3%	0.2%	0.5%	1.2%	3.4%	1.1%
Trigger efficiency	0.7%	0.7%	0.7%	0.7%	0.7%	0.7%
Reconstruction efficiency	0.9%	1.0%	1.2%	1.2%	1.3%	1.6%
Momentum resolution	0.4%	0.4%	1.4%	2.4%	3.1%	3.2%
Momentum scale	0.1%	0.1%	0.1%	0.1%	0.1%	0.1%
Curvature offset	0.4%	0.3%	1.7%	2.1%	3.3%	2.9%
Vertex efficiency	0.3%	0.3%	0.3%	0.3%	0.3%	0.3%
All experimental	1.4%	1.4%	2.7%	3.7%	5.9%	4.8%
Monte Carlo statistics	2.3%	4.8%	9.3%	13.5%	16.6%	15.5%
W/Z cross section	4.8%	6.1%	7.4%	9.1%	10.8%	11.0%
$t\bar{t}$ cross section	1.3%	0.8%	0.8%	0.8%	0.7%	0.8%
QCD	1.7%	1.9%	2.2%	2.2%	2.1%	1.5 %
Cosmic	0.0%	0.1%	0.2%	0.3%	0.5%	0.4%
All	5.9%	8.2%	12.4%	16.9%	20.8%	19.7%

Table 6.15: Final results for $W' \to \mu\nu$, $W^* \to \mu\nu$, and backgrounds with integrated luminosity of 36.4 pb^{-1} . Signal efficiencies, and expected numbers of signal and background events are corrected as explained in the text. Uncertainties are listed in the previous tables. The last column gives the number of observed events for the muon selection.

m [GeV]	signal	$\varepsilon_{\mathrm{sig}}$	N_{sig}	N_{bg}	N_{obs}
500	W'	0.339 ± 0.008	212 ± 17	20.01 ± 1.1	16
	W^*	0.228 ± 0.004	104 ± 8		
750	W'	0.362 ± 0.009	42.1 ± 2.7	5.48 ± 0.45	0
	W^*	0.230 ± 0.005	19.6 ± 1.5		
1000	W'	0.381 ± 0.010	11.6 ± 0.9	2.11 ± 0.26	0
	W^*	0.242 ± 0.005	5.4 ± 0.5		
1250	W'	0.386 ± 0.011	3.66 ± 0.33	1.03 ± 0.17	0
	W^*	0.237 ± 0.005	1.63 ± 0.20		
1500	W'	0.383 ± 0.012	1.24 ± 0.14	0.63 ± 0.13	0
	W^*	0.235 ± 0.006	0.54 ± 0.08		
1750	W'	0.360 ± 0.012	0.43 ± 0.06	0.49 ± 0.10	0
	W^*	0.239 ± 0.006	0.20 ± 0.04		

tion with corrected background levels, and QCD background estimated from data, are presented in Fig6.5.

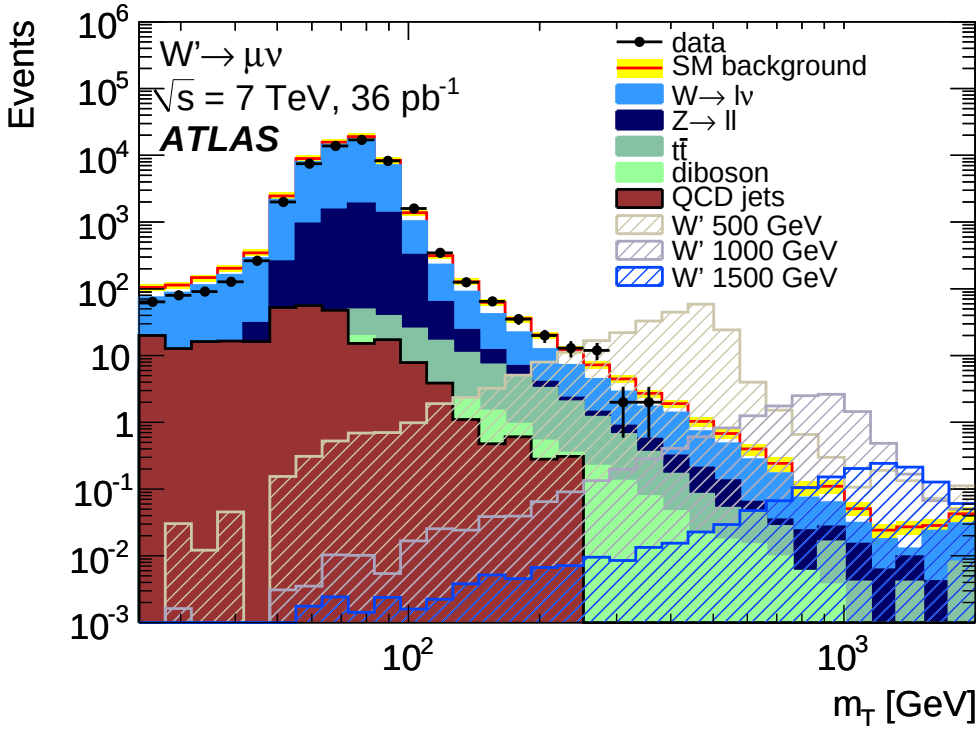

Figure 6.11: Final m_{T} spectrum, with all corrections applied. Signal samples are normalized to NNLO. QCD contamination is estimated from data. Yellow band corresponds to the overall background systematic uncertainty from table 6.14. For m_{T} <250 GeV, uncertainty is assumed to be dominated by the luminosity uncertainty $\pm$11%.

Bibliography

[1] D.L. Adams,...,D. Fassouliotis,...,C. Kourkoumelis,...,D. Popovic,..., N. Vranjes et al. Search for high-mass states with lepton plus missing transverse energy using the ATLAS Detector with 36 pb^{-1} of pp collisions at $\sqrt{s}$ = 7 TeV, ATL-COM-PHYS-2010-1073.

[2] K. Melnikov, F. Petriello, Electroweak gauge boson production at hadron colliders through O(alpha(s)**2), Phys. Rev. **D74**, 114017, [hep-ph/0609070] (2006).

[3] R. Gavin, Y. Li, F. Petriello *et al.*, FEWZ 2.0: A code for hadronic Z production at next-to-next-to-leading order, [arXiv:1011.3540 [hep-ph]] (2010).

[4] F. Petriello, private communication.

[5] J. M. Campbell and R. Ellis, Phys. Rev. D62, 114012 (2000), hep-ph/0006304.

[6] S. Frixione et al., JHEP 08, 007.349 (2003)
S. Frixione et al., JHEP 06, 029 (2002).

[7] ATLAS Collaboration, ATLAS Monte Carlo tunes for MC09, ATLPHYS-PUB-2010-002. `https://twiki.cern.ch/twiki/bin/view/AtlasProtected/McProductionCommonParameters09`

[8] V. A. Zykunov, Eur. Phys. J. C 3 (2001) [arXiv:hep-ph/0107059]; V. A. Zykunov, Weak radiative corrections to Drell-Yan process for large invariant mass of di-lepton pair, [arXiv:hep-ph/0509315]; S. Dittmaier and M. Kramer, Phys. Rev. D 65 (2002) 073007 [arXiv:hep-ph/0109062]; U. Baur and D. Wackeroth, Phys. Rev. D 70 (2004) 073015 [arXiv:hep-ph/0405191]; A. Arbuzov, D. Bardin, S. Bondarenko, P. Christova, L. Kalinovskaya, G. Nanava and R. Sadykov, Eur. Phys. J. C 46 (2006) 407 [arXiv:hep-ph/0506110].

[9] P. Golonka and Z. Was, PHOTOS Monte Carlo: A Precision tool for QED corrections in Z and W decays, Eur. Phys. J. C45 (2006) 97107, hep-ph/0506026.

[10] C. Carloni Calame, G. Montagna, O. Nicrosini, and A. Vicini, Precision electroweak calculation of the charged current Drell-Yan process, JHEP 0612 (2006) 016, arXiv:hep-ph/0609170[hep-ph].

[11] A. Martin and R. Roberts and W. Stirling and R. Thorne, Parton distributions incorporating QED contributions, Eur. Phys. J. C39 (2005).

[12] C. M. Carloni Calame, G. Montagna, O. Nicrosini, and A. Vicini, Precision electroweak calculation of the production of a high transverse-momentum lepton pair at hadron colliders, JHEP 10 (2007) 109, arXiv:0710.1722 [hep-ph].

[13] TeV4LHC-Top and Electroweak Working Group Collaboration, C. E. Gerber et al.,Tevatron-for-LHC Report: Top and Electroweak Physics, arXiv:0705.3251 [hep-ph].

[14] S. Dittmaier and M. Kramer, 1, Electroweak radiative corrections to W-boson production at hadron colliders, Phys. Rev. D65 (2002) 073007, arXiv:0109062 [hep-ph].

[15] ATLAS Collaboration, G. Aad et al., Luminosity Determination in pp Collisions at $\sqrt{s}$ =7 TeV Using the ATLAS Detector at the LHC, accepted by EPJC, arXiv:1101.2185 [hep-ex].

[16] ATLAS Collaboration, Updated Luminosity Determination in pp Collisions at $\sqrt{s}$ =7 TeV using the ATLAS Detector, ATLAS-CONF-2011-011.

[17] ATLAS Muon Momentum Resolution in the First Pass Reconstruction of the 2010 p-p Collision Data at $\sqrt{s}$=7 TeV, ATLAS-CONF-2011-046.

Chapter 7

Electron Channel

In this chapter electron selection in a search for new heavy gauge boson decaying to an electron and a neutrino is presented. Estimation of QCD background from data and relevant systematic uncertainties are briefly described. After QCD backgrounds estimation, and all corrections applied and uncertainties properly evaluated and taken into account, final results for $W' \to e\nu$ channel are given at the end of the chapter.

7.1 Event selection

7.1.1 Electron reconstruction and identification at ATLAS

The ATLAS standard electron reconstruction and identification algorithm (sometimes denoted as `egamma`)[1] is developed to enable electron reconstruction of high-E_T isolated electrons in the region covered by the Inner Detector, providing levels of background rejection optimized for high identification efficiencies. In addition to this, complementary algorithm [2], aims to the reconstruction of low-p_T or non-isolated electrons in jets. Since electrons that would originate from W'-type bosons are very energetic and isolated, in the following only electrons reconstructed by the `egamma` algorithm are used.

The standard electron reconstruction procedure is based on clusters reconstructed in the Electromagnetic Calorimeter using the Sliding Window algorithm [3]. Clusters are then associated to tracks of charged particles reconstructed in the Inner Detector. This algorithm has been developed to allow for an optimal reconstruction of the four-momentum of electrons for the full momentum and pseudorapidity range and for any luminosity. Information from both detectors is used to allow electrons to be identified with the lowest possible amount of background[1] , keep-

[1] For comparison the relative rate of QCD jet production compared to inclusive electron production is expected

ing in mind that the optimum between the identification efficiency and background rejection is analysis dependent.

The baseline electron identification in ATLAS relies on cuts using variables that provide good separation between isolated electrons and jets or converted photons faking electrons. These variables include calorimeter, tracker and combined calorimeter/tracker information. They can be applied independently and three reference sets of cuts have been defined with increasing background rejection power: Loose, Medium and Tight [1]. Each definition includes the cuts of the looser definitions. This setup of identification has been introduced for the first time in the "CSC-era"[1]. Since then definitions of the electron identification criteria (as well as reconstruction criteria) have evolved. The changes have been introduced in order to improve identification efficiency[2], with respect to the results obtained during CSC. Beside these, since the very early data taking periods in 2009 and the first collisions at 900 GeV[4], the data/Monte Carlo comparisons have highlighted discrepancies in the shower shape distributions. In particular, the electromagnetic showers are seen to be broader in data than in the MC, which translates into a shift in the relevant distributions R_η and ${w_{\eta 2}}^3$. This shift is consistently observed on pure hadronic background (on the very first electron candidates for example) as well as on isolated electrons from W or Z bosons decays[5]. The reason for this discrepancies are not clear, though it is believed to be lying in the `GEANT4` description of the electromagnetic calorimeter[6]. In order to maintain the robustness of the electron identification criteria, the cuts were reoptimized. This lead to the new definitions of Medium and Tight: so called *Robust Medium* and *Robuster Tight*[6]. Below electron reconstruction and identification as used in analysis of 2010 data are described. Prefixes *Robust(er)* are not used, though when speaking of Medium/Tight, only *Robust(er)* definitions are considered.

The electron candidates are searched among clusters with energy of $E_T > 2.5$ GeV in the second layer of the electromagnetic calorimeter. A matching track, extrapolated to the middle EM calorimeter layer, is searched for in a broad window of $\Delta\eta \times \Delta\phi$ distance of 0.05×0.10 amongst all reconstructed tracks with $p_T >$0.5 GeV. Reconstructed tracks are matched to seed clusters by extrapolating them from their last measurement point to the second layer of the calorimeter. The impact point η and ϕ coordinates are then compared to the corresponding seed cluster η and ϕ in that layer. If their difference is below a certain threshold then the track is considered matched to the cluster. Special care is taken in order to account for Bremsstrahlung

to be between 10 and 100 times higher than at the Tevatron. In addition, aspects of the detector itself complicate the analysis, such as the significant amounts of material in the Inner Detector.

[2]One of the main issues encountered during the CSC analysis, was the relatively low electron identification efficiency.

[3]R_η is the ratio in η of cell energies in 3×7 versus 7×7 cells, and $w_{\eta 2}$ is the lateral shower width in the second layer of the calorimeter.

losses which result in an asymmetric sign-dependent $\Delta\phi$ distribution. Thus, the sign-corrected $\Delta\phi$ window is larger on the side where the extrapolated track bends as it traverses the tracker magnetic field. In the case of tracks that do not contain silicon hits, the matching is restricted to the ϕ coordinate, due to the fact that the accuracy on the η coordinate, as measured by the TRT, is limited. In this case only a rough track matching, e.g. barrel track matched to a barrel cluster, is required. The closest-matched track to this layers cluster barycenter is kept as that belonging to the electron candidate. The final electron candidates have cluster sizes of $\Delta\eta \times \Delta\phi = 0.075 \times 0.175$ in the barrel calorimeter and 0.125×0.125 in the end-cap. The electromagnetic clusters with a matching track fulfilling these requirements are selected as electron candidates.

The identification criteria for each of the three electron candidate definitions is as follows.

- Loose: this basic selection uses EM shower shape information from the second layer of the EM calorimeter (lateral shower containment and shower width) and energy leakage into the hadronic calorimeters as discriminant variables. This set of requirements provides high and uniform identification efficiency with a cost of low background rejection.

- Medium: this selection provides additional hadronic rejection by evaluating the energy deposit patterns in the first layer of the EM calorimeter (the shower width and the ratio of the energy difference associated with the largest and second largest energy deposit over the sum of these energies), track quality variables (number of hits in the pixel and silicon trackers, the transverse impact parameter) and a cluster-track matching variable ($\Delta\eta$ between the cluster and the track extrapolated to the first layer of the EM calorimeter).

- Tight: this selection further rejects charged hadrons and secondary electrons from conversions by fully exploiting the electron identification potential of the ATLAS detector. The tight selection adds E/p (where E is measured by the Electromagnetic Calorimeter and the momentum p measured by the Inner Detector), B-layer hit requirements and the particle identification potential of the Transition Radiation Tracker through the number of hits in the TRT, and on the ratio of high-threshold to the total number of hits in the TRT. The tight selection has been adapted to take into account disabled B-layer modules. If the tight candidate electron crosses a disabled B-layer module, it is kept, where as it was rejected in the previous definition of tight. As result of broader $\Delta\eta$ and $\Delta\phi$ distributions observed in data than in Monte-Carlo due to at the time not yet optimal Calo-ID alignment, the new tight selection applies only the looser medium $\Delta\eta$ cut, while the $\Delta\phi$ cut is removed from the selection.

For the full list of identification variables, and values of baseline selection cuts used for the analysis of 2010 data, one should consult reference [6].

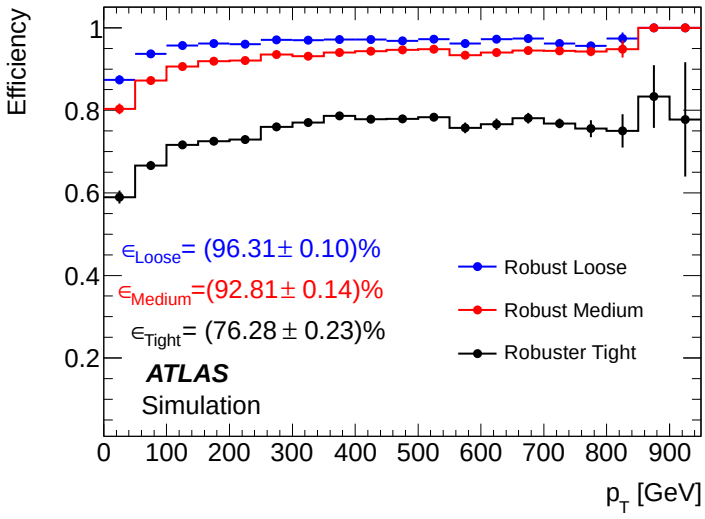

Figure 7.1: Electron reconstruction and identification efficiency for three identification criteria as a function of the true electron p_T in W' MC samples ($m_{W'}$= 1 TeV and $m_{W'}$= 1.5 TeV). Efficiency is defined as a fraction of true electrons (originating from W' decay) matched with reconstructed electrons in ΔR <0.1.

Electron identification in W' search with 2010 data. Figure 7.1 shows reconstruction and identification efficiency in $m_{W'}$= 1 TeV + $m_{W'}$= 1.5 TeV MC samples for three different levels of the electron identification, Loose, Medium and Tight as a function of the electron true p_T . The results are consistent with the ones presented in [6]. One can observe that efficiency predicted by the simulation is increasing with respect of p_T , saturating around 95% for Loose and Medium identification in the p_T of interest. Further, identification efficiencies of Loose and Medium at high p_T are close. For these reasons, applying Loose identification in W' search with 2010 data is ruled out, since one can achieve similar signal efficiency with higher rejection power with Medium. W and Z analysis have used Tight electron selection throughout the whole 2010 [5, 7] to ensure high purity of the signal samples. The identification efficiency of the Tight selection is, however, ∼20% lower (relatively) with respect to the Medium efficiency. Apart from this, applying the cut on the ratio of high threshold TRT hits over the total number of TRT hits, will not discriminate between pions and electrons and very high energies. The transition radiation in a given medium depends only on the Lorentz factor, $\gamma = E/m$, and when pion energy becomes high enough (≥200 GeV), there is no discriminating power between electrons and pions any more[8]. Furthermore, E/p distribution is becoming increasingly difficult to model for very high energy electrons due to the fact that the insufficient knowledge of the ID alignment affects momentum measurement of high momentum tracks. Following this argumentation, Medium requirement is chosen for the electron identification in $W' \to e\nu$ search with 2010 data. The

only remaining issue is the question of conversions, and these were suppressed by requiring B-layer hit present if expected. The motivation for B-layer selection requirement will be discussed latter in the text.

ATLAS EGamma combined performance group performed the in-situ calibration of the electromagnetic calorimeter and evaluation of linearity and energy resolution of the electron reconstruction using $Z \to ee$ events [9]. The study is initially performed only for two bins in η : for the barrel ($|\eta| < 1.37$) and endcups ($1.52 < |\eta| < 2.47$). Results from $Z \to ee$ analysis are used to derive energy scale corrections:

$$E_{corr} = \frac{E}{(1+\alpha)}, \tag{7.1}$$

with α = -0.0096 for the barrel and α = 0.0189 for the endcaps. More refined analysis was performed with full 2010 dataset, resulting in finer η granularity. The results are consistent with previously stated, except for very high η (>2.4) where $\pm$5% is obtained for the correction factor. However, electrons with such high η were not used in $W' \to e\nu$ analysis anyway. Residual miscalibration are not yet understood and are probably due to a combination of several effects like incorrect electronic calibration, incorrect high voltage correction in particular in the end-cap, extra-material in front of the calorimeter, difference in the calorimeter and presampler energy scale, difference in lateral leakage between data and MC. The scale correction α in this thesis is applied only to data, but not to Monte Carlo samples.

It should be noted that all calculations are performed using calorimeter cluster variables for electron energy, transverse energy and η and ϕ coordinates, with the exception of the calculation of m_{T} distribution, where η and ϕ are taken from the track.

7.1.2 Electron trigger

Electrons are triggered in the range $|\eta|$ <2.5 [9], where the EM calorimeter has a fine segmentation in both the lateral and longitudinal directions of the shower. The trigger also uses the information of the ID which provides precise track reconstruction in the same range of pseudorapidity. At Level 1 (L1) only calorimeter information with reduced granularity is used for triggering purposes. The L1 cluster is used as seed for the Level 2 (L2) trigger, which uses a fast calorimeter and track reconstruction algorithm for the electron trigger. The default calorimeter reconstruction works in a similar way as the offline algorithms described in the previous subsection. The main difference to the offline is the cluster seed finding step which is done using the hottest cell in the second EM layer at L2 while in the offline reconstruction the sliding window algorithm is used. Cluster building, calibration and cluster corrections are the same

as in the offline reconstruction. At the Event Filter (EF) level the same algorithms as for the offline identification are used, except for bremsstrahlung recovery. As for the offline, at the EF level the track reconstruction is started by hits in the Silicon detectors and completed by TRT standalone tracking.

During the data taking, two electron triggers were used. For low luminosity periods (from A up to run 160530 of period E) the L1 trigger `L1EM_14` is used with a nominal threshold E_T >14 GeV, while for the remaining periods the high level trigger `EF_e20_loose` is used, with a threshold E_T >20 GeV and loose electron requirement. Both triggers are highly efficient with respect to the offline selection employed, with efficiency of $99 \pm 1\%$. Among the triggers used in the W' analysis, only the first level (L1) was simulated, with a resulting efficiency of 100% [11].

7.1.3 Data and Monte Carlo Samples

Collision data. Data are collected from two streams: L1Calo stream (in periods A to D), and EGamma stream (periods E to I). Further, luminosity blocks are required to satisfy the good quality requirements as set by the data quality and preparation group. This can be summarized as having all tracking (pixel, SCT and TRT) and calorimeter (EM, HEC, FCAL and TILE) subdetectors and the electron trigger performing well, and the solenoid operating at the nominal current. The LHC beams must be stable and operate at 3.5 TeV and the luminosity calculations must be reliable. The list of requirements used in the Good Run List query are as follows:

- Run range: 152844-167844
- Beam status:`ptag data10_7TeV and lhc stablebeams true`
- Data requirements: partition ATLAS and db DATA
- Detector related quality requirements: `atlgl, atlsol, l1ctp, cp_eg_electron_endcap, cp_eg_electron_barrel, CP_MET_METCALO, L1CAL, TRELE and lumi`
- Database tag: `DetStatus-v03-pass1-analysis-2010I`

Events with good $W' \to e\nu$ candidates are required to pass the triggers listed in table 7.1. The table gives the corresponding integrated luminosity for each trigger period and the total for the channel. The integrated luminosity satisfying GRL criteria summed over all datasets is $\mathscr{L}_{\text{int}}$ = 36.39 pb^{-1} , very close to the one in the muon search.

During the initial LHC data-taking periods (periods A to C, corresponding to about 17 nb^{-1} of data that pass good run list requirements), only a subset of the Bunch Crossing Identification

Table 7.1: Triggers used to select data for $W' \to e\nu$ search, and corresponding integrated luminosities.

Run periods	Run numbers	Trigger	$\mathscr{L}_{\text{int}}$ [pb^{-1}]
D-E	158045-161948	L1_EM14	1.31
F-I	162347-167776	EF_e20_loose	35.08
D-I	158045-167776		36.39

(BCID) algorithms[4] was implemented, leading to a wrong assignment in case of saturated signals, and hence a potential loss of very high E_T electron events. Additional BCID algorithms were implemented for the majority of data and were shown to be efficient even in case of saturated signals. More details on this issue can be found in [11]. Since the fraction of data affected is very small, it has been decided not to include those runs (from 152844-158045) in the final dataset.

At the beginning of 2010 data taking (periods A to D), a problem with LAr Calorimeter occurred, where channel 0 from a Front End Board (FEB) was overwritten at the input of channel 63[12]. This has been known as a gain corruption problem. A study of the impact of the gain corruption problem that affected some physics data in seven-sample mode of Liquid Argon Calorimeter is reported in [11](Appendix I). The LAr gain switching bug has an impact of less than 1% on the $W' \to e\nu$ selection efficiency with 0.7 per mil uncertainty. More importantly, the reconstructed energy is systematically underestimated and is not likely to create fake high energy candidates. Therefore it has been decided to keep the data from period D.

Monte Carlo samples. Monte Carlo samples used to simulate backgrounds in $W' \to e\nu/(W^* \to e\nu)$ search are listed in Table7.2. Signal samples are already listed in Tables5.3,5.4. Simulation framework is the same as the one explained in the section5.2.2, with background samples generated and fully simulated in the ATLAS `MC09` framework from the "May reprocessing". Generated events are passed through the `GEANT`-based simulation of ATLAS detector, within `Athena` release 15.6.3.10, and then digitized and reconstructed with release 15.6.9.8 (reconstruction tags `r1302` or `r1306`). Dedicated samples for $W \to e\nu$ and $Z \to ee$, reconstructed within `Athena` release 15.6.10.4 (`r1388`), are used to model effect of pileup. As for the muon search all processes are normalized to the NNLO cross sections, except dibosons normalized to NLO and QCD were only LO are used. QCD is eventally estimated from data and not from the

[4]The Level 1 calorimeter trigger system has two functions: to measure the amplitude of the signal from the calorimeter trigger towers, and assign it to the correct bunch crossing (in units of 25 ns). The latter is done with BCID.

simulation.

Table 7.2: Monte Carlo background samples. Sources for the cross-sections are discussed in the text. Filtering efficiency is included in the cross section.

Process	Run number	σB [pb] LO	HO	N_{evt} [k]	$\mathscr{L}_{\text{int}}$ [pb^{-1}]
$W \to e\nu$	106043	8938	10460	7000	670
$W \to \tau\nu$ ($\lvert\eta_\tau\rvert < 2.8$))	106022	7804	9134	1000	109
$W(200,500) \to \ell\nu$	106604	8.90	10.42	60	5760
$W(500,1500) \to \ell\nu$	105274	0.242	0.283	60	212000
$W(1500,2500) \to \ell\nu$	105275	0.00079	0.00092	60	6540000
$Z \to ee$	106046	856	989	5300	5360
$Z \to \tau\tau$	106052	856	989	2000	2022
$Z(250,400) \to ee$	105468	0.416		20	48100
$Z(400,600) \to ee$	105469	0.0673		20	297000
$Z(600,800) \to ee$	105470	0.0111		20	1790000
$Z(800,1000) \to ee$	105471	0.00274		20	7290000
$Z(1000,1250) \to ee$	105472	0.000918		20	21800000
$Z(1250,1500) \to ee$	105473	0.000249		20	80300000
$t\bar{t} \to \ell X$	105200	80.2	89.4	1000	8650
WW	105985	11.49	17.82	250	14000
WZ	105987	3.481	6.07	250	41200
ZZ	105986	0.976	1.387	250	180000
$jj(8,17)$	105009	9860000000		1400	0.000142
$jj(17,35)$	105010	673000000		1400	0.00208
$jj(35,70)$	105011	41200000		1400	0.0340
$jj(70,140)$	105012	2190000		1400	0.639
$jj(140,280)$	105013	87900		1400	15.1
$jj(280,560)$	105014	2330		1400	601
$jj(560,1120)$	105015	33.6		800	2360

Pileup, scaling and smearing. In order to account for additional pileup interactions, dedicated MC samples with simulated minimum bias interactions overlaid on top of the hard-scattering events are used for main backgrounds $W \to e\nu$ and $Z \to ee$. Events in these samples are reweighted in a way that multiplicity of reconstructed vertices in MC match the one in data, as described in Section5.2.3. Event weights are listed in [11], Table 6, page 15.

In contrast to the muon channel, where final results are obtained from non-pileup samples with smearing calorimeter part[5] of $\not{E}_T$, in $W' \to e\nu$ analysis $W \to e\nu$ and $Z \to ee$ contributions

[5] In $W' \to e\nu$analysis $\not{E}_T$ is calculated from the topological clusters with local hadronic calibration, equations

are obtained from pileup samples. The reason for this choice is lying in the fact that it is not straightforward to smear non-lepton part of MET_LocHadTopo, where most of the energy is coming from the lepton itself. However, electron energy resolution is improving with the electron energy, and there are no tails in very high-m_{T} originating from low mass sample. This is illustrated in Fig7.2, where m_{T} distributions obtained from $W \to \mu\nu$ and $W \to e\nu$ MC samples are compared (after full selection, and after muon smearing applied). Thus, statistics of pileup $W \to e\nu$ sample is sufficient for the reliable estimate of the background. The effect of pileup is small in very high-m_{T} region[13], and it is neglected for high mass binned samples and signal samples.

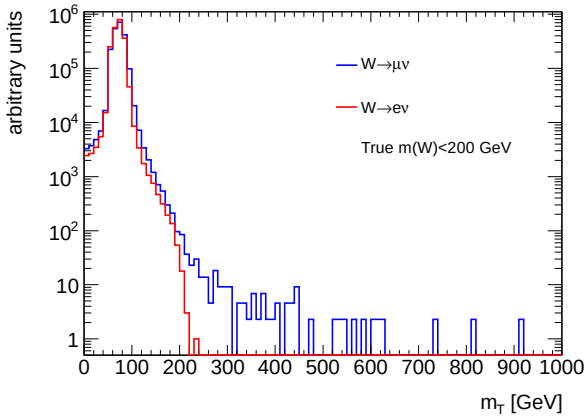

Figure 7.2: m_{T} distributions obtained from $W \to \mu\nu$ and $W \to e\nu$ MC samples, after full event selection. The distributions are normalized to the same area.

Measurements of the electron identification efficiency in data show that it is significantly lower than that predicted by the simulation. To account for this, a weight is applied to each Monte Carlo event which is the product of two η dependent scaling factors: one provided by the EGamma CP group group for the standard part of the electron selection[9], and an additional scaling factors computed specifically for the W' analysis to account for specific electron selections applied (calorimeter isolation, B-layer hit and impact parameter requirements). The evaluation of additional scaling factors is studied elsewhere and briefly described in W' supporting note [11](Appendix K.1). The values of the overall scaling factors along with corresponding uncertainties are presented in Table7.3. The largest relative uncertainty, found in the [-2.47,-2.01] η range, is 3.2%.

No additional smearing is applied to the energy of reconstructed electrons in MC. Discrepancy between data and MC is addressed later on, and treated as systematic uncertainties.

5.2 and 5.3. Since electrons deposit all their energy in the calorimeter, electron momentum is not added to the MET_LocHadTopo term.

Table 7.3: Overall electron efficiency scaling factors for different η bins.

η bin	[-2.47,-2.01]	[-2.01,-1.52]	[-1.37,-0.8]	[-0.8,0]
scale factor	0.936 ± 0.030	0.982 ± 0.028	0.968 ± 0.026	0.982 ± 0.025
η bin	[0,0.8]	[0.8,1.37]	[1.52,2.01]	[2.01,2.47]
scale factor	0.976 ± 0.025	0.983 ± 0.025	1.000 ± 0.028	0.960 ± 0.031

7.1.4 Preselection and Electron selection

The event preselection comprises of trigger requirement, vertex cut, and $\not{E}_T$ cleaning cuts. Vertex cut and $\not{E}_T$ cleaning cuts are the same as described in 5.3. The efficiency of the requirement of electromagnetic fraction <0.05 is higher then 99.9% for W' signal.

Additionally, events are required to satisfy channel specific selection criteria. Events are required to have exactly one electron defined as follows:

- Electron is reconstructed with the standard egamma algorithm (”electron author 1 or 3”);
- Electron candidate passes Medium identification;
- $|\eta| < 2.47$, excluding ”crack” region $1.37 < |\eta| < 1.52$;
- $E_T > 25$ GeV;
- Electron cluster outside the bad regions defined below;
- Track B-layer hit found if expected;
- $|d_0|$ <1 mm and $|z_0| < 5$ mm;
- Electron candidate is matched to the trigger object.

Here E_T ,η , and ϕ are those of the EM cluster associated with the electron.

Due to the presence of bad regions in the Liquid Argon calorimeter, a quality assessment of the energy measurement is performed by excluding such regions [5, 14]. This cut is colloquially known as the ”OTx” cut, and if the reconstructed electrons are located in one of these problematic regions they are therefore ignored. The reason of misbehaving in LAr are due to the high voltage or readout not working. The information about dead OTx regions is taken from the online LAr calorimeter monitoring system. This system provides separate two-dimensional ($\eta - \phi$) histograms for each layer and calorimeter subdetector on sides A and C. The level of detail of these histograms is very high, as required for monitoring purposes, with the granularity of an individual cell. During the 2010 data taking the number of dead regions were growing and most of the luminosity for W' search was taken with the calorimeter status of run 166479. Due to negligible gain of using the full run dependence available for the OTx cuts, just the final

one corresponding to run 166479, is applied to the full data and MC set. The loss of events caused by the exclusion of such bad regions rather significant, on the level of ∼5% per electron for $W \to e\nu$ analysis[7]. An average acceptance loss for both W' and W^* signal is of about 8%.

After selecting exactly one electron defined as above, events are removed if the electron has $2.40 < |\eta| < 2.47$ or it falls in the region $-1.4 < \eta < 0$ and $1.96 < \phi < 2.15$. The region with $2.40 < |\eta| < 2.47$ is excluded because there are insufficient statistics to evaluate the trigger board status, which was believed to be corrupted. It has been seen in calibration runs that a correct bunch crossing identification cannot be ensured for transverse energies above 350 GeV for the 28 trigger towers in the region $-1.4 < \eta < 0$ and $1.96 < \phi < 2.15$ and events with electrons in this region are also excluded.

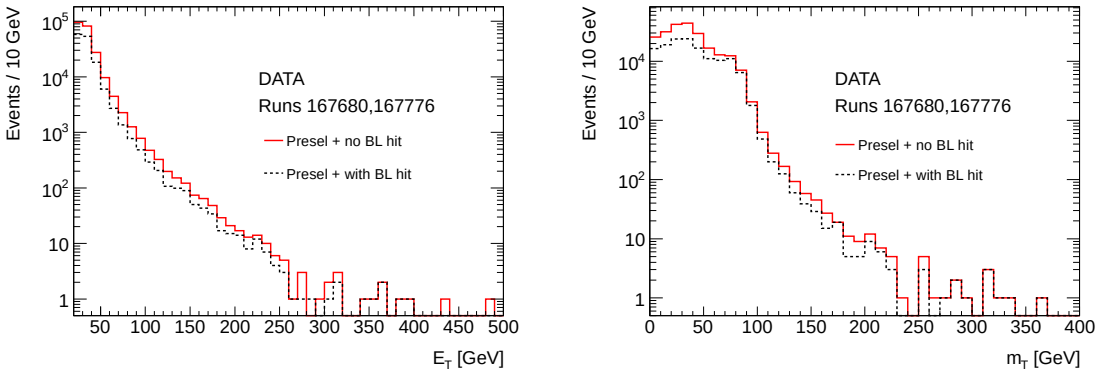

(a) (b)

Figure 7.3: E_T (a) and m_{T} (b) spectra for electron candidates passing preselection without and with B-layer hit requirement applied. Distributions come from data, collected in the last two runs, corresponding to about 8 pb^{-1} .

As discussed later in section 7.2.1, several independent estimates of the QCD background determined that even after requiring Medium identification, significant fraction of QCD background remains in the data sample. Part of this background comes from photon conversions. These electron candidates are expected to be isolated[6], and the events could have large missing energy. In order to supress QCD background from isolated photon conversions, in addition to the Medium identification, electron candidates are required to have hit in a B-layer, if this is expected (taking into account dead B-layer modules). The effect of this requirement is demonstrated in Fig7.3 showing electron E_T and m_{T} spectra in data with events passing full preselection without, and with B-layer hit required. One can observe that B-layer cut is removing large fraction (∼37%) of events in the tail of these distributions. The efficiency of the B-layer

[6]Electron isolation applied in W' search requires small deposited energy arround electron cluster in the calorimeter. Similar isolation requirement is used for the ATLAS direct photon cross section measurement.

hit for high-E_T electrons as a function of the electron true momentum is shown in Fig7.4. This efficiency is expected to be well modeled by the simulation. The effect on the signal efficiency is in range of 2-1.5% decreasing with W' mass. B-layer cut is included in the preselection step, and electron candidates failing this requirement are ignored.

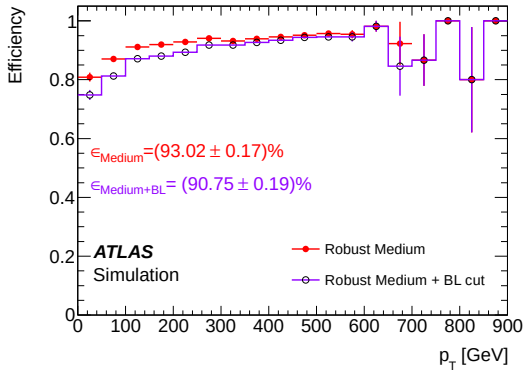

Figure 7.4: Electron reconstruction and identification efficiency for Robust Medium and Robust Medium identification with B-layer hit requirement applied in addition, calculated as before using W' MC sample, $m_{W'}$= 1 TeV.

In order to suppress electron candidates with the origin far away from the interaction point[7], electron candidates are required to have the position along the beam axis (measured with respect the position of the primary vertex) $|z_0| < 5$ mm, and the transverse distance of closest approach (also measured with respect to the same distance of the primary vertex) $|d_0|$ <1 mm. These requirement are harmonized with the muon selection requirements.

The ”trigger-matching” cut ensures that the electron that tags the event, is the one that actually fired the trigger. As for the muon selection, electrons are required to have $\Delta R_{trig} < 0.1$, where ΔR_{trig} is the η - φ distance between the reconstructed electron and the nearest passing trigger object.

7.1.5 Electron channel specific cuts: Calorimeter isolation and $\not{E}_T$ /E_T

The above requirements define the electron channel preselection but leave a significant amount of QCD background whose level is rather uncertain. Even after imposing $\not{E}_T$ >25 GeV cut, the amount of QCD is still high, especially in high-m_{T} region above 100 GeV. To reduce this background additional requirements are imposed:

[7] Produced in $c\bar{c}$ and $b\bar{b}$ processes for example.

- the electron cluster is required to be isolated from other energy depositions in the calorimeter, and
- the $\not\!\!E_T$ in the event is required to be balanced (in magnitude) with the electron E_T .

The isolation energy is measured using the calorimeter transverse energy in a cone $\Delta R < 0.4$ which simply sums all calorimeter energy in a cone minus the energy in the electron cluster (5×7 cells in the barrel and 5×5 cells in the endcap), and makes an additional correction for leakage of the electron energy into the surrounding isolation region. This leakage effect has been observed both in data and in Monte Carlo. In `Athena` release 15, the leakage correction has been taken from the Monte Carlo estimates, and this is expected to be replaced by the data-driven estimation for the analysis of 2011 data.

The isolation energy is required to be below a fixed threshold:

$$\sum E_T < 10 \text{ GeV} \tag{7.2}$$

The advantage of this corrected variable is that one can have a single cut which provides good discrimination against background for a fixed signal efficiency over a wide range of electron E_T . The other possibility is to apply the same isolation as in the muon channel using sum of momentum of tracks around electron track (normalized to the electron transverse energy). The distributions of calorimeter energy, and relative track-based isolation, plotted after preselection, are shown in Fig7.5. One can observe, that the effect of the relative track isolation (with the same cut of 0.05 as in the muon analysis) is similar (if not even higher) against QCD background than calorimeter isolation. However, the effect of the track isolation on the tail of m_{T} distribution is not as powerful as calorimeter isolation. This is demonstrated in Fig7.6, where m_{T} distributions are shown for events passing calorimeter and track isolation receptively. Data to MC ratio is significantly worse in the broad range of high-m_{T} region 100 GeV $< m_T <$250 GeV for the events that pass track isolation with respect to the the same distribution of events passing calorimeter isolation. Also, more events in data fail in QCD dominated low-m_{T} region $< m_T <$50 GeV if track isolation is used. These results indicate more QCD contamination if the track isolation is used instead of calorimeter isolation. Furthermore, the approach based on summing momentum of charged tracks measured by the ID is not sensitive to any energy from neutral particles. On the other side the distribution of calorimeter energy in Monte Carlo is shifted with respect to the data, with the shapes quite similar for both distributions. The observed shift is most likely related to the noise and/or cross-talk in the calorimeter not being modeled quite correctly. The effect of this shift is expected to be small, for a conservatively chosen cut on the value of calorimeter isolation.

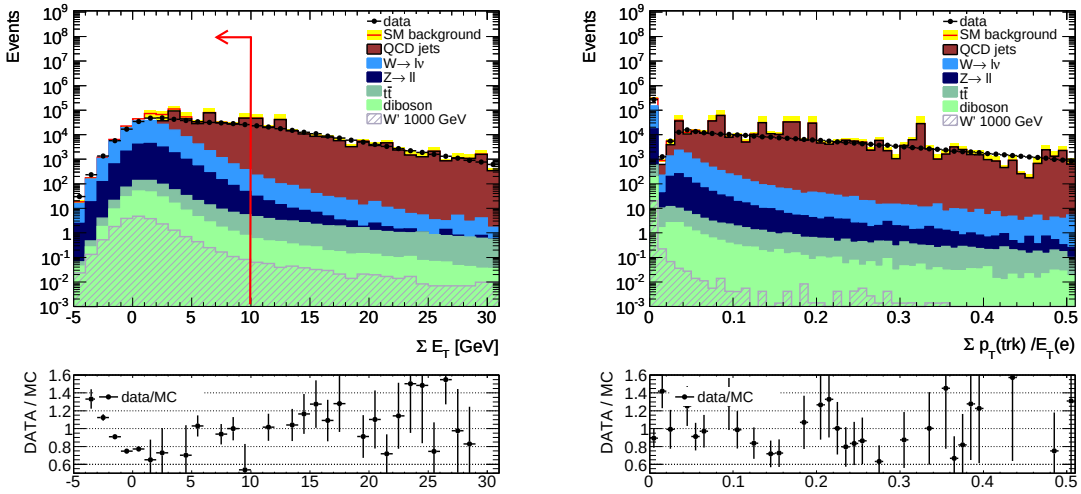

(a) (b)

Figure 7.5: Calorimeter isolation (a) and relative track isolation (b) in data and MC events after preselection. QCD is estimated from simulation, with cross sections arbitrarely scaled by 0.5 in order MC to match the data in the region where QCD should dominate over other backgrounds.

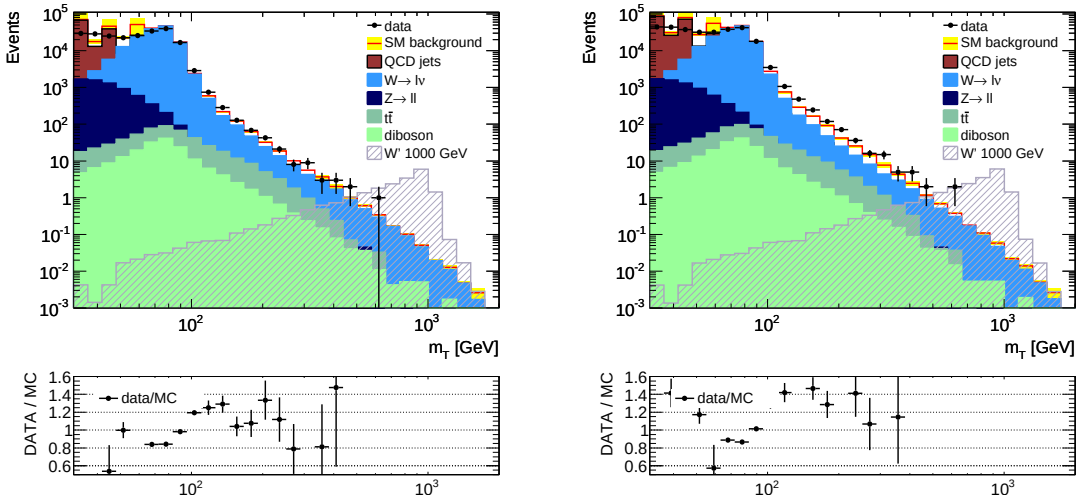

(a) (b)

Figure 7.6: Transverse mass distributions in data and MC after preselection and calorimeter isolation $\sum E_T < 10$ GeV (a) and track isolation $\Sigma p_T^{trk}/E_T(e) < 0.05$ (b). QCD is estimated from simulation, with cross sections arbitrarily scaled by 0.5 in order MC to match the data in the region where QCD should dominate.

Figure 7.7 shows the distributions of calorimeter isolation variable in data, obtained for different electron E_T bins (the bins were chosen according to the available statistics in the whole 2010 data sample). For this distribution, the selection is tightened, in the way that electrons are required to pass Tight identification, and events are required to have $\not\!\!E_T > 35$ GeV. These re-

quirements insure that the selected events contain mainly truely isolated electrons, originating from W/Z processes. This figure demonstrates that calorimeter isolation is largely independent of the electron E_T for true isolated electrons. However, some bias towards low-E_T electrons may be present, since the fraction of events that fail requirement 7.2, is increasing from (1.24±0.06)%, for the lowest E_T bin, (3.19±0.34)%, for the medium, and (5.8±1.2)% for the highest E_T bin. The discrepancy between data and simulation distribution is attributed to the leakge of energy in the surrounding cone, and systematic uncertainty is evaluted and presented in the next Section (consistuting one of the dominant signal systematic uncertainty for higher masses).

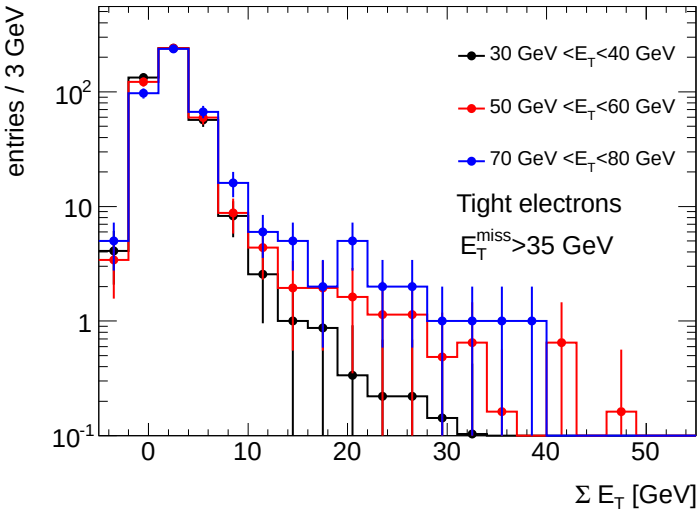

Figure 7.7: Calorimeter isolation shapes, obtained after preselection, but with electrons passing Tight identification, plus $\not{E}_T > 35$ GeV. Figure shows a comparison in data in three E_T bins. The distributions are normalized to the same area.

One of the initial motivations for track-based isolation variables was that it would likely be less sensitive to pileup. The effect of pileup on calorimeter energy around electron/photon candidate has been intensively investigated in the single isolated photon cross section measurement[15]. For this analysis, a single correction for the energy in the isolation region both from the underlying event and from pileup is derived. It has been shown that the effect of the underlying event is a shift in the isolation distribution of about 0.5 GeV and the shift due to pileup is about 1 GeV when the number of reconstructed vertices is increased in the event from 1 to 4. Given the distribution of vertices in the 2010 data (cf. Fig.5.5), this is a rather small effect and can be ignored if the cut on isolation is chosen a bit conservatively. Following this argumentation, for W' analysis a cut of 10 GeV rather than 8 GeV used for photon cross section measurement

has been imposed. This slightly more conservative cut has rather little effect on the remaining QCD background. Signal efficiency for the calorimeter isolation cut is still high, 97%-96%, decreasing with mass.

Even after isolation requrement, contamination from QCD retains high, especially in high-m_{T} events. This can be demonstrated by looking for example at $\not\!\!E_T\ / E_T$ distribution. Since the W has a relatively small transverse momentum (the same holds for W'), the $\not\!\!E_T\ / E_T$ distribution is expected to peak around unity and to take low values in dijet events where the $\not\!\!E_T$ largely comes from the mismeasurement of one of the jets. This is illustrated in Fig7.8, that shows $\not\!\!E_T\ / E_T$ in data and MC for events passing all selection critera including isolation requirement and $\not\!\!E_T$ >25 GeV. First distribution is plotted in events with low m_{T} (<40 GeV), where QCD obviously dominates. The other distribution is plotted in events with high m_{T} (>100 GeV). The same distribution is obtained for the muon channel, Fig5.26(b). It is obvious that contamination from QCD is still high, and that QCD should be estimated using data-driven techniques, and not from the simulation.

A selection requirement:

$$\not\!\!E_T\ / E_T\ > 0.6 \tag{7.3}$$

suppresses a large fraction of QCD background while staying very efficient on both the $W \to e\nu$ and $W' \to e\nu$ events. The efficiency on $W' \to e\nu$ samples is above 97%, as shown in the cuflow tables7.5.

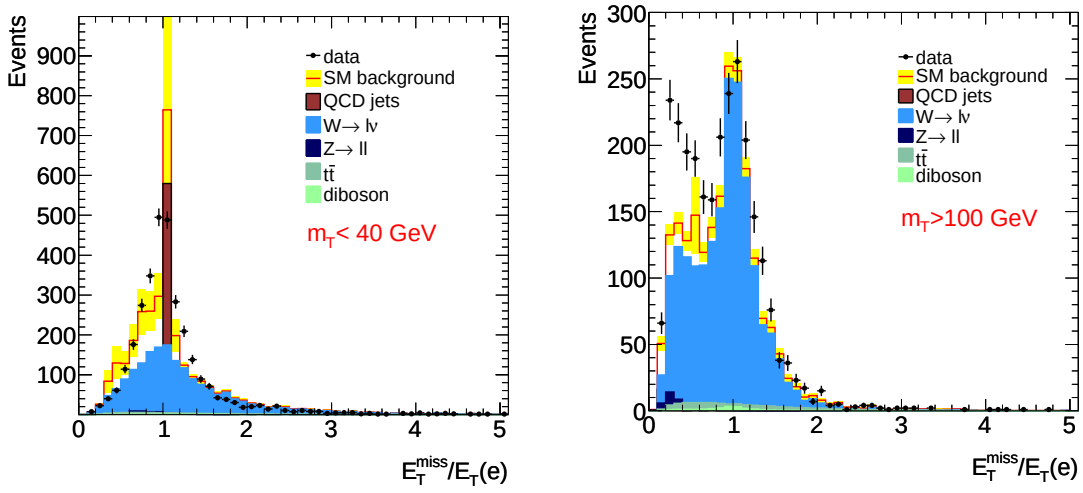

(a) (b)

Figure 7.8: $\not\!\!E_T\ / E_T$ in events with m_{T} <40 GeV (a) and m_{T} >100 GeV (b). Events pass all selection cuts including calorimeter isolation and $\not\!\!E_T$ >25 GeV.

The selection requirement is chosen to be asymmetric in order to maximize selection efficiency, since contamination on high-m_{T} events from QCD with high $\not\!\!E_T \ / E_T$ is small. The effect of this selection requirement on electron E_T and m_{T} spectra in data is illustrated in Fig7.9.

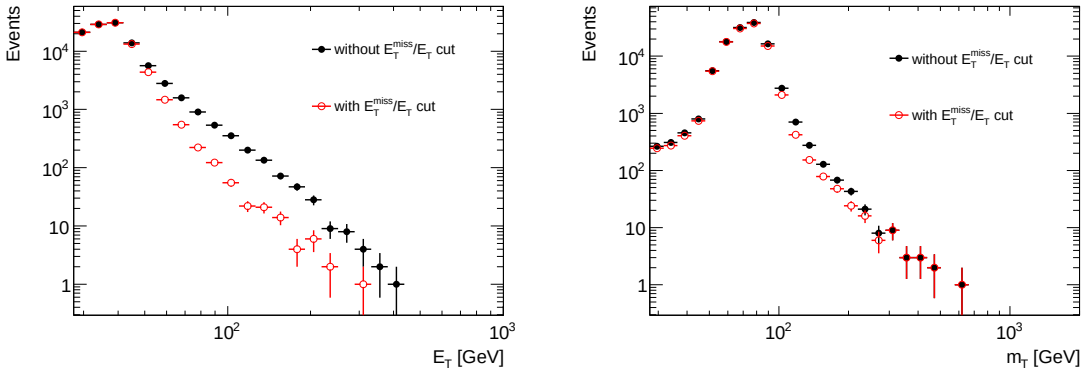

(a) (b)

Figure 7.9: E_T (a) and m_{T} (b) distribution in data without and with $\not\!\!E_T \ /E_T \ > 0.6$ selection requirement applied. Events pass all other selection criteria.

7.1.6 Initial results

The cut flow for the sample of collision data corresponding to integrated luminosity of 36.39 pb^{-1} is presented in Table 7.4. The cut flows for used Monte Carlo samples are presented after that in Tables 7.5,7.6, and 7.7. One important note for the cut flow from simulated samples, is that the efficiency corrections presented in the subsection 6.3.1 and listed in Table 7.3, are applied together with the cut $|\eta_{cl}|$ <2.4.

As in the muon analysis, events that would come from $W' \to \tau\nu$ process, where τ-lepton would decay into a electron and corresponding neutrinos, are filtered out before event selection is applied. This contribution to the signal is completely ignored.

Table 7.8 shows the number of observed and expected number of events after all selection criteria, and after a serie of m_{T}-threshold cuts. No excess above expectation provided by the Standard Model is observed. This conclusion is further validated by comparing data and simulated distributions shown in Fig7.1.6. As in the muon channel, there is a difference between data and MC around W-peak, but the agreement is much better on the tail of the m_{T} distribution. As stressed before, QCD contribution has to be replaced by the data-driven estimate, but this contribution is expected to be small after all imposed cuts, and not to change this conclusion. Table 7.9 gives selection efficiencies for W' and W^* for masses in range 500-1750 GeV. No additional corrections, except efficiency correction from section 6.3.1, are applied. Finally Table7.10 gives

Table 7.4: Cut flow of events in collision data for $W' \to e\nu$ search. In brackets, relative efficiency of a selection requirement with respect to previous requirement is given.

Selection requirement	Number of events (ε_{rel})
GRL	181293024
Preselection	17308998
egamma candidate	16699880 (96.4%)
$\lvert\eta_{cl}\rvert < 2.47$, no crack	16412343 (98.3%)
$E_T > 25$ GeV	5909856 (36.0%)
Medim identification	1044434 (17.7%)
B-layer hit	639043 (61.2%)
OTx	598190 (93.6%)
Impact par. cuts	569702 (95.2%)
Trigger Match	569353 (99.9%)
Exactly one electron	561448 (98.6%)
$\lvert\eta_{cl}\rvert < 2.4$	547960 (97.6%)
Exclude ($-1.4 < \eta_{cl} < 0$ and $1.96 < \phi_{cl} < 2.15$)	541430 (98.8%)
Isolation	386670 (71.4%)
$\not{E}_T > 25$ GeV	119650 (30.9%)
$\not{E}_T / E_T > 0.6$	113570 (94.9%)

the list of 24 events passing all selection cuts and m_{T} >250 GeV, with the highest-m_{T} event of 603 GeV bolded. The event display of this event is presented in Fig7.11.

Table 7.5: Cut flow of events in $W' \to e\nu$ MC signal samples. Numbers in the table represent fraction of events satisfying a particular selection requirement calculated with respect to the previous requirement. Before selection requirements are applied, events from $W' \to \tau\nu$ and $W' \to \mu\nu$ processes are filtered out from the samples. Generator cut corresponds to the fraction of $W' \to e\nu$ events. Quoted uncertainties are statistical.

MC sample	W'(500 GeV)	W'(750 GeV)	W'(1000 GeV)	W'(1250 GeV)	W'(1500 GeV)	W'(1750 GeV)
Generator cut	0.3319±0.0023	0.3345±0.0024	0.3343±0.0024	0.3349±0.0029	0.3318±0.0033	0.3369±0.0034
Trigger	0.9512±0.0023	0.9702±0.0023	0.9747±0.0023	0.9711±0.0028	0.9744±0.0033	0.9710±0.0033
Vertex cut	0.9866±0.0023	0.9863±0.0023	0.9871±0.0023	0.9863±0.0028	0.9871±0.0033	0.9871±0.0033
Jet cleaning	0.9992±0.0023	0.9995±0.0023	0.9992±0.0023	0.9993±0.0028	0.9992±0.0033	0.9956±0.0033
`egamma` candidate	0.9937±0.0023	0.9949±0.0023	0.9962±0.0023	0.9989±0.0028	0.9956±0.0033	0.9950±0.0033
$\lvert\eta_{cl}\rvert < 2.47$	0.9976±0.0023	0.9987±0.0023	0.9988±0.0023	0.9989±0.0028	0.9987±0.0033	0.9985±0.0033
Exclude crack	0.9693±0.0022	0.9753±0.0022	0.976212±0.0022	0.9777±0.0028	0.9800±0.0032	0.9777±0.0032
$E_T > 25$ GeV	0.9723±0.0021	0.9749±0.0022	0.9788±0.0021	0.9798±0.0028	0.9761±0.0032	0.9792±0.0031
Medium	0.9340±0.0021	0.9349±0.0021	0.9377±0.0021	0.9339±0.0027	0.9368±0.0032	0.9367±0.0030
B-layer	0.9794±0.0021	0.9842±0.0021	0.9853±0.0021	0.9851±0.0026	0.9883±0.0032	0.9879±0.0029
OTx	0.9167±0.0020	0.9095±0.0020	0.9139±0.0020	0.9132±0.0025	0.9104±0.0031	0.9159±0.0029
Impact par. cuts	0.9994±0.0020	0.9996±0.0020	1.0000±0.0020	1.0000±0.0025	0.9999±0.0030	0.9999±0.0029
Trigger Match	0.9994±0.0020	0.9988±0.0020	0.9989±0.0020	0.9991±0.0025	0.9986±0.0029	0.9993±0.0029
Exactly one electron	0.9994±0.0020	0.9996±0.0020	0.9996±0.0020	0.9999±0.0025	0.9994±0.0029	0.9996±0.0029
$\lvert\eta_{cl}\rvert < 2.4$	0.9719±0.0020	0.9736±0.0020	0.9738±0.0020	0.9747±0.0025	0.9738±0.0029	0.9744±0.0.0029
Exclude ($-1.4 < \eta_{cl} < 0$ and $1.96 < \phi_{cl} < 2.15$)	0.9846±0.0020	0.9873±0.0020	0.9859±0.0021	0.9826±0.0024	0.9860±0.0028	0.9744±0.0028
Isolation	0.9765±0.0020	0.9687±0.0020	0.9644±0.0020	0.9746±0.0024	0.9619±0.0028	0.9628±0.0028
$\not{E}_T > 25$ GeV	0.9972±0.0019	0.9984±0.0020	0.9988±0.0020	0.9986±0.0024	0.9987±0.0028	0.9984±0.0028
$\not{E}_T/E_T > 0.6$	0.9681±0.0019	0.9791±0.0020	0.9859±0.0020	0.9877±0.0024	0.9903±0.0028	0.9889±0.0028
Overall	0.2195±0.0019	0.2298±0.0020	0.2348±0.0020	0.2341±0.0024	0.2322±0.0028	0.2375±0.0028

MC sample	W^*(500 GeV)	W^*(750 GeV)	W^*(1000 GeV)	W^*(1250 GeV)	W^*(1500 GeV)	W^*(1750 GeV)
Trigger	0.9930 ± 0.0070	0.9942±0.0023	0.9963±0.0023	0.9966±0.0023	0.9972±0.0023	0.9982±0.0023
Vertex cut	0.9861 ± 0.0070	0.9863±0.0023	0.9861±0.0023	0.9860±0.0023	0.9863±0.0023	0.9861±0.0023
Jet cleaning	0.9997 ± 0.0070	0.9995±0.0023	0.9994±0.0023	0.9994±0.0023	0.9992±0.0023	0.9994±0.0023
`egamma` candidate	0.9901 ± 0.0070	0.9935±0.0023	0.9936±0.0023	0.9940±0.0023	0.9943±0.0023	0.9949±0.0023
$\lvert\eta_{cl}\rvert < 2.47$	0.9966 ± 0.0069	0.9969±0.0023	0.9977±0.0023	0.9978±0.0023	0.9979±0.0023	0.9978±0.0023
Exclude $1.37 < \lvert\eta_{cl}\rvert < 1.52$	0.9600 ± 0.0068	0.9589±0.0022	0.9564±0.0022	0.9558±0.0022	0.9553±0.0022	0.9504±0.0022
$E_T > 25$ GeV	0.9739 ± 0.0067	0.9722±0.0021	0.9747±0.0021	0.9728±0.0021	0.9704±0.0021	0.9733±0.0021
Medium	0.9508 ± 0.0066	0.9525±0.0021	0.9514±0.0021	0.9584±0.0021	0.9564±0.0021	0.9548±0.0021
B-layer	0.9748 ± 0.0065	0.978±0.0021	0.981±0.0021	0.9802±0.0021	0.9823±0.0021	0.9820±0.0021
OTx	0.9096 ± 0.0062	0.9151±0.0020	0.9138±0.0020	0.9158±0.0020	0.9130±0.0020	0.9820±0.0020
Impact par. cuts	0.9995 ± 0.0062	0.9995±0.0020	0.9998±0.0020	0.9997±0.0020	0.9998±0.0020	0.9185±0.0020
Trigger Match	0.9995 ± 0.0062	0.9998±0.0020	0.9993±0.0020	0.9997±0.0020	0.9997±0.0020	1.0000±0.0020
Exactly one electron	0.9999 ± 0.0062	0.9999±0.0020	0.9998±0.0020	0.9996±0.0020	0.9997±0.0020	0.9996±0.0020
$\lvert\eta_{cl}\rvert < 2.4$	0.9651 ± 0.0061	0.9652±0.0020	0.9690±0.0020	0.9700±0.0020	0.9687±0.0020	0.9997±0.0020
Exclude ($-1.4 < \eta_{cl} < 0$ and $1.96 < \phi_{cl} < 2.15$)	0.9888 ± 0.0060	0.9884±0.0020	0.9881±0.0020	0.9893±0.0020	0.9876±0.0020	0.9705±0.0020
Isolation	0.9857 ± 0.0060	0.9814±0.0020	0.9820±0.0020	0.9785±0.0020	0.9765±0.0020	0.9882±0.0020
$\not{E}_T > 25$ GeV	0.9976 ± 0.0060	0.9997±0.0020	0.9998±0.0020	1.0000±0.0020	1.0000±0.0020	0.9733±0.0020
$\not{E}_T/E_T > 0.6$	0.9932 ± 0.0060	0.9970±0.0020	0.9983±0.0020	0.9994±0.0020	0.9992±0.0020	1.0000±0.0020
Overall	0.7111 ± 0.0060	0.7199±0.0019	0.7257±0.0019	0.7306±0.0019	0.7232±0.0019	0.7256±0.0019

Table 7.6: Cut flow of events in W/Z MC background samples. Events with $M(W) >$200 GeV and $M(Z) >$250 GeV are filtered out from the inclusive $W \to e\nu$, $W \to \tau\nu$, and $Z \to ee$ samples. Generator cuts correspond to the fraction of events that pass true mass requirements.

	$W \to e\nu$	$W \to \tau\nu$	W200M500	W500M1500	W1500M2500
Generator cut*	0.9997±0.0015	0.9997±0.0015	1.0000±0.0058	1.0000±0.0058	1.0000±0.0058
Trigger	0.6498±0.0011	0.1502±0.0004	0.5296±0.0037	0.6418±0.0042	0.7017±0.0045
Vertex cut	0.9861±0.0019	0.9855±0.0038	0.9861±0.0079	0.9863±0.0071	0.9857±0.0068
Jet cleaning	0.9996±0.0019	0.9994±0.0039	0.9974±0.0080	0.9957±0.0072	0.9926±0.0069
egamma cand.	0.9802±0.0019	0.9619±0.0038	0.9794±0.0079	0.9852±0.0072	0.9860±0.0069
$\lvert\eta_{cl}\rvert < 2.47$	0.9918±0.0019	0.9930±0.0039	0.9963±0.0081	0.9990±0.0073	0.9993±0.0070
Exclude crack	0.9689±0.0019	0.9800±0.0039	0.9646±0.0079	0.9747±0.0072	0.9823±0.0069
$E_T >$ 25 GeV	0.7724±0.0016	0.4061±0.0021	0.8563±0.0074	0.9079±0.0069	0.9290±0.0067
Medium	0.9133±0.0021	0.7124±0.0049	0.6717±0.0067	0.6057±0.0054	0.5853±0.0050
B-layer	0.9531±0.0023	0.9508±0.0072	0.9658±0.0106	0.9725±0.0098	0.9523±0.0093
OTx	0.9224±0.0023	0.9275±0.0072	0.9183±0.0104	0.9132±0.0095	0.9129±0.0092
Impact par. cuts	0.9918±0.0025	0.9999±0.0079	0.9999±0.0116	0.9999±0.0106	0.9999±0.0103
Trigger Match	0.9910±0.0025	0.9885±0.0079	0.9983±0.0115	0.9987±0.0106	0.9989±0.0103
Exactly one electron	0.9999±0.0025	0.9998±0.0080	0.9995±0.0116	0.9994±0.0106	0.9993±0.0103
$\lvert\eta_{cl}\rvert < 2.4$	0.9565±0.0024	0.9562±0.0077	0.9685±0.0113	0.9736±0.0104	0.9759±0.0101
Exclude η-ϕ	0.9892±0.0026	0.9891±0.0081	0.9861±0.0116	0.9848±0.0107	0.9845±0.0103
Isolation	0.9945±0.0026	0.9970±0.0082	0.9810±0.0117	0.9663±0.0106	0.9455±0.0101
$\not\!\!E_T >$ 25 GeV	0.8521±0.0023	0.6259±0.0059	0.9814±0.0118	0.9940±0.0110	0.9981±0.0108
$\not\!\!E_T/E_T > 0.6$	0.9561±0.0027	0.9765±0.0102	0.9577±0.0117	0.9768±0.0109	0.9900±0.0108
Overall	0.2812±0.0006	0.0201±0.0002	0.2195±0.0021	0.2648±0.0024	0.2810±0.0025

	$Z \to ee$	$Z \to \tau\tau$	Z_{ee}250M400	Z_{ee}400M600	Z_{ee}600M800	Z_{ee}800M1000	Z_{ee}1000M1250	Z_{ee}1250M1500
Generator cut*	0.9994±0.0014	1.0000±0.0010	1.0000±0.0100	1.0000±0.0100	1.0000±0.0100	1.0000±0.0100	1.0000±0.0100	1.0000±0.0100
Trigger	0.8380±0.0012	0.2962±0.0005	0.9880±0.0099	0.9938±0.0100	0.9947±0.0100	0.9953±0.0100	0.9940±0.0100	0.9933±0.0100
Vertex cut	0.9867±0.0015	0.9869±0.0019	0.9868±0.0100	0.9869±0.0099	0.9872±0.0099	0.9872±0.0099	0.9873±0.0099	0.9873±0.0099
Jet cleaning	0.9995±0.0016	0.9861±0.0019	0.9995±0.0101	0.9992±0.0101	0.9990±0.0101	0.9988±0.0101	0.9992±0.0101	0.9991±0.0101
egamma cand.	0.9925±0.0016	0.9547±0.0019	0.9972±0.0101	0.9987±0.0101	0.9989±0.0101	0.9991±0.0101	0.9992±0.0101	0.9996±0.0101
$\lvert\eta_{cl}\rvert < 2.47$	0.9957±0.0016	0.9955±0.0020	0.9992±0.0101	0.9997±0.0101	0.9997±0.0101	0.9999±0.0101	0.9998±0.0101	0.9997±0.0101
Exclude crack	0.9856±0.0016	0.9850±0.0019	0.9896±0.0101	0.9929±0.0101	0.9950±0.0101	0.9960±0.0101	0.9962±0.0101	0.9966±0.0101
$E_T >$ 25 GeV	0.8562±0.0014	0.4091±0.0011	0.9837±0.0101	0.9919±0.0101	0.9951±0.0101	0.9959±0.0101	0.9962±0.0101	0.9963±0.0101
Medium	0.9563±0.0017	0.2922±0.0013	0.9743±0.0101	0.9802±0.0100	0.9840±0.0100	0.9864±0.0100	0.9877±0.0100	0.9877±0.0100
B-layer	0.9718±0.0017	0.8990±0.0053	0.9884±0.0103	0.9934±0.0102	0.9939±0.0102	0.9941±0.0102	0.9949±0.0102	0.9960±0.0102
OTx	0.9536±0.0017	0.9277±0.0057	0.9617±0.0102	0.9665±0.0101	0.9678±0.0100	0.9712±0.0100	0.9717±0.0100	0.9722±0.0100
Impact par. cuts	0.9967±0.0018	0.9992±0.0063	1.0000±0.0107	1.0000±0.0105	1.0000±0.0104	0.9999±0.0104	1.0000±0.0104	1.0000±0.0104
Trigger Match	0.9952±0.0018	0.9889±0.0063	0.9989±0.0107	0.9995±0.0105	0.9997±0.0104	0.9995±0.0104	0.9996±0.0104	0.9999±0.0104
Exactly one electron	0.6157±0.0013	0.9890±0.0063	0.5041±0.0066	0.4424±0.0059	0.4081±0.0056	0.3842±0.0054	0.3648±0.0052	0.3599±0.0051
$\lvert\eta_{cl}\rvert < 2.4$	0.9517±0.0022	0.9558±0.0062	0.9669±0.0147	0.9683±0.0154	0.9705±0.0160	0.9717±0.0164	0.9721±0.0168	0.9710±0.0169
Exclude η - ϕ	0.9881±0.0024	0.9890±0.0065	0.9826±0.0151	0.9840±0.0159	0.9832±0.0164	0.9830±0.0168	0.9805±0.0172	0.9809±0.0173
Isolation	0.9935±0.0024	0.9924±0.0065	0.9818±0.0152	0.9781±0.0159	0.9710±0.0164	0.9681±0.0167	0.9625±0.0171	0.9620±0.0172
$\not\!\!E_T >$ 25 GeV	0.0266±0.0003	0.2865±0.0028	0.0920±0.0035	0.1516±0.0048	0.2037±0.0059	0.2601±0.0071	0.3053±0.0080	0.3572±0.0089
$\not\!\!E_T/E_T > 0.6$	0.6941±0.0113	0.9471±0.0118	0.2561±0.0206	0.1729±0.0134	0.1469±0.0109	0.1134±0.0086	0.1058±0.0079	0.0961±0.0069
Overall	0.0064±0.0001	0.0066±0.0001	0.0097±0.0007	0.0098±0.0007	0.0104±0.0007	0.0097±0.0007	0.0100±0.0007	0.0105±0.0007

Table 7.7: Cut flow of events in $t\bar{t}$, diboson and QCD background samples.

	$t\bar{t}$	WW	WZ	ZZ
Trigger	0.8822±0.0013	0.6406±0.0021	0.6374±0.0020	0.6598±0.0022
Vertex cut	0.9870±0.0015	0.9874±0.0035	0.9867±0.0035	0.9874±0.0036
Jet cleaning	0.9927±0.0015	0.9961±0.0036	0.9952±0.0036	0.9951±0.0036
egamma cand.	0.9997±0.0015	0.9908±0.0036	0.9924±0.0036	0.9945±0.0036
$\lvert\eta_{cl}\rvert < 2.47$	0.9999±0.0015	0.9982±0.0036	0.9986±0.0036	0.9988±0.0036
Exclude crack	0.9994±0.0015	0.9893±0.0036	0.9905±0.0036	0.9943±0.0036
$E_T > 25$ GeV	0.7400±0.0012	0.7004±0.0028	0.7121±0.0028	0.7251±0.0029
Medium	0.3899±0.0009	0.7011±0.0034	0.6826±0.0032	0.6495±0.0031
B-layer	0.9650±0.0028	0.9607±0.0050	0.9653±0.0050	0.9740±0.0052
OTx	0.9227±0.0027	0.9213±0.0050	0.9302±0.0050	0.9484±0.0052
Impact par. cuts	0.9999±0.0030	1.0000±0.0055	1.0000±0.0055	1.0000±0.0055
Trigger Match	0.9928±0.0030	0.9932±0.0055	0.9944±0.0054	0.9962±0.0055
Exactly one electron	0.9626±0.0029	0.9699±0.0054	0.8694±0.0049	0.6490±0.0041
$\lvert\eta_{cl}\rvert < 2.4$	0.9728±0.0030	0.9636±0.0055	0.9637±0.0057	0.9606±0.0067
Exclude η - ϕ	0.9856±0.0031	0.9879±0.0057	0.9881±0.0059	0.9877±0.0070
Isolation	0.9256±0.0030	0.9800±0.0057	0.9798±0.0059	0.9683±0.0069
$\not{E}_T > 25$ GeV	0.8432±0.0029	0.7880±0.0049	0.6747±0.0046	0.3231±0.0033
$\not{E}_T/E_T > 0.6$	0.8152±0.0031	0.8357±0.0058	0.8364±0.0065	0.8073±0.0108
Overall	0.1292±0.0004	0.1584±0.0009	0.1219±0.0007	0.0431±0.0004

	$J0$	$J1$	$J2$	$J3$	$J4$	$J5$	$J6$
Trigger	0.000085±0.000009	0.009319±0.00009	0.1770±0.0004	0.7357±0.0010	0.9890±0.0011	0.9999±0.0012	0.999±0.0012
Vertex cut	0.99±0.14	0.99±0.013	0.987±0.003	0.987±0.001	0.987±0.0012	0.9870±0.0012	0.9863±0.0012
Jet cleaning	1.00±0.15	0.99±0.014	0.998±0.003	0.999±0.001	0.998±0.001	0.998±0.001	0.998±0.001
egamma cand.	0.63±0.10	0.84±0.012	0.972±0.003	0.997±0.001	0.999±0.001	0.999±0.001	1.000±0.001
$\lvert\eta_{cl}\rvert < 2.47$	1.00±0.18	0.994±0.015	0.997±0.003	0.999±0.001	0.999±0.001	0.999±0.001	1.000±0.001
Exclude crack	0.98±0.18	0.99±0.015	0.991±0.003	0.996±0.0014	0.998±0.0012	0.9996±0.0012	0.9996±0.0012
$E_T > 25$ GeV	-	0.0665±0.0028	0.22±0.001	0.548±0.001	0.921±0.001	0.996±0.001	0.999±0.001
Medium	-	0.037±0.008	0.0217±0.0007	0.006±0.0001	0.004±0.0006	0.0044±0.0006	0.0045±0.0006
B-layer	-	0.55±0.20	0.595±0.03	0.63±0.017	0.609±0.0140	0.641±0.014	0.641±0.014
OTx	-	1.00±0.40	0.906±0.06	0.927±0.028	0.913±0.023	0.915±0.021	0.92±0.02
Impact par cuts	-	1.00±0.43	0.982±0.06	0.987±0.03	0.992±0.027	0.997±0.023	0.997±0.023
Trigger Match	-	1.00±0.42	0.987±0.06	0.977±0.03	0.987±0.027	0.986±0.02	0.988±0.024
Exactly one electron	-	1.00±0.43	1.00±0.06	1.00±0.04	0.997±0.027	0.999±0.024	0.999±0.024
$\lvert\eta_{cl}\rvert < 2.4$	-	0.89±0.39	0.934±0.06	0.941±0.031	0.944±0.026	0.965±0.023	0.97±0.02
Exclude η - ϕ	-	1.0±0.45	0.989±0.06	0.989±0.033	0.989±0.028	0.988±0.024	0.985±0.024
Isolation	-	0.80±0.39	0.644±0.045	0.295±0.014	0.18±0.010	0.134±0.007	0.106±0.006
$\not{E}_T > 25$ GeV	-	0.123±0.133	0.017±0.007	0.067±0.012	0.206±0.023	0.404±0.036	0.659±0.058
$\not{E}_T/E_T > 0.6$	-	1.00±0.446	0.838±0.516	0.667±0.17	0.406±0.078	0.516±0.066	0.663±0.0689
Overall	-	0.000001±0.000001	0.000004±0.000002	0.00002±0.000003	0.00003±0.000004	0.00007±0.000007	0.0001±0.00001

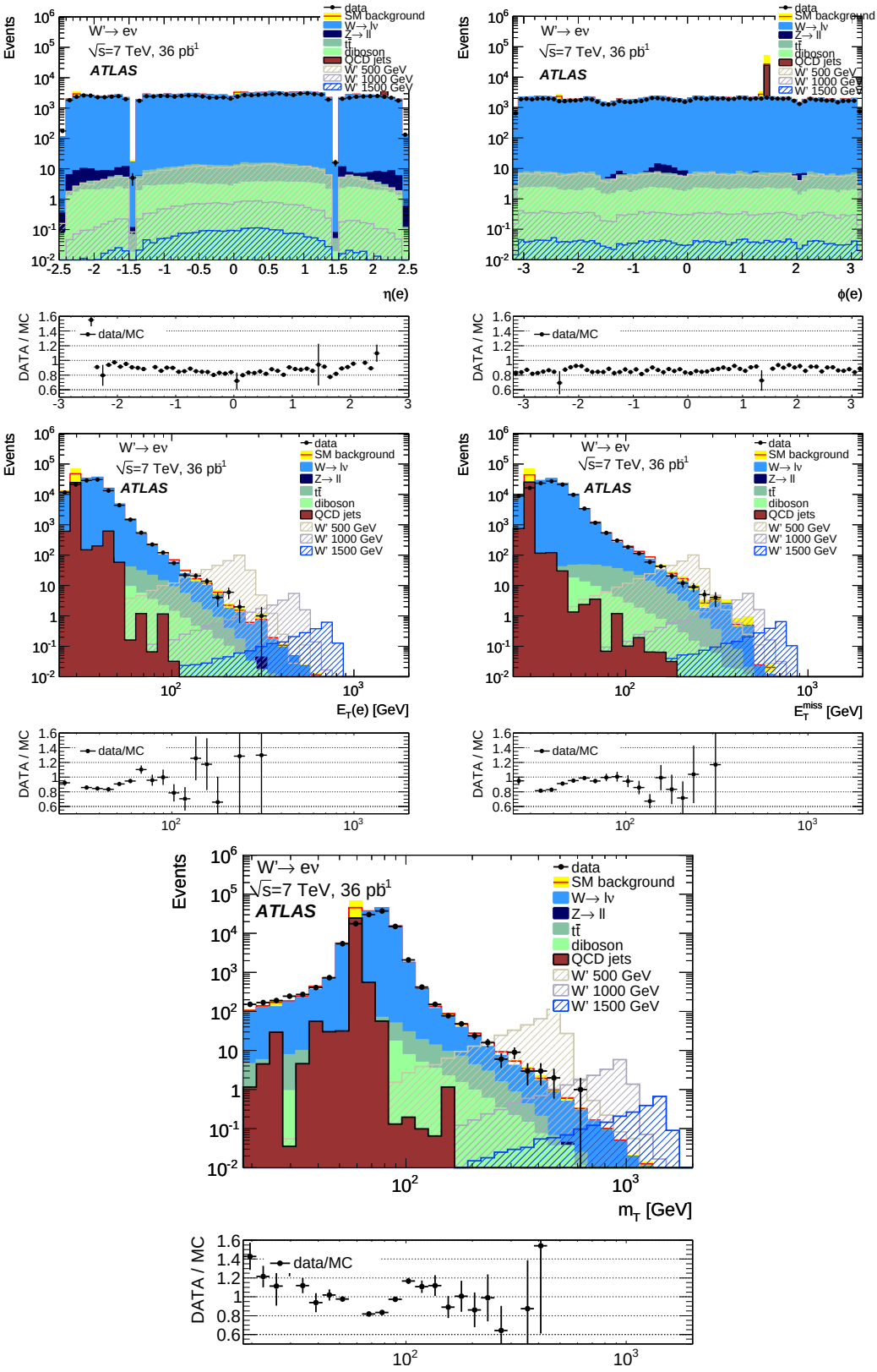

Figure 7.10: Uncorrected η , ϕ, E_T , $\not\!\!E_T$ and m_{T} distributions after all selection criteria applied. MC is normalized using theoretical cross sections, as explained in the text. Yellow uncertainty band is statistical only.

Table 7.8: Number of observed events in data, and expected number of events obtained from background and W' signal MC samples normalized to the integrated luminosity of $\mathscr{L}_{\rm int}$=36.39 pb^{-1} . Highest-order available cross sections are used for signal and background calculation, expect for QCD where LO cross sections are used. The last six columns give the number of selected events after the indicated m_T cut is applied. Quoted uncertainties are statistical only.

	$\not\!\!E_T >$ 25 GeV	$m_{\rm T} >$ 250 GeV	$m_{\rm T} >$ 375 GeV	$m_{\rm T} >$ 500 GeV	$m_{\rm T} >$ 625 GeV	$m_{\rm T} >$ 750 GeV	$m_{\rm T} >$ 875 GeV
Data	113570	**24**	**6**	**1**	**0**	**0**	**0**
SM BG	154329± 13200	**22.95± 0.13**	**4.50± 0.05**	**1.31±0.02**	**0.48 ± 0.01**	**0.202 ± 0.003**	**0.09 ± 0.01**
$W \to \ell\nu$	127082± 271	18.62 ± 0.09	3.91 ± 0.03	1.145 ± 0.004	0.439 ± 0.002	0.184 ± 0.002	0.082 ± 0.001
$Z \to \ell\ell$	339.44±6	0.20 ± 0.02	0.04 ± 0.01	0.032 ± 0.000	0.001 ± 0.000	0.000 ± 0.000	0.000 ± 0.000
$t\bar{t}$	418.07±1	3.17 ± 0.10	0.35 ± 0.03	0.058 ± 0.014	0.022 ± 0.009	0.003 ± 0.003	0.000 ± 0.000
diboson	125.55±1	0.96 ± 0.01	0.20 ± 0.01	0.065 ± 0.003	0.020 ± 0.001	0.014 ± 0.001	0.008 ± 0.001
QCD	26363± 13180	0.001± 0.01	0.001± 0.01	0.001 ± 0.01	0.001 ± 0.01	0.001 ± 0.01	0.001 ± 0.01
$W'(500)$	413.4±3.6	349±3.4	-	-	-	-	-
$W'(750)$	80.0±0.9	-	65.8±0.8	-	-	-	-
$W'(1000)$	21.44±0.18	-	-	17.11±0.15	-	-	-
$W'(1250)$	6.66±0.06	-	-	-	5.23±0.05	-	-
$W'(1500)$	2.24±0.03	-	-	-	-	1.71±0.03	-
$W'(1750)$	0.84± 0.01	-	-	-	-	-	0.59±0.01

Table 7.9: Event selection efficiencies after all event selection criteria and the $m_{\rm T}$ threshold equal to half of each W' mass. Results are shown for both $W' \to e\nu$ and $W^* \to e\nu$. Correction for reconstruction and identification efficiency is accounted for. The numbers in brackets represent signal efficiency of $W' \to \tau\nu$ process, which is latter ignored in the limit calculations. Uncertainties are statistical only.

mass	$\varepsilon_{\rm sig}^{\rm MC}$		
[GeV]	$W' \to e\nu$	$(W' \to \tau\nu)$	$W^* \to e\nu$
500	0.552 ± 0.007	(0.0262 ± 0.0013)	0.538 ± 0.006
750	0.562 ± 0.007	(0.0251 ± 0.0011)	0.531 ± 0.006
1000	0.566 ± 0.007	(0.0242 ± 0.0012)	0.530 ± 0.006
1250	0.555 ± 0.009	(0.0233 ± 0.0014)	0.522 ± 0.006
1500	0.530 ± 0.009	(0.0196 ± 0.0014)	0.512 ± 0.006
1750	0.513 ± 0.009	(0.0172 ± 0.0013)	0.513 ± 0.007

Table 7.10: List of high-m_{T} events in data, with event characteristics. Event with highest m_{T} is bolded.

Run	LB	Event	m_{T} [GeV]	E_T [GeV]	$\not\!\!E_T$ [GeV]	$\eta(e)$	$\phi(e)$
166786	402	49548855	316	121	229	-1.2917	-0.0469
166924	108	17272497	293	134	160	-0.5027	0.1853
167575	126	471786	282	146	145	0.0280	0.5482
167576	30	11271957	256	143	117	1.7069	-0.8895
167607	143	22186813	321	166	154	0.2267	-2.8507
161562	99	8282256	459	234	231	1.0622	2.2908
165703	127	7271146	416	203	215	0.5845	-0.2977
165815	**132**	**6783958**	**603**	**297**	**305**	**0.5372**	**2.6498**
167607	233	56120162	350	128	230	1.1610	2.6356
167680	138	38705912	255	133	127	0.5549	1.1737
167776	170	19531226	322	157	165	-1.9230	1.3356
166198	385	112940161	306	194	122	2.2866	2.2086
166786	478	76810778	326	100	264	-1.7757	-2.8501
166924	63	2756402	265	129	135	1.1945	2.1461
167576	19	6835477	477	238	237	-0.2631	1.7251
167607	204	45730121	392	201	192	0.3399	-1.0710
167661	392	9583287	333	154	174	-0.9918	2.3694
167776	149	11110375	284	124	163	1.5268	-2.8168
167776	515	178060130	338	141	205	0.88332	-0.5391
162347	199	16042786	330	163	166	0.76430	-0.2066
165632	276	21730061	256	126	129	-0.1673	1.9471
167576	285	133013102	315	156	158	1.1946	0.17120
167607	125	15488544	435	190	244	1.9444	3.1084
167776	189	27115224	312	154	157	-2.2902	-2.9850

7.2 Background estimation, corrections and uncertainties

7.2.1 QCD background estimation from data

For $W' \to e\nu$ search, several techniques have been used to estimate QCD background from data. These techniques described in detail in W' supporting note [11] have been performed by other contributors to the analysis with 2010 data. Briefly, these techniques are the following.

- The first technique, referred to as the "Inverted Electron ID" technique uses the fact that the kinematic distributions from QCD background are the same, or very similar, for jets that fail the Medium identification cut but pass the Loose identification as they are for jets that pass the Medium identification. Thus the kinematic distributions as a function of E_T , $\not\!\!E_T$, and m_{T} are determined from this reverse electron ID sample. The normalization is then determined by fitting these distributions with W/Z and $t\bar{t}$ backgrounds accounted for.

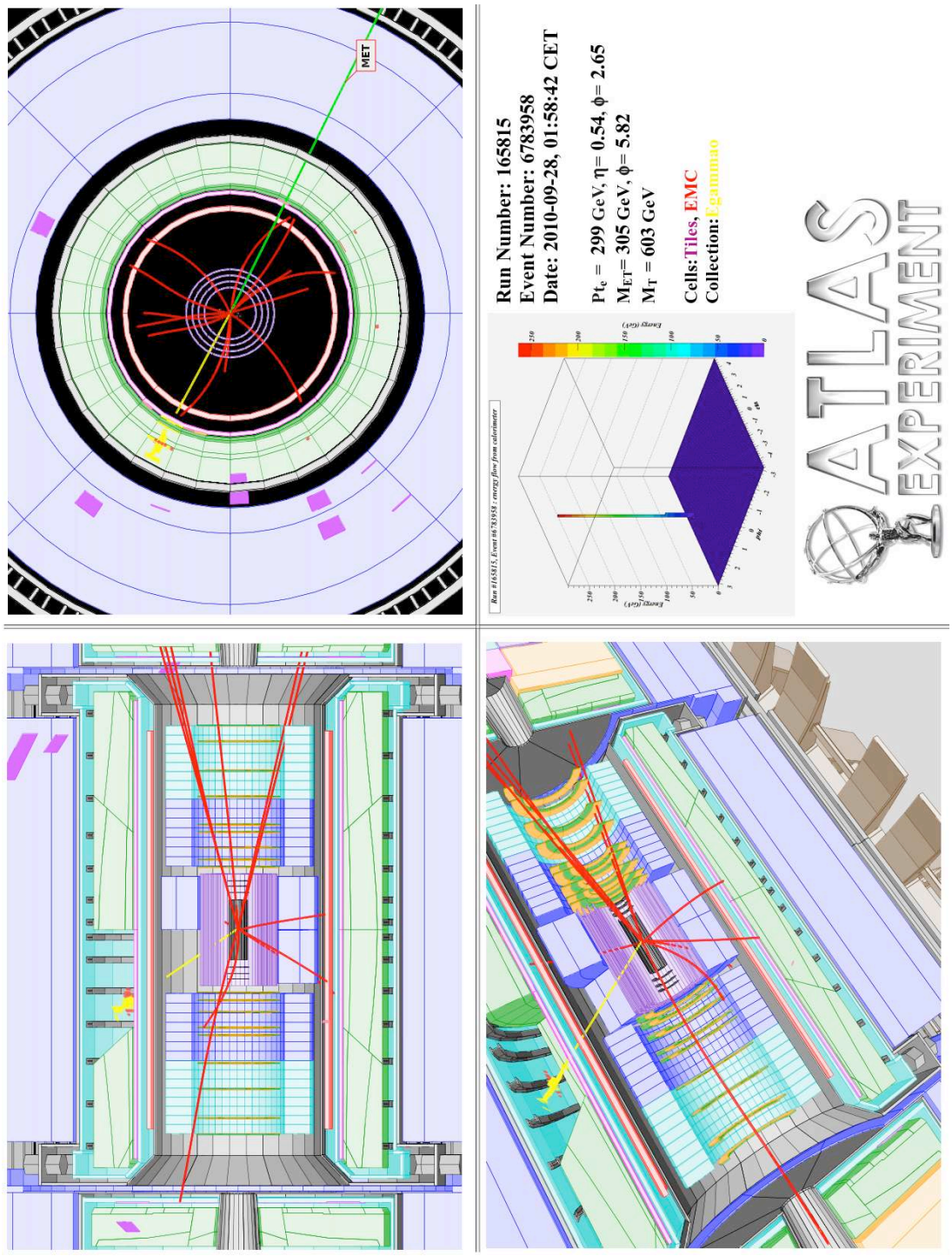

Figure 7.11: Event display of the event with the highest m_{T} (603 GeV) in 2010 dataset. Event passes all $W' \to e\nu$ selection criteria.

- The second technique, which is referred to as the "ABCD technique", assumes that calorimeter isolation (defined in section 6.1.5) is uncorrelated with $\not\!\!E_T$ for the QCD background. This is illustrated in Fig7.12, with A, B, C and D regions labeled. Region

D is the signal region ($\not\!\!E_T > 25$ GeV, E_T^{isol} <10 GeV), and QCD contamination in this region is estimated as follows:

$$N_D = \frac{N_A}{N_B} \times N_C \tag{7.4}$$

Here N_A and N_B are the total numbers of events in regions A and B, and N_C is the number of events in region C corrected for W/Z and $t\bar{t}$ contamination.

- The third technique, referred to as the "Calorimeter Isolation Template" method, uses again calorimeter isolation to estimate the background in the final signal sample based on the number of events which fail the isolation cut. The signal template, i.e. the distribution of isolation for isolated electrons, is taken from a sample of W events with the cut on $\not\!\!E_T$ tightened to $\not\!\!E_T > 35$ GeV to produce a very clean sample. Signal and background templates are fit to the observed isolation distribution to estimate the background contribution passing all selection cuts.

- The fourth technique, the "Matrix method" depends on the definition of two sets of electron identification criteria: Medium, corresponding to the selection used in this analysis, and Loose which relaxes these criteria.

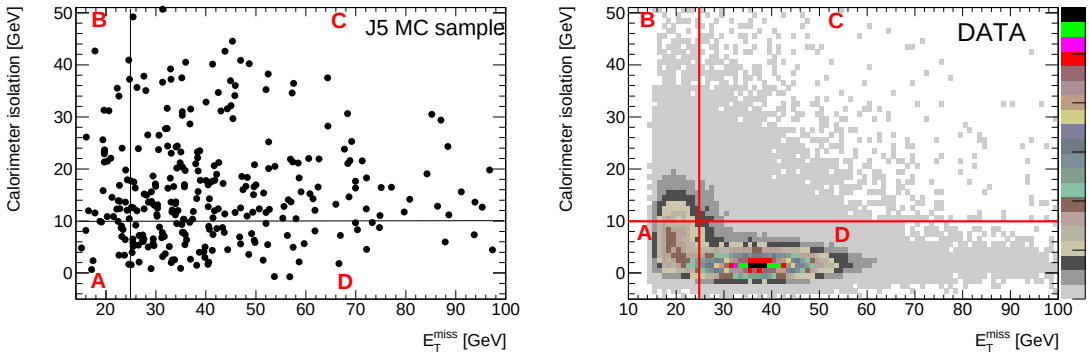

(a) (b)

Figure 7.12: (a) A,B,C and D regions in calorimeter isolation-$\not\!\!E_T$ plane in J5 MC sample. (b)A,B,C and D regions in calorimeter isolation-$\not\!\!E_T$ plane in data. Events pass preselection and $\not\!\!E_T$ / E_T requirement defined in the previous section.

To obtain the expected number of QCD background events after all selection cuts, and after a serie of different m_T-threshold cuts, results from all four techniques are combined. Once again, a power law fit[8] and extrapolation are used to obtain the numbers. Detail decsription of

[8]With the same functional form as for the muon channel: $y = p_0 \cdot x^{p_1}$

the fit, and uncertainty determination can be found elsewhere. The result of the fit is shown in Fig7.13, and estimated number of QCD events is given in Table7.11.

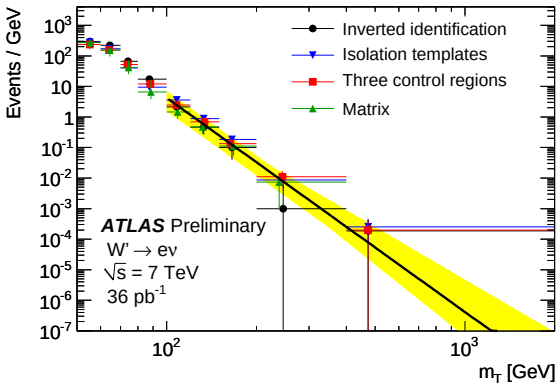

Figure 7.13: QCD background estimates from the four methods described in the text, as a function of m_{T}. Events pass all selection criteria including $\not\!\!E_T$ /E_T . The points are fitted with power law $y = p_0 \cdot x^{p_1}$. The plot is taken from [11].

Table 7.11: Number of estimated QCD background events with the indicated m_{T} threshold. Results obtained from [11].

m_{Tmin} [GeV]	QCD background (estim.)
0	$8214 \pm 280 \pm 982$
150	$6.4^{+4.7}_{-4.0}$
250	0.32 ± 0.30
375	$0.03^{+0.08}_{-0.02}$
500	$0.006^{+0.022}_{-0.003}$
625	$0.002^{+0.008}_{-0.001}$
750	$0.0005^{+0.0035}_{-0.0003}$
875	$0.0002^{+0.002}_{-0.0001}$

7.2.2 Corrections and uncertainties

In this section corrections and relevant systematic uncertainties are briefly described. Some of the corrections and uncertainties are common with the muon channel and are described in Chapter 6.

Theoretical corrections and uncertainties for the signal are evaluated and presented in the Chapter 3. In the previous chapter corrections and related uncertainties for W/Z background arising

from higher order QCD corrections and electroweak corrections. These are listed in Table 6.9. The same corrections and uncertainties are applied for the electron search.

Detector related systematic uncertainties involve uncertainty on luminosity, $\not\!\!E_T$ scale and resolution, trigger efficiency, reconstruction and identification efficiency, energy resolution and scale and isolation. Impact of all uncertainties (except for luminosity, which has uniform uncertainty of $\pm 11\%$) on the W' and W^* signal and background event selection are summarized in Tables 7.14, 7.15 and 7.16 respectively.

Trigger. The efficiency of the triggers used in the analysis was measured directly from the data using two different methods: one using an orthogonal $\not\!\!E_T$ trigger and the tag-and-probe method on $Z \to ee$ events, and are found to be $99 \pm 1\%$. The results are compatible with the measurement performed by the trigger group [10]. The above efficiency is valid up to about 250 GeV. For higher E_T , there are potential inefficiencies due to the saturation of the trigger signals above this threshold. These inefficiencies are found to be of at most 0.3% and are added as additional uncertainty on the trigger efficiency. The correction for the signal efficiency and background count assigned due to data/MC discrepancy is

$$C^e_{trig} = \varepsilon_{data}/\varepsilon_{MC} = 0.99 \ \pm \ 0.01. \tag{7.5}$$

Reconstruction and identification uncertainty. The reconstruction efficiency has been shown to be well modeled by Monte Carlo, leading to a scale factor of one with a systematic uncertainty of 1.5%. The exclusion of the clusters in dead OTx regions is found to add a small systematic uncertainty of 0.4%. The efficiency of the electron Medium identification was measured by the EGamma CP group [9] and scale factors were computed as a function of η with the largest relative uncertainty obtained of 1.8%. The efficiency of the additional impact parameter, B-layer and isolation requirements was also measured in data and Monte Carlo using the tag-and-probe method on $Z \to ee$ events and additional scale factors were computed as described previously. The systematic uncertainty on these factors is taken to be 3.2%, which is the one of the η bin with largest uncertainty. As in the trigger case, the above efficiencies are valid at transverse energies for electrons from $Z \to ee$ and $W \to e\nu$ processes. Their extrapolation at high E_T was studied both in the Monte Carlo and on real data [16], and it was found there were no additional uncertainty on the electron identification efficiency. Combining reconstruction and identification uncertainties, an overall systematic uncertainty from experimental sources of 3.6% is assigned to the efficiency.

Leakage correction for isolation efficiency. The discrepancy between Monte and Carlo and data for the lateral shower shape implying an extra loss of efficiency in the data. Rather

than reprocessing the data with a higher isolation threshold, mass-dependent correction factors are introduced for the signal selection efficiency and the Monte Carlo background level. These mass dependent factors for W'/W^*signal and W/Z backgrounds are listed in Table7.12, [11].

Table 7.12: Correction factors to account for the additional leakage from isolation cone in data.

m[GeV]	W'	W^*	W/Z
500	$0.993 \pm 0.3\%$	$0.995 \pm 0.2\%$	$0.978 \pm 1.7\%$
750	$0.990 \pm 0.5\%$	$0.989 \pm 0.4\%$	$0.975 \pm 2.0\%$
1000	$0.985 \pm 1.0\%$	$0.984 \pm 0.8\%$	$0.971 \pm 2.4\%$
1250	$0.980 \pm 1.6\%$	$0.977 \pm 1.2\%$	$0.966 \pm 3.0\%$
1500	$0.971 \pm 2.7\%$	$0.963 \pm 2.7\%$	$0.964 \pm 3.4\%$
1750	$0.961 \pm 3.0\%$	$0.949 \pm 3.8\%$	$0.961 \pm 3.6\%$

Energy scale and resolution. At very large E_T the energy resolution is dominated by the constant term (c), in the well-known parametrization of the energy resolution of the electromagnetic calorimeter: $\sigma(E)/E = a/\sqrt{E} \oplus b/E \oplus c$. In the simulation a constant term of 0.7% has been introduced. Following the EGamma group recommendation [9], systematic uncertainty on the constant term is conservatively assumed to be 100% for the barrel and 400% for the endcaps. The relative signal efficiency variation obtained assuming these uncertainties in the W' signal is however found to be small, of 0.1%, while for background the highest uncertainty is found to be about 4%.

As already stated in section 7.1, a correction is applied to the cluster energy of the electron candidates in data events: $E_{cor} = E/(1+\alpha)$, with $\alpha = -0.0096$ for the barrel and $\alpha = 0.0189$ for the endcaps. According to the EGamma CP group the systematic uncertainty on the energy scale is then 1% (3%) for the barrel (endcaps). The highest relative signal efficiency variation obtained by varying the energy scale within this uncertainty is found to be 0.8%(2%) for $W'(W^*)$ signal, and 9% for the background.

Vertex match. The uncertainty on vertex finding efficiency in the electron channel is obtained in the same way as for the muon channel (6.4). This uncertainty is found to be small, 0.1% for both signal and background.

Isolation uncertainty. Calorimeter isolation efficiency is evaluated for different jet multiplicities in the event. The relative calorimeter isolation efficiency is defined as the ratio of electrons passing the calorimeter isolation criteria, over the electrons passing the full W' selection up to the isolation requirement (before $\not{E}_T$ and $\not{E}_T/E_T$ requirements). The studied jet multiplicities are the following: no jets, at least one jet in the event (without p_t^{jet} require-

ment), and different p_T^{jet} thresholds for the leading jet, defining it as the highest energy jet that is at $\Delta R > 0.4$ from the selected electron. In the final stage of the selection, the difference in efficiency between events with jets above 20 GeV and events without jets is 1.3-1.6% (depending on the W' mass) for the signal, and about 1% for the background, leading to a systematic uncertainty of 1.5% to the signal efficiency and of 1% to the expected background level.

$\not\!\!E_T$ / E_T uncertainty. A requirement on the ratio between $\not\!\!E_T$ and E_T of the electron cluster to be higher than some value is sensitive to the jet activity in the event. Thus some systematic uncertainty related to the modeling of W' production and jet activity in the event is present. In order to estimate this uncertainty, the W' process was simulated using MC@NLO generator. The result is compared with the one obtained with PYTHIA, which is used for modeling the W' process in this analysis. The W' process was generated using the Standard Model W production in MC@NLO, with the mass and width of the W boson set to the mass and width of the W'. Events were then passed through HERWIG/JIMMY for fragmentation and hadronization. This was done inside ATLAS simulation software, so the same parameters as for other processes simulated with this generator were used. In order to quantify systematic uncertainty of the $\not\!\!E_T/E_T$ cut, the fraction of events that fail $p_T^\nu/p_T^e >$0.6 in MC@NLO is compared to the same fraction in PYTHIA. Events were required to have electron with $p_T^e > 25$ GeV and neutrino with $p_T^\nu > 25$ GeV for both generators. The ratio p_T^ν/p_T^e for W' masses of 1, 1.5 and 2 TeV obtained with MC@NLO and PYTHIA are shown in Fig 7.14. MC@NLO predicts slightly less events to fail the requirement at the generator level, and this is quantified in Table 7.13. The difference between the predictions of two generators is about 0.5%. The same efficiencies were also computed after applying the m_T threshold used in the limits computation; the difference is even smaller: about 0.2%, as shown in Table 7.13. Similar results are obtained for the SM W background. We therefore assign a 0.2% systematic uncertainty to the $\not\!\!E_T/E_T$ selection.

Table 7.13: Fraction of events that fail $p_T^\nu/p_T^e >$0.6 in PYTHIA and MC@NLO.

Generator	All masses		$m_T > \frac{1}{2}m_{W'}$	
	PYTHIA [%]	MC@NLO [%]	PYTHIA [%]	MC@NLO [%]
W'(1 TeV)	1.71±0.13	1.27±0.17	0.83±0.10	0.59±0.13
W'(1.5 TeV)	1.18±0.11	0.75±0.13	0.49±0.08	0.22±0.12
W'(2 TeV)	1.19±0.15	1.08±0.17	0.21±0.08	0.17±0.12

All systematic uncertainties, except luminosity uncertainty, are summarized in the following Tables. For the signal, the largest detector related uncertainty is reconstruction and identification

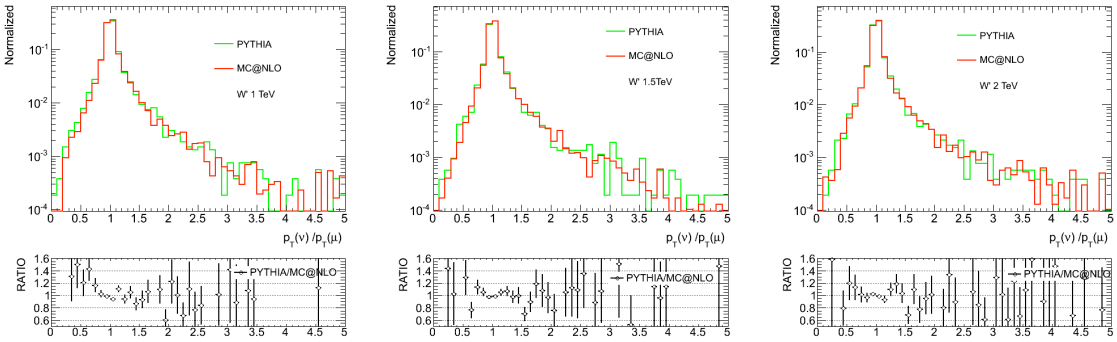

Figure 7.14: p_T^ν / p_T^e distribution in PYTHIA and MC@NLO. Events have $p_T^e > 25$ GeV and $p_T^\nu > 25$ GeV. Left: $m_{W'}$=1 TeV, middle: $m_{W'}$=1.5 TeV, right: $m_{W'}$=2 TeV.

uncertainty, which is found to be 3.6%. The other large sources of uncertainties are isolation uncertainty (1.5%) and limited MC statistics (∼1.5%). For the background, large uncertainties are arising from electron energy scale (up to 9%), and theoretical uncertainties (11%). Uncertainty due to limited MC statistics is much smaller compared to the muon channel (cf. Table6.14).

Table 7.14: $W' \to e\nu$ event selection efficiency uncertainties.

	m_{Tmin} [GeV]					
Source	250	375	500	625	750	875
$\not\!\!E_T$ resolution	0.2%	0.1%	0.1%	0.1%	0.1%	0.0%
$\not\!\!E_T$ scale	0.2%	0.2%	0.1%	0.1%	0.1%	0.2%
Trigger efficiency	1.0%	1.0%	1.0%	1.0%	1.0%	1.0%
Reco. and id. efficiency	3.6%	3.6%	3.6%	3.6%	3.6%	3.6%
Isolation leakage	0.3%	0.5%	1.0%	1.6%	2.7%	3.0%
Energy resolution	0.1%	0.0%	0.1%	0.1%	0.1%	0.1%
Energy scale	0.6%	0.9%	0.7%	0.7%	0.8%	0.7%
Vertex efficiency	0.1%	0.1%	0.1%	0.1%	0.1%	0.1%
All experimental	3.8%	3.9%	3.9%	4.0%	4.7%	4.8%
Monte Carlo statistics	1.3%	1.2%	1.3%	1.5%	1.7%	1.7%
NNLO	0.7%	0.7%	0.7%	0.7%	0.7%	0.7%
$\not\!\!E_T / p_T$	0.2%	0.2%	0.2%	0.2%	0.2%	0.2%
Isolation	1.5%	1.5%	1.5%	1.5%	1.5%	1.5%
All	4.4%	4.4%	4.5%	4.7%	5.3%	5.4%

Table 7.15: $W^* \to e\nu$ event selection systematic uncertainties.

	m_{Tmin} [GeV]					
Source	250	375	500	625	750	875
$\not\!\!E_T$ resolution	0.0%	0.0%	0.0%	0.0%	0.2%	0.1%
$\not\!\!E_T$ scale	0.0%	0.1%	0.1%	0.0%	0.2%	0.0%
Trigger efficiency	1.0%	1.0%	1.0%	1.0%	1.0%	1.0%
Reco. and id. efficiency	3.6%	3.6%	3.6%	3.6%	3.6%	3.6%
Isolation leakage	0.2%	0.4%	0.8%	1.2%	2.7%	3.8%
Energy resolution	0.2%	0.0%	0.1%	0.1%	0.0%	0.2%
Energy scale	1.4%	1.6%	1.7%	1.8%	1.9%	2.0%
Vertex efficiency	0.1%	0.1%	0.1%	0.1%	0.1%	0.1%
All experimental	4.0%	4.1%	4.2%	4.3%	5.0%	5.7%
Monte Carlo statistics	1.2%	1.1%	1.1%	1.1%	1.2%	1.4%
All	4.2%	4.2%	4.3%	4.5%	5.1%	5.9%

Table 7.16: Electron channel background level uncertainties.

	m_{Tmin} [GeV]					
Source	250	375	500	625	750	875
$\not\!\!E_T$ resolution	0.3%	0.7%	0.2%	0.3%	0.3%	0.2%
$\not\!\!E_T$ scale	0.6%	1.5%	1.2%	0.2%	1.1%	0.5%
Trigger efficiency	1.0%	1.0%	1.0%	1.0%	1.0%	1.0%
Reco. and id. efficiency	3.6%	3.6%	3.6%	3.6%	3.6%	3.6%
Isolation leakage	1.7%	2.0%	2.4%	3.0%	3.4%	3.6%
Energy resolution	0.1%	0.7%	1.3%	3.9%	2.4%	1.6%
Energy scale	7.0%	4.6%	4.7%	8.8%	6.6%	7.2%
Vertex efficiency	0.1%	0.1%	0.1%	0.1%	0.1%	0.1%
All experimental	8.1%	6.5%	6.7%	10.7%	8.7%	9.0%
Monte Carlo statistics	0.6%	1.1%	1.2%	2.1%	2.2%	1.5%
W/Z cross section	4.8%	6.1%	7.1%	9.1%	10.8%	11.0%
$t\bar{t}$ cross section	1.4%	0.8%	0.5%	0.5%	0.2%	0.0%
QCD	1.4%	2.0%	2.0%	2.0%	2.2%	2.9%
Isolation	1.0%	1.0%	1.0%	1.0%	1.0%	1.0%
All	9.6%	9.2%	10.3%	14.4%	14.3%	14.6%

7.3 Final results for the electron search

Final results for the electron search are presented in this chapter. All systematic uncertainties, except for luminosity uncertainty stated to be $\pm 11\%$ for all cases, for W' and W^* signal samples, along with systematic uncertainties of the background are presented in Tables 7.14, 7.15 and 7.16 respectively. Signal efficiency and background level, with appropriate uncertainties are presented in Table7.17. All corrections comprised of trigger correction, leakage correction for isolation efficiency, as well as correction on acceptance due to NNLO corrections, are applied. Corrections due to identification efficiency are applied at the previous stage.

The expected number of background events is obtained by correcting W/Z backgrounds for higher order QCD and electroweak corrections. For $t\bar{t}$ and diboson contribution no additional beside reconstruction and identification correction is applied. Numbers for QCD background are not corrected. The final m_{T} distribution with corrected background levels, and QCD background estimated from data using "ABCD" technique, are presented in Fig7.3.

Table 7.17: Final results for $W' \to e\nu$, $W^* \to e\nu$, and backgrounds with integrated luminosity of 36.4 pb^{-1} . Signal efficiencies, and expected numbers of signal and background events are corrected as explained in the text. Uncertainties are listed in the previous tables. The last column gives the number of observed events for the electron selection.

m [GeV]	signal	$\varepsilon_{\mathrm{sig}}$	N_{sig}	N_{bg}	N_{obs}
500	W'	0.556 ± 0.024	349 ± 30	23.08 ± 2.2	24
	W^*	0.455 ± 0.019	208 ± 18		
750	W'	0.565 ± 0.025	65.8 ± 4.8	4.36 ± 0.40	6
	W^*	0.466 ± 0.020	39.6 ± 3.5		
1000	W'	0.562 ± 0.025	17.1 ± 1.4	1.20 ± 0.12	1
	W^*	0.473 ± 0.021	10.5 ± 1.0		
1250	W'	0.552 ± 0.026	5.23 ± 0.51	0.431 ± 0.062	0
	W^*	0.469 ± 0.021	3.22 ± 0.42		
1500	W'	0.530 ± 0.028	1.71 ± 0.21	0.177 ± 0.025	0
	W^*	0.457 ± 0.023	1.06 ± 0.17		
1750	W'	0.503 ± 0.027	0.59 ± 0.09	0.075 ± 0.011	0
	W^*	0.454 ± 0.027	0.37 ± 0.07		

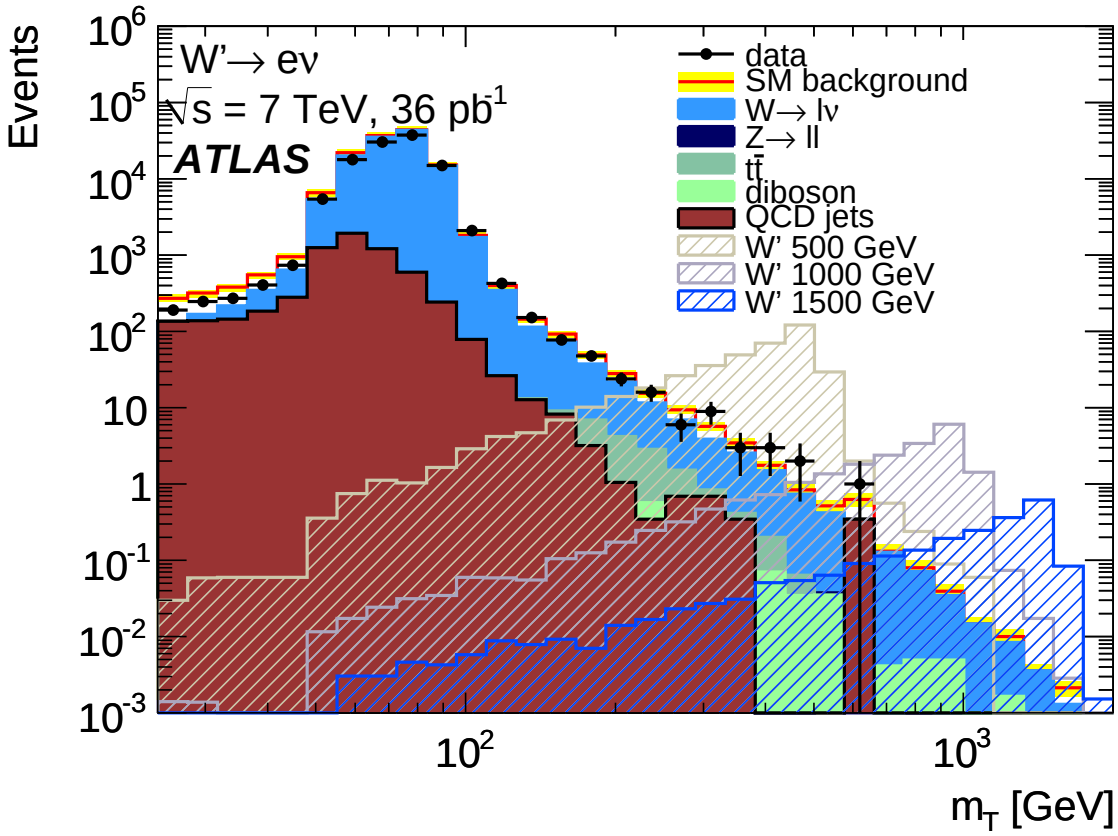

Figure 7.15: Final m_{T} spectrum, with all corrections applied. Signal samples are normalized to NNLO. QCD contamination is estimated from data. Yellow band corresponds to the overall background systematic uncertainty. For m_{T} <250 GeV, uncertainty is assumed to be dominated by the luminosity uncertainty $\pm$11%.

Bibliography

[1] ATLAS Collaboration, Reconstruction and Identification of Electrons, ATL-PHYS-PUB-2009-004 (part of CERN-OPEN-2008-020).

[2] ATLAS Collaboration, Reconstruction of Low-Mass Electron Pairs, ATL-PHYS-PUB-2009-007 (part of CERN-OPEN-2008-020).

[3] W. Lampl et al., Calorimeter clustering algorithms: Description and performance, ATL-LARG-PUB-2008-002.

[4] ATLAS Collaboration, Performance of the ATLAS Detector using First Collision Data, JHEP 09, 056 (2010).

[5] M. Aharrouche et al., Wenu and Zee observations supporting note, ATL-PHYS-INT-2010-109. M. Aharrouchea et al., $W \to e\nu$ and $Z \to ee$ cross-section measurements in proton-proton collisions at $\sqrt{s} = 7$ TeV with the ATLAS Detector, ATL-PHYS-INT-2010-130

[6] M. Aharrouche et al., Expected electron performance in the ATLAS experiment, ATL-PHYS-INT-2010-126.
`https://twiki.cern.ch/twiki/bin/view/AtlasProtected/ElectronIdentification`

[7] ATLAS Collaboration, $W \to l\nu$ and $Z \to ll$ cross-sections measurements in proton-proton collisions at $\sqrt{s} = 7$ TeV with the ATLAS Detector ATLAS-CONF-2011-041.

[8] `https://twiki.cern.ch/twiki/bin/view/AtlasPublic/TRTPublicResults`, see Transition radiation onset.

[9] M. Agustoni, et al., Electron energy scale in-situ calibration and performance, ATL-COM-PHYS-2011-263
ATLAS EGamma Combined Performance Group,
`https://twiki.cern.ch/twiki/bin/view/AtlasProtected/EnergyScaleResolutionRecommendations`
`https://twiki.cern.ch/twiki/bin/view/AtlasProtected/EfficiencyMeasurements`

[10] J. T. Childers, R. Stamen, A. Tricoli, and M. Wielers. Performance of the electron and photon trigger in p-p collisions at $\sqrt{s}$ = 7 TeV, ATL-COM-DAQ-2011-008

[11] D.L. Adams,...,D. Fassouliotis,...,C. Kourkoumelis,...,D.Popovic,..., N.Vranjes et al. Search for high-mass states with lepton plus missing transverse energy using the ATLAS Detector with 36 pb^{-1} of pp collisions at $\sqrt{s}$ = 7 TeV, ATL-COM-PHYS-2010-1073.

[12] G. Unal, Emulation of LAr cell gain problem, `https://twiki.cern.ch/twiki/bin/view/Atlas/LArCellGainPathology`

[13] See: D. Fassouliotis, C. Kourkoumelis, D. Popovic, N. Vranjes, Update on W' analysis `https://indico.cern.ch/getFile.py/access?contribId=3&resId=0&materialId=slides&confId=110906`

[14] `https://twiki.cern.ch/twiki/bin/view/AtlasProtected/ObjectQualityMaps`

[15] ATLAS Collaboration, Measurement of the inclusive isolated prompt photon cross section in pp collisions at s = 7 TeV with the ATLAS detector, Phys. Rev. D 83, 052005 (2011).

[16] L. R. Flores Castillo et al., Electron identification variables as a function of electron transverse energy, ATL-COM-PHYS-2010-1002.

Chapter 8

Limits And Prospects

8.1 W' and W^* limits with 2010 data

As stated before, data show no excess above Standard Model expectation. Thus, one needs to set the upper limits on on the production cross section multiplied with branching ratio (σB) on W' and W^* signal.

A single-bin likelihood analysis is performed to set the limits for each decay channel at each mass using the observed number of events with $m_{\mathrm{T}} > m_{\mathrm{Tmin}}$ where the threshold m_{Tmin} is taken to be half the W' (and W^*) mass. The expected number of events in each channel is

$$N_{\mathrm{exp}} = N_{\mathrm{sig}} + N_{\mathrm{bg}} \tag{8.1}$$

where N_{bg} is the expected number of background events and N_{sig} is the predicted number of signal events:

$$N_{\mathrm{sig}} = \mathscr{L}_{\mathrm{int}} \varepsilon_{\mathrm{sig}} \sigma B \tag{8.2}$$

Here $\mathscr{L}_{\mathrm{int}}$ is the integrated luminosity of the data sample and $\varepsilon_{\mathrm{sig}}$ is the event selection efficiency (including the requirement $m_{\mathrm{T}} > m_{\mathrm{Tmin}}$).

Using Poisson statistics, the likelihood to observe N_{obs} events is:

$$\mathscr{L}(\sigma B) = \frac{(\mathscr{L}_{\mathrm{int}} \varepsilon_{\mathrm{sig}} \sigma B + N_{\mathrm{bg}})^{N_{\mathrm{obs}}} e^{-(\mathscr{L}_{\mathrm{int}} \varepsilon_{\mathrm{sig}} \sigma B + N_{\mathrm{bg}})}}{N_{\mathrm{obs}}!} \tag{8.3}$$

and this expression is used to set limits on σB. Uncertainty in any of the parameters characterizing this expression are included by multiplying this likelihood by the probability density function (pdf) characterizing that uncertainty. In general, if N such nuisance parameters $\theta_1, \ldots, \theta_N$

are identified, then the likelihood becomes

$$\mathscr{L}(\sigma B, \theta_1, ..., \theta_N) = \mathscr{L}(\sigma B) \prod g_i(\theta_i), \tag{8.4}$$

where $g_i(\theta_i)$ is the pdf for parameter θ_i. It is assumed that this factor is of the Gaussian form:

$$g_i(\theta) = \frac{1}{\sqrt{2\pi}\sigma_i} e^{-\frac{(\theta-\bar{\theta}_i)^2}{2\sigma_i^2}} \tag{8.5}$$

where $\bar{\theta}_i$ is the central value for parameter θ_i and σ_i is the uncertainty assigned to that value.

Rather than introduce a nuisance parameter for each source of systematic uncertainty, the nuisance parameters are taken to be $\mathscr{L}_{\text{int}}$, ε_{sig} and N_{bg}. The inputs for the limit settings are taken from the Tables 6.15 (Section 6.5) for the muon channel, and 7.17 (Section 7.2.2) for the electron channel. Uncertainty on luminosity is not part of uncertainties in the given tables, and is taken to be $\pm 11\%$.

To avoid excluding or discovering signals to which the search has no sensitivity, the limit calculations make use of the CL_s method [1, 2], a modification of purely classical statistical analysis. Following [1], the likelihood $\mathscr{L}$ from equation 8.3 is used to define the *LLR* (Log Likelihood Ratio) as a test statistic:

$$LLR = -2ln\frac{\mathscr{L}(data|s+b)}{\mathscr{L}(data|b)} \tag{8.6}$$

and two p-values are defined: $CL_{s+b} = P_{s+b}(LLR \geq LLR_{obs})$ and $CL_b = P_b(LLR \geq LLR_{obs})$ under the signal plus background and background only hypotheses, respectively. The modified frequentist renormalization described above is $CL_s = CL_{s+b}/CL_b$. The 95% CL upper limit on σB is defined to be the value for which $CL_s = 0.05$. It is clear from the form of equation 8.6 that the test statistic for the combined electron and muon result is just the sum the individual *LLR*'s.

Uncertainties in the signal event selection efficiency and the expected number of background events (excluding the contributions from the integrated luminosity) are handled as uncorrelated nuisance parameters. Neglect of correlation is not fully justified because, even without the luminosity, the signal and background uncertainties have common systematic sources. However, correlations between these are neglected afterall due to the small effect that the nuisance parameters themselves have on the limits, as demonstrated below. Also some systematic sources of uncertainty have postive and other negative correlation so overall the effect is negligible. The integrated luminosity is treated as a nuisance parameter with full correlation between signal

and background and between channels in the combined (electron plus muon) limit calculations. This correlation is performed with 1M toy Monte Carlo experiments.

Tables 8.1 and 8.2 show observed and expected limits obtained for W'. The first table shows observed limits, assuming no systematic uncertainties, systematic uncertainties only for the signal efficiency, for signal efficiency and background level without luminosity, and with luminosity taken to be not correlated for the signal and background, and finally to be correlated for the signal and background. The second table gives the expected excluded cross sections (for all systematic uncertainties including luminosity) for the central value of the background level, as well as statistical fluctuations of the background for $\pm 1\sigma$ and $\pm 2\sigma$.

Table 8.1: The 95% CL upper limits on $W'\sigma B$in fb. Labels indicate the nuisance parameters for which uncertainties are included: S for the event selection efficiency (ε_{sig}), B for the background level (N_{bg}), and L for the integrated luminosity ($\mathscr{L}_{\text{int}}$). SBL(uncorr.) represents the excluded cross sections assuming no correlation between signal and background for the luminosity, while SBL(corr.) assumes this correlation. The later is used to evaluate mass limits. Results are given for the electron and muon channels and the combination of the two.

mass [GeV]		none	S	SB	SBL(uncorr.)	SBL(corr.)
	$e\nu$	602	605	643	709	769
500	$\mu\nu$	640	641	656	731	806
	both	393	394	419	464	570
	$e\nu$	383	384	387	400	411
750	$\mu\nu$	230	230	230	235	251
	both	181	181	183	189	205
	$e\nu$	199	200	200	205	207
1000	$\mu\nu$	218	219	219	223	229
	both	106	106	107	108	114
	$e\nu$	151	151	151	155	155
1250	$\mu\nu$	216	216	216	220	223
	both	89	89	89	90	92
	$e\nu$	157	158	158	161	161
1500	$\mu\nu$	218	218	218	222	224
	both	91	91	91	92	94
	$e\nu$	166	166	167	170	170
1750	$\mu\nu$	231	231	231	236	238
	both	97	97	97	98	99

The excluded cross section as function of W' mass is given in Fig 8.1 for $W' \to e\nu$ and $W' \to \mu\nu$ separately, and in Fig 8.2 for the combination. The numbers of observed events are in good agreement with the expected numbers of background events except for the second mass

Table 8.2: Expected 95% CL upper limits on W' σB in fb. Full systematic uncertainty is considered. Luminosity is taken to be correlated between signal and background in the same way as for the observed limit. Expected limits are given also for $\pm 2\sigma$ and $\pm 1\sigma$ statistical fluctuation of the expected background.

mass[GeV]	channel	-2σ	-1σ	expected	+1σ	+2σ
500	$e\nu$	379	510	724	1021	1370
	$\mu\nu$	582	754	1058	1464	2041
	both	360	448	613	861	1188
750	$e\nu$	186	219	303	471	598
	$\mu\nu$	287	381	509	758	1048
	both	140	180	245	350	483
1000	$e\nu$	154	154	207	271	411
	$\mu\nu$	229	290	366	547	645
	both	94	113	151	212	293
1250	$e\nu$	155	155	155	228	306
	$\mu\nu$	223	223	306	402	505
	both	92	92	122	162	227
1500	$e\nu$	161	161	161	248	247
	$\mu\nu$	224	223	223	321	536
	both	94	94	115	143	198
1750	$e\nu$	170	170	170	170	266
	$\mu\nu$	238	238	238	347	465
	both	99	99	99	123	188

point in the muon channel. A discrepancy is observed for $m_{\mathrm{T}} > 750$ GeV where $\sim$5.5 muon events are predicted and none are observed, a result for which the Poisson probability is only 0.4%. However, the muon p_T spectrum in Fig 5.24 shows no evidence of any discrepancy between data and predicted background at high p_T , confirming that, as expected, the muon efficiency remains stable at high p_T .

The intersection of the cross section with an interpolation between the limits is used to set lower limits the W' mass. For W', respective limits of 1360 and 1290 GeV are obtained independently in the electron and muon channels and a limit of 1490 GeV is obtained when the two channels are combined. These values fall to 1340, 1270 and 1460 GeV if the lower uncertainty curve is used in place of the central value for the cross section. The limits improve by 5-10 GeV if all input uncertainties are neglected.

W^* limits are set in the same way as the limits for the W'. The obsereved as well as the expected limits (including statsitical fluctuation of the expected background) are presented in the Table 8.3. The observed and expected limits as a function of W^* mass are presented in Fig8.3. The corresponding limits mass limits are 1260, 1120, and 1350 GeV respectively for the electron, muon and combination, falling to 1240, 1115 and 1330 GeV using the 1-σ cross

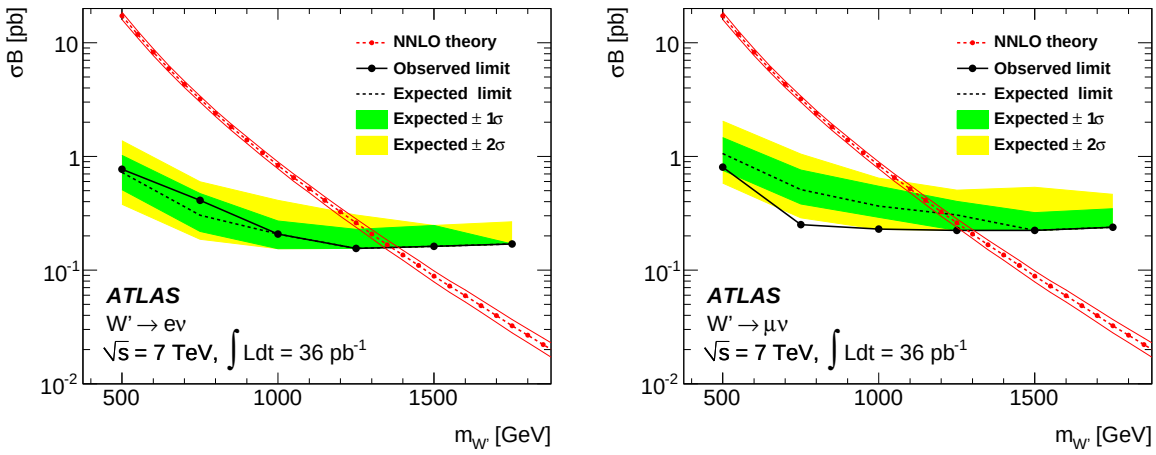

Figure 8.1: Limits at 95% CL for $W' \to e\nu$ (left) and $W' \to \mu\nu$ (right) production. The solid lines show the observed limits with all uncertainties. The expected limit is indicated with dashed lines surrounded by 1σ and 2σ shaded bands. Dashed lines show the theory predictions (based on NNLO calculation) between solid lines indicating their uncertainties. The W' σB uncertainties are obtained by varying renormalization and factorization scales and by varying PDFs.

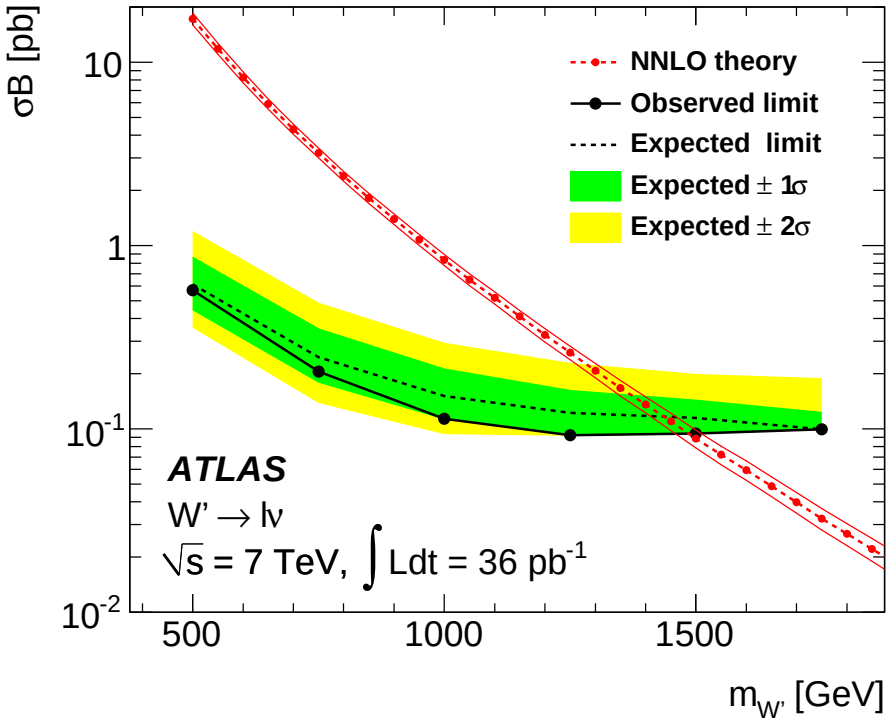

Figure 8.2: Limits at 95% CL for the combination of the electron and muon channel.

section curve. The limits fall by 5-10 GeV if all input uncertainties are neglected.

Table 8.3: Observed and expected 95% CL upper limits on W^* σB. The labels are the same as for W'. Expected limits are also presented for $\pm 2\sigma$ and $\pm 1\sigma$ statistical fluctuation of the expected background. Results are given for the electron and muon channels and the combination of the two.

mass[GeV]	channel	SBL(obs.)	-2σ	-1σ	central (exp.)	+1σ	+2σ
500	$e\nu$	940	472	620	885	1245	1674
	$\mu\nu$	1201	872	1124	1573	2175	3035
	both	746	419	581	791	1112	1515
750	$e\nu$	497	227	266	368	500	724
	$\mu\nu$	397	455	600	800	1192	1652
	both	288	182	234	321	454	624
1000	$e\nu$	247	183	183	247	322	488
	$\mu\nu$	361	361	457	576	860	1015
	both	154	124	148	193	270	376
1250	$e\nu$	183	183	183	183	269	361
	$\mu\nu$	363	364	363	498	655	821
	both	123	123	123	157	203	296
1500	$e\nu$	187	187	187	187	287	287
	$\mu\nu$	365	365	365	365	522	875
	both	124	124	124	147	184	246
1750	$e\nu$	188	188	188	188	189	295
	$\mu\nu$	358	358	358	358	523	699
	both	123	123	123	123	149	227

8.2 $W' \to \mu\nu$ search with 2011 data

W' search performed using data collected in the first part of 2011 corresponding to the 205 pb^{-1} is very similar to the one described through this thesis. The 2010 analysis included two flavors of leptons: electron and muons, and here only the muon channel is included. The details of the analysis can be found here [3]. The events were required to pass a trigger with a muon $p_T > 22$ GeV. Muon tracks reconstructed independently in both the ID and MS, and the muons used in this study are required to have matching tracks in both systems. The acceptance of the two systems covers $|\eta| < 2.5$, but most of the regions with $1.0 < |\eta| < 1.3$ and $|\eta| > 2.0$ are excluded. Most chambers in the middle station arround $|\eta| \sim 1.3$ are not installed thus the muons fail the requirement of three hits in each station, while the knowledge of the alignment of CSC chambers in $|\eta| > 2.0$ was not sufficiant to ensure well enough control of the very high-p_T muons resolution. About 70% of the muons in the remaining regions fire the trigger and pass selection requirements including hits in all three muon stations.The main difference for the

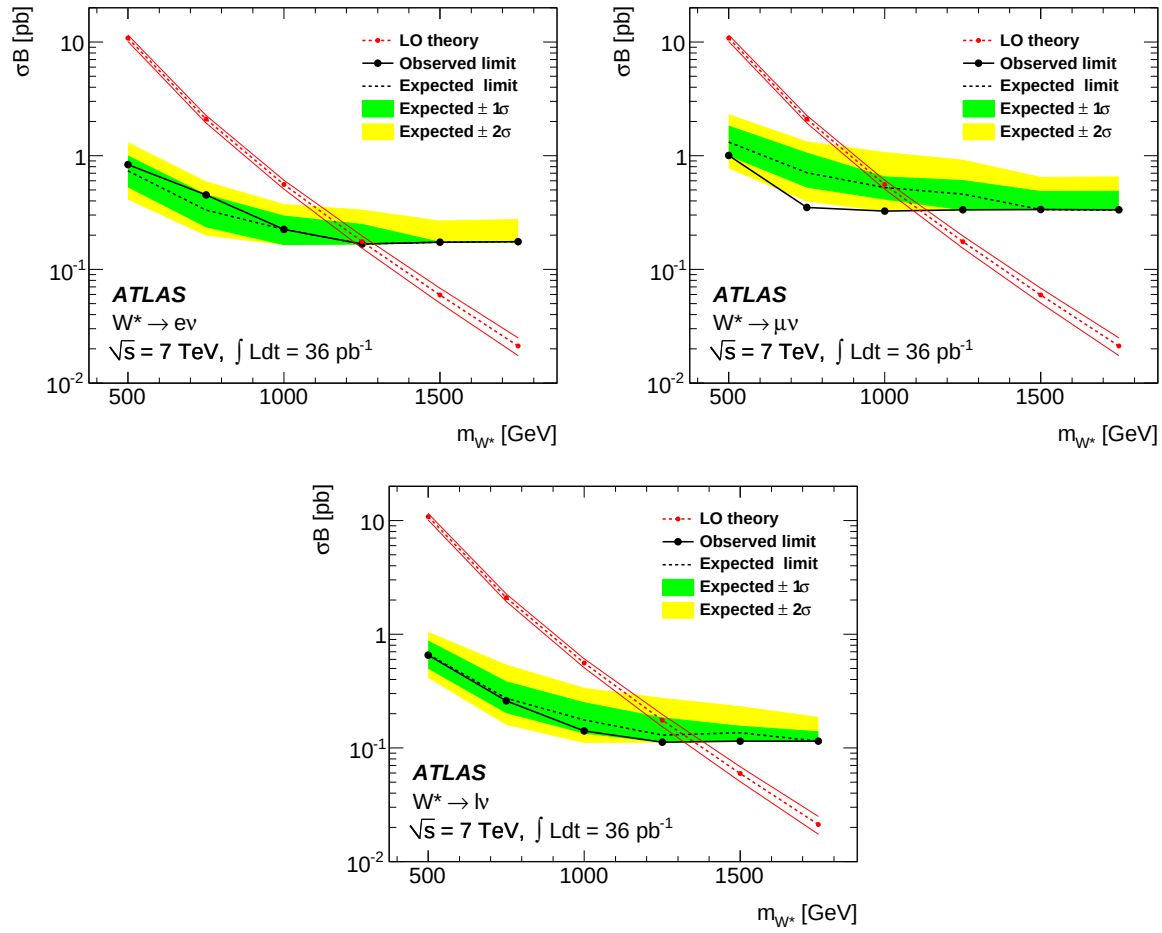

Figure 8.3: Limits at 95% CL for $W^* \to e\nu$ (left) $W^* \to \mu\nu$ (right) production in the decay channels and the combination of these (bottom). The solid lines show the observed limits with all uncertainties. The expected limit is indicated with dashed lines surrounded by 1σ and 2σ shaded bands. Dashed lines show the theory predictions (based on LO calculation) between solid lines indicating their uncertainties.

muon selection with respect to the 2010 analysis is in the fact that the momentum of the muon is obtained from a weighted average of the measurements in the two detector systems (combined measurement). As a consequence, the momentum resolution is improved and the expected level of the background in high-m_{T} region is reduced. The momentum resolution (with calibration and alignment at the time being) is about 20% at $p_T = 1$ TeV.

Events are required to pass the preselection consistent with the one applied in 2010 analysis, and to have exactly one candidate muon. A muon is considered a candidate if it has $p_T >$ 25 GeV, has matching tracks in the inner detector and muon spectrometer, and is compatible with originating from the primary vertex. To suppress the QCD background, the muon is further required to be isolated, with the same isolation requirement as in 2010 analysis. Finally, a $\not{E}_T$

threshold, $\not\!\!E_T > 25$ GeV, is applied to further suppress the QCD background. These criteria define the final event selection. The limit for each W' mass is set by counting events passing this selection and satisfying $m_{\mathrm{T}} > 0.5 m_{W'}$.

The data show no significant evidence for any excess above SM expectations and are used to set limits on σB for W' production. The limits are evaluated using the same statistical procedure as described above. The uncertainties on $\varepsilon_{\mathrm{sig}}$ and N_{bg} account for theoretical and experimental systematic effects as well as the statistics of the simulation samples. The amount by which the Monte Carlo pileup is varied to overestimate the $\not\!\!E_T$ provides the systematic variation used to assess $\not\!\!E_T$ systematic uncertainties. The leading contributor to the uncertainty on the signal efficiency is the $\not\!\!E_T$ /pileup.

Most of the performance metrics are measured at relatively low p_T and their values are extrapolated to the high-p_T regime relevant to this analysis. The uncertainties due to the extrapolations from low p_T lepton values are included but are too small to significantly affect the W' limits. Theoretical systematic uncertainties arise from the calculation of cross sections and their kinematical distributions, and are dominant source of uncertainty for the background.

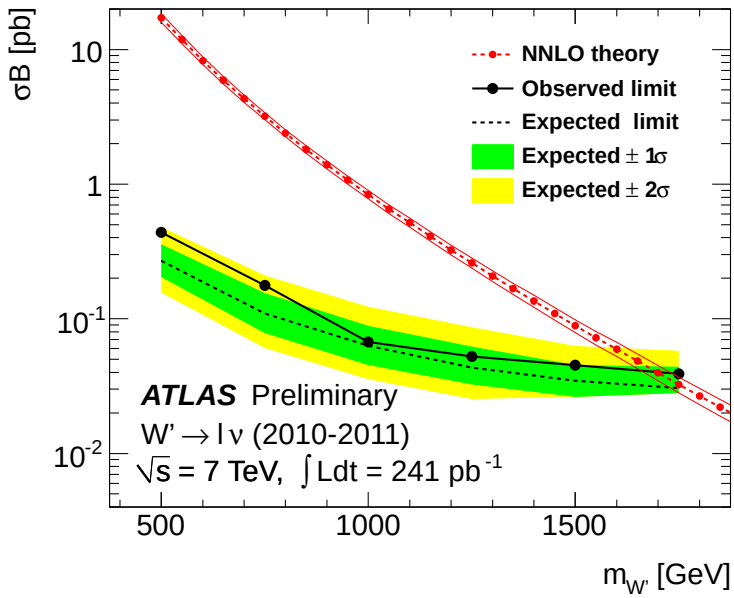

Figure 8.4: Expected and observed limits on the $W' \to \ell\nu$ σB. The limits are obtained by combining ATLAS measurements from 2010 and 2011. The NNLO calculated cross section and its uncertainty are also shown.

Finally the results from ATLAS searches in the $W' \to e\nu$ and $W' \to \mu\nu$ channels in 2010 are combined with the 2011 $W' \to \mu\nu$ results. Although much less integrated luminosity was used in the 2010 analysis, the addition of the $W' \to e\nu$ channel, with its higher event selection

efficiency, leads to a relative improvement in sensitivity.

The observed combined limits on σB are shown in Fig. 8.4. The figure also shows the expected limits and the theoretical σB for the W' production. The expected mass limit is 1770 GeV and the observed limit is 1700 GeV.

8.3 Prospects

The ATLAS physics potential in the searches for high-mass lepton-neutrino resonances, has been evaluated as a function of the LHC center-of-mass energy $\sqrt{s}$, for a few values of the total integrated luminosity [4]. The evaluation is done using benchmark model of W' with SM-like couplings to fermions since this should cover the potential of the search for heavy gauge bosons in various LHC running scenarios. Specifically, the searches for dilepton and lepton-neutrino resonances (where *lepton* stands for electron or muon) are studied for $\sqrt{s}$ =7, 8 and 9 TeV, and assuming total integrated luminosities between 1 and 10 fb^{-1}.

For this study, W', σB for $\sqrt{s}$ =7, 8 and 9 TeV are obtained using PYTHIA 6.421 [5] and MRST LO* [6] parton distribution functions. The results are shown in Table 8.4.

Table 8.4: Widths and production cross sections times branching ratio for several W' masses at different values of $\sqrt{s}$. Values are obtained with PYTHIA using MRST LO* PDF. No cut is applied on the invariant mass of the W' state.

W' mass	$\Gamma_{W'}$	σB [fb]		
[TeV]	[GeV]	$\sqrt{s}$ =7 TeV	$\sqrt{s}$ =8 TeV	$\sqrt{s}$ =9 TeV
1.0	35	791	1120	1480
1.5	53	93.3	148	217
2.0	71	15.0	27.1	44.1
2.5	89	3.11	6.08	10.7
3.0	108	0.937	1.68	2.99

The reach for discovery and limit setting in these channels is obtained from a simple counting approach, using as input the expected number of signal and background events. The expected numbers of events at $\sqrt{s}$ =7 TeV are obtained applying the selection criteria as in this thesis. The discovery reach is evaluated using the luminosity needed to obtain ten signal events after selection. This criterion is adopted instead of the customary 5σ significance because, in searches with very low expected background levels (like these), the 5σ threshold is reached with very few events, posing strong requirements on the understanding of instrumental uncertainties.

For each hypothesized mass of the W', exclusion limits are obtained counting signal and background events in the transverse mass window $m_T > 0.5 m_{W'}$ for the W' search.

Results are shown for the combination of the electron and muon channel. The expected number of events, $N(\sqrt{s})$, at $\sqrt{s}$ =8 TeV and 9 TeV is obtained by applying the following correction to the number at 7 TeV:

$$N(\sqrt{s}) = N(7\text{ TeV}) \times \frac{\sigma(\sqrt{s})}{\sigma(7\text{ TeV})} \times \frac{\varepsilon(\sqrt{s})}{\varepsilon(7\text{ TeV})} \tag{8.7}$$

The correction is a product of:

1. The ratio of cross sections (estimated with PYTHIA LO*)

2. The ratio of efficiencies (estimated with PYTHIA LO* and fast simulation samples)

The difference in efficiencies at different center-of-mass (CM) energies is mainly due to kinematic effects on the phase-space which affects the acceptance in the mass (or transverse mass) window used to count the number of signal events. The same scale factors were used for the background estimation.

Table 8.5: Total integrated luminosity, in pb^{-1}, needed for 95% CL exclusion for the production of a W' boson below several mass values by combining both leptonic channels. Numbers in parenthesis show the luminosity required when only the electron channel is used.

W' mass [TeV]	Luminosity [pb^{-1}]		
	$\sqrt{s}$ =7 TeV	$\sqrt{s}$ =8 TeV	$\sqrt{s}$ =9 TeV
1.0	3.3 (6.3)	2.3 (4.5)	1.7 (3.3)
1.5	30 (58)	19 (37)	13 (24)
2.0	230 (590)	110 (200)	66 (120)
2.5	2200 (4900)	780 (1600)	400 (860)
3.0	28000 (67000)	6400 (14000)	2400 (5300)

No correction factors are used to account for efficiency discrepancies between collision data and MC simulations since such discrepancies have been measured to be small in 2010 data. For the evaluation of limit-setting and discovery reach in this study, overall systematic uncertainties of 7%-30% (driven by theoretical uncertainties), for the mass range 1-3 TeV are assumed for both signal and background. These uncertainties are added in quadrature to a conservative systematic uncertainty of 11% from the measurement of the total integrated luminosity.

Table 8.5 shows the total integrated luminosity required to exclude several values of W' mass. This evaluation is obtained using the modified frequentist approach to set the limits, as in

the analysis of 2010 data.

Table 8.6 show the luminosity needed to have ten expected signal events observed (*i.e.*, after selection cuts).

Table 8.6: Total integrated luminosity, in pb^{-1}, corresponding to ten W' signal events observed (adding both channels).

W' mass [TeV]	Luminosity [pb^{-1}]		
	$\sqrt{s}$ =7 TeV	$\sqrt{s}$ =8 TeV	$\sqrt{s}$ =9 TeV
1.0	11	8	6
1.5	99	62	41
2.0	731	360	215
2.5	4950	1990	1010
3.0	35300	11100	4570

Figures 8.5 provide a graphical representation of the information shown in Tables 8.5 to 8.6.

An increase of the LHC center-of-mass energy by 1 TeV increases the physics reach in the W' channels by about 10%; for example, the mass limit for the W' (with 0.5 fb^{-1}) goes from 2.17 to 2.38 TeV when $\sqrt{s}$ goes from 7 to 8 TeV, and from 2.38 to 2.56 TeV when $\sqrt{s}$ goes from 8 to 9 TeV. Doubling the total integrated luminosity has a similar effect in the physics reach.

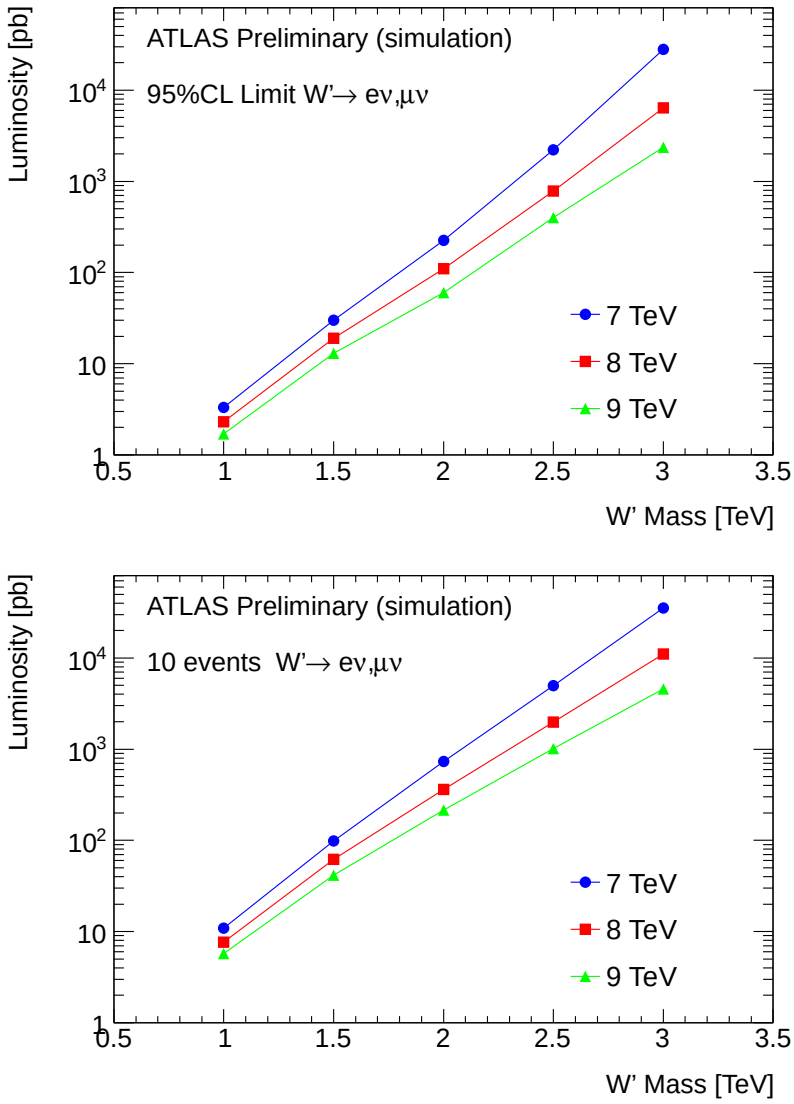

Figure 8.5: Top: Luminosity required to set 95% CL exclusion limits for heavy gauge bosons obtained combining the results from the e and μ channels, for three values of the LHC center-of-mass energy. Bottom: Luminosity required to have ten signal events (electron plus muon channel) for three values of the LHC center-of-mass energy.

Bibliography

[1] T. Junk, Confidence Level Computation for Combining Searches with Small Statistics, Nucl. Instrum. Meth. A434, 435 (1999), arXiv:9902006 [hep-ex].

[2] A. L. Read, Modified Frequentist Analysis Of Search Results (The CLs method), CERN-OPEN-2000-205 (2000).

[3] ATLAS Collaboration, Search for high-mass states with one muon plus missing transverse momentum in proton-proton collisions at $\sqrt{s}$=7 TeV with the ATLAS detector, ATLAS-CONF-2011-082, D.L.Adams,...,N.Vranjes et al. ATLAS-COM-CONF-2011-096.

[4] ATLAS Collaboration, Physics potential of Z' and W' searches with the ATLAS Detector as a function of the LHC center-of-mass energy, ATL-PHYS-PUB-2011-002, ATL-COM-PHYS-2011-020.

[5] T. Sjostrand et al., JHEP 05, 026. 352 (2006).

[6] A. Sherstnev and R. S. Thorne, Parton Distributions for LO Generators, Eur. Phys. J. C55 (2008) 1296 553575, arXiv:0711.2473v3 [hep-ph].

Chapter 9

Summary and Outlook

In this thesis, a search for high-mass states, such as heavy charged gauge bosons ($W'$and W^*), decaying to a lepton (a muon or an electron) and a neutrino is presented. Since 30 March 2010 LHC at CERN has been colliding protons at the center of mass energy of $\sqrt{s}$ =7 TeV. The analysis in this thesis is performed using the entire dataset of pp collisions collected with ATLAS detector during 2010 corresponding to an integrated luminosity of about 36 pb^{-1} . The search is performed in the context of the reference benchmark model, where W' appears as a heavy copy of the Standard Model W boson: its couplings to fermions are the same as for SM W, the other decay channels ($W' \to WZ$) are suppressed, while mixing between W' and W is negligible. Beside Standard Model like W', another model where such a boson is denoted as W^*, representing the charged partner to the chiral bosons, is considered.

For $W' \to \ell\nu$ production, σB (cross sections times branching ratios for each channel) are calculated in the Next-to-Next-to Leading Order QCD approximation using `FEWZ` program, and found to be in range 17.25 -0.00234 pb for W' masses 0.5-2.5 TeV. Relevant systematic uncertainties have been evaluated from PDF error sets of MSTW pdfs, the difference between the predictions of MSTW and CTEQ PDF sets, and standard variations of renormalization and factorization scales. The uncertainties have been evaluated to be in range 6-19% for W' masses 0.5 - 2.5 TeV.

In order to search for high-mass muon+neutrino candidates, muon performance and selection criteria have been studied. Prior analysis of 2010 data, performance of the muon reconstruction has been tested using data collected in 2009 with pp collisions at 900 GeV, and good agreement is found between data and simulation indicating a reasonable understanding of the initial performance of the Muon Spectrometer with collision data. In order to select high-mass muon+neutrino candidates in 2010 dataset, muon candidates are required to be independently reconstructed by the Inner Detector and Muon Spectrometer, with momentum obtained from

MS. Muon candidates were restricted to the barrel part of MS, where the alignment was best understood, in particular using high-energy cosmic rays. The muon quality criteria are studied in order to improve momentum resolution and prevent selecting high-m_{T} events originating from muons with largely overestimated momentum or fake signals originating from misidentified jets and cosmic rays. The optimal quality criteria is found to be the requirement that muon candidates have at least 3 hits in each of the three barrel muon stations, and that muons origin is consistent with primary vertex. About 80% of the muons in barrel are reconstructed, where most of the loss came from regions with limited coverage. Also, isolation criteria based on Inner Detector track information was established and found to be robust against pileup. Possible additional selection criteria have been also studied and found to have small effect on the overall background level and data-to-simulation comparison.

For the selection of high mass electron+neutrino candidates, electron identification criteria are studied based on lateral shower shapes in the in the first two layers of the Electromagnetic Calorimeter, and the fraction of energy leakage into the Hadronic Calorimeter. The "medium" set of requirements has been found to be optimal. Electron candidates containing cells overlapping with problematic regions of the calorimeter are removed leading to 8% loss in signal efficiency. Further, electron candidates are required to have a hit in the first pixel layer in order to reduce background from photon conversions. Additional selection criteria based on calorimeter isolation of the electron cluster and balance of $\not{E}_T$ and cluster E_T have been tested in order to suppress fakes in high-m_{T} region above 100 GeV originating from misidentified jets.

The dominant background comes from high-m_{T} events of $W \to \ell\nu$ processes. Other backgrounds are Z bosons decaying into two leptons where one lepton is outside acceptance, W and Z decaying to τ leptons, where τ decays to an electron or a muon, and diboson production. In addition, important source of background is $t\bar{t}$ production, which is important for lowest W'/W^* masses, constituting 20% of the overall background. Background from QCD jet production and cosmic rays are also present. The background level of W/Z, $t\bar{t}$ processes are evaluated with simulated Monte Carlo samples normalized to NNLO QCD cross sections and the integrated luminosity of data. Correction factors for W/Z production have been estimated in order to account for higher order corrections dependence on the m_{T}. These corrections multiplied by electroweak correction factors were found to be in range 99%-81% for m_{T} threshold 250 GeV - 875 GeV. Background arising from cosmic muons, and from QCD multijet production, have been estimated using data driven techniques. Cosmic background has been found to be negligible, while QCD was estimated to be at most 4% of the total background in high-m_{T} region, with relative uncertainty of 100%.

The data show no evidence of excess above SM expectations, and are used to set limits on

σB for W' and W^* with masses in range 0.5-1.75 TeV. The limits are evaluated using a single bin likelihood analysis by counting event that pass $m_T > \frac{1}{2} m_{W'/W^*}$ for each mass point. The input in the limit calculation consist of signal selection efficiency, background level, integrated luminosity and systematic uncertainties. Uncertainties in the signal event selection efficiency and the expected number of background events are handled as uncorrelated nuisance parameters since their impact on the observed limit is found to be small. The integrated luminosity is treated as a nuisance parameter with full correlation between signal and background and between channels in the combined (electron plus muon) limit calculations.

To account for data to simulation discrepancies, correction factors were obtained and applied to signal efficiency and background level: 3% for the trigger efficiency in the muon channel, and up to 3.6% difference for the electron identification and 3.5% for isolation leakage have been accounted for. Also, for W' signal a small corrections up to 4% have been taken applied to account for differences between kinematical distributions at NNLO and those in LO simulation. Contribution from $W'/W^* \to \tau\nu$ have been neglected and would increase signal efficiency by 3-4%. Further, all systematic uncertainties, theoretical and detector related, are evaluated. Detector related uncertainties estimation is based on the performance of the ATLAS detector established with data available in 2010 run. Signal detector related uncertainties for the muon channel are found to be in range 2-3% dominated by the reconstruction efficiency uncertainty extrapolation to very high-p_T . For the electron channel, overall systematic uncertainties for signal were estimated to be 4-6%, dominated by identification, energy scale, and isolation leakage uncertainty. The systematic uncertainties on the background are found to be dominated by the theory uncertainties (5%-12%) and in the muon channel by limited statistics of Monte Carlo samples (2%-17%) being a consequence of non-Gaussian tails arising from the stand alone measurement of the muon momentum. The background uncertainty in the electron channel is found to be 10-15% dominated by the same components as for the signal. All stated uncertainties do not incorporate uncertainty in the integrated luminosity which is taken to be 11%.

Limits for 95% CL (confidence level) exclusion on σB are derived using the $CL_s = CL_{s+b}/CL_b$ estimator. Good agreement between data and background expectation is found for the electron channel and the lowest m_{T} threshold for the muon channel. For higher values of m_{T} threshold 0 events are observed in the muon channel while more is expected by the background, in particular for $m_T > 375$ GeV, 5.48 ± 0.45 events are expected which corresponds to Poisson probability of 0.4%. However, the muon p_T spectrum show no evidence of any discrepancy between data and expectations, confirming that muon reconstruction efficiency is stable at high p_T .

The observed and expected limits along with $\pm 1(2)\sigma$ for W' and W^* are presented in Tables 8.1, 8.2 and 8.3. The observed upper mass limits are converted into lower mass limits. A W'

with SM couplings is excluded for mass below 1.49 TeV at 95% CL, while the exclusion for W^* with couplings set in accordance is 1.35 TeV.

The search for W' has been continued also in 2011. With the data collected in the first part of the year, corresponding to about 205 pb^{-1} , $W' \to \mu\nu$ search has been performed. The data is consistent with the Standard Model expectations, and no excess has been found yet. Combining the results of $W' \to e\nu$ and $W' \to \mu\nu$ search presented in this thesis, with the results of the search for $W' \to \mu\nu$ with the 2011 data, mass limit has been extended to 1.70 TeV. For the middle of 2011, 1 fb^{-1}of data has been foreseen, and the sensitivity of the search should be increased above 2 TeV. If no signal appears, only a modest increase of the signal sensitivity is expected with the increase of the integrated luminosity or collision energy to 8 or 9 TeV which remains as a possible scenario for 2012 run. Beside, the search for SM-like W' with the lepton plus $\not{E}_T$ signature, it is possible to extend the search with new models. For example it is possible to consider a model where new heavy charged gauge boson decays predominantly to WZ pairs with investigation of (semi)lepton signatures of such production. Another challenging channel that could be investigated in the near future is the decay of new heavy charged gauge boson to the pair of heavy quarks tb.

Acknowledgments

This thesis was carried out within the collaboration of the ATLAS experiment, and within the framework of Joint PhD program between University of Belgrade and National and Kapodistrian University of Athens. I would like to thank the rectors of both universities, as well as the dean of the Faculty of Physics at the BU and the dean Faculty of Physics at the UoA for their support for this joint PhD.

I would like to thank my supervisors, Professor Dr. Dragan Popović from the Institute of Physics Belgrade, and Professor Dr. Christine Kourkoumelis, from the University of Athens. I sincerely thank Prof. Popović for his willingness to serve as my supervisor, and for giving me the opportunity to work in the highly challenging environment of the ATLAS Collaboration. His constant support, not just as the thesis supervisor, but also in his capacity of the team leader of ATLAS group at the Institute of Physics, was crucial for me. I must say that I have learned a lot from Dragan's vast academic experience.

I would like to express my gratitude to Prof. Kourkoumelis for her guidance and huge support during these several years, and her constant interest for my work. Christine did me a lot of favor, forcing me to prepare results all the time, and to actively and frequently participate at the meetings where results were discussed. Her great knowledge of high energy physics and experience and dedicated work have been of a real inspiration for me.

There is a person I would especially like to thank: Dr. Dimitris Fassouliotis, assistant professor at UoA with whom I have collaborated intensively for the past several years. I consider Dimitris to be an excellent physicist and a great teacher as well. I appreciate and respect him not just because of his superb scientific qualities, but also for his character and personal integrity. I owe him my eternal gratitude for the support and ecouregement in many very difficult situations during the last few years, and for bringing me back on course.

I would like to thank members of the W' analysis group, lepton + X subgroup and ATLAS Exotics Working Group, members of editorial boards and convenors, for fruitful discussions, suggestions and constructive criticism during the past several years and the preparation of several notes and papers. In that sense I would like to thank D. L. Adams, L. R. Flores

Castillo, Daniel Froidevaux, C. Issever, H. Bachacou, L. Pontecorvo, A. S. Mete, D. Fortin, M. I. Pedraza-Morales, O. Stelzer-Chilton, S. Banerjee, S. Willocque, S. Viel, G. Siragusa, C. Schroder, H. W. Williams, D. Olivito, F. Ledroit, C. Mills, V. Perez Reale, K.M.Black, J. Zhu, and L. Ma. I thank T. Nunnemann for providing the electroweak corrections, and F. Petriello for the discussion about the results of W' higher order corrections obtained with FEWZ.

I am deeply grateful to Professors D. Krpić, I. Aničin, P. Adžić and C. Petridou, members of the examining committee, for reviewing the thesis, and support its defense. I would also like to thank Dr. Goran Škoro, now Applied Nuclear Physicist at Rutherford Appleton Laboratory, and Dr. Lj. Simić from the IPB who introduced me to research in experimental particle physics. Especially I would like to thank Goran who had great influence on my career.

From the ATLAS team at IPB, I have to mention Acad. Prof. Djorđe Šijački, who all of us students admired. With his deep understanding of physics, academic experience and great sence of humor, Prof. Šijački has been a great inspiration to me.

I would like to thank my colleagues, first of all Kostas Nikolopoulos, for his help and scientific discussions, but also for his friendship beyond the professional interaction. I also thank B.Cvetković, B.Nikolić, Lj. Davidović, I. Salom, I. Borjanović, G,Milutinović A.Antonaki, P.Iordanidou for being such good friends. I am also greatfull to our fellow colleague D.Vudragović for setting up our small cluster in Belgrade on which many of the analysis was performed.

I appreciate the financial support of the Ministry of Science of Republic of Serbia, which partly covered expenses of my visits to CERN and made the collaboration with Athens group possible. I would like to thank Ministry of Science of the Hellenic Republic for making my visits to UoA possible.

Finaly...

Желим да се захвалим мојој породици. Мом оцу Слободану и мојој мајци Љиљани, и мојој сестри Светлани на несебичној подршци и љубави. Вечну захвалност дугујем онима који нису више са нама, али који заувек остају да живе у нашим сећањима и нашим срцима: мојим дедама Ђорђу и Глиги и бакама Блажи и Анђелки. Без њих не бих постао оно што сам данас. Желим да се захвалим и мојим пријатељима, Игору, Миловану, Љубиши, Драгану, Аци, Милошу, Гортану и Влади што су ме "трпели оволике године оваквог какав сам". Желим да се захвалим и мојој ,,другој" породици, Миди, Десанки, Ивану, Сенки, Милици и Петру.

На крају, желим да се захвалим најзначнијој особи у мом животу, мојој Марији. Без Тебе не бих успео. Теби посвећујем ову тезу.